Robert Marskar

Few- and Single-Cycle Coherent Pulse Propagation in Multi-Level Media

Thesis for the degree of Philosophiae Doctor

Trondheim, May 2014

Norwegian University of Science and Technology
Faculty of Information Technology, Mathematics and Electrical Engineering
Department of Electronics and Telecommunications

NTNU – Trondheim
Norwegian University of
Science and Technology

NTNU
Norwegian University of Science and Technology

Thesis for the degree of Philosophiae Doctor

Faculty of Information Technology, Mathematics and Electrical Engineering
Department of Electronics and Telecommunications

ISBN 978-82-326-0230-8 (printed ver.)
ISBN 978-82-326-0231-5 (electronic ver.)
ISSN 1503-8181

Doctoral theses at NTNU, 2014:154

Printed by NTNU-trykk

Biographical sketch

The author of this thesis was born in Narvik, Norway on September 18, 1984. He entered in the Physics and Applied Mathematics program at the Norwegian University of Science and Technology (NTNU) in August 2004 and received the degree Master of Science and Technology in 2009 with a specialization in fluid mechanics. The author spent the summer of 2008 working in the process and flow technology department at SINTEF, a research institution in Norway. He entered the doctoral program at the Department of Electronics and Telecommunication at NTNU in December 2009, and carried out his doctoral research under the supervision of Professor Ulf L. Österberg.

The research work conducted in this thesis was carried out by Robert Marskar under the advisement of Professor Ulf L. Österberg. This thesis is based on the following publications.

List of Publications

Paper I: R. Marskar and U. Österberg,
Multi-level Maxwell-Bloch simulations in inhomogeneously broadened media,
Optics Express **19**, 16784 (2011).

Paper II: R. Marskar and U. Österberg,
Linear and non-linear optics precursors with self-induced transparency,
Physical Review A **86**, 063286 (2012).

Paper III: R. Marskar and U. Österberg,
Backpropagation and decay of Self-Induced Transparency Pulses,
Physical Review A **89**, 023828 (2014).

Paper IV: R. Marskar and U. Österberg,
Multi-level reduced Maxwell-Bloch equations: Application to femtosecond conical emis-

sion in atomic sodium,
In preparation.

Paper V: R. Marskar and U. Österberg,
Single-cycle coherent terahertz pulse propagation in rigid rotor molecular media,
Submitted to Physical Review **A** (2014).

Acknowledgements

I want to sincerely thank my scientific advisor, Professor Ulf L. Österberg, for his guidance and unprecedented patience while suffering through my incoherent ramblings the past four years. Your perseverance and unwavering support have been pivotal for the completion of this work, and are attitudes that I one day hope to emulate. I also wish to thank Professor Joseph H. Eberly for accomodating me with the graduate students at the Department of Physics and Astronomy during my visit at the University of Rochester. I also thank the institutions that helped bring this work to fruition by providing financial or computational resources. These include travel grants from Department of Electronics and Telecommunication, and allocation of computational resources from NOTUR, the Norwegian Metacenter For Computational Science.

I would also like to extend my gratitude to my fellow graduate students in both Trondheim and Rochester for their cherished friendships. A wholehearted thanks goes out to my parents Turid and Øystein. Finally, I wish to thank my significant other, Silje Erstad, for her patience, encouragement, and unconditional love.

Abstract

Recent experimental realizations of single-cycle pulses in the terahertz, infrared, and optical regions provide promising light sources for applications in telecommunication, medical imaging, spectroscopy, and coherent control. In the resonant regime, the short duration of such pulses imply that they may escape certain effects that are detrimental to coherence; spontaneous emission is one such example. In combination with an octave-spanning spectral bandwidth, an adequate theoretical approach necessitates a semiclassical coherence model outside the conventional few-level, rotating wave, and slowly varying envelope approximations. The evolution equations that govern the underlying dynamics of such systems are inherently nonlinear and possess solutions only in certain idealized, limiting cases. In this thesis we investigate the viability of obtaining general-purpose numerical solutions to such problems.

A computational approach based on Maxwell's equations coupled with a multi-level quantum mechanical model for homogeneously and inhomogeneously broadened media is reported. The formulation leads to a numerical algorithm applicable to bi-directional propagation of pulses of arbitrary duration along all three spatial coordinates. For sufficiently dense inhomogeneously broadened materials we show, numerically, that when the forward propagation approximation of Maxwell's wave equation is not valid, certain types of optical solitons may lose a significant amount of energy with increasing propagation distance through the co-excitation of a backward mode.

A second set of computational routines is based on neglection of optical backpropagation in Maxwell's wave equation. The resulting propagation equation generalizes the paraxial wave equation to the single-cycle pulse regime and is shown to be susceptible to numerical integration in conjunction with quantum theory. Our computer code is applied to femtosecond conical emission in atomic sodium. We find that cone emission occurs together with spatiotemporal pulse breakup analogous to the soliton-type splitting observed in self-induced transparency. We furthermore support these results by presenting complementary numerical calculations of the same phenomenon in the picosecond pulse regime. The angular structure of the conical emission observed numerically agrees with experi-

mental measurements performed by others. Our computational results resolve some of the underlying questions surrounding conical emission in alkali metal vapors.

Consideration of optical selection rules in rigid-rotor molecules is shown to greatly simplify the numerical evaluation of single-cycle pulse propagation in multi-level molecular systems. Numerical application of linearly polarized single-cycle terahertz pulses in rigid rotor molecular media, incorporating a full rotational manifold, shows that coherent bleaching effects ultimately lead to self-steepening of the driving pulse. A possible practical consequence of these results is that coherent, nonlinear saturation effects may partially cancel dispersion-induced temporal broadening of single-cycle pulses, opening up the possibility of increased energy transmission of terahertz pulses through molecular media.

Contents

List of Figures

Chapter 1

Introduction

Electromagnetic waves are extremely versatile for controlling matter in all of its phases. Often, control over an atom or a molecule is exerted by using coherent light pulses shorter than the spontaneous emission lifetime of the medium, and the experimenter is then concerned with the induced electronic or nuclear motion and the propagation characteristics of the pulse - onto which the response of the probed medium is encoded. In resonance studies using moderately intense laser beams, the contemporary theoretical approach is ”half quantum”, meaning that the electromagnetic field is imposed as a spatially and temporally varying classical field, while the medium is treated with quantum theory. The composite model accounts for electromagnetic wave and quantum coherence, and has led to the prediction and comprehension of a number of exotic, non-classical optical effects like adiabatic following [1, 2], electromagnetically induced transparency (EIT) [3, 4], slow light [3, 5], fast light [6, 7] and so on. One of the most surprising phenomena was also one of the first to be discovered. In the late 60s when the production of laser light systems was still under development, McCall and Hahn [8] studied the propagation light pulses tuned close to a resonance in a helium-cooled ruby absorber rod, with surprising results. Remarkably, the reaction of the molecules to the external laser field was to absorb only a fraction of the light - the remainder of the laser light was reshaped into a pulse with a special shape-kinematic relationship that traveled over anomalously long distances without losing significant energy. The phenomenon was termed self-induced transparency (SIT), and McCall and Hahns experimental effort is rightfully regarded to be the first observation of an optical soliton. Their work [8, 9] provoked immediate experimental extensions [10–14] to other kinds of media. Today, solitons are ubiquitous in physics. They represent special mathematical solutions to certain nonlinear wave problems where dispersive and nonlinear wave effects cancel such that a wave form travels with constant shape and velocity.

Technological advances in laser science has currently reached a point where extremely short and intense laser pulses may be generated by using commercially available table-top laser systems. Such pulses are either applied directly or used for generating other pulses in different frequency regions, which are then used by researchers for experimental probing into new venues of physics. For example, optical pumping of a nonlinear crystal with a femtosecond (fs) pulse may, through optical rectification, result in the emission of terahertz radiation [15]. Terahertz (THz) occupies, loosely speaking, the spectral region between microwaves and infrared radiation. Unlike optical radiation which predominantly excites valence electrons in atoms or molecules, THz waves excite low-energy modes like molecular rotations [16], lattice vibrations [17], or spin waves [18]. Nonlinear terahertz technology is still in its infancy, but is presently emerging as a promising research field with applications in biomedical imaging [19], quantum information [20], population control [21], molecular orientation [22], and high-harmonic generation [23]. A theoretical analysis of nonlinear wave THz wave propagation phenomena is inherently difficult because several of the traditional approximations that are invoked in the conventional "half quantum" model are stretched to their limits - or even broken - in this newly opened regime of nonlinear optics [24]. Heralded single-cycle pulses are, for example, now a reality in the terahertz [25], infrared [26], and optical [27] spectral regions, and their spectral widths break with some of the bandwidth constraints that are directly or implicitly engaged in SIT or EIT theory.

The difficulty in obtaining theoretical predictions to nonlinear propagation problems outside the standard approximations has prompted researchers to promote the use of numerical simulations for calculating the material response and its effect on the propagating laser field. Calculations are usually performed within the framework of the finite-difference time-domain (FDTD) method [28] for Maxwell's equations, usually coupled with quantum theory under the two-level restriction [29].

The primary purpose of this work is to detail new numerical methods for pulse propagation models outside the standard approximations, and then apply these methods to the exploration of new physics. To accomplish these goals, this thesis work will be organized as follows. Chapter 2 develops the necessary theoretical framework starting from the Maxwell equations for the electrodynamic field variables, and the Schrödinger equation for the medium. The brief summary provided in this chapter details the notational convention used, and is a theoretical precursor to the remaining contents of this thesis.

Chapter 3 presents a theoretical study of bi-directional SIT pulse propagation. After first carefully deriving a three-dimensional generalized pulse propagation equation, which replaces the paraxial wave equation in the single-cycle regime, we quantify the limitations of the uni-directional propagation assumption. Expanding on the pre-existing set of numerical methods based on the FDTD technique, we report on a numerical method

for homogeneously and inhomogeneously broadened *multi-level* media. This numerical integrator relies on an operator splitting method for the quantum mechanical material response and a pseudospectral method for Maxwell's equations. The algorithm is applied to the McCall-Hahn solution under standard conditions, except for one important distinction; that of a comparatively long Beer's length. We will find that when backpropagation corrections are non-negligible, the McCall-Hahn pulse gradually loses energy with increasing propagation distance through the co-excitation of a backward propagating wave.

Chapter 4 discusses the possible co-existence between a self-induced transparency pulse and an optical precursor. Precursors are forerunners to a main signal and are predicted for almost all kinds of waves; in linear optics, they arise due to color dispersion. We find that nonlinear optical precursors can originate by the injection of an initially transform-limited and resonant pulse with initial pulse area between π and 3π. The generated pre-pulse excites the red and blue wings of the absorption line and is trailed by a soliton with a large time retardation. Our results offers a comparatively straightforward way of measuring both linear and nonlinear optical precursors.

Chapter 5 provides a study of femtosecond conical emission in atomic sodium. Conical emission is surrounded by a controversial history and has been one of the more elusive phenomenon to be explained over the past 4 decades. Presently, no generally accepted theory for pulsed conical emission exists. Conical emission occurs when a near-resonant light pulse propagates on the self-focusing side of an optical resonance, and it manifests itself as a bright ring of light surrounding the central beam spot. Realizing that direct Maxwell simulations are incapable of numerically resolving the macroscopic propagation distances that are involved in conical emission experiments, we develop propagation models based on the propagation equation derived in Chapter 3, which mitigates the shortcomings of direct methods. This numerical algorithm is applied to the propagation of 20 fs few-cycle wavepackets in atomic sodium and we present, for the first time, fully non-perturbative calculations of cone emission in agreement with experiments.

Drawing further on the uni-directional propagation equation, Chapter 6 discusses the propagation of linearly polarized single-cycle THz pulses in rigid rotor molecular media. Exact solutions are derived in the linear propagation regime, and these appear as temporal beats in the time domain. Physically, we suggest that the impulses are the result of interference between various 0π pulses [30]. We supplement these solutions by computer simulations in the nonlinear interaction regime. Notably, a significant improvement is the incorporation of an unprecedented large number of possible energy eigenstates. In the nonlinear propagation regime we find that saturation effects lead to coherent bleaching and self-steepening of single-cycle pulses.

Finally, Chapter 7 provides some concluding remarks.

Chapter 2

The Maxwell-Bloch model

2.1 Introduction

The Maxwell-Bloch (MB) theoretical model is a semi-classical model which describes the interaction of electromagnetic laser pulses with dielectric media, where the electromagnetic field variables are treated as classical fields and the medium is treated quantum mechanically. This model is valid when the laser field intensity is (i) sufficiently high so that single-photon correlations are negligible, and (ii) sufficiently low so that ionization can be disregarded. The first assumption implies that the electromagnetic field may be treated as a continuous variable. The second condition presumes that the field intensity is so low that one may neglect the possibility of molecular dissociation or detachment of a valence electron, and the electronic or nuclear motion is thus confined to bound energy eigenstates. The MB model uses the full electromagnetic wave equation to describe the propagation of the laser field and the Schrödinger equation, or von Neumann equation if density matrices are required, to describe the temporal evolution of the material.

In the remainder of this chapter we discuss the MB theoretical model. We will describe the N-level optical Bloch equations in Sec. 2.2 and their damping mechanisms, before moving on to discussing Maxwell's equations in Sec. 2.3. These equations constitute the theoretical basis for the subsequent chapters in this thesis.

2.2 The optical Bloch equations

The starting point for the optical Bloch equations is the classical Hamiltonian

$$H = \sum_i \frac{(\boldsymbol{p}_i - Q_i \boldsymbol{A})^2}{2m} + q_i \Phi + V, \tag{2.1}$$

where $\boldsymbol{p}_i$ is the canonical momentum of a particle indexed by i, q_i its charge, $\boldsymbol{A}$ and Φ are the electromagnetic vector and scalar potentials, and V is the usual Coloumb interaction. For quantum mechanical systems the continuous field variables become *operators* $H \rightarrow \hat{H}$. In the semi-classical Maxwell-Bloch model, only the atoms are treated quantum mechanically while $\boldsymbol{A}$ is retained as a continuous quantity. One then proceeds by choosing the radiation gauge $\nabla \cdot \boldsymbol{A} = 0$, and then presume that $\boldsymbol{A}$ varies little over the dimensions of an atom or a molecule. Atomic dimensions are on the order of 10^{-10} m, so this approximation, called the *dipole approximation*, may be safely applied even to soft X-rays.

Under the dipole approximation, the Hamiltonian becomes

$$\hat{H} = \hat{H}_0 - \hat{\boldsymbol{\mu}} \cdot \boldsymbol{E}(t, \boldsymbol{r}), \tag{2.2}$$

where $\hat{H}_0 = \frac{\hat{\boldsymbol{p}}^2}{2m} + V$ is the free Hamiltonian and $\hat{\boldsymbol{\mu}}$ is the dipole moment operator. This Hamiltonian is the starting point for an optical Bloch model, where electric charges move not only according to an internal Hamiltonian $\hat{H}_0$, but also due to an externally applied electric field $\boldsymbol{E}$. In principle, $\boldsymbol{E}$ denotes the total electric field. We are, however, concerned with pulse intensities considerably higher than the single-photon level and the contribution of the atomic-self field to $\boldsymbol{E}$ is therefore provisionally ignored.

The time evolution of an atom or a molecule follows the Schrödinger equation

$$i\hbar \frac{\mathrm{d}}{\mathrm{d}t} |\Psi\rangle = \hat{H} |\Psi\rangle , \tag{2.3}$$

where the vector $|\Psi\rangle$ can be expanded in an appropriate set of eigenfunctions. This eigenset is chosen to be the set of eigenfunctions $\{|k\rangle\}$ for $\hat{H}_0$, and one can write

$$|\Psi\rangle = \sum_k c_k |k\rangle . \tag{2.4}$$

It is customary to normalize the state vector such that $\langle\Psi|\Psi\rangle = 1$, in which case the complex coefficients c_k obey the normalization condition $\sum_k |c_k|^2 = 1$, indicating preservation of probability. For real media the number of possible configurations $|k\rangle$ that electric charges can occupy in an atom or a molecule are discretely distributed, but otherwise infinite in extent. However, an external electromagnetic field will usually only couple the lowest excited energy eigenstates of the system, and one may often consider only a finite number of possible electronic or nuclear configurations. The time evolution of this finite set constitutes the optical Bloch equations.

2.2.1 Density matrix equations

In the field of nonlinear optics one usually deals with materials consisting of a number of atoms or molecules so large that it is generally impossible to write down the wavefunction

for the system. The situation is worsened by the fact that the medium is normally coupled to a thermal bath which causes decoherence and ultimately relaxation into a state in thermal equilibrium. While there is no way of writing down the wavefunction of such systems, one may safely treat the medium as a statistical ensemble when the number of particles becomes very large. The density operator of such systems is defined as an ensemble average

$$\hat{\rho} = \sum_i p_i \left|\Psi_i\right\rangle\left\langle\Psi_i\right|, \tag{2.5}$$

where $|\Psi_i\rangle$ is a pure state wave function, representing one of the infinite number of possible microstates in the ensemble. The scalar quantities p_i are probability weights associated with these microstates. In the present context where the medium is treated as a statistical mixture of atoms or molecules, p_i may be thought of as the fraction of atoms or molecules that occupy a microstate $|\Psi_i\rangle$. The sum generally runs over all possible quantum mechanical microstates available in the system. One important advantage of the density operator is that it describes a statistical ensemble in a compact way, while simultaneously incorporating quantum mechanical uncertainties (due to the uncertainty principle) and classical uncertainties (due to incomplete knowledge of particle correlations). In the density operator formalism the Schrödinger equation for the time evolution a pure state is replaced by the von Neumann equation

$$i\hbar \mathrm{d}_t \hat{\rho} = \left[\hat{H}, \hat{\rho}\right], \tag{2.6}$$

for the time evolution of the ensemble. The notation $\mathrm{d}_t \equiv \mathrm{d}/\mathrm{d}t$ is used as a shorthand notation for differentiation, and the square brackets $[,]$ indicate the commutator, i.e. $\left[\hat{H}, \hat{\rho}\right] = \hat{H}\hat{\rho} - \hat{\rho}\hat{H}$.

Expanding the pure states $|\Psi_i\rangle = \sum_k c_k^i |k\rangle$ in Eq. (2.5) expresses $\hat{\rho}$ in the basis states $|k\rangle$,

$$\begin{aligned} \hat{\rho} &= \sum_{k,k'} \left(\sum_i p_i c_k^i {c_{k'}^i}^* \right) \left|k\right\rangle\left\langle k'\right| \\ &\equiv \sum_{k,k'} \rho_{kk'} \left|k\right\rangle\left\langle k'\right|. \end{aligned} \tag{2.7}$$

Equation (2.6) then allows one to consider the evolution of completely mixed states

$$\hat{\rho} = \begin{pmatrix} \rho_{11} & 0 & \dots & 0 \\ 0 & \rho_{22} & \ddots & \vdots \\ \vdots & \ddots & \ddots & 0 \\ 0 & \dots & 0 & \rho_{NN} \end{pmatrix}, \tag{2.8}$$

the special case of pure states

$$\hat{\rho} = \begin{pmatrix} c_1 c_1^* & c_1 c_2^* & \dots & c_1 c_N^* \\ c_2 c_1^* & c_2 c_2^* & \dots & c_2 c_N^* \\ \vdots & \vdots & \ddots & \vdots \\ c_N c_1^* & c_N c_2^* & \dots & c_N c_N^* \end{pmatrix}, \tag{2.9}$$

and any other mixed state fitting in between these two categories. The density operator $\hat{\rho}$ is always semi positive definite. That is, all eigenvalues of $\hat{\rho}$ are greater than or equal to zero. For closed systems, which are the only systems considered in this thesis, probability is conserved $\left(\sum_i p_i = 1\right)$ and $\hat{\rho}$ always has unity trace $\mathrm{Tr}\,(\hat{\rho}) = 1$. The diagonal elements ρ_{kk} are called *populations* because they indicate the probability of measuring a particle in the system in state $|k\rangle$. Since the off-diagonal elements essentially describe the purity of the mixed state (i.e. define a phase-relationship between the atoms or molecules), these are called *coherences*.

In the density matrix formalism detailed above the medium is essentially treated as a statistical mixture of atoms or molecules. To motivate the use of density matrices on a classical level one can consider that an atom resembles, pedagogically speaking, an electron connected to a nucleus with a spring. For an external, harmonically time-varying electric field the equilibrium position of the electron relative to the nucleus will be interrupted and the electron begins to oscillate. The oscillatory motion $x_i(t)$ of the valence electron attached to atom i has both an amplitude x_{0i} and a phase ϕ_i, and can be represented by

$$x_i(t) = x_{0i}(t)\cos(\omega t + \phi_i), \tag{2.10}$$

where it is assumed that the electron oscillates at frequency ω. If one now considers several such atoms occupying a spatial region smaller than an optical wavelength but larger than an atom, the average displacement of the electrons from their respective nuclei is

$$X = \frac{1}{\mathcal{N}} \sum_i x_{0i}(t)\cos(\omega t + \phi_i), \tag{2.11}$$

where $\mathcal{N}$ is the number of atoms or molecules per unit volume. The sum runs over the atoms occupying this unit volume. It is immediately apparent that if all the atoms have the same displacement x_{0i}, and are phased equally ($\phi_i = 0$, for the sake of argument), then X reaches a maximum value of $\pm x_{0i}$ at times $\omega t = n\pi$ where $n = 0, 1, 2, \dots$. On the other hand, if the amplitudes are the same but the phases ϕ_i are distributed randomly, then X evaluates to zero. This simplified physical picture demonstrates the distinction between pure states and mixed states; pure states are states with maximum correlation, or coherence, between each atom (i.e. the individual atoms are described by the same wavefunction) at a specific spatial position in the medium. Mixed states represent states where

the atoms are unequally phased so that macroscopic quantities (or expectation values) can partially or completely wash out by averaging over several measurements. For a completely mixed state there is no definite phase relationship between the atoms or molecules.

For initially pure states a number of physical phenomena may lead to deterioration of the state purity, causing the gradual transition into a mixed state. A handful of these mechanisms are discussed below.

2.2.2 Homogeneous broadening

If an atom is excited, emission of a photon and de-excitation of the valence electron to a lower energy state may occur. This relaxation process occurs at a rate equal to or faster than the reciprocal spontaneous emission lifetime of the relevant transition, and will destroy the excitation amplitude x_{0i} of the oscillator. Spontaneous emission is additionally an incoherent process (i.e. it does not conserve the relative phase of the wavefunction), implying that the relative phases ϕ_i are also affected.

In multi-atomic systems, for example a vapor of alkali metal atoms, the constituents will, due to thermal motion, have a non-zero velocity relative to the laboratory frame and collide with one another. Collision processes may, broadly speaking, be divided into two categories. The first is elastic collisions, where random Stark shifts are imposed on each atom during the collision process. This randomizes the phases of the colliding atoms relative to the remainder of the medium, and leads to decoherence without changes in state populations. The second category is inelastic collisions, where the collision process additionally leads to a collision-induced transition from the excited state to a lower state. In the language of the oscillator picture discussed in the previous section, the two processes randomize the phases ϕ_i (elastic) and destroy the amplitudes x_{0i} (inelastic). Both of these processes lead to homogeneous broadenening of the transition line.

Homogeneous broadening is incorporated by writing Eq. (2.6) in Lindblad form

$$i\hbar \mathrm{d}_t \hat{\rho} = \left[\hat{H}, \hat{\rho}\right] + i\hbar \hat{R}, \tag{2.12}$$

where

$$\hat{R} = \sum_{k,l} \left(\hat{\gamma}_{kl} \hat{\rho} \hat{\gamma}_{kl}^{\dagger} - \frac{1}{2} \hat{\rho} \hat{\gamma}_{kl}^{\dagger} \hat{\gamma}_{kl} - \frac{1}{2} \hat{\gamma}_{kl}^{\dagger} \hat{\gamma}_{kl} \hat{\rho} \right), \tag{2.13}$$

is a relaxation operator. The dagger indicates the Hermitian adjoint, equal to the conjugate transpose for finite-dimensional systems. Here, $\hat{\gamma}_{kl} = \sqrt{\gamma_{kl}} \, |k\rangle\langle l|$, where γ_{kl} is a positive real number, is a damping operator. Operators $\hat{\gamma}_{kl}$ with $k = l$ lead to decoherence, and operators with $k \neq l$ lead to population transfer from state $|l\rangle$ to $|k\rangle$. Note that $\hat{R}$ is introduced phenomenologically, but in a physically meaningful way. Namely, this form of $\hat{R}$ preserves both the semi definite positiveness and trace of $\hat{\rho}$. Effective lifetimes for

each coherence and population element of $\hat{\rho}$ may be derived from Eq. (2.12), and these generally depend on the various relaxation rates γ_{kl}. Writing out Eq. (2.12) elementwise yields

$$\mathrm{d}_t \rho_{mn} = \frac{1}{i\hbar}\left[\hat{H}, \hat{\rho}\right]_{mn} - \sum_j \left(\frac{\gamma_{jm} + \gamma_{jn}}{2}\right) \rho_{mn} \text{ for } m \neq n, \tag{2.14a}$$

$$\mathrm{d}_t \rho_{mm} = \frac{1}{i\hbar}\left[\hat{H}, \hat{\rho}\right]_{mn} + \sum_{j \neq m} \gamma_{mj} \rho_{jj} - \sum_{j \neq m} \gamma_{jm} \rho_{mm}. \tag{2.14b}$$

Here, the sum in Eq. (2.14a) defines the decoherence time $T_2^{(mn)}$ for the ρ_{mn} coherence. Although $T_2^{(mn)}$ is different for each coherence we will condense notation by denoting all of these times by T_2. In cases where this notation becomes ambiguous, we specify which coherence T_2 is associated with. Typically, for dilute alkali metal vapors the homogeneous width T_2^{-1} is on the order of a few hundred MHz, implying that T_2 is tens of nanoseconds long. The sums in Eq. (2.14b) define two processes for the population of state $|m\rangle$. The first sum describes population transfer to state $|m\rangle$ from other states $|j\rangle$, and the second describes population transfer from $|m\rangle$ to other states $|j\rangle$. Following convention, we will denote the time in which population escapes from $|m\rangle$ by $T_1^{(mm)}$, or just T_1 for short.

2.2.3 Inhomogeneous broadening

In real media the effective resonance frequency may differ from atom to atom. In gases, this arises due to the Doppler effect where atoms that move with velocity v relative to the propagation axis effectively see a laser beam with a different central frequency. In the laboratory frame this is equivalent to taking the eigenstate energy of each atom to be $\hbar\omega_i = \hbar\omega_{0i}(1 + v/c)$, where $\hbar\omega_{0i}$ is the eigenstate energy in the rest frame, and $\omega_{0i} v/c$ is the Doppler shift.

By the analogy of the simple oscillator picture, the average displacement for such a medium may be written as

$$X = \frac{1}{\mathcal{N}} \sum_i x_{0i}(t) \cos(\omega_i t + \phi_i), \tag{2.15}$$

where a distribution of resonance frequencies ω_i is incorporated. Like homogeneous broadening, inhomogeneous broadening can also lead to a vanishing X, but through an entirely different process. The medium is now described by a distribution of atoms with different velocities v, where the weight of each v is estimated from the Maxwell-Boltzmann distribution for gases

$$g(v) = \frac{1}{\sqrt{2\pi} v_\mathrm{p}} \exp\left(-\frac{v^2}{2v_\mathrm{p}^2}\right), \tag{2.16}$$

where v_p is the velocity standard deviation. Thus $g(v)\mathrm{d}v$ indicates the fraction of atoms with velocities in the interval $[v, v+\mathrm{d}v]$. Considering $x_{0i} = 1$, $\phi_i = 0$ at $t = 0$, for the sake of simplicity, and evaluating X for such a distribution gives

$$\begin{aligned} X &= \frac{1}{2\sqrt{2\pi}v_\mathrm{p}} \mathrm{e}^{i\omega_{0i}t} \int_{-\infty}^{\infty} \exp\left(-\frac{v^2}{2v_\mathrm{p}^2} + i\frac{\omega_{0i}v}{c}t\right)\mathrm{d}v + \text{c.c.} \\ &= \exp\left(-\frac{t^2}{2T_2^{*2}}\right)\cos(\omega_{0i}t), \end{aligned} \tag{2.17}$$

where $T_2^* = c/(\omega_{0i}v_\mathrm{p})$. Equation (2.17) shows that the macroscopic signal X is exponentially damped at the inhomogeneous lifetime T_2^*. Unlike homogeneous damping, inhomogeneous relaxations may, in certain cases, be reversible because the atomic wavefunction phase changes by a predictable amount, in this case due to a fixed Doppler shift of each atom. Because of this important distinction between the two damping mechanisms, we will refer to inhomogeneous damping as "dephasing", and homogeneous damping as "decoherence".

To incorporate inhomogeneous broadening in the Bloch equations we include a parametric dependence of the free Hamiltonian and density operator on an inhomogeneous broadening variable δ (not necessarily the velocity), such that $\hat{\rho}(t,\boldsymbol{r}) \rightarrow \hat{\rho}(t,\boldsymbol{r};\delta) \equiv \hat{\varrho}_\delta(t,\boldsymbol{r})$. The master equation becomes

$$i\hbar \mathrm{d}_t \hat{\rho}_\delta = \left[\hat{H}_\delta, \hat{\rho}_\delta\right] + i\hbar\hat{R}_\delta. \tag{2.18}$$

In cases where inhomogeneous broadening is disregarded the subscript δ is omitted.

The above method of incorporating inhomogeneous broadening is tantamount to solving Eq. (2.12) for a range of velocities, resonance frequencies, or detunings. In terms of the density matrix the macroscopic polarization of the medium is written as an ensemble average

$$\begin{aligned} \boldsymbol{P} &= \mathcal{N}\int_{-\infty}^{\infty} \mathrm{Tr}\left(\hat{\rho}_\delta\hat{\boldsymbol{\mu}}\right) g(\delta)\mathrm{d}\delta \\ &\equiv \mathcal{N}\langle \mathrm{Tr}(\hat{\rho}_\delta\hat{\boldsymbol{\mu}})\rangle_\delta, \end{aligned} \tag{2.19}$$

where $\mathcal{N}$ is the atomic number density and $g(\delta)$ is normalized such that

$$\int_{-\infty}^{\infty} g(\delta)\mathrm{d}\delta = 1. \tag{2.20}$$

The term $\mathrm{Tr}\left(\hat{\rho}_\delta\hat{\boldsymbol{\mu}}\right)$ is the expectation value of the dipole moment operator of atoms indexed by the inhomogeneous broadening variable δ, and represents essentially the polarization

contribution of these atoms. The macroscopic polarization is then given by the sum of individual atomic or molecular contributions. To condense notation, averaging over the inhomogeneous lineshape is denoted by subscripted angular brackets, i.e. $\langle(\ldots)\rangle_\delta$. In some cases we will sum over detunings Δ or resonances frequencies ω_s, in which case the notation $\langle(\ldots)\rangle_\Delta$ or $\langle(\ldots)\rangle_s$ is used interchangeably.

Without external fields inhomogeneous broadening will lead to dephasing between the atoms and a deterioration of the macroscopic polarization. In the optical regime T_2^* may be less than one nanosecond (ns) and the corresponding inhomogeneous linewidth is usually on the order of tens of GHz. In liquids or glasses different mechanisms dominate, for example fluctuations in the amorphous environment of liquids or doping impurities in glasses. In doped glasses it is most notably material inhomogeneities that lead to inhomogeneous broadening. These impurities lead to local electric and magnetic field variations that are experienced differently at each ion site. The variously experienced local fields then produce, via the Stark effect, local variations in the energy levels leading to inhomogeneous broadening of the transition line. The corresponding spectral width of the inhomogeneous lineshape in bulk media is usually much larger than in gases. In a neodymium glass (Nd:glass) laser, for example, inhomogeneous line widths up to several THz ($T_2^* < 1$ ps) are realistic.

2.3 Maxwell's equations

The propagation of the classical electromagnetic field follows Maxwell's equations

$$\nabla \cdot \boldsymbol{E} = -\frac{1}{\epsilon_0}\nabla \cdot \boldsymbol{P}, \tag{2.21a}$$

$$\nabla \times \boldsymbol{E} = -\frac{\partial \boldsymbol{B}}{\partial t}, \tag{2.21b}$$

$$\nabla \cdot \boldsymbol{B} = 0, \tag{2.21c}$$

$$\nabla \times \boldsymbol{B} = \frac{1}{c^2}\frac{\partial \boldsymbol{E}}{\partial t} + \frac{1}{\epsilon_0 c^2}\frac{\partial \boldsymbol{P}}{\partial t}, \tag{2.21d}$$

where a dielectric material is assumed. Here, $\boldsymbol{B}$ is the magnetic field and the constants ϵ_0 and μ_0 are the permittivity and permeability of free space.

Incorporation of the atomic response via $\boldsymbol{P}$ is standard practice in the treatment of field-matter interactions, and leads to a very complicated nonlinear wave propagation problem. The starting point for such problems is either Eq. (2.21) or the inhomogeneous wave equation which is readily derived from Eq. (2.21) as

$$\partial_t^2 \boldsymbol{E} - c^2\nabla^2 \boldsymbol{E} + c^2\nabla(\nabla \cdot \boldsymbol{E}) = -\frac{1}{\epsilon_0}\partial_t^2 \boldsymbol{P}, \tag{2.22}$$

where $\partial_t \equiv \partial/\partial t$. This equation is susceptible to different levels of approximations discussed later in this thesis.

2.4 Physical Bloch systems

Real atoms and molecules have many possible energy eigenstates and the reduction to an optical Bloch model, which relies either on bandwidth contraints or selection rules, deserves explicit demonstration. A level configuration which has been heavily exploited in quantum optics is the D_2 transition line in ^{87}Rb, which is shown in Fig. 2.1. The ^{87}Rb isotope is often favored over the ^{85}Rb isotope because the ^{87}Rb hyperfine structure has cycling transitions that are more useful for optical pumping. Rubidium has 37 electrons, but in the ground state electronic configuration only one electron occupies the outermost s-shell. This is the only electron that is assumed to respond to the external laser field, while the remaining 36 electrons are presumed to be tightly bound in the $1s^2 2s^2 2p^6 3s^2 3p^6 3d^{10} 4s^2 4p^6$ orbitals. By Unsölds theorem the inner electrons completely fill the inner shells and constitute a spherically symmetric wavefunction, and only the valence electron and the nucleus are dynamic participants. Rubidium therefore behaves, roughly speaking, similarly to the hydrogen atom. The D_2 line is the transition of the active electron between the $5^2S_{1/2}$ and $5^2P_{3/2}$ orbitals at around 780 nm. An additional transition exists from the $5^2S_{1/2}$ to the $5^2P_{1/2}$ level at $\sim$ 795 nm which is known as the D_1 line transition. The ground state $5^2S_{1/2}$ and the excited state $5^2P_{3/2}$ of the outermost electron are each resolved into hyperfine levels F. Each of these levels can again be split into various Zeeman sublevels $m_F = -F, -F+1, \ldots, F-1, F$ by applying an external magnetic field. The hyperfine splitting of the ground state $5^2S_{1/2}$ in ^{87}Rb is approximately 6.83 GHz, while the hyperfine splitting of the excited states is at least one order of magnitude smaller.

If one considers a linearly polarized initial pulse at 780 nm with a bandwidth smaller than the ground state hyperfine splitting but larger than the excited state hyperfine splitting, Fig. 2.1 can be represented as a three-level Λ-system where the $F = 1$ and $F = 2$ manifolds of the $5^2S_{1/2}$ orbital become the two ground states, and the hyperfine manifolds of the excited $5^2P_{3/2}$ are collapsed into a single excited state. If one applies an optical pulse with a bandwidth larger than 6.83 GHz (i.e. duration shorter than 150 ps), the two hyperfine ground states cannot be resolved from one another and may be represented as a single ground state. The D_1 line is not excited if the bandwidth is smaller than 7 THz, placing the pulse duration between 1 ps and 150 ps, in which case Fig. 2.1 may be represented as a two-level Bloch system. In addition to disregarding near-degenerate levels, higher-lying excited states may occasionally be ignored, particularly if they are not close to one- or two-photon resonance. For example, the coupling from the $5^2S_{1/2}$ into one of

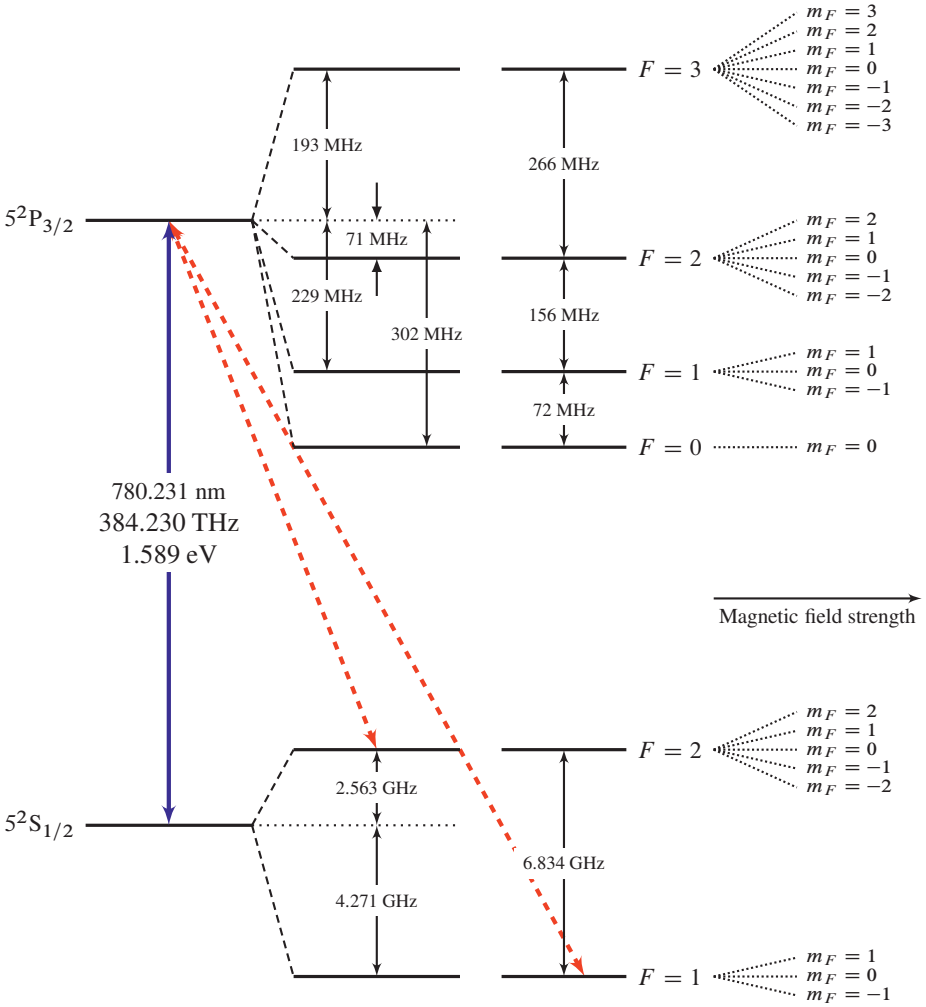

FIG. 2.1: The ^{87}Rb D_2 transition line is an example of a physically realizable two- or three-level system. The dashed line indicate a possible laser configuration for experimentally realizing a Λ-system. The blue line indicates a possible two-level configuration. The line data is obtained from Steck [31].

the fine structure levels of the higher-lying $4d$-orbital may occur if the transition via $5p$ is two-photon resonant. The $5^2S_{1/2} \leftrightarrow 5^2P_{1/2}$ and $5^2S_{1/2} \leftrightarrow 5^2P_{3/2}$ transitions then become virtual transitions, and the valence electron is excited into the $4d$ orbital instead of the $5p$ orbital.

Multi-electron atoms may also be represented as simplified Bloch models where only the motions of the electrons occupying the outermost shell are considered. An example

of such an atom is Strontium, an element with one more nuclear proton than Rubidium. The ground state configuration of atomic strontium is $1s^2 2s^2 2p^6 3s^2 3p^6 3d^{10} 4s^2 4p^6 5s^2$ where two electrons occupy the outer $5s$ shell. In the presence of an external laser field, one, or even two, of these electrons may move into a higher orbital. A transition in Strontium that is exploited in conical emission experiments [32] is the $5s^2\,{}^1\mathrm{S}_0 \rightarrow 5s5p\,{}^1\mathrm{P}_1$ transition at 461 nm.

Bloch models are not unique to atomic electrons, and the relative motion of molecular nuclei may also be described by carefully investigating the possible excitation paths. The energy required to excite nuclear motions is usually considerably smaller than the energy required to excite a valence electron, and for this reason the absorption lines are usually found in the infrared to microwave spectral regions. It is, for example, the molecular librations of liquid water that are responsible for its large absorption coefficient in the microwave region. The prototypical examples of molecular excitations are the rotational, ro-vibrational, and vibronic transitions of a diatomic molecule. In the case of rotational excitation the external laser field exerts a torque through the permanent dipole moment of the molecule, transferring one unit of angular momentum to the molecule which begins to rotate in the laboratory frame. In the case of vibrational excitation, an external laser field causes the two nuclei to oscillate relative to each other.

A model sketch of the energy levels of a diatomic molecule composed of two different nuclei is depicted in Fig. 2.2. The vertical lines show possible excitation patterns for linearly polarized lasers. Like atoms, each angular momentum state j may be split into its Zeeman sublevels by applying a strong, external magnetic field. Labelling each eigenstate of a specific electronic orbital as $|\nu, j, m\rangle$ where j and ν are the rotational and vibrational quantum numbers, and m the Zeeman level, the rotational and ro-vibrational optical transition rules for linearly polarized fields are

$$|\nu, j, m\rangle \leftrightarrow |\nu, j \pm 1, m\rangle \quad \text{(rotational)}, \tag{2.23a}$$

$$|\nu, j, m\rangle \leftrightarrow |\nu \pm 1, j \pm 1, m\rangle \quad \text{(vibrational)}. \tag{2.23b}$$

In addition, for molecules where the spin or orbital angular momentum is non-zero (such as e.g. nitric-oxide), Q-branch transitions $|\nu, j, m\rangle \leftrightarrow |\nu \pm 1, j, m\rangle$ are weakly allowed. For circularly polarized light fields the rotational transition rules are only slightly more complicated, and can be written as $|\nu, j, m\rangle \leftrightarrow |\nu, j \pm 1, m \pm 1\rangle$. That is, circularly polarized fields couple rotational Zeeman levels.

2.5 Naming conventions

The Bloch systems and laser pulses investigated in this report differ in terms of complexity and approximations. For example, we investigate both bi-directional and uni-directional

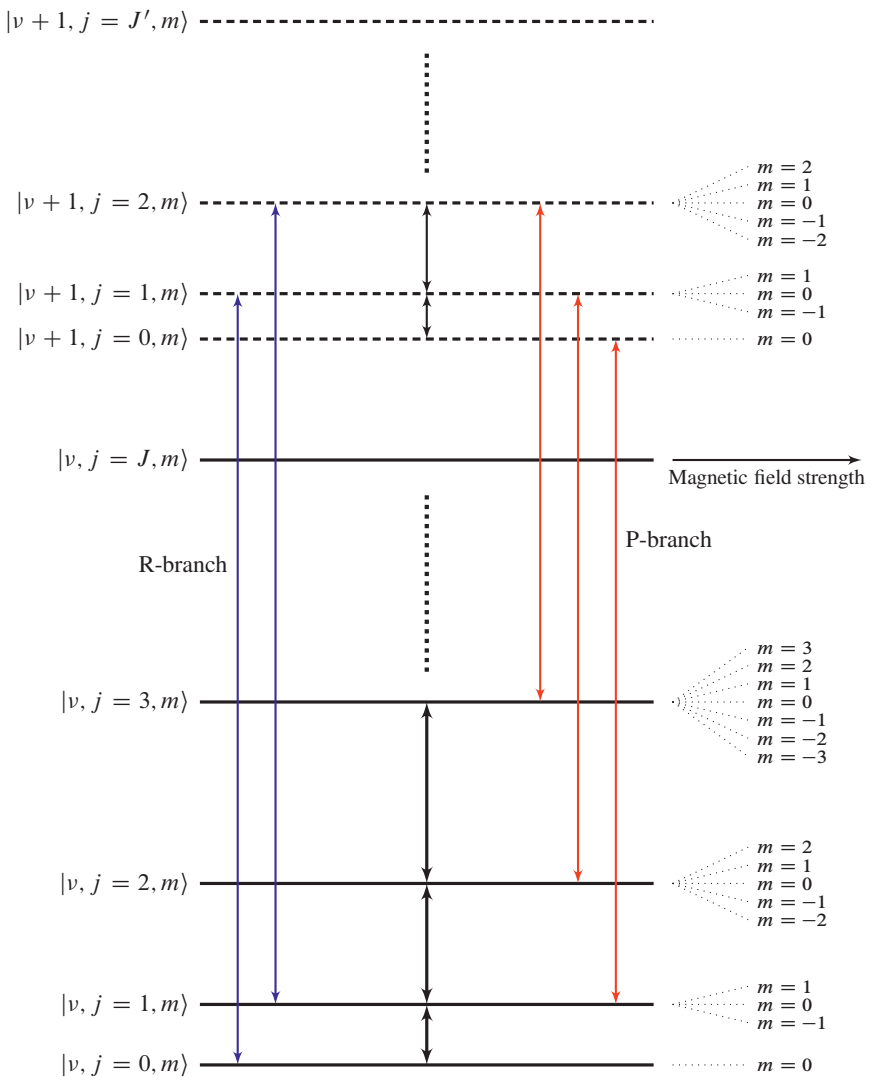

FIG. 2.2: Sketch of the vibrational and rotational level structure of a diatomic molecule with a non-zero permanent dipole moment and zero electronic orbital angular momentum. Vertical lines indicate levels that can be coupled by applying an external laser field.

pulse propagation for both long and short pulses under different levels of approximation. Correspondingly, the equations of motion vary throughout this thesis. To avoid future disorder in referral to the various sets of equations, these are outlined below on a purely pedagogical level. The three categories investigated are:

Maxwell-Bloch equations: The MB equations constitute the full set of equations summarized in this chapter (i.e. the full Maxwell's equations and an optical Bloch model). The MB equations allow bi-directional wave propagation along all three spatial coordinates. We apply these equations to the study of optical backpropagation of SIT pulses in Chapter 3.

Reduced Maxwell-Bloch (RMB) equations: The RMB equations are an approximation of the MB equations when backscattering is neglected and slow spatial evolution over a wavelength is assumed. These equations are applied in Chapter 5 in the study of conical emission, and in Chapter 6 for investigating single-cycle pulse propagation in linear molecules.

SIT equations: The McCall-Hahn set of equations. SIT theory employs the two-level restriction, neglects backscattering, and invokes the rotating wave and slowly varying envelope approximations. We apply the SIT equations in Chapter 4 when investigating optical precursors, and the paraxial SIT equations (i.e. including a transverse spatial dependence) in Chapter 5 in the investigation of conical emission.

Chapter 3

Nonlinear optical backpropagation

3.1 Introduction

In this chapter we model the propagation of linearly polarized ultrashort (i.e. shorter than the homogeneous lifetime) femtosecond pulses in inhomogeneously broadened saturable media. The definitions of the system considered are shown in Fig. 3.1. A laser with central frequency ω_c is presumed to propagate in a medium composed of two-level atoms with resonance frequencies $\omega_s = \overline{\omega} + \Delta$, where $\overline{\omega}$ denotes the center frequency of the absorption line, and Δ denotes the relative atomic detuning. The medium is homogeneously and inhomogeneously broadened with transverse lifetimes T_2 and T_2^* respectively.

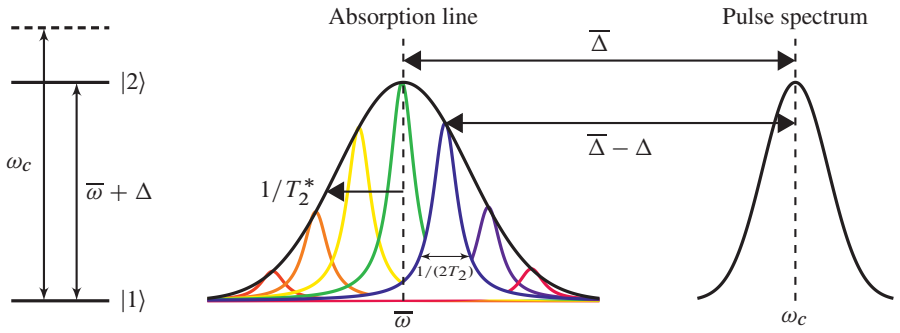

FIG. 3.1: Theoretical two-level medium. The resonance frequency of each atom is $\omega_s = \overline{\omega} + \Delta$ and is distributed according to a normalized function $g(\Delta)$. The average initial laser detuning from the line center is $\overline{\Delta} = \omega_c - \overline{\omega}$.

In Sec. 3.5 we will consider propagation of linearly polarized pulses $\boldsymbol{E} = E_y(t,z)\hat{\boldsymbol{y}}$, $\boldsymbol{B} = B_x\hat{\boldsymbol{x}}$ in a two-level medium with a number density sufficiently high so that the

slowly varying envelope and slowly evolving wave assumptions [33] will break down. The equations of motion are the MB equations under the plane wave assumption,

$$\partial_t E_y = c^2 \partial_z B_x - \frac{1}{\epsilon_0} \partial_t P_y, \tag{3.1a}$$

$$\partial_t B_x = \partial_z E_y, \tag{3.1b}$$

$$i\hbar \mathrm{d}_t \hat{\rho}_\Delta = \left[\widehat{H}_\Delta, \hat{\rho}_\Delta\right], \quad \widehat{H}_\Delta = \widehat{H}_{0\Delta} - \hat{\mu}_y E_y = \begin{pmatrix} 0 & -\mu_{12} E_y \\ -\mu_{12} E_y & \hbar(\overline{\omega} + \Delta) \end{pmatrix}, \tag{3.1c}$$

where $\hat{\mu}_y = \mu_{12}(|1\rangle\langle 2| + |2\rangle\langle 1|)$ is the projection of $\hat{\boldsymbol{\mu}}$ onto the polarization axis of $\boldsymbol{E}$, presumed to lie along y. The diagonal terms of $\widehat{H}_{0\Delta}$ constitute the free Hamiltonian and represent free rotation of the state vector in the Hilbert space spanned by the states $|1\rangle$ and $|2\rangle$. The off-diagonal terms represent interaction with the external laser. By convention, the energy level of $|1\rangle$ is taken to be zero, while the energy of $|2\rangle$ is taken to be equal to the transition energy $\hbar(\overline{\omega} + \Delta)$. Equation (3.1) is a bidirectional propagation model (i.e. it allows propagation along $\pm z$) which must be analyzed numerically in the general case. A numerical procedure for dealing with such problems is presented in Sec. 3.4.

3.2 The McCall-Hahn solution

Before analyzing Eq. (3.1), it is of interest to first review the SIT equations and the McCall-Hahn soliton solution [8, 9], a special solution under the rotating wave and slowly varying envelope approximations. By engaging these approximations the problem is reduced to a one-way propagation model with simplified temporal and spatial evolution. This solution will be compared with numerical solutions in Sec. 3.5 when the one-way propagation approximation is violated.

3.2.1 The rotating wave approximation

The rotating wave approximation (RWA) is an approximation of the interaction Hamiltonian $\hat{\boldsymbol{\mu}} \cdot \boldsymbol{E}$ and applies near resonance $\overline{\Delta} \ll \omega_c$. When the electric field is written

$$E_y(t,z) = \hat{\boldsymbol{y}} \mathcal{E}(t,z) \mathrm{e}^{-i\omega_c t + i k_c z} + \text{c.c.}, \tag{3.2}$$

where $\mathcal{E}(t,z)$ is the pulse envelope, ω_c the carrier frequency, and the wavenumber is defined as $k_c = \omega_c/c$, the RWA is equivalent to approximating $\widehat{H}_\Delta$ as

$$\widehat{H}_\Delta \approx \begin{pmatrix} 0 & -\mu_{12} \mathcal{E}(t,z)^* \mathrm{e}^{i\omega_c t - i k_c z} \\ -\mu_{12} \mathcal{E}(t,z) \mathrm{e}^{-i\omega_c t + i k_c z} & \hbar(\overline{\omega} + \Delta) \end{pmatrix}, \tag{3.3}$$

where column ordering $|1\rangle$, $|2\rangle$ is assumed. Classically, the RWA is equivalent to mathematically disregarding rapidly oscillating exponential terms that quickly average out under

time integration of the Schrödinger equation. The RWA is applicable if the pulse duration is comparatively long with respect to the carrier period, and the pulse is tuned sufficiently close to resonance. For quantized fields, the RWA is equivalent to disregarding virtual photon transitions. That is, one disregards terms in the Hamiltonian representing simultaneous excitation of both atom and field. Such interaction terms lead to, for example, the Lamb shift if only the atomic self-field is considered. When additional external laser fields are present, which is the case here, the RWA leads to neglection of the Bloch-Siegert shift [34], a stimulated shift of the atomic resonance frequency which is relevant when the driving field is strong [35].

The oscillating exponentials in Eq. (3.3) suggest transformation of the state vector (or $\hat{\rho}_\Delta$) into a frame of reference rotating at ω_c. Based on the differential equation

$$i\hbar \mathrm{d}_t \rho_{\Delta,21} = \hbar(\overline{\omega} + \Delta)\rho_{\Delta,21} + \mu_{12}\mathcal{E}\mathrm{e}^{-i\omega_c t + ik_c z}(\rho_{\Delta,22} - \rho_{\Delta,11}) \tag{3.4}$$

for the $\rho_{\Delta,21}$ coherence the transformation $\rho_{\Delta,21} = \varrho_{\Delta,21}\mathrm{e}^{-i\omega_c t + ik_c z}$ is seen to be useful. Furthermore, we take $\varrho_{\Delta,11} = \rho_{\Delta,11}$ and $\varrho_{\Delta,22} = \rho_{\Delta,22}$ [‡]. When this substitution is applied, the von Neumann equation simplifies to

$$i\,\mathrm{d}_t \hat{\varrho}_\Delta = \left[\widehat{\mathcal{H}}_\Delta, \hat{\varrho}_\Delta\right], \quad \widehat{\mathcal{H}}_\Delta = \begin{pmatrix} 0 & -\frac{1}{2}\Omega^* \\ -\frac{1}{2}\Omega & \Delta - \overline{\Delta} \end{pmatrix}, \tag{3.5}$$

where $\overline{\Delta} = \omega_c - \overline{\omega}$ is the detuning of the central laser frequency from the absorption line center. We have defined the pulse Rabi frequency as

$$\Omega = \frac{2\mu_{12}\mathcal{E}}{\hbar}. \tag{3.6}$$

Equation (3.5) describes the atomic evolution in terms of the density operator $\hat{\varrho}_\Delta$ in a frame of reference rotating at ω_c.

3.2.2 The slowly varying envelope approximation

To obtain an equation describing the spatiotemporal evolution of the laser field one proceeds by deriving the wave equation from Eq. (3.1):

$$\left(\partial_z^2 - \frac{1}{c^2}\partial_t^2\right) E_y = \frac{1}{\epsilon_0 c^2}\partial_t^2 P_y. \tag{3.7}$$

The polarization is given by

$$\begin{aligned} P_y &= \mathcal{N}\langle \mathrm{Tr}(\hat{\mu}_y \hat{\rho}_\Delta)\rangle_\Delta \\ &= \mathcal{N}\mu_{12}\left\langle \varrho_{\Delta,21}\mathrm{e}^{-i\omega_c t + ik_c z}\right\rangle_\Delta + \mathrm{c.c.}, \end{aligned} \tag{3.8}$$

[‡]In all that follows, the rotating frame density operator is denoted by $\hat{\varrho}$ and the laboratory frame density operator by $\hat{\rho}$.

where the lineshape average runs over detunings Δ.

Inserting Eq. (3.2) and Eq. (3.8) into Eq. (3.7) and invoking the slowly varying envelope approximation,

$$|\partial_t \mathcal{E}(t,z)| \ll \omega_c \, |\mathcal{E}(t,z)| \,, \tag{3.9a}$$

$$|\partial_z \mathcal{E}(t,z)| \ll k_c \, |\mathcal{E}(t,z)| \,, \tag{3.9b}$$

$$|\partial_t \varrho_{\Delta,21}(t,z)| \ll \omega_c \, |\varrho_{\Delta,21}| \,, \tag{3.9c}$$

leads to a first-order differential equation for the Rabi frequency,

$$(\partial_t + c\partial_z)\,\Omega = i\,\frac{\mathcal{N}\omega_c |\mu_{12}|^2}{\epsilon_0 \hbar} \langle \varrho_{\Delta,21} \rangle_\Delta . \tag{3.10}$$

The slowly varying envelope approximation assumes that the pulse duration is much longer than a carrier period. For optical wavelengths ($\lambda \sim 600$ nm) the carrier period is approximately 0.3 fs so that the temporal part of the SVEA [Eq. (3.9a)] can be safely applied to pulses longer than 30 fs. The spatial part of the SVEA [Eq. (3.9b)] assumes that the pulse envelope evolves slowly over an optical wavelength, an assumption which is equivalent to requiring that the absorption length is much longer than said wavelength. Although this approximation is indeed encountered in most nonlinear optics experiments, the condition may be broken for resonant propagation in dense atomic vapors, as evidenced in the local field experiments by Maki et al. [36]. The final part of the SVEA assumes that the rotating frame atomic variables evolve slowly in time relative to the carrier period of the field, an approximation which is valid when the Rabi frequency is smaller than ω_c. From Eq. (3.1c) it is implied that $|\mu_{12}|E_0/\hbar \ll \omega_c$. For alkali metals $\mu_{12} \sim 10^{-29}$ Cm hence $\omega_c\hbar/\mu_{12} \sim 3.3 \times 10^{10}$ V/m in the optical regime, and if slow evolution is required then E_0 should be smaller than $\sim 3.3 \times 10^8$ V/m, corresponding to intensities less than 15 GW/cm^2.

Traveling reference frame

Equation (3.10) suggests substitution to a new variable $\tau = t - z/c$ that describes the evolution in terms of a delayed time. Formally, introduce

$$\tau = t - z/c = a(\tau, z), \tag{3.11a}$$

$$\xi = z/c = b(\tau, z) \tag{3.11b}$$

and

$$t = e(\tau, \xi) = \tau + \xi, \tag{3.12a}$$

$$z = f(\tau, \xi) = c\xi. \tag{3.12b}$$

Introduce new functions $\Omega'(\tau, z) = \Omega[e(\tau, z), f(\tau, z)] = \Omega[t(\tau, \xi), z(\xi)]$. One finds

$$\begin{aligned} \partial_\xi \Omega' &= \frac{\partial t}{\partial \xi}\frac{\partial \Omega}{\partial t} + \frac{\partial z}{\partial \xi}\frac{\partial \Omega}{\partial z} \\ &= \partial_t \Omega + c\partial_z \Omega, \end{aligned} \tag{3.13}$$

and $\partial_\tau \Omega' = \partial_t \Omega$. Letting $\Omega'(\tau, z) \to \Omega(\tau, z)$ yields $c\partial_z \Omega(\tau, z) = (\partial_t + c\partial_z)\Omega(t, z)$ transforming Eq. (3.10) to

$$\partial_z \Omega = i\frac{\mathcal{N}\omega_c |\mu_{12}|^2}{\epsilon_0 \hbar c}\langle \varrho_{\Delta,21}\rangle_\Delta, \tag{3.14}$$

where $\Omega = \Omega(\tau, z)$ and $\hat{\varrho}_\Delta = \hat{\varrho}_\Delta(\tau, z)$ describe the spatiotemporal evolution in terms of the delayed time τ.

3.2.3 The 2π soliton solution

In this section we will review the propagation of pulses tuned exactly to resonance $\overline{\Delta} = 0$. Homogeneous relaxations are ignored, implying that we investigate time scales much shorter than T_2. The equations of motion are

$$i\,\mathrm{d}_\tau \hat{\varrho}_\Delta = \left[\widehat{\mathcal{H}}_\Delta, \hat{\varrho}_\Delta\right], \quad \widehat{\mathcal{H}}_\Delta = \begin{pmatrix} 0 & -\frac{1}{2}\Omega^* \\ -\frac{1}{2}\Omega & \Delta \end{pmatrix}, \tag{3.15a}$$

$$\partial_z \Omega = i\kappa \langle \varrho_{\Delta,21}\rangle_\Delta, \tag{3.15b}$$

where we condense notation by defining $\kappa \equiv \mathcal{N}\omega_c |\mu_{12}|^2/(\epsilon_0 \hbar c)$. These equations are the McCall-Hahn SIT equations, and they hold under the RWA and SVEA for times $\tau \ll T_2$.

Although Eq. (3.15) is a nonlinear wave equation, a number of exact solutions exist. These solutions can be derived through use of the inverse scattering transform (IST) [37–39], which is essentially a nonlinear Fourier transform where $\Omega(\tau, 0)$ decomposes into a set of "scattering eigenvalues" defined by a Zahkarov-Shabat eigenvalue problem. These eigenvalues "propagate" along z analogous to the way Fourier coefficients do for linear time-invariant problems. Alternative approaches for deriving solutions are through Bäcklund transformation methods [40, 41] or direct integration [8, 9].

The most significant solution to Eq. (3.15) is the 2π soliton solution

$$\Omega(\tau, z) = \frac{2}{T}\,\mathrm{sech}\left[\frac{\tau - z(v_g^{-1} - c^{-1})}{T}\right], \tag{3.16}$$

where T is the nominal pulse duration and v_g is the pulse velocity in the laboratory frame. One notices that Eq. (3.16) is a solution with constant wave form propagating at fixed

velocity v_g in the laboratory frame. This solution represents an optical soliton and is called a 2π pulse because the pulse area

$$\theta(z) = \int_{-\infty}^{\infty} \Omega(\tau, z)\mathrm{d}\tau \tag{3.17}$$

evaluates to $\theta(z) = 2\pi$ for any z. In addition, it is apparent that the 2π pulse does not lose energy during propagation, despite the fact that it propagates resonantly with an atomic transition. For this reason Eq. (3.16) is called a self-induced transparency (SIT) pulse.

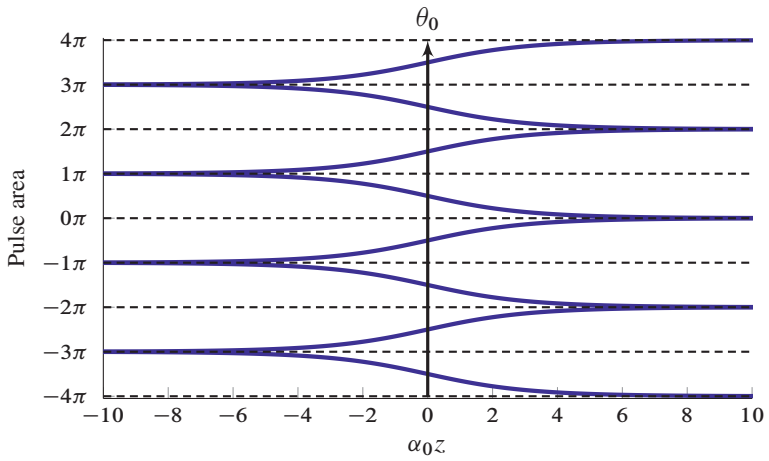

FIG. 3.2: Pulse area theorem. The curves are drawn from Eq. (3.19) for initial areas $\theta_0 = (n + 1/2)\pi$, $n = -4, -3, -2, -1, 0, 1, 2, 3$. Starting at $z = 0$, the solutions move away from odd multiples of π and towards even multiples as $z \to \infty$, corresponding to the attenuator area theorem. Analogously, the area moves away from even multiples of π and toward odd multiples as $z \to -\infty$, corresponding to the amplifier area theorem.

It is possible to derive an evolution equation for the pulse area under restricted conditions. This equation is

$$\partial_z \theta(z) = \mp \frac{\alpha_0}{2} \sin\theta(z), \tag{3.18}$$

where α_0 is the absorption coefficient $\alpha_0 = \pi\kappa g(0)$ [42] and the $\mp$ indicates preparation of the atoms either as an absorber $(-)$, where all the atoms are initially in $|1\rangle$, or as an amplifier $(+)$ where all the atoms are initially prepared in state $|2\rangle$. Equation (3.18) holds provided that (i) the input pulse is resonant and transform-limited (i.e. not chirped), and (ii) the inhomogeneous broadening line is symmetric around its center [43]. One notices immediately from Eq. (3.18) that areas which are integer multiples of π remain constant

during propagation because $\partial_z \theta(z) = \sin n\pi = 0$. When the input area is slightly perturbed from $n\pi$, the area moves toward one of many asymptotes.

The solutions to Eq. (3.18) lead to the pulse area theorem

$$\theta(z) = 2n\pi + 2\arctan\left(\mathrm{e}^{\mp\alpha_0 z/2}\tan\frac{1}{2}\theta_0\right), \tag{3.19}$$

where $\theta_0 = \theta(0)$ is the area on the input plane. For absorbers, the pulse area theorem shows that pulses with initial areas $\theta_0 < \pi$ will evolve into pulses with 0π areas when $z \to \infty$, pulses with areas $\pi < \theta_0 < 3\pi$ will evolve into 2π pulses, areas $3\pi < \theta_0 < 5\pi$ will result in a 4π pulse and so on. For amplifiers, the pulse area theorem shows that pulses will evolve into pulses whose area is always an odd multiple of π. That is, an initial area between 0π and 2π will result in a π-pulse, an initial pulse with area between 2π and 4π will tend to a 3π pulse etc. We have illustrated the pulse area theorem in Fig. 3.2 which shows the evolution of the pulse area along $\pm z$ for various choices of θ_0. Starting at $z = 0$, the attenuator area theorem may be read towards $z > 0$, and the amplifier area theorem towards $z < 0$.

The various asymptotes shown in Fig. 3.2 correspond to different soliton solutions, with the $\pm 2\pi$ asymptotes representing the McCall-Hahn solution. Although the pulse area theorem is immensely helpful in the search for explicit soliton solutions, it is also of limited applicability. For example, the pulse area does not directly pertain to the pulse energy. Broadly speaking, the area obeys the relationship $\theta \sim \Omega_0 T$ while the energy is $\propto |\Omega_0|^2 T$. That is, a shorter 2π soliton is more intense and energetic than a longer 2π soliton. The area theorem does not distinguish between these solutions. Moreover, there is a class of non-trivial independent solutions corresponding to 0π pulse areas. Amongst these solutions is an obvious linearized solution by Crisp [30], but also a nonlinear 0π breather solution [41], which is essentially a coupled oscillation between a 2π pulse and a -2π pulse of the McCall-Hahn type. Moreover, these 0π solutions may occur together with the 2π pulse, without appearing explicitly in the area theorem. In addition, it is also clear that the conditions of resonance, zero chirp, and symmetric line broadening are not necessarily always met and that the area theorem therefore does not always apply. For example, the area does not monotonically approach its stable value if the pulse is initially launched off resonance [43–46].

If the material is prepared as an attenuator, the corresponding solution for the rotating

frame density operator $\hat{\varrho}_\Delta$ is

$$\varrho_{\Delta,11} = \frac{1}{1+(\Delta T)^2}\left(\tanh^2\left[\frac{\tau - z(v_g^{-1}-c^{-1})}{T}\right] + (\Delta T)^2\right), \tag{3.20a}$$

$$\varrho_{\Delta,22} = \frac{1}{1+(\Delta T)^2}\operatorname{sech}^2\left[\frac{\tau - z(v_g^{-1}-c^{-1})}{T}\right], \tag{3.20b}$$

$$\begin{aligned}\varrho_{\Delta,12} = {} & \frac{i}{1+(\Delta T)^2}\operatorname{sech}\left[\frac{\tau - z(v_g^{-1}-c^{-1})}{T}\right] \\ & \times\left(\tanh\left[\frac{\tau - z(v_g^{-1}-c^{-1})}{T}\right] - i\,\Delta T\right),\end{aligned} \tag{3.20c}$$

and $\varrho_{\Delta,21} = \varrho^*_{\Delta,12}$. The explicit solution for $\hat{\varrho}_\Delta$ also demonstrates the transparency of the 2π pulse. One finds that when $\tau \to \pm\infty$ then $\varrho_{\Delta,11} \to 1$ and $\varrho_{\Delta,22} \to 0$ for all detunings Δ, which shows that all atoms are returned to their ground state $|1\rangle$ after the pulse has passed. The 2π SIT pulse owes its transparency to a coherent exchange of energy between the pulse and the medium. Its leading edge is sufficiently strong to coherently excite atoms into state $|2\rangle$, and the pulse is sufficiently short so that the trailing edge coherently brings the atoms back to $|1\rangle$. Note in particular that $\mathrm{Im}(\varrho_{\Delta,21}) > 0$ indicating absorption of the leading edge [recall Eq. (3.14)], while the pulse tail is amplified since $\mathrm{Im}(\varrho_{\Delta,21}) < 0$. By evaluating Eq. (3.20b) it is evident that the pulse completely excites all the resonant atoms $\Delta = 0$ since $\varrho_{0,22} = 1$ at the pulse peak $\tau = z\left(v_g^{-1} - c^{-1}\right)$. The McCall-Hahn 2π pulse solution is plotted in Fig. 3.3 for various times τ and detunings Δ.

The solution for the rotating frame density operator $\hat{\varrho}$ characterizes the evolution of the valence electron when exposed to the McCall-Hahn pulse without detailing the expected location of the electron relative to the nucleus, nor its expected motion relative to the direction of the electric field. Although the McCall-Hahn solution is a solution to a generic two-level system (not necessarily an alkali metal vapor), examination of these quantities in greater detail, which is most conveniently done in terms of the probability density, exposes the remarkable nature of SIT even further. It is sufficient to investigate the behaviour of the resonant atoms $\Delta = 0$. Specifically, one may consider degenerate D_1 and D_2 line transitions, in which case the approximate electronic wave function orbitals are the spherical harmonics $Y_0^0(\theta,\varphi)$ and $Y_1^0(\theta,\varphi)$ for the ground and excited states, respectively. Explicit expressions for these functions, as well as the probability density for density operators, are found in subsection 6.2.3. Here, θ is associated with the polar angle the electron makes with the quantization axis, which is chosen to lie along y (the polarization axis)[‡]. The electronic wave function is then $\Psi(\tau;\theta) = c_1(\tau)Y_0^0(\theta,\varphi) + c_2(\tau)Y_1^0(\theta,\varphi)$, which

[‡]For rotor molecules, the angle θ is reversed and indicates the angle the molecular axis makes with the quantization axis.

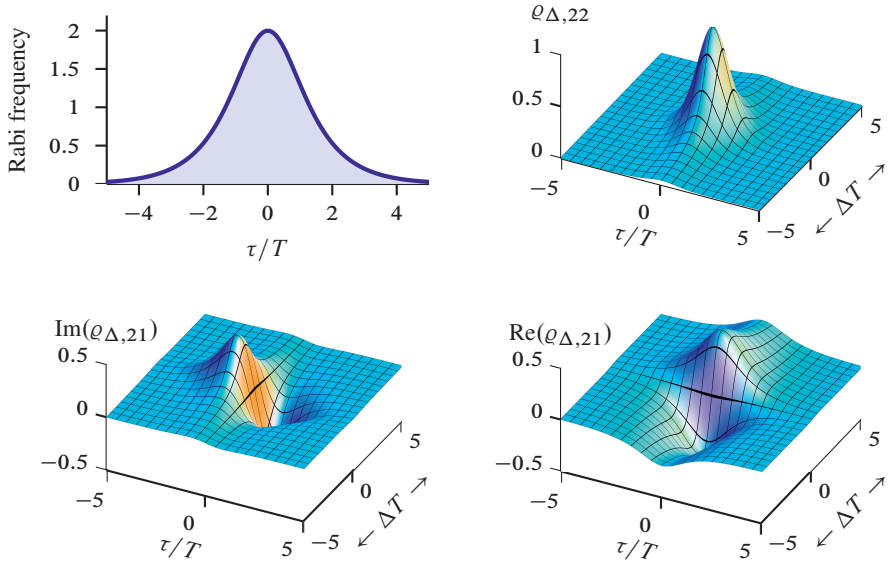

FIG. 3.3: Top left panel: Plot of the McCall-Hahn pulse solution [Eq. (3.16)]. The vertical axis is the Rabi frequency in units of T^{-1} and the horizontal axis the time in units of T. The area under the curve is 2π. Top right panel: Corresponding solution for the excited state population $\hat{\varrho}_{\Delta,22}$ at various detunings Δ (measured in units of T^{-1}). Bottom left panel: Imaginary (absorbtive) part of the rotating frame coherence $\varrho_{\Delta,21}$. Bottom right panel: Real (dispersive) part of the rotating frame coherence $\varrho_{\Delta,21}$. Curves are drawn from Eqs. (3.16) and (3.20).

is symmetric around the quantization axis. Optical selection rules for linearly polarized fields prevent excitation into the $Y_1^1(\theta,\varphi)$ and $Y_1^{-1}(\theta,\varphi)$ orbitals. The notation $\sigma(\tau;\theta)$ indicates the probability of observing the electron at an angle θ from the polarization axis at time τ. For pure states the probability density may be calculated as $\sigma(\tau;\theta) = |\Psi(\tau;\theta)|^2$. The color-coding in Fig. 3.4 shows the probability density $\sigma(\tau;\theta)$ under the excitation of a 5 fs long McCall-Hahn 2π pulse at $z = 0$. The solid line in Fig. 3.4 shows the electric field $E(\tau) = \Omega(\tau)e^{-i\omega_c\tau}$ + c.c. in arbitrary units, where $\Omega(\tau)$ is the McCall-Hahn envelope at $z = 0$, and the dashed line shows the corresponding polarization. All data are generated by numerically solving the rotating frame Bloch equations, and the rotating frame variables are then transformed back into the laboratory frame. Strictly speaking, the SVEA and RWA are not very well satisfied at 5 fs excitation - the short pulse is used only to expose the carrier oscillations of the electron in greater detail, without affecting the interpretation of the phenomenon.

The excitation of the D-lines with a McCall-Hahn pulse forces the initially symmetric probability density to oscillate between the two poles, $\pi/2$ radians out of phase with the

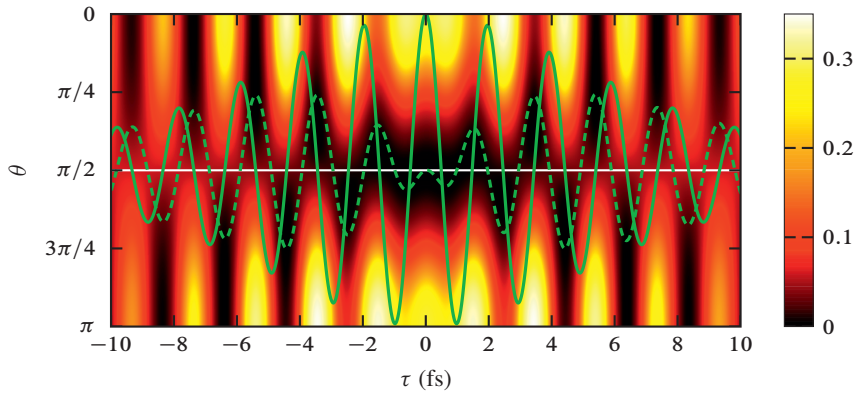

FIG. 3.4: Electronic probability density (color coded) under excitation with a McCall-Hahn 2π pulse. The solid and dashed lines indicate the full electric field and polarization, respectively. The lines are plotted in arbitrary units against the baseline at $\theta = \pi/2$.

electric field. Moving from negative to positive times in Fig. 3.4, one observes that at times where $E = 0$, the probability density $\sigma(\tau;\theta)$ peaks at one of the poles, and $\partial_\tau P = 0$. During the first half of the pulse, the electron moves much like a classical harmonic oscillator with a gradually increasing amplitude. At the crossing-points $E = 0$ in the left half of the figure, one notices that when E becomes positive the electronic probability density is driven towards $\theta = \pi$, and vice versa when E becomes negative, analogous to what is expected from a classical response. When half of the pulse has entered the medium, the valence electron is completely excited into the Y_1^0 orbital. At the second half of the pulse the relative phase between the polarization and the electric field has shifted by an additional factor of π. The implication of this phase change is that the second half of the pulse drives the electron opposite to what is expected from a classical, electrostatic point of view. Starting again from one of the crossing points of E in the right half of the figure, one finds that when E becomes positive the electron is driven towards $\theta = 0$ and the electric and polarization fields will tend to anti-align. Consequently, energy will tend to leave the medium during the second half of the pulse. From the von Neumann equation it may be verified that $\partial_\tau \mathcal{N} \left\langle \mathrm{Tr}\left(\hat{\rho}_\Delta \hat{H}_{0\Delta}\right)\right\rangle_\Delta = E\partial_\tau P$. In the first half of the pulse where $E > 0$ has a turning point $\partial_\tau E = 0$, one finds $\partial_\tau P > 0$ showing that the material is excited by the pulse. At equivalent turning points of E in the second half of the figure, $\partial_\tau P < 0$, showing that the pulse tail drives the electron back towards the Y_0^0 orbital. A remarkable property of the special shape of the hyperbolic secant 2π pulse is that this motion is possible also for symmetrically detuned atoms, showing that an entire absorption line can be coherently excited and de-excited with a single McCall-Hahn 2π

pulse. Overall, one thus finds that the transparency of the 2π pulse is due to coherent energy return on the pulse tail. Note that the process depends intimately on preservation of a definite phase relationship between the induced polarization and the driving pulse; decoherence ruins the return process and prevents complete return to the Y_0^0 orbital.

3.2.4 Other explicit solutions

The McCall-Hahn single pulse solution is by far the most commonly quoted example of SIT. However, other explicit solutions describing lossless propagation exist. Multi-soliton solutions [47] may for example evolve from initial pulses with areas $> 3\pi$. The input pulse may then split into different pieces where each individual piece evolves into a 2π hyperbolic secant pulse. The solitons separate from one another as $\alpha_0 z$ becomes large. Along the same vein, collision of initially separated pulses may also occur. In particular, if one considers a temporally separated initial pair of 2π pulses, one fast and one slow, a collision between the two pulses occurs when the fastest pulse catches up with the slower one. The collision process does not at all occur like the overtaking of linear waves, but in such a way that a phase shift is imposed on the two colliding components - demonstrating a particle-like type of collision. In passing we mention that SIT breather solutions do not break up with propagation distance; they travel with a constant group velocity but contain "internal oscillations". They are discussed in greater detail in the context of the reduced Maxwell-Bloch (RMB) equations in the subsequent section.

An entirely different class of solutions to the SIT equations also exists. Crisp [48] and Eberly [49] have demonstrated the existence of optical pulse train solutions described in terms of Jacobian elliptic functions. Unlike the 2π pulse solution which was experimentally observed immediately after its theoretical prediction, the wave train solution was first observed more than 25 years after its theoretical prediction, then by Shultz and Salamo [50]. It is not surprising that elliptic solutions to the SIT equations exist because under certain conditions the SIT equations reduce to the Sine-Gordon (SG) equation. The SG equation is the equation of motion of a pendulum, for which the solutions are well-known to be elliptic functions.

3.2.5 Few-cycle SIT pulses

We have seen that explicit nonlinear solutions to the SIT equations are possible. Eilbeck et al. [51] have shown that forward-traveling pulse solutions are possible outside both the RWA and the temporal part of the SVEA. To derive their equations one must reduce Eq. (3.7) to a first order differential equation in z by neglecting the effects of backscattering, without invoking the SVEA. We will discuss this reduction in greater detail in the subsequent section. The resulting equations of motion are, by convention, called the

reduced Maxwell-Bloch (RMB) equations, and are analogous to the McCall-Hahn SIT equations. One then proceeds in the same way and derives solutions either through the use of nonlinear transforms or by direct integration. Eilbeck and Bulloughs breather solutions [51–53] hold the same physical significance as the McCall-Hahn solution, and reduce to the McCall-Hahn 2π pulse in the limiting case of temporally long pulses $\omega_c T \gg 1$.

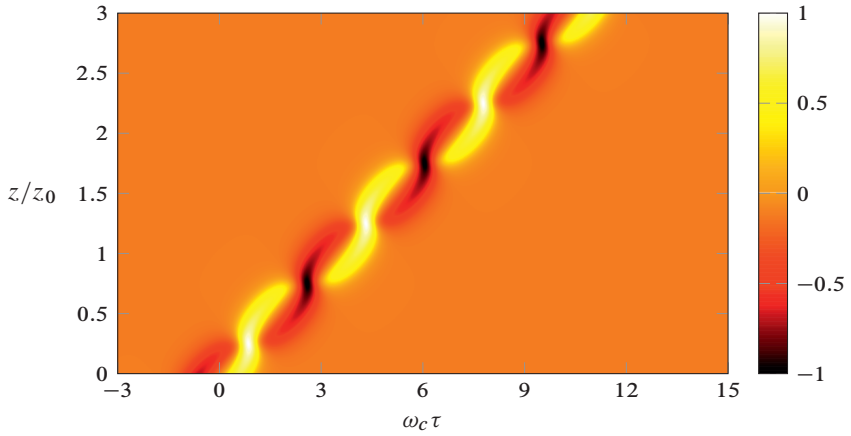

FIG. 3.5: 0π few-cycle breather pulse solution. The color-coded data indicates the value of Ω (in units of $2\Omega_0$) and is drawn from Eq. (3.21) under the condition of exact resonance, $\gamma = 3$, $\delta_R = 0$, and $\delta_I = -\pi/2$. The vertical axis shows the propagation length measured in units of the reshaping length $z_0 = 2\pi c/[\omega_c(m_e - m_c)]$. The horizontal axis indicates the delayed time τ in units of ω_c^{-1}.

Specifically, the generalization of the 2π McCall-Hahn soliton for arbitrary durations is the 0π breather solution

$$\Omega(t,z) = 2\Omega_0 \operatorname{sech}\theta_R \frac{\cos\theta_I - \gamma \sin\theta_I \tanh\theta_R}{1 + \gamma^2 \sin^2\theta_I \operatorname{sech}^2\theta_R}, \tag{3.21}$$

where $\theta_R = \frac{1}{2}\Omega_0(t - m_e z/c) + \delta_R$, $\theta_I = \omega_c(t - m_c z/c) + \delta_I$, and $\gamma = \Omega_0/(2\omega_c)$. Note that in Eq. (3.21), Ω denotes the full Rabi frequency, and is defined $\Omega = \mu_{12}E(t,z)/\hbar$. We otherwise apply the definition $\Omega = 2\mu_{12}\mathcal{E}(\tau,z)/\hbar$ for complex fields. The expressions for the refractive indices m_e and m_c in the sharp line regime are found in e.g. the paper by Bullough et al. [53]. Figure 3.5 shows the propagation of this breather solution for a few propagation lengths. One finds that the RMB breather solution propagates at a reduced group velocity and contains internal oscillations. The pulse recovers its initial temporal shape after propagation lengths that are integer multiples of $2\pi c/[\omega_c(m_e - m_c)]$. In the limit of long pulses $\gamma \to 0$ Eq. (3.21) decomposes into a carrier-envelope expression for

the field and becomes the McCall-Hahn solution [Eq. (3.16)], while to first order in γ the corrections in Eq. (3.21) describes a chirped 2π McCall-Hahn pulse.

The upshot of Eq. (3.21) is that SIT is possible for arbitrary pulse durations and detunings, provided that backscattering corrections of the forward propagation pulse can be ignored. A recent review of the present state of SIT is presented by Maimistov et al. [54], where the McCall-Hahn and RMB solutions are compared in greater detail.

3.3 The uni-directional approximation

Before addressing backpropagation in SIT, we present a relatively straightforward argument in order to reduce the inhomogeneous wave equation into a generic wave equation which allows propagation only along $+z$. The advantage of deriving such an equation, rather than invoking it by the assumption, is that a measure of the influence of backpropagation is returned. The starting point for this derivation is Maxwell's wave equation

$$\partial_t^2 \boldsymbol{E} - c^2\nabla^2\boldsymbol{E} + c^2\nabla(\nabla\cdot\boldsymbol{E}) = -\partial_t^2\chi \star \boldsymbol{P} - \frac{1}{\epsilon_0}\partial_t \boldsymbol{P}_{\rm nl} \tag{3.22}$$

where the total polarization $\boldsymbol{P} = \epsilon_0\chi\star\boldsymbol{E} + \boldsymbol{P}_{\rm nl}$ is presumed to decompose into linear and nonlinear contributions. The star symbol ($\star$) indicates a temporal convolution. We now scale $\boldsymbol{E}$ and $\boldsymbol{P}$ by constants E_c and P_c such that

$$\boldsymbol{E}' = \frac{\boldsymbol{E}}{E_c}, \tag{3.23a}$$

$$\boldsymbol{P}'_{\rm nl} = \frac{\boldsymbol{P}_{\rm nl}}{P_c}, \tag{3.23b}$$

are quantities of order unity. Taking the Fourier transform of Eq. (3.22) yields

$$\left[(i\omega)^2 - c^2\partial_z^2\right]\boldsymbol{E}' = c^2\left[\nabla_\perp^2\boldsymbol{E}' - \nabla(\nabla\cdot\boldsymbol{E}')\right] - (i\omega)^2\chi(\omega)\boldsymbol{E}' - \varepsilon(i\omega)^2\boldsymbol{P}'_{\rm nl}, \tag{3.24}$$

where $\perp$ indicates the transverse components (e.g. $\nabla_\perp^2 = \partial_x^2 + \partial_y^2$), and $\varepsilon \equiv P_c/(\epsilon_0 E_c)$ is assumed to be a small parameter. It is implied in Eq. (3.24) that $\boldsymbol{E}'$ and $\boldsymbol{P}'_{\rm nl}$ are dependent on the variables $(\omega, z, \boldsymbol{r}_\perp)$. To reduce Eq. (3.24) to a uni-directional wave equation, the strategy is to look for solutions with dominant forward traveling parts and forward and backward traveling perturbations,

$$\boldsymbol{E}' = \boldsymbol{E}'_0(\omega,\boldsymbol{r}_\perp)\mathrm{e}^{-i\omega z n/c} + \boldsymbol{E}'_1(\omega,z,\boldsymbol{r}_\perp)\mathrm{e}^{-i\omega z(n-1)/c} + \ldots, \tag{3.25a}$$

$$\boldsymbol{P}'_{\rm nl} = \boldsymbol{P}'_0(\omega,\boldsymbol{r}_\perp)\mathrm{e}^{-i\omega z n/c} + \boldsymbol{P}'_1(\omega,z,\boldsymbol{r}_\perp)\mathrm{e}^{-i\omega z(n-1)/c} + \ldots, \tag{3.25b}$$

where $n(\omega) = \sqrt{1+\chi(\omega)}$ is the linear refractive index of the material. This type of expansion has been applied by Bullough et al. [53] in the development of the RMB equations, but then ε has referred to the total polarization response. Here, we generalize this

argument by taking out the underlying (i.e. linear) evolution and extending it to fully three-dimensional problems. This simple step is sufficient for (i) obtaining a quantitative measure for the uni-directional approximation, and (ii) deriving a three-dimensional uni-directional propagation equation valid for arbitrary pulse durations. This equation is essentially the paraxial wave equation without the slowly varying envelope approximation, and is a very useful starting point for coupling to the optical Bloch equations. The logic behind the expansion in Eq. (3.25) is that backpropagation must necessarily be a nonlinear effect since $\boldsymbol{E}' = \boldsymbol{E}_0'(\omega, \boldsymbol{r}_\perp)\mathrm{e}^{-i\omega z n/c}$ ($\nabla^2 \boldsymbol{E}_0' = 0$) is an exact solution propagating along $+z$ for any $n(\omega)$ when $\varepsilon = 0$. Note that we consider only spatially homogeneous materials. For layered materials, or more generally when $\chi(\omega) \to \chi(\omega, z)$, a wave propagating along $-z$ may arise due to constructive interference of reflections from individual spatial inhomogeneities. The zeroth order solution $\boldsymbol{E}' = \boldsymbol{E}_0'(\omega, \boldsymbol{r}_\perp)\mathrm{e}^{-i\omega z n/c}$ is a wave moving along $+z$ only, and the Ansatz in Eq. (3.25) is not applicable to such media.

Inserting Eq. (3.25) into Eq. (3.24) gives, after some lengthy but straightforward algebra, to order ε:

$$\left(\frac{i\omega n}{c} + \partial_z\right)\boldsymbol{E}' = \frac{c}{2in\omega}\left[\nabla_\perp^2 \boldsymbol{E}' + \frac{\varepsilon}{n^2}\nabla(\nabla\cdot\boldsymbol{P}_{\mathrm{nl}}')\right] - \varepsilon\frac{i\omega}{2nc}\boldsymbol{P}_{\mathrm{nl}}' + \mathcal{O}(\varepsilon^2). \qquad (3.26)$$

Note that $\varepsilon \ll 1$ is central to the convergence of Eq. (3.25) and the derivation of Eq. (3.26); the reduction to a wave equation that is a first order differential in the propagation coordinate then arises primarily due to the fact that the nonlinear polarization propagates as a forward wave to order ε, with backscattered corrections becoming $\mathcal{O}(\varepsilon^2)$. Note that this equation is derived by assumption, but self-consistently to $\mathcal{O}(\varepsilon)$.

Equation (3.26) shows that the electric field obeys a forward propagation equation along $+z$ and demonstrates that phase-matching of a counter-propagating pulse can be disregarded to first order if the optical nonlinearity is sufficiently small, provided that the field originally propagates in the forward direction. This is true without invoking assumptions about the underlying evolution (e.g. slow evolution over a wavelength). We point out that $\varepsilon \ll 1$ is a *sufficient* but not a necessary condition for one-way propagation. In fact, exact solutions to Eq. (3.1) describing forward propagating half-cycle solitons that are immune against backpropagation for any ε have been derived by Bullough and Ahmad [55].

3.3.1 Simplified propagation equations

Having shown that phase-matching of a backwards pulse is negligible for $\varepsilon \ll 1$, we will now proceed by showing that several known wave equations are automatically retrieved using this condition. Firstly, the definition of a propagation problem usually coincides with the assumption of a weak nonlinearity and a comparatively long Beer's length. Further

simplifications than Eq. (3.26) are then possible. Letting $\chi(\omega) \sim \mathcal{O}(\epsilon)$ in Eq. (3.24) and denoting the scaled total polarization by $\boldsymbol{P}'$ has the effect of giving $n \to 1$ and $\boldsymbol{P}'_{\mathrm{nl}} \to \boldsymbol{P}'$ in Eq. (3.25), where ε now also contains linear contributions. We then obtain in the time domain

$$\partial_t \left(\frac{1}{c} \partial_t + \partial_z \right) \boldsymbol{E}' = \frac{c}{2} [\nabla_\perp^2 \boldsymbol{E}' + \varepsilon \nabla (\nabla \cdot \boldsymbol{P}')] - \frac{\varepsilon}{2c} \partial_t^2 \boldsymbol{P}'. \tag{3.27}$$

In physical terms, this is equivalent to the slowly evolving wave assumption [33], indicating that the material induces negligible changes to the field over a distances comparable to a wavelength. In principle, Eq. (3.27) can be used for analyzing nonlinear pulse propagation in the forward direction, although the divergence term $\nabla(\nabla \cdot \boldsymbol{P}')$ contains complicated z-derivatives and does not straightforwardly transform into a moving frame. A simplified equation can be derived when the field polarization is sufficiently transverse during propagation. Taking $\boldsymbol{P}' = \boldsymbol{P}'_\perp + \varepsilon P'_z \hat{\boldsymbol{z}}$ in Eq. (3.27) one obtains to order ε:

$$\partial_t \left(\frac{1}{c} \partial_t + c \partial_z \right) \boldsymbol{E}'_\perp = \frac{c}{2} \left[\nabla_\perp^2 \boldsymbol{E}'_\perp + \varepsilon \nabla_\perp (\nabla_\perp \cdot \boldsymbol{P}'_\perp) \right] - \frac{\varepsilon}{2c} \partial_t^2 \boldsymbol{P}'_\perp. \tag{3.28}$$

This allows switching to a traveling reference frame with delayed fields

$$\boldsymbol{E}'(t, z, \boldsymbol{r}_\perp) \to \boldsymbol{E}'(\tau, z, \boldsymbol{r}_\perp) \tag{3.29}$$

which yields

$$\partial_{z\tau} \boldsymbol{E}'_\perp = \frac{c}{2} [\nabla_\perp^2 \boldsymbol{E}'_\perp + \varepsilon \nabla_\perp (\nabla_\perp \cdot \boldsymbol{P}'_\perp)] - \frac{\varepsilon}{2c} \partial_\tau^2 \boldsymbol{P}'_\perp, \tag{3.30}$$

where $\boldsymbol{E}' = \boldsymbol{E}'(\tau, z, \boldsymbol{r}_\perp)$ and $\boldsymbol{P}' = \boldsymbol{P}'(\tau, z, \boldsymbol{r}_\perp)$ are the delayed fields. The conditions under which the longitudinal electric field component remains negligibly small during propagation can be quantified as follows. Using delayed fields for the longitudinal component, Eq. (3.27) changes to

$$\partial_{z\tau} E'_z = \frac{c}{2} \left[\nabla_\perp^2 E'_z + \varepsilon (\partial_z - c^{-1} \partial_\tau)(\nabla_\perp \cdot \boldsymbol{P}'_\perp) \right]. \tag{3.31}$$

Next, $\nabla_\perp^2 E'_z$ describes diffraction of the longitudinal component and is physically uninteresting in comparison to the remainder of the right-hand side. Under the slowly evolving wave assumption we can approximate

$$\left(\partial_z - c^{-1} \partial_\tau \right) (\nabla_\perp \cdot \boldsymbol{P}') \approx -c^{-1} \partial_\tau \left(\nabla_\perp \cdot \boldsymbol{P}'_\perp \right) \tag{3.32}$$

since the characteristic wavelength $\lambda_c = c/f$, where $1/f$ is a typical time scale (usually the carrier period) of the field, is shorter than the length scale L which describes the distance over which changes to the pulse are induced by the polarized material. Keeping this term and letting $\nabla_\perp = \nabla'_\perp / R_c$ where the constant R_c is a length scale such that $\nabla'_\perp \cdot \boldsymbol{P}'_\perp$ is of order unity yields $\partial_z E'_z \sim \varepsilon / R_c$. Hence, if the longitudinal component is initially

zero then it will certainly remain negligible if the propagation distance is $z \ll R_c/\varepsilon$. In most cases R_c denotes the beam waist so this holds under quite general conditions, and Eq. (3.30) is therefore a useful substitute for Eq. (3.22). Traditionally, the divergence term $\nabla_\perp \left(\nabla_\perp \cdot \boldsymbol{P}'_\perp\right)$ is dropped despite the apparent conflict with the underlying form of the solutions $\left[\text{i.e. } \boldsymbol{P}'_\perp = \boldsymbol{P}'_\perp(\tau, z, \boldsymbol{r}_\perp)\right]$, which constitutes the transition to a scalar wave equation and has been discussed by Lax [56]. Having derived Eq. (3.34) cognizant of the divergence term being of order ε in the absence of transverse spatial inhomogeneities in the medium, we can quantify the conditions under which $\nabla(\nabla \cdot \boldsymbol{E})$ can be dropped from Eq. (3.22). Using the previous scaling where $1/f$ is a typical timescale and letting $\partial_\tau \boldsymbol{P}'_\perp = f\,\partial_T \boldsymbol{P}'_\perp$ where $\partial_T \boldsymbol{P}'_\perp$ is of order unity, Eq. (3.30) leads to

$$\partial_{zT} \boldsymbol{E}'_\perp = \frac{\lambda_c}{2}\left(\frac{1}{R_c^2}\nabla'^{\,2}_\perp \boldsymbol{E}'_\perp + \frac{\varepsilon}{R_c^2}\nabla'_\perp(\nabla'_\perp \cdot \boldsymbol{P}'_\perp) - \frac{\varepsilon}{\lambda_c^2}\partial_T^2 \boldsymbol{P}'_\perp\right). \tag{3.33}$$

For weakly focused beams $R_c \gg \lambda_c$ the divergence term is the least dominant term on the right-hand side and can be dropped. The plane wave limit is also recovered when $2\varepsilon R_c^2 \gg \lambda_c^2$. For strongly focused beams, $R_c \sim \lambda_c$, the longitudinal field component grows roughly as λ_c/ε. Meanwhile, Eq. (3.33) shows that diffraction dominates the evolution of the transverse field on the length scale λ_c, which is much shorter than the length scale associated with the longitudinal component. Under such focusing conditions both the divergence term and the source term $\partial_T^2 \boldsymbol{P}'_\perp$ must be kept. Recovering standard units we now find for Eq. (3.30)

$$\partial_{z\tau} \boldsymbol{E} = \frac{c}{2}\left[\nabla_\perp^2 \boldsymbol{E} + \epsilon_0^{-1}\nabla_\perp(\nabla_\perp \cdot \boldsymbol{P})\right] - \frac{1}{2\epsilon_0 c}\partial_\tau^2 \boldsymbol{P}. \tag{3.34}$$

In Eq. (3.34) and all that follows, we have omitted the subscript $\perp$ such that $\boldsymbol{E}$ and $\boldsymbol{P}$ denote the delayed transverse fields.

Equation (3.34) is the forward wave equation (FWE) which is a forward propagation approximation to Maxwell's wave equation. It applies to the electric field $\boldsymbol{E}$ without requiring a pulse envelope and phase, and describes the three-dimensional vectorial propagation of pulses of arbitrary duration and intensity. It was derived from the assumption of a sufficiently small nonlinearity and disregards backpropagation. Note that backpropagation is a nonlinear bulk phenomenon unrelated to spatial inhomogeneities in the medium, and qualitatively resembles pulsed self-reflection. However, backpropagation is a real effect and the conditions under which it becomes relevant have most likely been met in the local field experiments by Maki et al. [36]. In practice, macroscopic backpropagation is most likely to occur near a very strong optical resonance. Note also that Eq. (3.34) implies a long Beer's length but not necessarily a refractive index close to unity. Formally one may take $\chi(\omega) = \chi_0 + \varepsilon\chi_1(\omega)$ in Eq. (3.24), which just has the effect $c \to c/\sqrt{1+\chi_0}$, $\varepsilon \to \varepsilon/(1+\chi_0)$ in Eq. (3.30). In other words, if the absorption length is long but the

refractive index is high, then this is equivalent to taking c in Eq. (3.34) to be the background phase velocity in the material. We anticipate that Eq. (3.34) therefore holds for most cases of practical interest. Using $P_c = \mathcal{N} p_c$ where p_c is a measure of the single atom/molecule nonlinear polarization and $\mathcal{N}$ is the number density of the material shows that the backpropagation approximation is primarily one of *density*.

The FWE is consistent with other wave equations found in the literature: Generalized self-induced transparency theories [52] use the FWE under the simplifying approximations $\boldsymbol{E} = E(t,z)\hat{\boldsymbol{x}}$, $\nabla_\perp^2 \boldsymbol{E} = 0$, and a similar first-order equation has been derived by Leblond et al. [57] by using multiple scales analysis. By disregarding $\nabla_\perp(\nabla_\perp \cdot \boldsymbol{P})$ we recover the first order propagation (FOP) equation derived by Geissler et al. [58]

$$\partial_{z\tau} \boldsymbol{E} = \frac{c}{2} \nabla_\perp^2 \boldsymbol{E} - \frac{1}{2\epsilon_0 c} \partial_\tau^2 \boldsymbol{P}. \tag{3.35}$$

By taking the Fourier transform of Eq. (3.35) with respect to τ and $\boldsymbol{r}_\perp$ we recover the spectral wave equation found by Kolesik and Moloney [59] which was derived by modal expansions of $\boldsymbol{E}$ and retaining the forward traveling parts. A similar approach was considered by Husakou and Herrmann [60]. We also mention the projection equation by Kolesik et al. [61] and the useful factorization approach by Kinsler [62], which solves for pairwise forward/backward fields (Eq. (3.26) is formally equivalent to the forward field equation in the paper by Kinsler [62]).

The power of the above approach is that the premature assumption of unidirectionality is avoided, and that a criterion for making the forward propagation approximation in the first place is obtained. The validity of this approximation in theoretical models is justified either through experimental knowledge or analytic or numerical computations of the nonlinear optical properties of the material. Intuitively, one may initially suspect that knowledge of a full solution to Eq. (3.22) is necessary before a uni-directional propagation assumption can be justified. Unlike other results [58–62] which rely on Maxwell's equations, we show that only the constitutive relation $\boldsymbol{P} = \boldsymbol{P}(\boldsymbol{E})$ is necessary for establishing a unidirectional approximation. Knowledge of this criterion is pivotal for determining whether a specific pulse propagation problem should use the full or reduced version of Eq. (3.22). We emphasize that this condition is *local*, and is easily evaluated numerically for a few test-pulses before solving (or even choosing!) a pulse propagation equation.

3.3.2 Envelope equations

The FWE governs the propagation of the electric field rather than its envelope. Nevertheless, complex envelope and enhanced envelope equations can be recovered straightfor-

wardly: Let

$$\boldsymbol{E}(\tau, z, \boldsymbol{r}_\perp) = \boldsymbol{\mathcal{E}}(\tau, z, \boldsymbol{r}_\perp)\mathrm{e}^{-i\omega_c\tau} + \text{c.c.}, \tag{3.36a}$$

$$\boldsymbol{P}(\tau, z, \boldsymbol{r}_\perp) = \boldsymbol{\mathcal{P}}(\tau, z, \boldsymbol{r}_\perp)\mathrm{e}^{-i\omega_c\tau} + \text{c.c.}, \tag{3.36b}$$

where ω_c is the carrier frequency as determined on the input plane. Substituting these expressions into the FWE yields

$$\partial_z\boldsymbol{\mathcal{E}} = \frac{c}{2}(\partial_\tau - i\omega_c)^{-1}\left[\nabla_\perp^2\boldsymbol{\mathcal{E}} + \epsilon_0^{-1}\nabla_\perp(\nabla_\perp\cdot\boldsymbol{\mathcal{P}})\right] - \frac{1}{2\epsilon_0 c}(\partial_\tau - i\omega_c)\boldsymbol{\mathcal{P}}, \tag{3.37}$$

which is the nonlinear envelope equation (NEE) derived by Brabec and Krausz [33]. It is readily verified that dropping the terms proportional to ∂_τ in Eq. (3.37) constitutes the SVEA and returns the paraxial wave equation,

$$\partial_z\boldsymbol{\mathcal{E}} = \frac{i}{2k_c}\nabla_\perp^2\boldsymbol{\mathcal{E}} + \frac{i\omega_c}{2\epsilon_0 c}\boldsymbol{\mathcal{P}}. \tag{3.38}$$

We will apply this equation in Chapter 5 when investigating conical emission in two-level media. Under the additional approximation $\nabla_\perp^2\boldsymbol{\mathcal{E}} \approx 0$ one recovers

$$\partial_z\boldsymbol{\mathcal{E}} = i\frac{\omega_c}{2\epsilon_0 c}\boldsymbol{\mathcal{P}}, \tag{3.39}$$

which is equivalent to Eq. (3.10). We remark however that Eq. (3.34) puts the paraxial wave equation in a broader reference frame since only the assumption of uni-directionality is a necessary ingredient. In light of Eq. (3.34), which is valid for arbitrary pulse durations, the SVEA is associated only with the temporal pulse duration and is just an optional addition. Neglect of backpropagation and assumption of a long Beer's length are more important approximations. Complete conformance with the NEE is achieved by disregarding the divergence term and extracting the linear polarization $\boldsymbol{\mathcal{P}}_\mathrm{l}$ from $\boldsymbol{\mathcal{P}} = \boldsymbol{\mathcal{P}}_\mathrm{l} + \boldsymbol{\mathcal{P}}_\mathrm{nl}$, and then calculating the linear contribution $\boldsymbol{\mathcal{P}}_\mathrm{l} = \epsilon_0\mathcal{F}^{-1}[\chi(\omega)\boldsymbol{\mathcal{E}}(\omega)]$ where the linear susceptibility $\chi(\omega)$ is expanded in a Taylor series around ω_c. $\mathcal{F}^{-1}$ denotes the inverse Fourier transform. By discarding the diffraction term $\nabla_\perp^2\boldsymbol{\mathcal{E}}$, the resulting equation can be further reduced to the nonlinear Schrödinger equation (NLS) in Kerr media [33].

3.3.3 Energy conservation

An energy conservation equation which replaces Poynting's theorem can be derived for Eq. (3.34) in the frequency domain. Letting $\boldsymbol{E} = E_1\hat{\mathbf{1}} + E_2\hat{\mathbf{2}}$ where $\hat{\mathbf{1}}$ and $\hat{\mathbf{2}}$ are the transverse polarization eigenvectors (e.g. $\hat{\boldsymbol{x}}$, $\hat{\boldsymbol{y}}$ or $\hat{\boldsymbol{r}}$, $\hat{\boldsymbol{\varphi}}$), taking the Fourier transform of Eq. (3.34), multiplying by $\boldsymbol{E}^*(\omega)$ and adding the complex conjugate yields

$$\nabla\cdot\boldsymbol{J}(\omega) + \frac{i\omega}{2}\left[\boldsymbol{E}^*(\omega)\cdot\boldsymbol{P}(\omega) - \boldsymbol{E}(\omega)\cdot\boldsymbol{P}^*(\omega)\right] = 0, \tag{3.40}$$

where $\boldsymbol{J}(\omega)$ is the spectral energy "current" with longitudinal and transversal components

$$J_z(\omega) = \epsilon_0 c|\boldsymbol{E}(\omega)|^2, \tag{3.41}$$

$$\boldsymbol{J}_\perp(\omega) = \frac{i\epsilon_0 c^2}{2\omega}\left(\sum_{i=1,2} E_i^*(\omega)\nabla_\perp E_i(\omega) - \boldsymbol{E}^*(\omega)[\nabla_\perp \cdot \boldsymbol{E}(\omega)]\right) + \text{c.c.} \tag{3.42}$$

The inverse transform of Eq. (3.40) yields a continuity equation in the time domain, demonstrating that energy is conserved (to $\mathcal{O}(\varepsilon)$) in the forward propagation approximation. Note that $J_z \geq 0$ which is necessary for any uni-directional model. As mentioned above, the divergence term activates when the beam waist becomes comparable to a wavelength. Retaining this term is necessary, for example, in the modeling of catastrophic self-focusing in Kerr media [63]. Furthermore, we define the vector fluence

$$\boldsymbol{F} = \int_{-\infty}^{\infty} \boldsymbol{J}(\omega)\mathrm{d}\omega, \tag{3.43}$$

such that the quantity $\boldsymbol{F} \cdot \mathrm{d}\boldsymbol{S}$ describes the energy delivered through a differential surface $\mathrm{d}\boldsymbol{S}$.

3.4 Numerical Maxwell-Bloch methods

It is expected that when $\varepsilon = P_c/(\epsilon_0 E_c)$ becomes comparable to unity the uni-directional approximation may break down. It is evident that uni-directional SIT theory cannot capture the complete evolution of the electromagnetic field because it a priori assumes that the backscattering corrections are negligible. It is of considerable interest to investigate the behavior of the 2π SIT pulse when these approximations do not apply.

To theoretically analyze the bi-directional propagation of a pulse the full wave equation is called for. Although we will analyze propagation only in the plane wave approximation, a generic computer algorithm can be formulated for the full Maxwell equations for multi-level media. This method is of particular interest for analyzing the propagation of short pulses in nonlinear crystals, but is in principle applicable to any system whose spatial dimensions are no larger than a millimeters (for optical frequencies).

3.4.1 Tetradic notation: Liouville space

We consider first the time evolution equation for the density operator $\hat{\rho}_\delta$ which is assumed to be of finite dimension $N \times N$. A parametric dependence of the density operator on an inhomogeneous variable δ is also assumed in the remainder of this section. In computer

implementations it is convenient to use tetradic notation and parametrize $\hat{\rho}_\delta$ into a column-major ordered vector $|\rho_\delta\rangle\!\rangle$ defined by

$$|\rho_\delta\rangle\!\rangle = \begin{pmatrix} \rho_{\delta,11} \\ \rho_{\delta,21} \\ \vdots \\ \rho_{\delta,12} \\ \rho_{\delta,22} \\ \vdots \\ \rho_{\delta,N-1,N} \\ \rho_{\delta,NN} \end{pmatrix}. \tag{3.44}$$

Every other operator (e.g. $\widehat{H}$, $\hat{\boldsymbol{\mu}}$) follows the same flattening. Following convention we will refer to this space as Liouville space. Note that the ordering of the entries in the super-ket $|\rho_\delta\rangle\!\rangle$ is not important; for computational efficiency however, column- or row-major ordering should be used for compilers that favor column- or row-major ordering memory.

For column-ordered vectors the matrix equation

$$\widehat{C} = \widehat{A}\widehat{X}\widehat{B} \tag{3.45}$$

where $\widehat{A}$, $\widehat{B}$, $\widehat{C}$, and $\widehat{X}$ are $N \times N$ matrices can be written as an equivalent vector equation

$$|C\rangle\!\rangle = \left(\widehat{B}^{\mathsf{T}} \otimes \widehat{A}\right)|X\rangle\!\rangle \tag{3.46}$$

in Liouville space. From Eq. (2.18) it is then straightforward to verify that $|\rho_\delta\rangle\!\rangle$ obeys the Schrödinger equation

$$\mathrm{d}_t\,|\rho_\delta\rangle\!\rangle = \left(\check{L}_\delta + \boldsymbol{E}\cdot\check{\boldsymbol{L}}_1\right)|\rho_\delta\rangle\!\rangle\,, \tag{3.47}$$

where

$$\check{L}_\delta = i\,\widehat{H}_\delta^{\mathsf{T}} \oplus \left(-\widehat{H}_\delta\right) + \sum_{k,l}\left[\hat{\gamma}_{kl}\otimes\hat{\gamma}_{kl} - \frac{1}{2}(\hat{\gamma}_{kl}^{\mathsf{T}}\hat{\gamma}_{kl}) \oplus \left(\hat{\gamma}_{kl}^{\mathsf{T}}\hat{\gamma}_{kl}\right)\right], \tag{3.48a}$$

$$\check{\boldsymbol{L}}_1 = -i\,\hat{\boldsymbol{\mu}}^{\mathsf{T}} \oplus (-\hat{\boldsymbol{\mu}})\,, \tag{3.48b}$$

where $\check{L}_\delta$ is the free Liouville operator and $\boldsymbol{E}\cdot\check{\boldsymbol{L}}_1$ is an interaction operator. Here, $\otimes$ is the tensor product and $\oplus$ is the Kronecker sum $\widehat{A}\oplus\widehat{B} = \widehat{A}\otimes\hat{I}_{\dim\left(\widehat{B}\right)} + \hat{I}_{\dim\left(\widehat{A}\right)}\otimes\widehat{B}$, where $\hat{I}$ is the unity operator. Note that Eq. (3.47) is just the von Neumann rewritten in a column-major form; no actual calculations or approximations have been made. As such, the formulation in Liouville space may seem unnecessarily extravagant. In fact, the singular theoretical advantage of using tetradic notation is that Eq. (3.47) is the Schrödinger

equation, and well-known formally exact solutions exist even in the presence of homogeneous relaxations.

For every operator $\widehat{\mathcal{O}}$ in Hilbert space there exists an equivalent column vector $|\mathcal{O}\rangle\!\rangle$ in Liouville space. The vectors are expanded as

$$|\mathcal{O}\rangle\!\rangle = \sum_{j,k} \mathcal{O}_{jk}\, |jk\rangle\!\rangle\,. \tag{3.49}$$

We define a bra-vector $\langle\!\langle\mathcal{O}|$ that corresponds to $\widehat{\mathcal{O}}^\dagger$ and a scalar product of two vectors defined by

$$\langle\!\langle\mathcal{O}_1|\,\mathcal{O}_2\rangle\!\rangle = \mathrm{Tr}\left(\widehat{\mathcal{O}}_1^\dagger \widehat{\mathcal{O}}_2\right). \tag{3.50}$$

The macroscopic polarization is equal to

$$\begin{aligned} \boldsymbol{P} &= \mathcal{N}\big\langle \mathrm{Tr}\,(\hat{\rho}_\delta \hat{\boldsymbol{\mu}})\big\rangle_\delta \\ &= \mathcal{N}\big\langle \langle\!\langle \boldsymbol{\mu}|\,\rho_\delta\rangle\!\rangle\big\rangle_\delta. \end{aligned} \tag{3.51}$$

We will also need the temporal rate of change of the polarization,

$$\begin{aligned} \partial_t \boldsymbol{P} &= \mathcal{N}\partial_t\big\langle \langle\!\langle \boldsymbol{\mu}|\,\rho_\delta\rangle\!\rangle\big\rangle_\delta \\ &= \mathcal{N}\Big\langle \langle\!\langle \boldsymbol{\mu}|\check{L}_\delta + \boldsymbol{E}\cdot\check{\boldsymbol{L}}_1|\rho_\delta\rangle\!\rangle\Big\rangle_\delta. \end{aligned} \tag{3.52}$$

3.4.2 Maxwell's equations: Pseudospectral time-domain

The first numerical discretization of the two-level MB equations [Eq. (3.1)] appears in a paper by Ziolkowski et al. [29] who employed a finite-difference time-domain (FDTD) method for Maxwell's equations in conjunction with a Crank-Nicholson method for the temporal evolution of the atomic variables. Ziolkowskis method has been adopted by others [64–66]. The approach leads to a coupled set of equations which can be solved with fixed point routines such as a predictor-corrector method. The coupled method works very well provided that the plane wave and two-level approximations holds. An extension of the two-level FDTD method for inhomogeneously broadened media has been presented by Schlottau et al. [67]. When more than two-levels are considered, the Crank-Nicholson method leads to a discretization scheme that does not necessarily preserve the semi-definite positiveness of $\hat{\rho}_\delta$ [68]. In addition, for propagation in two or three dimensions the staggered Yee grid inherent in the FDTD method leads to a very large coupled linear set of equations that is very time consuming to invert for anything but micrometer sized optical components [69, 70]. Both of these drawbacks can be remedied by applying different discretization methods.

To reduce accumulation of numerical round-off errors the Maxwell-Bloch equations are first scaled into a dimensionless set of equations where the variables are scaled according to a characteristic field magnitude E_c and a characteristic dipole moment μ_c such that

the variables

$$\boldsymbol{E} \to \frac{\boldsymbol{E}}{E_c}, \tag{3.53a}$$

$$\boldsymbol{B} \to \frac{\boldsymbol{B}}{cE_c}, \tag{3.53b}$$

$$\hat{\boldsymbol{\mu}} \to \mu_c \hat{\boldsymbol{\mu}}, \tag{3.53c}$$

are quantities of order unity. In the same way, we scale the time and space coordinates

$$t \to \frac{\mu_c E_c}{\hbar} t, \tag{3.54a}$$

$$\boldsymbol{r} \to \frac{\mu_c E_c}{\hbar c} \boldsymbol{r}, \tag{3.54b}$$

$$\check{L} \to \frac{\hbar}{\mu_c E_c} \check{L}. \tag{3.54c}$$

Note that time is now measured in units of the reciprocal characteristic Rabi frequency $E_c \mu_c / \hbar$ and length in units of $\hbar c / (\mu_c E_c)$.

With the scalings above the Maxwell-Bloch equation set is summarized by the two dimensionless Maxwell curl equations and the Schrödinger equation

$$\frac{\partial \boldsymbol{B}}{\partial t} = -\nabla \times \boldsymbol{E}, \tag{3.55a}$$

$$\frac{\partial \boldsymbol{E}}{\partial t} = \nabla \times \boldsymbol{B} - \zeta \left\langle \left\langle\!\left\langle \boldsymbol{\mu} \middle| \check{L}_\delta + \boldsymbol{E} \cdot \check{\boldsymbol{L}}_1 \middle| \rho_\delta \right\rangle\!\right\rangle \right\rangle_\delta, \tag{3.55b}$$

$$\mathrm{d}_t \left| \rho_\delta \right\rangle\!\right\rangle = \left(\check{L}_\delta + \boldsymbol{E} \cdot \check{\boldsymbol{L}}_1 \right) \left| \rho_\delta \right\rangle\!\right\rangle, \tag{3.55c}$$

where $\zeta \equiv \frac{1}{\epsilon_0} \frac{\mathcal{N} \mu_c}{E_c}$, and $\check{L}_\delta$ and $\check{\boldsymbol{L}}_1$ are given by Eq. (3.48).

A pseudospectral method [71, 72] together with leap-frog time-stepping can be applied for the integration of Eq. (3.55) in the general case. Pseudospectral methods allow the use of co-located spatial grids for all the fields, while at the same time offering a significant improvement over finite difference method in terms of numerical accuracy. We consider a Cartesian numerical grid where the fields are sampled on co-located grids with equidistant grid spacings. Specifically, the fields are sampled on

$$x_\mathrm{i} = \mathrm{i} \triangle x, \tag{3.56a}$$

$$y_\mathrm{j} = \mathrm{j} \triangle y, \tag{3.56b}$$

$$z_\mathrm{k} = \mathrm{k} \triangle z, \tag{3.56c}$$

where $\triangle x$, $\triangle y$, and $\triangle z$ are the numerical step sizes for each of the three spatial dimensions. We define the Fourier derivative operator in the spatial d-direction by

$$\partial_d^{\mathcal{F}} G = \mathcal{F}_d^{-1} \left[2\pi i k_d \mathcal{F}_d(G) \right], \tag{3.57}$$

where k_d is the spatial frequency in the d-direction, and G is a field component of either $\boldsymbol{E}$ or $\boldsymbol{B}$. $\mathcal{F}_d$ and $\mathcal{F}_d^{-1}$ denote the Fourier and inverse Fourier transforms in the d-direction, and are implemented using a Fast Fourier Transform (FFT) technique [73]. When discretized, the approximated temporal time-stepping is denoted by $\partial_t G \approx \mathbb{D}^t G$. We will consider temporally staggered grids such that $\boldsymbol{E}$ is stored at integer time steps $t_{\mathrm{n}} = \mathrm{n}\triangle t$, while $\boldsymbol{B}$ and $|\rho_\delta\rangle\!\rangle$ are stored at half integer time steps $t_{\mathrm{n}+1/2} = (\mathrm{n}+1/2)\triangle t$. With this discretization scheme, Maxwell's equations become

$$\mathbb{D}^t B_x\big|^{\mathrm{n}}_{\mathrm{i,j,k}} = -\left(\partial_y^{\mathcal{F}} E_z - \partial_z^{\mathcal{F}} E_y\right)\big|^{\mathrm{n}}_{\mathrm{i,j,k}}, \tag{3.58a}$$

$$\mathbb{D}^t B_y\big|^{\mathrm{n}}_{\mathrm{i,j,k}} = -\left(\partial_z^{\mathcal{F}} E_x - \partial_x^{\mathcal{F}} E_z\right)\big|^{\mathrm{n}}_{\mathrm{i,j,k}}, \tag{3.58b}$$

$$\mathbb{D}^t B_z\big|^{\mathrm{n}}_{\mathrm{i,j,k}} = -\left(\partial_z^{\mathcal{F}} E_y - \partial_y^{\mathcal{F}} E_x\right)\big|^{\mathrm{n}}_{\mathrm{i,j,k}}, \tag{3.58c}$$

and

$$\mathbb{D}^t E_x\big|^{\mathrm{n}+1/2}_{\mathrm{i,j,k}} = \left(\partial_y^{\mathcal{F}} B_z - \partial_z^{\mathcal{F}} B_y\right)\big|^{\mathrm{n}+1/2}_{\mathrm{i,j,k}} - \zeta\left\langle\!\!\left\langle \mu_x \middle| \check{L}_\delta + \boldsymbol{E}\cdot\check{\boldsymbol{L}}_1 \middle| \rho_\delta \right\rangle\!\!\right\rangle_\delta\Big|^{\mathrm{n}+1/2}_{\mathrm{i,j,k}}, \tag{3.59a}$$

$$\mathbb{D}^t E_y\big|^{\mathrm{n}+1/2}_{\mathrm{i,j,k}} = \left(\partial_z^{\mathcal{F}} B_x - \partial_x^{\mathcal{F}} B_z\right)\big|^{\mathrm{n}+1/2}_{\mathrm{i,j,k}} - \zeta\left\langle\!\!\left\langle \mu_y \middle| \check{L}_\delta + \boldsymbol{E}\cdot\check{\boldsymbol{L}}_1 \middle| \rho_\delta \right\rangle\!\!\right\rangle_\delta\Big|^{\mathrm{n}+1/2}_{\mathrm{i,j,k}}, \tag{3.59b}$$

$$\mathbb{D}^t E_z\big|^{\mathrm{n}+1/2}_{\mathrm{i,j,k}} = \left(\partial_z^{\mathcal{F}} B_y - \partial_y^{\mathcal{F}} B_x\right)\big|^{\mathrm{n}+1/2}_{\mathrm{i,j,k}} - \zeta\left\langle\!\!\left\langle \mu_z \middle| \check{L}_\delta + \boldsymbol{E}\cdot\check{\boldsymbol{L}}_1 \middle| \rho_\delta \right\rangle\!\!\right\rangle_\delta\Big|^{\mathrm{n}+1/2}_{\mathrm{i,j,k}}. \tag{3.59c}$$

The use of Fourier transforms for calculating the spatial derivatives means that the spatial derivatives are calculated exactly as long the sampling period is above the Nyquist limit. Usually, the temporal time stepping is taken as a second order Yee-type leapfrogging method

$$\mathbb{D}^t G\big|^{\mathrm{n}+1/2} \approx \frac{G^{\mathrm{n}+1} - G^{\mathrm{n}}}{\triangle t} + \mathcal{O}\left(\triangle t^2\right). \tag{3.60}$$

Due to the second order accuracy of this time stepping scheme, we will refer to this as a PSTD-2 method.

Note that although the PSTD spatial scheme allows the use of relatively rough spatial grids (in principle the sampling rate may be as low as the Nyquist limit), the Yee time stepping is a source of numerical dispersion. This implies that the temporal resolution must be considerably finer than the Nyquist limit in order to counteract the effects of numerical dispersion accumulation. The limitations of the PSTD-2 method can be partially overcome by using higher order time stepping [74]. The starting point for a higher order method is the Taylor expansion of G around the time step t_{n}:

$$\begin{aligned} G^{\mathrm{n}\pm1/2} \approx\ & G^{\mathrm{n}} \pm \frac{\triangle t}{2}\left(\partial_t G\right)^{\mathrm{n}} + \frac{1}{2!}\left(\frac{\triangle t}{2}\right)^2\left(\partial_t^2 G\right)^{\mathrm{n}} \pm \frac{1}{3!}\left(\frac{\triangle t}{2}\right)^3\left(\partial_t^3 G\right)^{\mathrm{n}} \\ & + \mathcal{O}\left(\triangle t^4\right), \end{aligned} \tag{3.61}$$

such that

$$(\partial_t G)^{\mathrm{n}} \approx \frac{G^{\mathrm{n}+1/2} - G^{\mathrm{n}-1/2}}{\triangle t} - \frac{1}{24}\left(\partial_t^3 G\right)^{\mathrm{n}} + \mathcal{O}\left(\triangle t^4\right). \tag{3.62}$$

Note that this stepping is of order $\triangle t^4$ since the time derivative operators of even order cancel in Eq. (3.62). Rather than discretizing the third order time derivatives $\partial_t^3 G$ these may be converted to spatial derivatives through Maxwell's curl equations, and they may then be calculated with Fourier transforms. This is referred to as a PSTD-4 method. Provided that ζ is sufficiently small, one can disregard the contributions from the polarization terms and calculate the fourth order corrections using the electromagnetic field variables alone.

Since the largest computational burden of the full Maxwell-Bloch equations is the numerical update of the optical Bloch equations, the PSTD-4 method generally performs faster than the PSTD-2 method at the same accuracy because rougher spatial grids can be used.

The PSTD method has a more stringent condition on the maximum allowed time step size than the FDTD scheme does. The temporal resolution must be chosen according to $\triangle t \leq 2\min\left(\triangle x, \triangle y, \triangle z\right)/\left(\sqrt{D}\pi\right)$ where D is the dimensionality of the system.

The periodicity implied by the use of numerical Fourier transforms means that absorbing boundary conditions must be placed on the computational boundaries in order to prevent reflections from the truncated simulation regions. We have implemented absorbing layers by using the perfectly matched layer (PML) technique by Berenger [75].

3.4.3 Discretization of the Bloch equations: The Magnus series

The Bloch equations can be solved exactly in terms of a time-ordered propagator. Noting that $\check{L}_\delta$ are constant operators, i.e. operators without any time-dependence, one may first transform the Bloch equations into the interaction picture by defining

$$\check{U}_\delta(\triangle t) = \exp\left[\check{L}_\delta(t - t_0)\right], \tag{3.63a}$$

$$|\rho_{\delta,I}\rangle\rangle = \check{U}_\delta^{-1}\,|\rho_\delta\rangle\rangle\,. \tag{3.63b}$$

This leads to a Schrödinger equation for the interaction picture density operator $|\rho_{\delta,I}\rangle\rangle$

$$\mathrm{d}_t\,|\rho_{\delta,I}\rangle\rangle = \check{L}_{\delta,I}\,|\rho_{\delta,I}\rangle\rangle\,, \tag{3.64}$$

where

$$\check{L}_{\delta,I} = \check{U}_\delta^{-1}\left(\boldsymbol{E}\cdot\check{\boldsymbol{L}}_1\right)\check{U}_\delta, \tag{3.65}$$

is the interaction picture Liouville operator. The above equations are identical to the von Neumann equation for the interaction picture density operator $\hat{\rho}_{\delta,I}$, but written in vector form for incorporation of relaxations.

The exact solution to Eq. (3.65) is a time-ordered solution

$$|\rho_{\delta,I}(t)\rangle\!\rangle = \exp_+\left(\int_{t_0}^{t} \check{L}_{\delta,I}(\tau)\mathrm{d}\tau\right)|\rho_{\Delta,I}(t_0)\rangle\!\rangle\,, \tag{3.66}$$

where $\exp_+$ indicates time-ordering of the propagator. The time-ordered exponential operator can be expanded in an explicit series known as the Magnus series [76]

$$\exp_+\left(\int_{t_0}^{t} \check{L}_{\delta,I}\mathrm{d}t\right) = \exp\left[\sum_{n=1}^{\infty} \check{M}_n(t,t_0)\right], \tag{3.67}$$

where the first few terms are

$$\check{M}_1 = \int_{t_0}^{t} \mathrm{d}\tau_1 \check{L}_{\delta,I}(\tau_1), \tag{3.68a}$$

$$\check{M}_2 = \int_{t_0}^{t} \mathrm{d}\tau_1 \int_{t_0}^{\tau_1} \mathrm{d}\tau_2 \left[\check{L}_{\delta,I}(\tau_2), \check{L}_{\delta,I}(\tau_1)\right], \tag{3.68b}$$

$$\begin{aligned}\check{M}_3 = \int_{t_0}^{t} \mathrm{d}\tau_1 \int_{t_0}^{\tau_1} \mathrm{d}\tau_2 \int_{t_0}^{\tau_2} \mathrm{d}\tau_3 \Big(&\Big[\check{L}_{\delta,I}(\tau_3), [\check{L}_{\delta,I}(\tau_2), \check{L}_{\delta,I}(\tau_1)]\Big] \\ &+ \Big[[\check{L}_{\delta,I}(\tau_3), \check{L}_{\delta,I}(\tau_2)], \check{L}_{\delta,I}(\tau_1)]\Big]\Big).\end{aligned} \tag{3.68c}$$

The higher-order terms of the Magnus series rapidly become incalculable. Numerically, we therefore consider a time step $t - t_0 = t_{\mathrm{n}+1/2} - t_{\mathrm{n}-1/2} = \triangle t$ which is sufficiently small so that the higher-order contributions are negligible. Under this assumption the solution for $|\rho_{\delta,I}\rangle\!\rangle$ is approximated as

$$\left|\rho_{I,v}^{\mathrm{n}+1/2}\right\rangle\!\rangle \approx \exp\left[\check{M}_1(\triangle t)\right]\left|\rho_{I,v}^{\mathrm{n}-1/2}\right\rangle\!\rangle. \tag{3.69}$$

We approximate the integral by the central midpoint rule:

$$\begin{aligned}\check{M}_1(\triangle t) &= \int_{t_{\mathrm{n}-1/2}}^{t_{\mathrm{n}+1/2}} \mathrm{d}t \check{L}_{\delta,I}(t) \\ &\approx \check{L}_{\delta,I}^{\mathrm{n}} \triangle t.\end{aligned} \tag{3.70}$$

Furthermore, consistent with the first-order Magnus series approximation we may take $\check{L}_{\delta,I} \approx \boldsymbol{E}^{\mathrm{n}} \cdot \check{\boldsymbol{L}}_1$ since the corrections introduced in Eq. (3.65) become second order in $\triangle t$ in the exponential argument. This implies that only one interaction propagator needs to

be calculated at each spatial point at each time step, dramatically reducing the number of floating point operators necessary for evaluating inhomogeneously broadened systems.

We note furthermore that the matrix exponential $\exp(\boldsymbol{E}^{\mathrm{n}} \cdot \check{\boldsymbol{L}}_1)$ is an $N^2 \times N^2$ dimensional square matrix. One can use the property

$$\exp\left(\widehat{\mathcal{O}}_1 \oplus \widehat{\mathcal{O}}_2\right) = \exp\left(\widehat{\mathcal{O}}_1\right) \otimes \exp\left(\widehat{\mathcal{O}}_2\right), \tag{3.71}$$

of the Kronecker sum and the hermiticity of $\hat{\boldsymbol{\mu}}$ to reduce this matrix to a tensor product between two $N \times N$ matrices

$$\begin{aligned} \exp(\boldsymbol{E}^{\mathrm{n}} \cdot \check{\boldsymbol{L}}_1) &= \exp\left(-i\,\boldsymbol{E}^{\mathrm{n}} \cdot [\hat{\boldsymbol{\mu}}^{\intercal} \oplus (-\hat{\boldsymbol{\mu}})]\right) \\ &= \exp\left(i\,\boldsymbol{E}^{\mathrm{n}} \cdot \hat{\boldsymbol{\mu}}\,\triangle t\right)^{*} \otimes \exp\left(i\,\boldsymbol{E}^{\mathrm{n}} \cdot \hat{\boldsymbol{\mu}}\,\triangle t\right). \end{aligned} \tag{3.72}$$

Obviously, only one of these matrices need to be calculated numerically. Finally, the numerical solution for the Schrödinger picture density operator is then

$$\left|\rho_{\delta}^{\mathrm{n}+1/2}\right\rangle\!\!\right\rangle = \check{U}_{\delta}\left[\exp\left(i\,\boldsymbol{E}^{\mathrm{n}} \cdot \hat{\boldsymbol{\mu}}\,\triangle t\right)^{*} \otimes \exp\left(i\,\boldsymbol{E}^{\mathrm{n}} \cdot \hat{\boldsymbol{\mu}}\,\triangle t\right)\right]\left|\rho_{\delta}^{\mathrm{n}-1/2}\right\rangle\!\!\right\rangle. \tag{3.73}$$

One can increase the rate of convergence by splitting the free propagator in Eq. (3.73)

$$\left|\rho_{\delta}^{\mathrm{n}+1/2}\right\rangle\!\!\right\rangle = \check{U}_{\delta}^{1/2}\left[\exp\left(i\,\boldsymbol{E}^{\mathrm{n}} \cdot \hat{\boldsymbol{\mu}}\,\triangle t\right)^{*} \otimes \exp\left(i\,\boldsymbol{E}^{\mathrm{n}} \cdot \hat{\boldsymbol{\mu}}\,\triangle t\right)\right]\check{U}_{\delta}^{1/2}\left|\rho_{\delta}^{\mathrm{n}-1/2}\right\rangle\!\!\right\rangle, \tag{3.74}$$

which leads to a second-order method in $\triangle t$. Reading from right to left, Eq. (3.74) is essentially a second-order split step method where propagation of the density operator in time is performed by first taking a half linear step followed by a full nonlinear step followed by another half linear step. Since the discretization method was based on the Magnus series, $\hat{\rho}$ is guaranteed to be semi positive definite and have unity trace for *any* choice of $\triangle t$. That is, Eq. (3.74) is an absolutely stable discretization method for the homogeneously and inhomogeneously broadened multi-level Bloch equations of arbitrary dimension N.

The matrix exponential in Eq. (3.74) must be calculated in order to advance $\left|\rho_{\delta}^{\mathrm{n}-1/2}\right\rangle\!\!\right\rangle$ in time. A straightforward way of calculating the matrix exponential is through the second-order approximation

$$\exp\left(i\,\boldsymbol{E}^{\mathrm{n}} \cdot \hat{\boldsymbol{\mu}}\,\triangle t\right) \approx \left(\hat{I} - \frac{i\,\boldsymbol{E}^{\mathrm{n}} \cdot \hat{\boldsymbol{\mu}}\,\triangle t}{2}\right)^{-1}\left(\hat{I} + \frac{i\,\boldsymbol{E}^{\mathrm{n}} \cdot \hat{\boldsymbol{\mu}}\,\triangle t}{2}\right), \tag{3.75}$$

which allows calculating the matrix exponential through an inverse matrix. Here, $\hat{I}$ denotes the N-dimensional identity matrix. Temporal evolution is unitary in this approximation since evaluation of

$$\left[\left(\hat{I} - i\,\hat{A}\right)^{-1}\left(\hat{I} + i\,\hat{A}\right)\right]^{\dagger} = \left(\hat{I} - i\,\hat{A}\right)\left(\hat{I} + i\,\hat{A}\right)^{-1}, \tag{3.76}$$

where

$$\widehat{A} = \frac{\boldsymbol{E}^{\mathrm{n}} \cdot \hat{\boldsymbol{\mu}} \triangle t}{2}, \tag{3.77}$$

leads to

$$\left[\left(\hat{I} - i\,\widehat{A}\right)^{-1}\left(\hat{I} + i\,\widehat{A}\right)\right]^{\dagger}\left(\hat{I} - i\,\widehat{A}\right)^{-1}\left(\hat{I} + i\,\widehat{A}\right) = \hat{I}. \tag{3.78}$$

We also mention that direct computation of the matrix exponential is also possible. The software package `expokit`[77] contains several computational routines based on various levels of approximations that are well suited for such calculations. A few numerical examples of the use of the PSTD-4 method have been demonstrated by Marskar and Österberg [78].

3.4.4 Parallellization & Performance

The largest computational burden is the update of the optical Bloch equations. Optimization of the computer algorithm will usually be necessary. Firstly, we note that the operators $\check{U}_{\delta}$ are usually very sparse and that numerical multiplication by these matrices can be done very efficiently by storing them in a sparse format and using optimized matrix multiplication routines. This results in a dramatic increase in performance, especially for multi-level systems. Secondly, we have purposefully constructed an explicit numerical scheme where no iterative corrections are necessary. One observes that the numerical update of the density operators $|\rho_{\delta}\rangle\!\rangle$ occurs simultaneously with the calculation of the $\boldsymbol{B}$-field. Moreover, the entire spatial grid can be updated simultaneously which means that these calculations may be distributed over a number of processes using the Message Passing Interface (MPI) and Open Multi-Processing (OpenMP) protocols, leading to very efficient parallelization.

In practice, direct Maxwell-Bloch simulations, although they are valid for two-way propagation along all three spatial coordinates and incorporate all the physical features associated with Maxwell's equations, do not scale very well with propagation distance. The reason is that even with pseudospectral methods and high-order time stepping the spatial resolution must be finer than an optical wavelength, and this will rapidly lead to exhaustion of computational resources. The method is therefore most useful for propagation distances up to a few millimeters. It is, nevertheless, possible to obtain three-dimensional numerical solutions for pulses of arbitrary duration propagating over long distances in multi-level materials if one starts out from a different propagation equation. We will consider such a model in Chapter 5.

3.5 Optical backpropagation of 2π pulses

Having reviewed SIT theory, RMB theory, and numerical Maxwell-Bloch methods, we are now in a position to address the case of backscattering corrections to SIT. First, for mutual consistency between the McCall-Hahn definitions and the results derived by Marskar and Österberg [79], we define the quantities

$$\Omega \equiv \frac{\mu_{12} E_y}{\hbar}, \tag{3.79a}$$

$$\Omega_B \equiv \frac{\mu_{12} c B_x}{\hbar}, \tag{3.79b}$$

and $\xi = z/c$ such that Eq. (3.1) may be written as the system

$$\partial_t \Omega = \partial_\xi \Omega_B - \omega_\kappa \partial_t p, \tag{3.80a}$$

$$\partial_t \Omega_B = \partial_\xi \Omega, \tag{3.80b}$$

$$i\,\mathrm{d}_t \hat{\rho}_\Delta = \left[\hat{H}_\Delta, \hat{\rho}_\Delta\right] + \hat{R}_\Delta, \quad \hat{H}_\Delta = \begin{pmatrix} 0 & -\Omega \\ -\Omega & \overline{\omega} + \Delta \end{pmatrix}. \tag{3.80c}$$

The missing factor of 2 in the definition of the Rabi frequency in Eq. (3.79) is due to the use of complex fields in McCall-Hahn SIT theory. Equations (3.80) are the two-level MB equations. By definition, the coupling frequency ω_κ is defined $\omega_\kappa = \mathcal{N}|\mu_{12}|^2/(\epsilon_0 \hbar)$. Furthermore, the average atomic polarization and material inversion are given by

$$p = \int \mathrm{d}\Delta g(\Delta)(\rho_{\Delta,12} + \rho_{\Delta,21}), \tag{3.81a}$$

$$w = \int \mathrm{d}\Delta g(\Delta)(\rho_{\Delta,22} - \rho_{\Delta,11}), \tag{3.81b}$$

where we consider a Gaussian distribution

$$g(\Delta) = \frac{T_2^*}{\sqrt{2\pi}} \exp\left[-\frac{\left(\Delta T_2^*\right)^2}{2}\right]. \tag{3.82}$$

The medium is otherwise characterized by $\overline{\omega} = 6\pi \times 10^{13}$ rad/s ($\overline{\lambda} = 10\ \mu$m), $\mu_{12} = 5$ D, and $T_2^* = 50$ fs. Homogeneous damping which removes the energy that is locked in the dipoles via e.g. spontaneous emission is incorporated in $\hat{R}_s$, with $T_1 = 1$ ms and $T_2 = 0.1$ ms, substantially longer than the pulse durations we consider below. The spatial and temporal discretization lengths are $\triangle z = \overline{\lambda}/100$ and $\triangle t = 2\triangle z/(\pi c)$, and we have verified that the output from our computer simulations do not change with increased resolution.

By introducing the pseudofields

$$\Omega^\pm = \frac{1}{2}\left(\Omega \mp \Omega_B\right), \tag{3.83}$$

the Poynting vector $\boldsymbol{S} = \epsilon_0 c^2 \boldsymbol{E} \times \boldsymbol{B}$ may be written in the plane wave approximation as

$$\begin{aligned} \boldsymbol{S} &= -\Omega \Omega_B \hat{z} \\ &= \left(\Omega^{+2} - \Omega^{-2}\right) \hat{z}. \end{aligned} \tag{3.84}$$

The two fields $\Omega^{\pm}$ represent forward (Ω^{+}) and backward (Ω^{-}) propagating modes.

In what follows below, Eq. (3.79) is solved for up to 5000 different values of Δ using the PSTD-2 method discussed in the previous section. We consider a Gaussian shaped input pulse

$$\Omega(t, 0) = \Omega_0 \exp\left(-\frac{t^2}{2T^2}\right) \sin(\omega_c t), \tag{3.85}$$

which is emitting from a total field-scattered field [28] two-point source at $z = 0$ in vacuum. Double sources are used in order to minimize Gibbs' phenomenon. This pulse propagates in free space for 250 μm before penetrating a medium of length L. After propagating through the medium the pulse exits back into free space again. The computational boundaries are padded with perfectly matched layers that prevent backreflection from the truncated simulation regions. We consider a resonant pulse ($\omega_c = \overline{\omega}$) with input peak amplitude $E_0 = 8.27 \times 10^7$ V/m ($\Omega_0 \approx 10^{13}$ rad/s) and duration $T = 250$ fs. This fixes the input area defined by the Gaussian envelope slightly below 2.6π and ensures that the input pulse is a temporally slowly varying pulse $\omega_c T \sim 50$. We are therefore in the conventional McCall-Hahn SIT regime where the pulse duration fits between the two transverse lifetimes ($T_2 \gg T > T_2^*$). As a sidenote, an alternative to solving Eq. (3.1) directly is to derive separate evolution equations for $\Omega^{\pm}$ that are coupled through Eq. (2.6), and then address these equations simultaneously.

3.5.1 Conventional SIT results

Consistent with the derivations in Sec. 3.3 we expect the emergence of a backwards pulse when ω_κ becomes comparable to the peak Rabi frequency Ω_0. To verify the reliability of our computational results we first investigate SIT behavior in the conventional regime $\omega_\kappa \ll \Omega_0$. We take $\mathcal{N} = 5 \times 10^{23}$ m^{-3} and $L = 2.5$ mm which gives $\Omega_0 \approx 88\omega_\kappa$. The optical density of the dielectric is $\alpha_0 L \approx 14.5$. With the numbers above, $\alpha_0^{-1} \approx 17.2\overline{\lambda} = 172$ μm. Figure 3.6 shows that the standard SIT features, which are expected to hold at these conditions, are captured by our numerical code: The initial pulse partially reflects while the remaining part penetrates the material. It is then compressed and amplified over the first few absorption lengths and reshapes into a hyperbolic secant pulse with pulse area 2π which propagates stably and with constant energy. We have calculated the pulse area as the Fourier transform of $\Omega(t, z)$ on the line center, i.e. $\theta(z) = |\Omega(\overline{\omega}, z)| = \left|\int_{-\infty}^{\infty} \Omega(t, z) \mathrm{e}^{-i\overline{\omega}t} \mathrm{d}t\right|$, and the pulse energy is found by integration of the Poynting vector.

The top panel in Fig. 3.6 shows that the computer solution agrees very well with the area theorem $\theta(z) = 2n\pi + \arctan[\exp(\alpha_0 z/2)\tan(\theta_0/2)]$, where θ_0 is the input area. We nevertheless point out that it is the soliton feature and not the area theorem which is the fundamental property of the system. Although the soliton feature holds whenever $T \ll T_2$ and backpropagation can be ignored (even when the slowly varying and rotating wave approximations are not valid), the area theorem holds only when the initial pulse is resonant, transform-limited, slowly varying through the material, and the absorption line is symmetric around $\overline{\omega}$ [43]. These conditions are fulfilled by the parameters above.

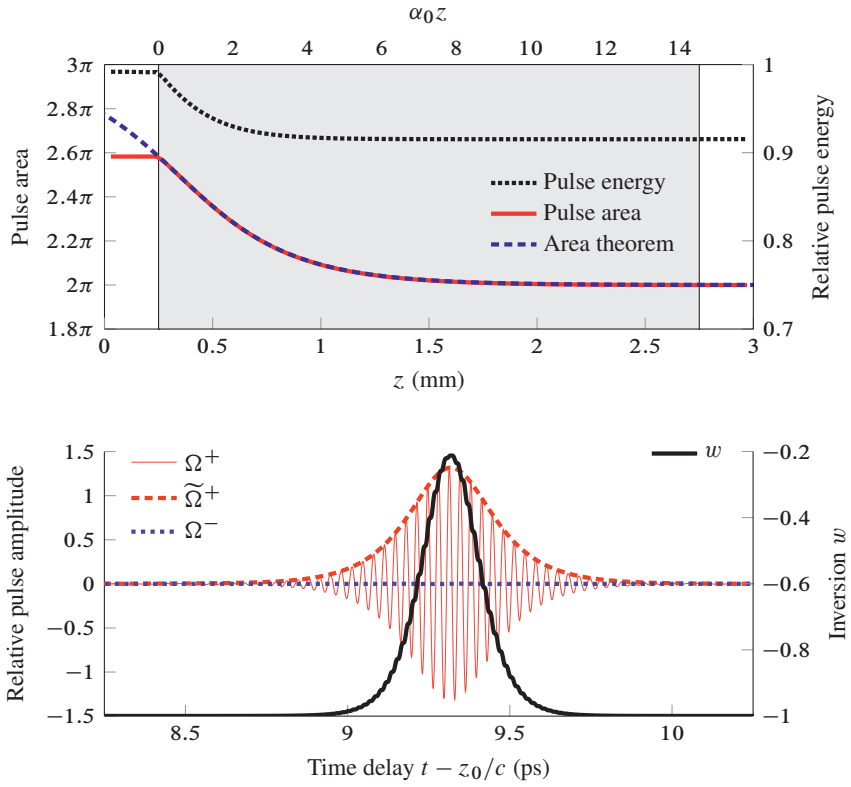

FIG. 3.6: Top panel: Normalized pulse energy (dotted line, plotted against the right vertical axis) and area (solid line) compared with the area theorem (dashed line). The shaded region indicates the presence of the two-level medium. Bottom panel: Average material inversion w (thick solid line, plotted against the right vertical axis). Plotted against the left vertical axis is the forward field Ω^+ (thin solid line), its envelope (dashed line), and the backward field Ω^- (dotted line). The data are taken from a distance $z_0 = 1.75$ mm ($\alpha_0 z_0 \approx 10$) into the material.

The bottom panel in Fig. 3.6 shows the auxiliary fields $\Omega^\pm$ and their corresponding envelopes $\widetilde{\Omega}^\pm$ after penetrating 2 mm into the dielectric. We have obtained the envelopes

$\widetilde{\Omega}^{\pm}$ via the analytic signals of $\Omega^{\pm}$. The full electric field profile coincides with the forward field Ω^{+} and has been confirmed to be a hyperbolic secant with area $\approx 2\pi$. It inverts the material and completely reverts it to its ground state. The presence of the negative flux field Ω^{-} is clearly negligible. After the formation of the 2π pulse, the long time behavior of the system is $\Omega^{\pm}(t \to \infty, z) = 0$ and $w(t \to \infty, z) = -1$, which makes this particular pulse an SIT pulse.

3.5.2 Bidirectional SIT

Having established the reliability for our computational model with $\Omega \gg \omega_\kappa p$ we can now address the regime $\Omega \sim \omega_\kappa p$ where backpropagation is expected to have a non-negligible effect. The density is now taken as $\mathcal{N} = 4.4 \times 10^{25}$ m^{-3} which gives $\Omega_0 \approx \omega_\kappa$. The absorption length is $\alpha_0^{-1} \approx 0.195\overline{\lambda}_s$, and the material is essentially opaque for linear transmission of resonant radiation. We take the length of the material to be $L = 0.5$ mm long so that its optical thickness is $\alpha_0 L \approx 256$. We consider the same Gaussian input pulse.

The top panel in Fig. 3.7 shows the envelopes $\widetilde{\Omega}^{+}$ and $\widetilde{\Omega}^{-}$ a distance $z_0 = 0.25$ mm into the material, and the negative flux field Ω^{-} is readily discerned. The most important difference between the behaviors in Figs. 3.6 and 3.7 lies in the fact that $\Omega^{+} \neq \Omega$ and that the long term behavior is $w(t \to \infty, z) \neq -1$ for the denser material. In Fig. 3.7 we see that $\Omega^{\pm}(t \to \infty) = 0$, $w(t \to \infty) \approx -0.98$, and the pulse leaves behind energy in the material. It is therefore not an SIT soliton. This failure to return the material to the ground state after the passage of the pulse is not related to the initial shedding of energy that usually takes place when a non-SIT pulse reshapes into a soliton under ideal SIT conditions, which is seen in Fig. 3.6 as an initial decline in pulse energy over the first few absorption lengths. Even at a distance $z_0 = 0.25$ mm into the material, the pulse in Fig. 3.7 has propagated $\alpha_0 z_0 \approx 128$ absorption lengths, a substantial distance. Under ideal SIT conditions (i.e. no backpropagation or other losses), a 2π soliton would be expected at this penetration depth. Here, the pulse instead leaves behind a trail of inversion $w > -1$ and a soliton does not form. The inset in the top panel in Fig. 3.7 shows that although the residual material excitation is relatively small, it has a profound impact on the pulse over many absorption lengths. The initial dip in energy is associated with the initial reshaping into a sech pulse while the decay from $\alpha_0 z \approx 10$ to $\alpha_0 z \approx 256$ is connected to a backpropagation loss. It is interesting that this decay is almost linear up to $\alpha_0 z \approx 170$ and that the final state of inversion lies close to -1, which is indicative of a small-area backward-propagating pulse. Indeed, as seen in the top panel of Fig. 3.7 the area under $\widetilde{\Omega}^{+}$ is much larger than that under $\widetilde{\Omega}^{-}$. The flattening of the pulse energy after $\alpha_0 z \sim 170$ is most likely due to an edge-effect where the backpropagating pulse is being generated from a smaller spatial region. To expose the pulse in greater detail, the bottom panel in

Fig. 3.7 shows the full field Ω and a comparison between the corresponding envelope $\widetilde{\Omega}$ (dashed line) and a numerical least squares fit (LSQ, dotted line) of a hyperbolic secant pulse envelope $f(t) = A\,\mathrm{sech}\,[(t - t_0)/\tau]$. The pulse in Fig. 3.7, unlike the pulse in Fig. 3.6, is not a pure 2π hyperbolic secant pulse, although it remains so to a very good approximation. Plotted against the right vertical axis in Fig. 3.7(b) is also the spectral intensity of the pulse. We notice that the center frequency of the pulse is slightly blue shifted to a value $\approx 1.005\overline{\omega}$.

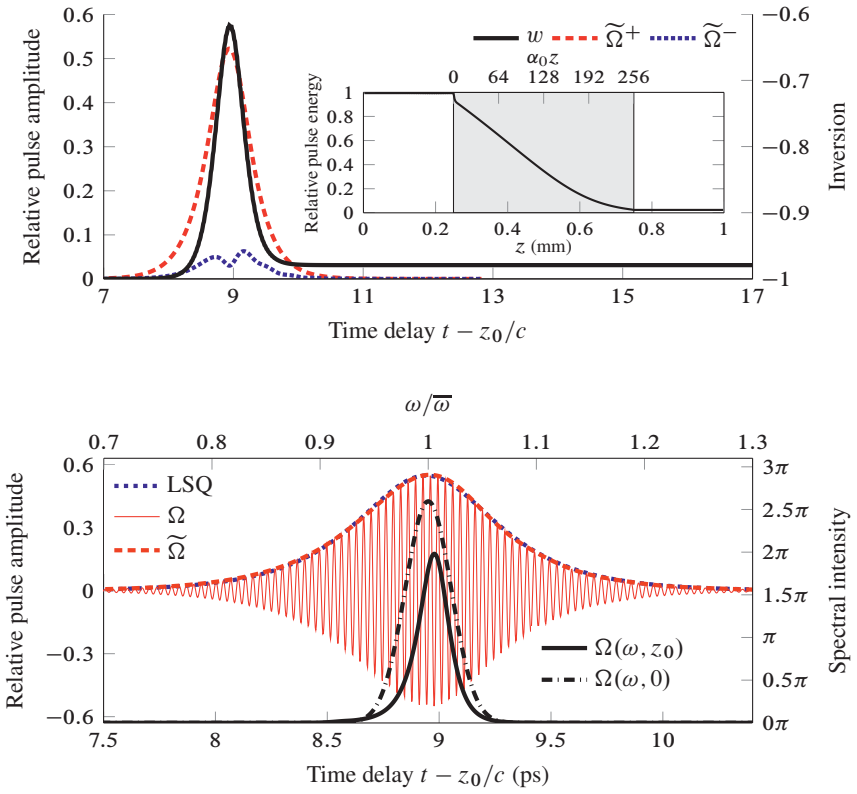

FIG. 3.7: Top panel: Plotted against the left vertical axis are the envelopes of Ω^+ (dashed line) and Ω^- (dotted line). The inversion w (solid line) is plotted against the right vertical axis. The inset shows the pulse energy normalized to the input pulse energy as a function of propagation distance. The bottom panel shows the full field Ω (thin solid line) and its envelope (dashed line) compared with a least squares fit (LSQ, dotted line) of a hyperbolic secant pulse. Plotted against the second set of axes is the input pulse spectrum (dashed-dotted) and the spectrum $\Omega(\omega, z_0)$ (thick solid line). The data in both panels are taken at a propagation length of $z_0 = 0.25$ mm ($\alpha_0 z_0 \approx 128$) into the material.

To compare the forward and backward fields, the two panels in Fig. 3.8 show the

propagated spectra of $\Omega^{\pm}$ plotted together with the inhomogeneous broadening line $g(\omega_s)$ (dotted line) and also the initial pulse spectrum $\Omega(\omega, 0)$ (solid line). Several features of the computer solution deserve mention: Firstly, we observe that the forward spectrum broadens over the first few Beer's length, indicating that temporal compression of the pulse due to spatiotemporal reshaping into a quasi-SIT pulse is taking place. The subsequent narrowing of the spectrum is due to backpropagation losses that lead to temporal elongation. Note also that although the spectral intensity of the input pulse around $\omega/\overline{\omega} \approx 0.78$ is zero, there is such a peak in the spectrum of the reflected field Ω^{-} and no such feature for Ω^{+}. Nonlinear reflection from interfaces has been studied by Forysiak et al. [80] in the incoherent regime $T_2 \ll T \ll T_1, T_2^*$, and a red-shift has been predicted due to the Doppler shifted reflection from the moving saturation front that is formed in the material when the pulse penetrates the interface. This explanation presumably holds true here as well. The pulse velocity v near the interface in Fig. 3.9 is roughly $v/c \approx 0.11$ and matches the Doppler shift $\Delta\omega \approx 0.22\overline{\omega}$. The small color shifts of $\Omega^{\pm}(\omega, z)$ during propagation are, to the best of our knowledge, not predicted by any existing theory. It is established, on the other hand, that if the rotating wave and slowly varying envelope approximations in time and space are valid, frequency pushing of an initially off-resonance 2π hyperbolic secant soliton may occur [45, 46]. In our computer simulations, the input pulse is resonant and transform limited, therefore any initial pulse chirp or change in center frequency occurs as a result of either propagation, or frequency biased reflection/transmission from the interface.

Figure 3.9 shows the spatiotemporal reshaping that is induced by the backwards propagating mode. The two horizontal axes are the temporal pulse delay $t - z/c$ and the propagation distance z into the medium in units of α_0^{-1}. Only the spatiotemporal reshaping over the first 176 absorption lengths is shown. The solid line plotted in the top plane indicates the peak pulse delay at various z. Its curvature in the $(t - z/c, z)$ plane indicates a non-constant group velocity. We find that over the first few absorption lengths the pulse is temporally compressed. This initial reshaping is not surprising considering the initial conditions that are applied. According to the area theorem, which holds as a first approximation over the first absorption lengths, the Fourier coefficient of $\Omega^{+}(\overline{\omega}, z)$ must decrease to 2π during the initial reshaping to a hyperbolic secant pulse. During this reshaping the excess spectral energy at line center is either absorbed by the medium or pushed into the spectral wings of the pulse, which results in spectral broadening and temporal compression. With further propagation we observe the non-standard features: As the pulse energy diminishes with increasing propagation distance the temporal pulse width increases and the pulse travels with further reduced group velocity. For an even longer material, the pulse will eventually broaden to timescales that are comparable to the homogeneous decoherence time T_2 and is then rapidly absorbed by the material. This type

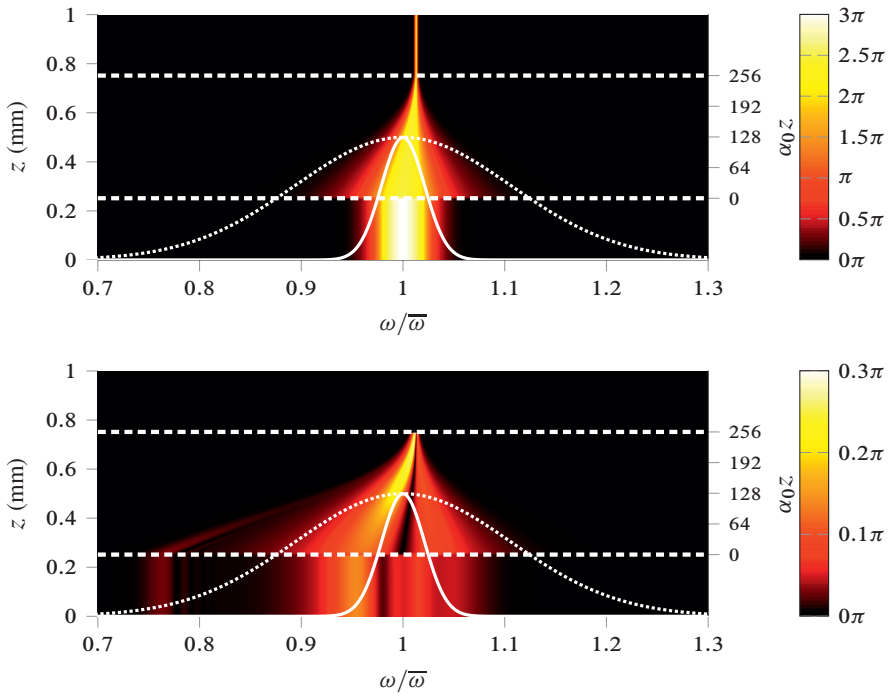

FIG. 3.8: Top panel: Spatial propagation of the spectrum of the forward spectrum $\Omega^+(\omega, z)$ (color coded) inside and outside the material. The inhomogeneous absorption line $g(\omega_s)$ and the initial pulse spectrum $\Omega(\omega, 0)$ are shown with dotted and solid lines, respectively. The dashed lines indicate the position of the material/vacuum interfaces. Bottom panel: Same as for the top panel, but for $\Omega^-(\omega, z)$.

of pulse stretching is typical of solitonic systems with loss, and has been studied by others through the introduction of phenomenological loss terms (see e.g. Diels and Hahn [45] or Alhasan et al. [81]). The loss mechanism considered here is not phenomenological but is an inevitable part of Maxwells wave equation. It will be finite also for less dense materials having the same optical thickness, although homogeneous damping will then dominate. To our knowledge, the only soliton solution to Eq. (3.1) known at present is the half cycle hyperbolic secant $\Omega(t, z) = \Omega_0 \operatorname{sech}[\Omega_0(t - z/v_g)]$ (i.e. a hyperbolic secant without carrier) [55], and its N-soliton generalizations. These solitary pulses do not satisfy the multi-dimensional Maxwell's equations in vacuum, and are presently therefore of little practical relevance. Whether such solitons can stabilize in a material through a compensation of self-focusing and diffractive effects is an intriguing question, and requires a study of the three-dimensional Maxwell-Bloch equations. To the best of our knowledge, such a study has not been performed to date.

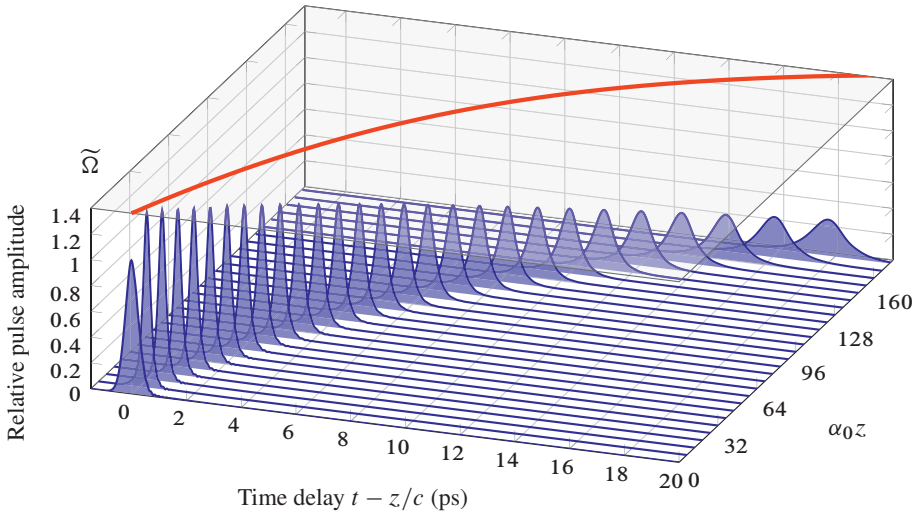

FIG. 3.9: Spatiotemporal reshaping over the first 176 absorption lengths. The two horizontal axes are the pulse delay $t - z/c$ and the propagation distance in units of α_0^{-1}. The vertical axis indicates the magnitude of the full field pulse envelope. The solid line plotted in the top horizontal plane indicates the peak time delay at various propagation distances.

We now briefly mention that if the inhomogeneous lifetime becomes longer such that $T < T_2^* \ll T_1, T_2$, the pulse behavior changes and a larger blue shift (see e.g. [82] for the sharp-line case) can move the pulse completely outside the absorption band of the material where it can propagate a longer distance. Nevertheless, we have numerically verified also for dense media that off-resonant hyperbolic secant pulses are also incapable of completely returning the material back to the ground state and also lose energy during propagation, although to a considerably smaller extent than for resonant pulses in inhomogeneously broadened media. Obviously, in the artificial undamped limit $T_1, T_2, T_2^* \to \infty$ the excited dipoles radiate forever and optical transparency is difficult to avoid. Additionally, insofar as SIT is valid down to the single cycle regime so are the results of this section. We have verified that the breather solution Eq. (3.21), which is valid in the forward wave approximation $\Omega \gg \omega_\kappa p$, coincides with computer solutions when we consider close-to single-cycle input pulses, and that when the forward wave approximation is not valid, these pulses also leave the material slightly excited after they have passed.

3.5.3 Energy versus distance behavior

The energy vs distance decay of SIT pulses has a complicated structure that depends on the input pulse shape and the relation between the pulse duration and the transverse and

longitudinal lifetimes. For example, after exciting the medium with non-SIT pulses of duration $T < T_2^*$ in the uni-directional approximation, a long-lived precursor might precede the driving pulse [78]. Even when the soliton has formed after many Beer's length, this forerunner might persist due to its spectral location around the wings of the absorption line where it experiences little absorption. The forerunner will be discussed in greater detail in Chapter 4. In the case of an SIT pulse propagating in an inhomogeneously broadened attenuator, which is the scenario considered in this paper, the energy decay is adequately explained by phenomenologically incorporated loss terms in the Bloch equations. Figure 3.10 shows a computer solution of the propagation of the pulse above, but under the rotating wave and slowly varying envelope approximations and with the inclusion of a spontaneous emission lifetime $T_1 = 20$ ps. That is, this pulse fits between the two transverse lifetimes $T_2^* < T < T_2$. Although the long-term behavior of this system $w \to -1$, the same qualitative pulse behavior is recovered in this simplified model. The pulse energy decays linearly with propagation distance, the pulse broadens temporally and propagates with a reduced group velocity. On the whole, the propagational results elaborated on in this section may be understood in terms of uni-directional solitonic SIT systems with phenomenologically incorporated loss terms.

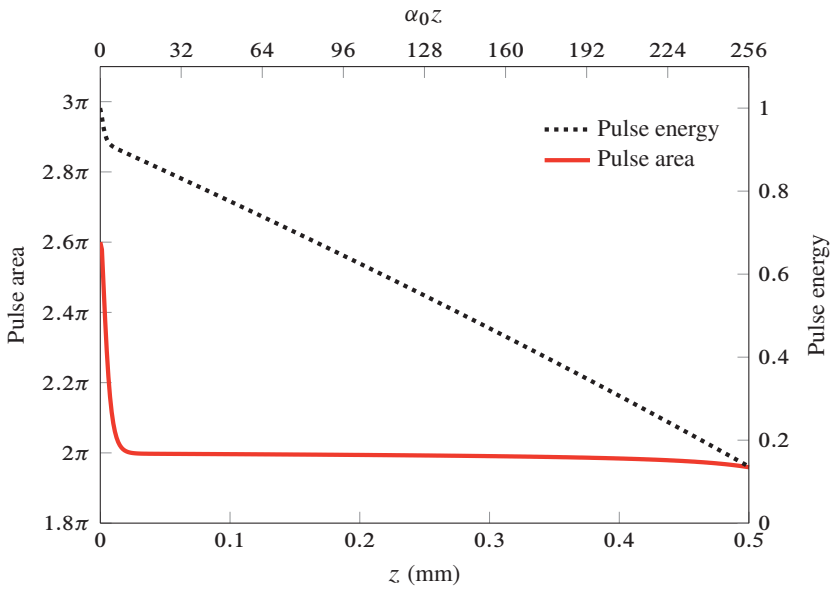

FIG. 3.10: Energy versus distance (dotted line) and area versus distance (solid line) for a computer solution under the rotating wave and slowly varying envelope approximations. The conditions are the same as in Figs. 3.6-3.9, but neglecting backpropagation and including a spontaneneous emission lifetime of 20 ps.

Relation to other studies

We briefly mention that the above results relate to recent studies of the area theorem using Eq. (3.1) in the undamped limit: Hughes [83] considered propagation of initial pulses

$$\Omega(t,0) = \Omega_0 \,\mathrm{sech}\left(\frac{t}{T}\right)\sin(\omega_c t), \tag{3.86}$$

with areas between 2π and 12π (i.e. $\Omega_0/(2\omega_c) \sim 0.1 - 1$) and showed that these pulses did not return the material to its initial state. A similar analysis was performed by Xiao et al. [84] and Novitsky [85]. We remark that if the Rabi frequency is comparable to ω_c then in view of Eq. (3.21) the initial pulses used by Hughes [83], Xiao et al. [84], and Novitsky [85] are not SIT pulses but must be reshaped by the material before propagating as solitons. The residual energy left behind in the material in [83, 85] is a sign of this reshaping. With the indicated parameters in the above references, the systems investigated are nevertheless solitonic, supporting SIT pulses down to arbitrary durations.

3.6 Summary

This chapter reviews McCall-Hahn SIT theory and the uni-directional pulse propagation approximation. After obtaining a measure of negligible backpropagation we derive several forward wave equations under various levels of approximation. We then reviewed the formulation of a general numerical Maxwell-Bloch model that incorporates multi-level effects and inhomogeneous broadening. This numerical integrator was applied to the propagation of pulses in the traditional SIT regime under the presence of optical back-propagation. We found that the McCall-Hahn SIT solution decays slowly with propagation distance due to a co-excited backward propagation pulse that prevents reversion of the material to the ground state. The results were adequately explained by the introduction of phenomenological loss terms in the optical Bloch equations.

Several of the results and equations derived are useful in the later chapters in this thesis. In particular, the FOP equation and the corresponding energy conservation equation are the starting equations for the RMB model. This model is employed in Chapter 5 where we analyze conical emission of few-cycle pulses in a multi-level sodium atomic model.

Chapter 4

Nonlinear optical precursors with SIT

4.1 Introduction

In their theoretical study of superluminal group velocity in causal, linear dielectrics, Brillouin [86] and Sommerfeld [87] showed that a precursor (or forerunner) can significantly precede a main signal. In their studies, they investigated the propagational characteristics of a step-function pulse propagating in a dielectric medium described by a single Lorentz resonance. They found that the main signal is preceded by one or two forerunners, which represented spectral regions of the initial pulse that propagated with group velocities different from that of the main pulse.

The theoretical literature on optical precursors has been improved over the years, and is now quite extensive [88]. However, only a handful of experimental observations of the elusive precursor have actually been made. With the exception of Pleshko and Palócz [89], most experiments have been performed in the past two decades. Aaviksoo et al. [90] used one-sided exponential pulses propagating close to a narrow excitation line in Gallium-Arsenide, Jeong et al. [91] observed optical precursors in the anomalous dispersion regime of a laser-cooled Potassium vapor, Du et al. [92] observed precursors at the biphoton level using slow light, and Wei et al. [93] performed optical precursor experiments in a laser-cooled Rubidium vapor. There have also been reports of precursors in water [94], but these claims have been contested [95, 96].

Only recently has the search for optical precursors been extended to the regime of nonlinear interactions. Palombini and Oughstun [97] investigated the propagation of Gaussian pulses placed on the red side of a Lorentz resonance, but with one important addition; they included the effects of a cubic nonlinearity which accounts for self-phase modulation and odd harmonic generation. On the whole, they find that the precursor fields are conserved to a considerable extent also for nonlinear interactions, but with quantiative changes in the

strength of the precursor field. Macke and Ségard [98] suggested that precursors can coexist with SIT in homogeneously broadened media (i.e. excluding Doppler broadening). We mention also analogous results encountered by Crisp [99], and also by Diels and Hahn [44, 45], where a forerunner was observed, but not rigorously analyzed.

For comparison, we investigate here the possibility of optical precursor propagation in hot vapors, thus incorporating the effects of Doppler broadening. We show that coexisting transform-limited SIT and precursor pulses may originate by the application of a resonant $> \pi$ area pulse. The precursors observed are essentially 0π pulses [30] and may individually interact nonlinearly with the material.

4.2 Theoretical basis

The equations of motion are the resonant McCall-Hahn SIT equations [Eq. (3.5) and (3.10)]

$$i\,\mathrm{d}_\tau \hat{\varrho}_\Delta = \left[\widehat{\mathcal{H}}_\Delta, \hat{\varrho}_\Delta\right] + i\,\hat{R}_\Delta, \quad \widehat{\mathcal{H}}_\Delta = \begin{pmatrix} 0 & -\frac{1}{2}\Omega^* \\ -\frac{1}{2}\Omega & \Delta \end{pmatrix}, \tag{4.1a}$$

$$\partial_z \Omega = i\kappa \langle \varrho_{\Delta,21} \rangle_\Delta, \tag{4.1b}$$

where we recall Fig. 3.1 for definitions. Here, the medium is Doppler broadened according to Eq. (3.82). To numerically solve Eq. (4.1) we apply a standard implicit trapezoidal method for both equations. This results in implicitly coupled discretized equations, and these are iterated to convergence by using a predictor-corrector method. Because we presume that the pulse duration is much shorter than the homogeneous transverse lifetime, decoherence is disregarded in what follows.

4.3 Gaussian excitation

Following Marskar and Österberg [100] we consider first the propagation of Gaussian pulses. For the physical parameters, we take the transition wavelength $\lambda = 800$ nm ($\overline{\omega} = 7.5\pi \times 10^{14}$ rad/s), the inhomogeneous lifetime $T_2^* = 0.5$ ns, and a number density $\mathcal{N} = 10^{17}$ m^{-3}. The transition dipole moment is taken as $\mu_{12} = 2.75 \times 10^{-29}$ Cm. These numbers correspond to a Beer's length $\alpha_0 \approx 2.5$ mm. The medium is $L = 8$ cm long which yields an optical thickness of $\alpha_0 L \approx 32$. As the initial state of the medium, we presume that all atoms are in their ground state before the pulse enters into the material.

The input pulse shape is described by a Gaussian

$$\Omega(\tau, 0) = \Omega_0 \exp\left(-\frac{\tau^2}{2T^2}\right), \tag{4.2}$$

which is turned on at $\tau = -10T$ and off at $\tau = 10T$ such that the leading and trailing edges of the pulses are very small. The area of the Gaussian pulse described by Eq. (4.2) is $\theta_0 = \sqrt{2\pi}\Omega_0 T$. We recall that the area can be taken as DC value of Fourier component of Ω, and can be found numerically via Fast Fourier Transforms rather than Gaussian quadrature.

We mention that we refrain from exciting the medium using pulses that are already 2π SIT pulses. Such pulses are exact solutions to Eq. (4.1) and have no forerunners. In addition, we use the term "precursors" only for pulses that significantly precede a main signal, propagates with group velocity $v_g \approx c$, and which itself is not an SIT pulse.

First, we keep the area constant at $\theta_0 = 1.1\pi$ and change the pulse duration from $T = 0.15T_2^*$ to $T = 2T_2^*$. Since the area is proportional to the DC Fourier coefficient of Ω, decreasing the pulse duration while maintaining a constant area implies that the energy in the spectral wings of the input pulse increases. Following Parseval's theorem the energy of the pulse as a whole increases as well. The five panels in Fig. 4.1 show the exit pulses after propagating through the material. In each panel, the input pulse duration T is different. We have plotted the phase $\phi = \arctan[\Omega_I(t,z)/\Omega_R(t,z)]$ where $\Omega(\tau,z) = \Omega_R(\tau,z) + i\,\Omega_I(\tau,z)$ against the right vertical axis in each panel, which shows that the exit pulses are not phase modulated. We have verified that this is true in all of our simulations when we consider resonant propagation. As noted by Hopf and Scully [101], the absence of phase modulation is understood from the formal solution for $\varrho_{21}(t,z,\Delta)$:

$$\varrho_{\Delta,21}(\tau,z) = \frac{i}{2}\int_{-\infty}^{\tau} \mathrm{d}\tau' \Omega(\tau',z) \mathrm{e}^{-i\Delta(\tau-\tau')} \left[\varrho_{\Delta,22}(\tau',z) - \varrho_{\Delta,11}(\tau',z)\right]. \tag{4.3}$$

Under the conditions of exact resonance, no initial chirp, and symmetric Doppler line broadening, then the in-phase component of the polarization vanishes after taking the ensemble average $\langle\rangle_\Delta$ of Eq. (4.3). Insertion of this result into Eq. (4.1b) shows that the field propagates without acquiring a modulated phase. The envelopes that are plotted in Fig. 4.1 are normalized to the individual Rabi peak amplitudes, and show that the magnitude of the precursor decreases when the input pulse duration increases. In addition we note that the peak amplitude of the pulse is reduced roughly by a factor of $1/5$ in each simulation. By the area theorem it is apparent that temporal elongation of pulses with initial areas $< 2\pi$ is expected during propagation. Since the area is equivalent to the DC Fourier coefficient of the Rabi frequency, this coefficient must grow to 2π if the area theorem is fulfilled. The energy required for this increase is taken from the spectral wings of the pulse; the spectrum narrows and the pulse broadens. For the longest pulses there are no immediate signs of a precursor and only the main signal can be clearly seen (although it's not discernible in Fig. 4.1, there is an oscillating front with a relative peak amplitude 2.6×10^{-4} for $T = 2T_2^*$, and a front with relative peak amplitude 2.5×10^{-3} for $T = 1.25T_2^*$). By

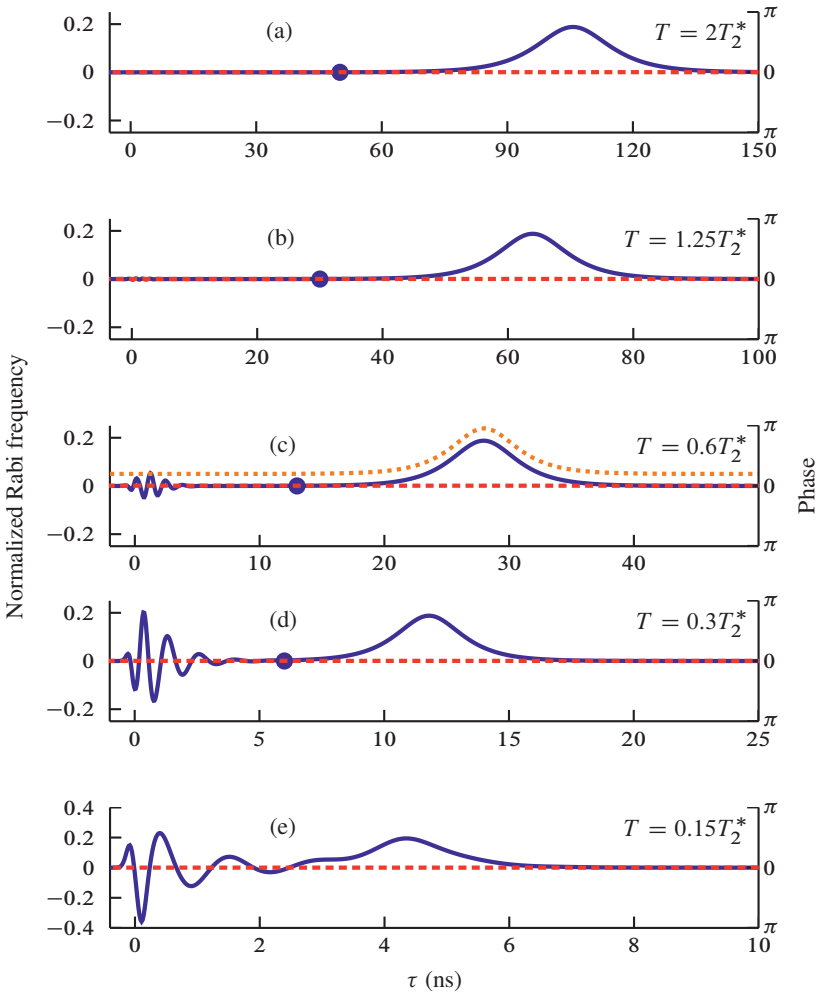

FIG. 4.1: Amplitude (solid line) and phase (dashed line) of the exit pulses for input pulses with durations $T = 0.15T_2^*, 0.3T_2^*, 0.6T_2^*, 1.25T_2^*$, and $2T_2^*$. The dotted line for $T = 0.6T_2^*$ shows a hyperbolic secant fit to the main pulse, displaced vertically for enhanced readability. The y-axis is normalized against the individual input peak Rabi frequencies. The dots mark breakpoints used for separation of the precursor and the main pulse.

curve fitting a hyperbolic secant shape $\Omega_{\text{fit}}(\tau) = A\,\text{sech}[(\tau - \tau_0)/T_{\text{fit}}]$ to the numerical results, we have confirmed that the main pulses (apart from $T = 0.15T_2^*$) are hyperbolic secant pulses. The parameters that give the elevated dotted curve for $T = 0.6T_2^*$ in Fig. 4.1 are $A/\Omega_0 = 0.189$, $\tau_0 = 28.0$ ns, and $T_{\text{fit}} = 2.3$ ns, and gives a pulse velocity $v_g \approx c/106$ and area $\theta \approx 2\pi$. The pulse velocity is estimated from the peak delay τ_0

and is given by $v_g = c/(1 + c\tau_0/L)$. As the initial pulse duration decreases and the energy increases, there are clearer signs of a pulse propagating at a velocity close to c with the trailing main pulse propagating at a lower velocity. For the shortest of these pulses ($T = 0.15T_2^*$), we cannot distinguish between the main pulse and the precursor.

Figure 4.2 shows a comparison between the computer calculated pulse area and the area evolution as predicted by the pulse area theorem. We find that the area theorem agrees very well with our numerical solutions. Note that although $T < T_2^*$ the area theorem accurately describes the pulse evolution since the conditions of resonance, zero chirp, and symmetric line broadening are fulfilled. We also mention a rederivation of the area theorem by Eberly [102], who showed that the pulse area theorem holds even for chirped pulses, provided that the inequality $T \gg T_2^*$ is fulfilled.

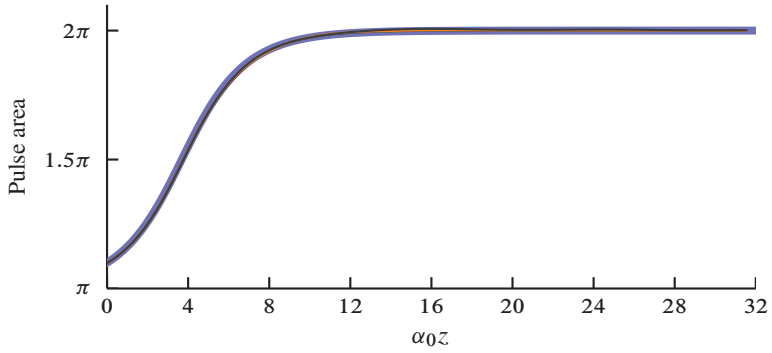

FIG. 4.2: Comparison between the area theorem and numerical solutions in Fig. 4.1. The area predicted by the pulse area theorem for an initial area of 1.1π overlaps with the calculated area from the computer simulations.

Note that the existence of Doppler broadening is not required for the area theorem per se, but that the dynamic evolution from an initial Gaussian pulse to a hyperbolic secant envelope will generally depend on its presence. In the language of IST theory [38, 39] the initial pulse envelope decomposes into a set of scattering eigenvalues. One part of this spectrum is discrete; these eigenvalues correspond to optical solitons and propagate without change through the medium. The other part of the spectrum is continuous; this part of the spectrum is ”radiation”, representing energy that will be absorbed by the medium as the pulse moves through it. For an inhomogeneous broadened medium $T_2^* \ll T$ this absorption is very efficient and the radiation part of the spectrum is rapidly removed during the first few Beer lengths, and only the discrete spectrum can propagate long distances. Note that in this language solitons are not actually created; they are already present in the initial pulse and emerge when the inhomogeneous medium has peeled away all the

"radiation" of the initial pulse. Each of the optical precursors observed in Fig. 4.1 is "radiation", and will eventually be completely absorbed by the medium. Overall, we thus understand that the role of Doppler broadening is to smooth out the pulse evolution, eliminating any ringing preceding or trailing the 2π soliton. This is the reason why a precursor may be observed for $T = 0.3T_2^*$ but not $T = 2T_2^*$. In the latter case Doppler broadening is sufficiently effective to entirely eliminate the forerunner before temporal separation occurs.

To investigate linearity, spectrum, and pulse area of the precursors in Fig. 4.1, we perform a frequency analysis of these pulses. The field is split into two contributions, $\Omega(\tau, L) = \Omega_p(\tau, L) + \Omega_{2\pi}(\tau, L)$, where $\Omega_p(\tau, L)$ is the precursor pulse, defined as $\Omega(\tau, L)$ up to the breakpoints shown in Fig. 4.1 and zero otherwise. The main pulse is denoted by $\Omega_{2\pi}(\tau, L)$ and is zero for all times before the breakpoint, and equal to $\Omega(\tau, L)$ for times after. This decomposition of the electric field is artificial and can only be performed once the temporal separation between Ω_p and $\Omega_{2\pi}$ is unambiguous. The separation occurs in all of our computer simulations except when the input pulse duration becomes much shorter than T_2^*. For example, there is no clear distinction between the precursor and the main signal for $T = 0.15T_2^*$ in Fig. 4.1 after 32 Beer lengths, but we have verified that there is after a distance of 60 Beer lengths.

The top panel in Fig. 4.3 shows the spatiotemporal reshaping of the initial Gaussian pulse with duration $T = 0.6T_2^*$ as it propagates through the medium. The horizontal axis shows the pulse delay time τ and the vertical axis shows the propagation depth z in units of the Beer's length. The bottom panel in Fig. 4.3 shows the spectrum of the precursor (solid line) and the main pulse (dashed line) at the exit face of the material, plotted together with the initial pulse spectrum (dotted line) and the inhomogeneous lineshape $g(\Delta)$ (dashed-dotted line). It is evident that the main pulse is indeed a 2π hyperbolic secant pulse by the time it exits the material. The precursor itself is seen to be a 0π pulse, which is evidenced by a vanishing DC Fourier coefficient. The spectral contents of the precursor are located primarily in the wings of the absorption line. We find that the the main pulse and the forerunner are well separated after a propagation distance $\alpha_0 z \approx 16$. Moreover, the precursor propagates along $\tau \sim 0$, indicating that it propagates approximately with velocity c, substantially faster than the main pulse which propagates with group velocity $v_g \approx c/106$. We observe also that the temporal beats of the precursor are occuring more rapidly with increasing propagation distance. The physical explanation of this is that the absorption is stronger closer to the line center so that with increasing propagation depth, the two spectral bumps of the precursor move further apart. The precursor observed here is similar to the 0π pulse first suggested by Crisp [30] (later experimentally observed by Rothenberg et al. [103]); it is linear, located around the wings of the absorption band, shows temporal beats, is slowly decaying, and has a 0π area. In fact, the connection between traditional

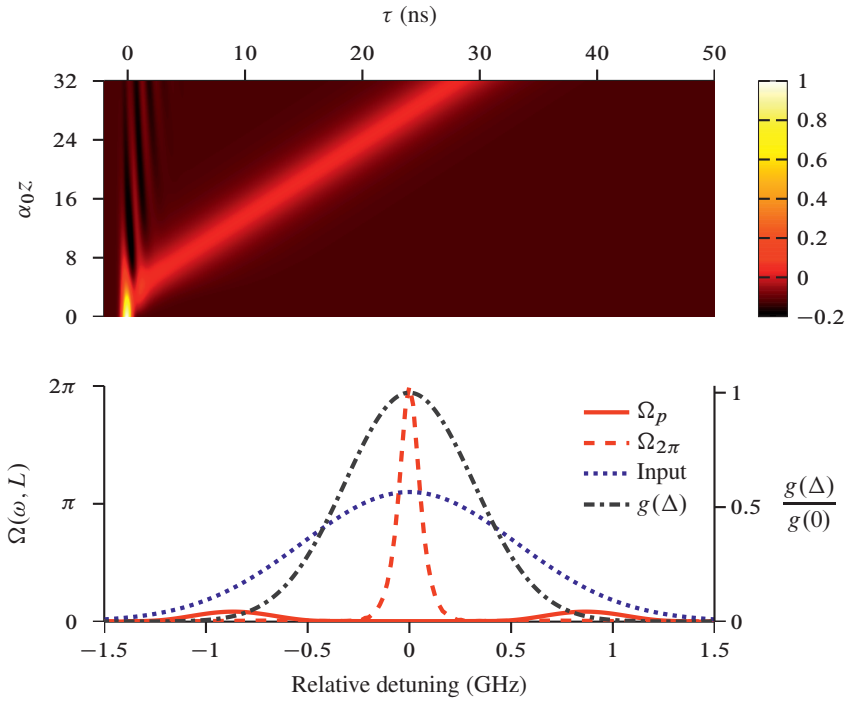

FIG. 4.3: Top panel: Reshaping of a Gaussian input pulse with duration $T = 0.6T_2^*$ and initial area 1.1π. The color coding shows the normalized amplitude of the field. Bottom panel: Spectral magnitude of the exit pulse after propagating a distance $\alpha_0 L = 32$. The solid line shows the spectrum of the precursor, the dashed line the spectrum of the soliton, and the dotted line shows the spectrum of the initial Gaussian pulse. The dashed-dotted line shows the inhomogeneous absorption line of the medium.

optical precursors and 0π pulses has already been established in the literature (see e.g. Jeong and Österberg [104] and references therein). We have also verified that after the precursor and the main signal begin to separate around $\alpha_0 z \sim 8$, the maximum population transfer caused by the precursor is less than 2.5% and occurs for atoms that are detuned approximately 675 MHz from the line center (i.e. where the spectral magnitude of the precursor is largest). Hence, this precursor approximately interacts linearly with the material. This is not surprising since the amplitude of the precursor is in the linear regime, as noted by both Macke and Ségard [98] and Crisp [99]. Eventually, for a material with sufficient optical depth the precursor is completely absorbed by the detuned atoms, and they are left in an excited state. Due to the 0π area of the precursor, the atoms on the line center are essentially unaffected by the precursor passage.

We have confirmed that when the input pulse duration becomes longer than $T \sim$

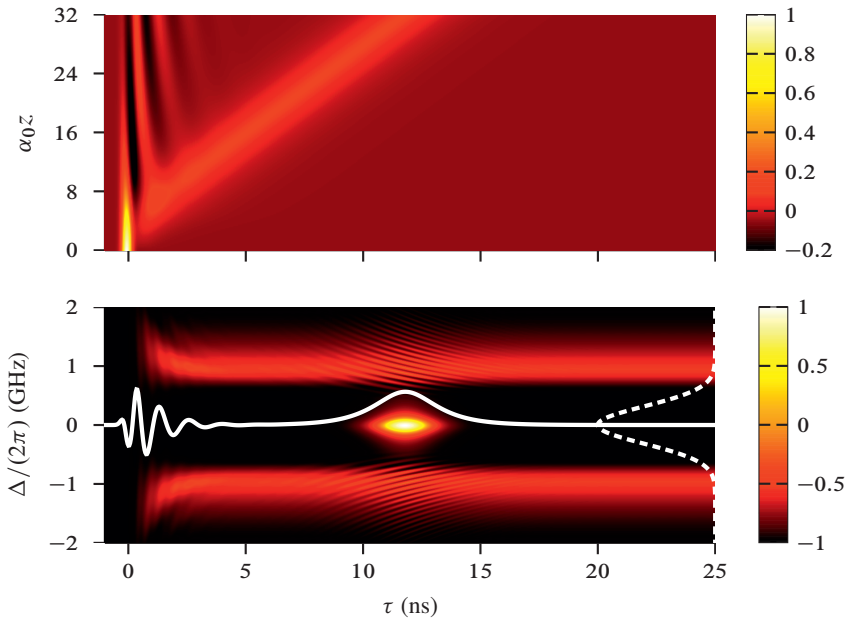

FIG. 4.4: Top panel: Reshaping of a Gaussian input pulse with initial duration $T = 0.3T_2^*$ and area $\theta_0 = 1.1\pi$. The color coding shows the normalized amplitude of the field. Bottom panel: Excitation of the absorption line at $\alpha_0 L = 32$. The color coding shows the inversion $\varrho_{\Delta,22}(\tau, L) - \varrho_{\Delta,11}(\tau, L)$, the solid line shows the exit pulse and the dashed line shows $g(\Delta)$ (the height of both lines are in arbitrary units).

$0.6T_2^*$, even less population is transferred during the precursor passage. However, when the initial pulse duration becomes shorter, the precursor becomes sufficiently strong to excite the red and blue wings of the absorption line; that is, the interaction between the precursor pulse and the medium becomes nonlinear. The top panel in Fig. 4.4 shows the spatiotemporal reshaping of a pulse with $T = 0.3T_2^*$, analogous to the top panel in Fig. 4.3. The color-coding in the bottom panel in Fig. 4.4 shows the material inversion $\varrho_{\Delta,22}(\tau, L) - \varrho_{\Delta,11}(\tau, L)$ for a time window large enough to contain the precursor and the main pulse, and for a range of Δ sufficiently broad to contain the entire absorption line. The solid line shows the pulse plotted against the horizontal axis, and the dashed line shows $g(\Delta)$. We find that the precursor pulse excites the blue and red wings of the absorption line, and that the population transfer is actually quite high; Up to 30% of the atoms at Doppler detuning $\Delta/(2\pi) \sim 1$ GHz are transferred to state $|2\rangle$ during the precursor passage. Although the relative atomic density at this detuning is only 1%, Fig. 4.4 shows that the McCall-Hahn solution is very stable against these perturbations. It is clear that the detuned atoms are prepared by the forerunner to a certain degree, but that this preparation

affects the soliton solution to a minor degree. It is readily seen that the 2π pulse interacts also with the pre-excited atoms, which is observed as ringing along the vertical coordinate Δ for $\tau \sim 12$ ns in the bottom panel of Fig. 4.4. The pre-excited atoms are returned to their precursor-prepared state after the main pulse has completely passed.

4.4 Box-car excitation

Next, we consider resonant excitation with box-car input pulses

$$\Omega(\tau, 0) = \begin{cases} 0, & |\tau| > T/2 \\ \Omega_0, & \tau \leq T/2. \end{cases} \tag{4.4}$$

The input pulse duration is taken as $T = T_2^*$ and the input area as $\theta_0 = 1.1\pi$. Initially, the pulse spectrum has several sidelobes (see Fig. 4.5) that are individually strong enough to nonlinearly interact with the absorption wings of the medium. Figure 4.5 shows the spectrum of the precursor, main pulse and input pulse for the boxcar pulse. At the exit face of the medium we again find that the precursor occupies the spectral sidelobes at ± 1 GHz and that the main pulse area is 2π.

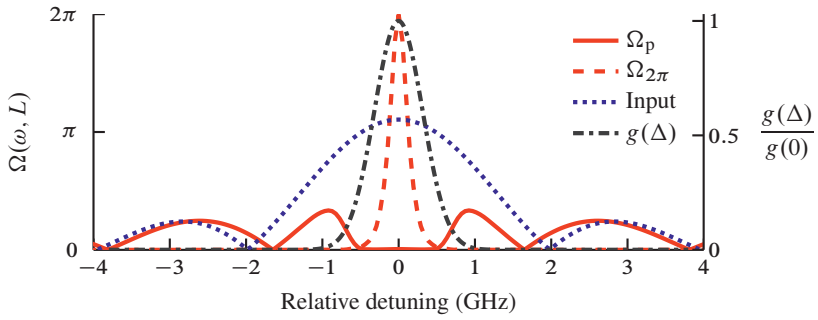

FIG. 4.5: Box-car pulse spectrum at the exit face. The duration and area of the input box-car pulse duration are $T = T_2^*$ and $\theta_0 = 1.1\pi$. The solid line shows the spectrum of the precursor, the dashed line the spectrum of the main pulse. For comparison, the dotted line shows the input spectrum. The inhomogeneous lineshape (dashed-dotted line), normalized against $g(0)$, is plotted against the right vertical axis.

Figure 4.6 depicts the reshaping of the boxcar pulse as it propagates through the medium. Similarly to the smooth Gaussian input pulse, a precursor starts to separate from the main pulse around $\alpha_0 z \sim 8$ and the two are temporally well-separated at the exit face of the medium. There are two rapid oscillations on $\tau = \pm T_2^*/2$ that were not present for the Gaussian input pulse. These two oscillations coincide with the initial unit

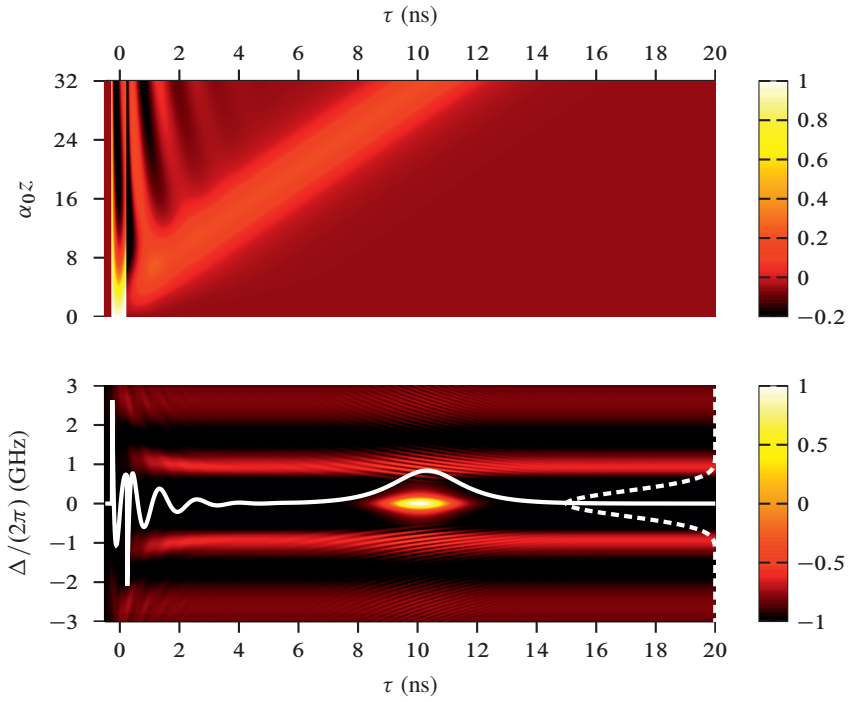

FIG. 4.6: Pulse evolution of a boxcar input pulse with duration $T = T_2^*$ and initial area $\theta_0 1.1\pi$. Top-panel: Spatio-temporal reshaping of the pulse, the horizontal axis indicates the pulse delay τ and the vertical axis indicates the propagation distance in units of α_0^{-1}. Bottom panel: Excitation of the absorption line at the exit face. The solid line shows the exit pulse, and the dashed line indicates the absorption line of the medium (height of both lines are in arbitrary units). The color coding indicates the material inversion $\varrho_{\Delta,22}(\tau, L) - \varrho_{\Delta,11}(\tau, L)$.

steps of the input pulse, showing that the pulse fronts propagate at the speed of light in vacuum. In most other aspects, this precursor shows similar qualitative behaviour as for the Gaussian input pulse: the main pulse is a hyperbolic secant with area 2π, the precursor has 0π area, the frequency pushing of the lobes closest to resonance persists, and neither the precursor or the main pulse are phase modulated. The bottom panel in Fig. 4.6 shows that the precursor excites detuned atoms $\Delta/(2\pi) \sim \pm 1$ GHz and $\Delta/(2\pi) \sim \pm 3$ GHz, which coincides with the two closest lobes in $\Omega_p(\omega, L)$. However, the low atomic density at the 3 GHz detuning ensures that these atoms contribute little or nothing to the pulse evolution. We also remark that the box-car pulse produces much larger precursors than Gaussian pulses do. In particular, our simulations show that using a boxcar pulse with duration $\tau_0 = 2T_2^*$ and area 1.1π produces a precursor with a peak amplitude $\sim 0.95\Omega_0$, while for a Gaussian pulse with comparable pulse duration the precursor amplitude was

negligible (see Fig. 4.1). The reason is that the two rapid oscillations at the leading and trailing edges of the box-car input pulse will generally persist with increasing propagation distance because the active electron has a non-zero inertial mass, and therefore cannot respond to the infinitely fast oscillation. Precursors excited by step-function pulses are therefore exceptionally long-lived.

A note on homogeneous broadening

In this study, pulse energy loss through spontaneous emission which occurs at a rate of $1/T_1$ is not incorporated. Typically, the emerging 2π soliton is not stable if it does not exit the material well within T_1, and can collapse to a 0π pulse [81]. The physical reason for this collapse is that although spontaneous emission is negligible for the duration of the pulse, small losses through spontaneous emission may accumulate during propagation such that a significant amount of energy is lost during propagation. The process is shown explicitly in Fig. 3.10. This results in temporal elongation of the pulse, and the pulse will propagate with a lower group velocity. Eventually, the pulse will will elongate to timescales comparable to the decoherence time and is then absorbed by the medium. This effect could be included with an additional degree of theoretical complexity, but does not provide further insight into the physics. Nevertheless, it places restrictions on the materials and pulses one can use for the experimental verification of the above results. For example, an input area of 1.1π may result in a soliton that is so slow that it loses most of its energy through spontaneous emission before it exits the material. To satisfy the time scale requirement $\tau_0 \ll T_1$, τ_0 being the peak delay, one might decide to use even shorter pulses, in which case a colder vapor must also be considered.

Chapter 5

Pulsed conical emission

5.1 Introduction

When a propagating laser beam is tuned close to the blue (self-focusing) side of an alkali metal D-line, a diffuse ring of light may in certain cases be observed around the central beam spot (see Fig. 5.1). This is called conical emission (CE), a phenomenon surrounded by much controversy since its first observation by Grischkowsky [1]. Conical emission is a physically rich phenomenon which has been observed in several of the alkali metals, such as potassium [1, 105, 106], sodium [107–111], rubidium [112], and cesium [113]. CE has also been observed in the alkaline earth metals barium [114] and strontium [32] (near the $5s^2\,{}^1\mathrm{S}_0 \rightarrow 5s5p\,{}^1\mathrm{P}_1$ transition at 461 nm). The emission of a light cone is, however, not unique to near-resonance propagation in vapors, and cone emission has been observed as a non-resonant process in bulk media such as liquid water [115–117] and glasses, where the results are adequately explained by the excitation of linear X-waves [116–120]. Broadly speaking, X-waves are non-diffracting and non-dispersive solutions to the ubiquitous nonlinear Schrödinger equation; they are invariant in the propagation coordinate and describe cylindrically traveling modes with a prominent X-profile in the angular-frequency spectrum.

In the alkali and alkaline earth metals, near-resonant cone emission has been observed over a wide range of experimentally adjustable parameters. In most experiments performed when the laser beam is tuned to the blue side of resonance, self-focusing of the laser beam is observed. Presently, self-focusing is generally believed to be necessary for conical emission. Experiments are performed using either continuous wave (cw) laser beams or pulsed lasers. For pulsed excitation, CE has been observed for pulse durations ranging from several nanoseconds down to only 100 fs. It is clear, particularly in the picosecond and femtosecond regimes, that coherence may play a central part in

the spatial and temporal evolution of the pulse. Moreover, pulsed CE experiments have shown that conical emission is observable over a range of detunings $\overline{\Delta}$. In the nanosecond pulse experiments by Paul et al. [32], cone emission was observed in the range $\overline{\Delta}/(2\pi) \in [100\,\text{GHz}, 270\,\text{GHz}]$, in the picosecond experiments by Sarkisyan et al. [105] $\overline{\Delta}/(2\pi) \in [100\,\text{GHz}, 400\,\text{GHz}]$, and in the femtosecond experiments by Vaičaitis and Paulikas [110] $\overline{\Delta}/(2\pi) \in [10\,\text{THz}, 40\,\text{THz}]$. In practically all pulsed CE experiments in alkali metal vapors where a cone is observed, the central frequency of the cone emission is red-detuned with respect to the atomic resonance frequency. Moreover, in most cases the cone and the laser beam are observed roughly symmetrically around the resonance frequency, i.e. $\omega_{\text{laser}} - \overline{\Delta} = \omega_{\text{CE}} + \overline{\Delta}$. In addition to the detuning $\overline{\Delta}$, CE is observable over a range of densities $\mathcal{N}$. Typically, the atomic density in CE experiments lies somewhere in the $10^{20} - 10^{22}$ m^{-3} range. Moreover, sufficient optical depth is required for observing CE, indicating that cone emission is a propagation phenomenon. In experiments, typical propagation lengths are $L = 1 - 20$ cm depending on the investigated elements, the density $\mathcal{N}$, and the detuning $\overline{\Delta}$.

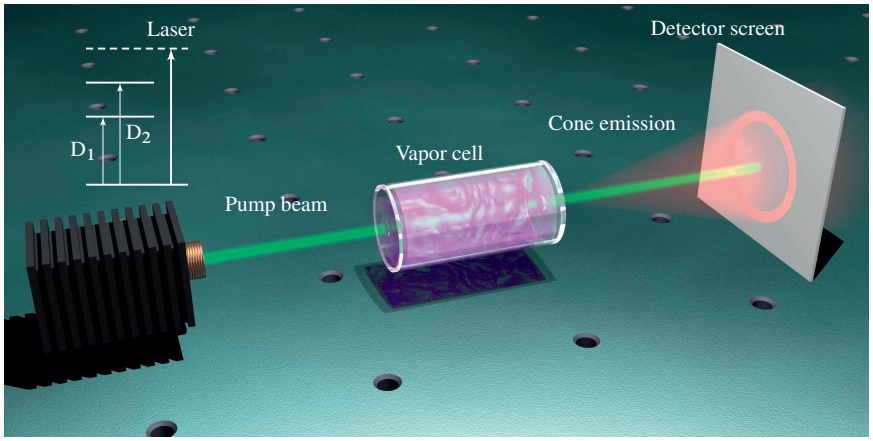

FIG. 5.1: Conical emission sketch. A laser tuned to the blue (self-focusing) side of one (or both) of the D-lines generates a sideband at longer wavelengths propagating conically with respect to the optical axis.

On a superficial level, conical emission is still a controversial subject because no theory, or numerical calculations, have been able to predict the experimentally observed angular structure that appears when a pulse is tuned to the self-focusing side of a one-photon transition. In the continuous-wave regime cone emission appears to be reasonably well explained by four-wave mixing within a quasi-trapped light filament, but the pulsed regime has withstood theoretical treatments. The problem is rooted in the complexity of the equations of motion to which no analytic solutions are known, and which require a supercom-

puter for numerical analysis. However, a computational approach opens up the possibility of investigating the spatiotemporal reshaping of the pulse in the interior of the medium, and is definitely called for.

In this chapter we numerically investigate, with two objectives in mind, conical emission in atomic sodium and rubidium. Firstly, we formulate a computational algorithm based on the RMB equations for investigating three-dimensional propagation of few-cycle laser pulses in multi-level media, thereby mitigating the shortcomings of the MB equations, which are computationally expensive due to the presence of bi-directional wave propagation. Secondly, we apply this numerical integrator to blue-detuned propagation in atomic sodium in order to highlight new features of cone emission. Sodium is chosen as a model medium in the femtosecond regime because the fine structure splitting of the $3p$ orbital is small, around 500 GHz, allowing degenerate treatment of the D_1 and D_2 lines for light pulses shorter than 2 ps. For longer pulses which resolve both absorption lines, the interaction with both lines may result in the emission of multiple cones [121]. Based on the inhomogeneously broadened paraxial SIT equations, we will also examine the picosecond regime, in which case we investigate propagation through rubidium. ^{87}Rb is chosen because picosecond pulses, whose bandwidths are on the order of tens of GHz or smaller, cannot excite both the $5P_{3/2}$ and $5P_{1/2}$ levels since the fine structure splitting is over 7 THz.

This chapter is organized as follows. In the subsequent section we first provide brief summaries of the most commonly cited models of conical emission. We proceed by presenting a numerical method for the RMB equations in Sec. 5.3. A multi-level sodium model is then introduced in Sec. 5.4 and explicit computer solutions are discussed in Sec. 5.5. We also compare these results with the predictions of the paraxial SIT model in Sec. 5.5.5. It will be shown that two-level theory is not quantitatively adequate in the femtosecond regime. In Sec. 5.6 we analyze, using the paraxial SIT equations, the inhomogeneously broadened picosecond regime for resonant, red- and blue-detuned pulses propagating in atomic rubidium. Finally, we summarize the results of this chapter in Sec. 5.7.

5.2 Conical emission models

Presently, the most complete descriptions of conical emission are those due to Valley et al. [122], Harter and Boyd [123], and Paul et al. [124]. Valley et al. [122] investigated cone emission for continuous-wave (cw) laser beams under steady state conditions. A brief summary of this model is as follows: The pump beam at ω_{laser} is, due to a careful balance between diffraction and self-focusing, quasi-trapped during propagation through the medium. The term quasi-trapped implies that the beam is trapped into a filament whose radius oscillates with propagation distance, but which is otherwise smaller than what is

expected from diffraction. Generation of new frequencies $\omega_3 > \omega_{\text{laser}}$ occurs through Raman gain amplification of the resonance fluorescence, and four-wave mixing between ω_3 and the pump wave results in a red sideband at $\omega_4 = 2\omega_{\text{laser}} - \omega_3 < \omega_{\text{laser}}$. The field envelope A_4 at ω_4 is split into two contributions $A_{4\text{L}}$ and $A_{4\text{R}}$ by optically Stark-shifted absorption, and the field envelope at ω_3 is divided into $A_{3\text{L}}$ and $A_{3\text{R}}$ by a four-wave mixing coupling. The propagation of the $A_{4\text{L}}$ component through the spatially dependent refractive index prepared by the pump beam results in the formation of a cone.

The model by Harter and Boyd [123, 125] is based on resonantly enhanced four-wave mixing of the Rabi sidebands of a two-level atom [126]. In the Harter-Boyd model, the pump beam is presumed to be trapped or quasi-trapped through self-action effects into single- or multiple light filaments that propagate along the vapor. Generation of new frequencies at $\omega_3 = \omega_{\text{laser}} + \Lambda$ occurs through the three-photon effect (i.e. due to transitions between the dressed atomic states) inside the saturated filaments. Here, Λ is the generalized Rabi frequency

$$\Lambda = \sqrt{\Omega^2 + \overline{\Delta}^2}. \tag{5.1}$$

Emission at $\omega_4 = \omega_{\text{laser}} - \Lambda$ is presumed to occur through a phase-matched four-wave mixing process between the pump beam and the sideband at $\omega_{\text{laser}} + \Lambda$. Due to saturation inside the filament, the sideband at ω_4 is anti-guided and ejected from the filament at an angle predicted by Snell's law, resulting in the apperance of a cone.

Perhaps the most complete model of CE is that due to Paul et al. [124]. The authors solved the two-level density matrix equations in the dressed atomic frame for cylindrically symmetric self-trapped beams. The calculations are performed in terms of the pump beam and the red and blue Rabi sidebands, and include both Doppler broadening and transverse diffraction. The authors assert that their model is valid also for beam breakup into multiple filaments, but for comparison with experimental results [32] they presume that only a single cylindrically symmetric light filament is formed inside the vapor. Computational limitations prevented Paul et al. [124] from obtaining time-dependent solutions of their model, and they analyze CE in the steady state regime. The observed gain in their model did not agree with the experimentally observed gains for pulsed experiments, and the authors conjectured that the low gain predicted theoretically is due to the neglection of higher-order radial modes of the laser beam.

For pulsed CE there is a serious problem with the four-wave mixing model of cone emission, which predicts as much scattering into the blue sideband as into the red, because the blue sideband required for phase matching is not observed experimentally [127]. Figure 5.2 shows a typical far-field conical emission spectrum, measured in terms of the angle θ each frequency component makes with the propagation axis. The concentration of contour lines surrounding the region $\theta \approx 18.5$ mrad, $\nu_r - \nu_l \approx 225$ GHz indicates conical

emission. Notably, no blue sideband is observed propagating either axially or conically. Presently, the most viable explanation of pulsed CE appears to be that due to Crenshaw and Cantrell [128, 129], who numerically investigated the propagation of a strong laser beam tuned 60 GHz above a one-photon resonance in two-level approximation. The propagation distance in their computer simulations is sufficiently short so that self-focusing effects, although incorporated into their calculations, had an almost negligible effect on propagation. Their numerical calculations show that when a transverse variation is incorporated into the initial conditions for an 8π pulse propagating off resonance, temporal pulse breakup leads to a transverse spatial variation which they argue is CE. The somewhat angularly isolated frequency components asserted by Crenshaw and Cantrell [128] to be cone emission, were detuned to the blue side of the resonance, in direct conflict with experimental results. Presumably, computational limitations at the time prevented propagating the pulse a sufficiently long distance to place a sideband on the red side of the resonance.

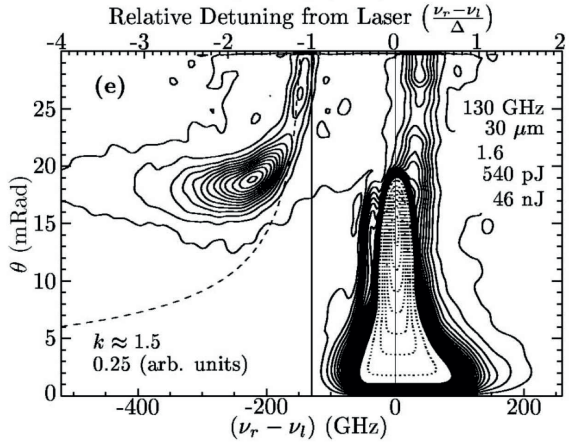

FIG. 5.2: From Paul et al. [32] with permission. The data show the angular-frequency spectrum after propagation through a strontium vapor. The contour lines surrounding the region $\theta \approx 18.5$ mrad, $\nu_r - \nu_l \approx 225$ GHz indicates cone emission. The numbers in the top right corner indicate the initial detuning (130 GHz), the beam radius (30 μm), the cone energy (540 pJ), and the input pulse energy (46 nJ).

Another model that has attracted considerable attention is the Cherenkov radiation model [130–132]. According to this model, saturation of atoms inside the filament causes the appearance of a traveling polarization field at velocity $c/n(\omega_{\text{laser}})$, where $n(\omega_{\text{laser}})$ is the index of refraction of the pump laser. The induced polarization produces radiation at the Rabi sideband $\omega_{\text{laser}} - \Lambda$ which propagates with velocity $c/n(\omega_{\text{laser}} - \Lambda)$. The velocity difference between the polarization wave and the laser beam is responsible for the cone

emission of the Rabi sideband, with a cone angle $\cos\theta_{\rm CE} = \frac{n(\omega_{\rm laser})}{n(\omega_{\rm laser}-\Lambda)}$. However, these suggestions do not solve the mystery of the missing sideband [127].

Cone emission may be observed also under different experimental conditions, and we now mention a few experiments where the results are adequately explained by existing theoretical models. Kauranen et al. [108] have investigated two-beam-excited conical emission in a sodium vapor, and the experimental data are well explained by presuming that the medium responds as a Kerr material where the cone emission then occurs as a result of a perfectly phase-matched four-wave mixing process. Krasinski et al. [107] have investigated the propagation of light beams tuned close to the $3s \rightarrow 4d$ two-photon transition in atomic sodium, which resulted in cone emission at frequencies near the $4d \rightarrow 3p$ and $3p \rightarrow 3s$ transitions. The propagation of the beam through the medium occured without influence from self-focusing, and the data were in excellent agreement with theoretical predictions based on a four-wave mixing model.

Self-focusing is generally believed to participate in the formation of the light cone. Provided that the input beam does not saturate the medium, self-focusing becomes possible if the input power exceeds the critical power

$$P_{\rm cr} = K\pi \frac{c^2}{\omega_c^2 n_2}, \tag{5.2}$$

where ω_c is the carrier frequency of the input beam, $K \approx 1.896$ for Gaussian beams, and

$$n_2 = \frac{\mathcal{N}|\mu_{12}|^2}{2c\epsilon_0^2\left(\hbar\overline{\Delta}\right)^3} \tag{5.3}$$

is the Kerr refractive index [133]. These expressions are valid provided that saturation and linear absorption are negligible, the two-level restriction holds, and homogeneous broadening dominate. In general, expressions for n_2 and $P_{\rm cr}$ require averaging over the Doppler velocity distribution [134] and incorporation of background absorption contributions [135]. The inclusion of both effects tends to increase critical power compared to the predictions of Eq. (5.2). Nonetheless, even when these corrections are taken into account, n_2 remains antisymmetric in the detuning $\overline{\Delta}$. The effective refractive index for a continuous-wave beam is, by the Kerr effect, given by $n(r) = n_0 + n_2 I(r)$, where $I(r)$ is the beam intensity. For conventional laser beams $I(r)$ peaks at $r = 0$ and decreases monotonically outwards in r, and in this case $n(r)$ becomes largest on the axis for lasers tuned to the blue side, implying that the effective phase velocity on the axis is lower than that in the radial periphery. Due to the difference in phase velocity in the different annular slices of the beam, the wave fronts develop a concave curvature during propagation, quite analogous to the curvature that is induced by a convex lens. The process leads to self-focusing. In certain limited cases self-focusing and diffraction may balance, leading

to *trapping* of the beam. Evidently, on the red side of resonance both diffraction and the Kerr effect act to expand the beam profile since $n_2 < 0$.

Several pulsed CE experiments are performed in the coherent strong-field regime where Rabi oscillations presumably take place. For alkali metal D-lines the transition dipole moment is on the order of 2×10^{-29} Cm. Letting Ω_0 be the input peak Rabi frequency, estimated input intensities from experiments are then as follows: $\Omega_0/\overline{\Delta} \sim 1$ in the experiments by Paul et al. [32]; $\Omega_0/\Delta \sim 1 - 20$ in the experiments by Sarkisyan et al. [105]; $\Omega_0/\overline{\Delta} \sim 1$ in the experiments by Vaičaitis and Paulikas [110]. The inclusion of self-focusing will tend to raise these values somewhat, and it is immediately apparant that an analysis of alkali metal CE requires a Maxwell-Bloch approach rather than employing models based on parametric wave amplification.

5.3 The RMB equations of motion

Before analyzing conical emission, we will briefly review a computational method for the RMB equations. Recalling that direct Maxwell-Bloch models require a spatial resolution finer than a wavelength, it is evident that the MB equations are incapable of generating reliable numerical solutions to the macroscopic propagation distances where conical emission is observed. In the case of a medium $L = 20$ cm long and $R = 3$ mm wide, the numerical grid necessitated by direct MB simulations consists of billions of grid points, ruling out direct MB methods as a viable numerical approach. From a numerical point of view, one might nonetheless argue that long-range propagation can be implemented in direct MB simulations simply by adjusting the density $\mathcal{N}$ such that the desired propagation length $\sim \mathcal{N}L$ is obtained. This conjecture is inconsistent with the underlying physics. Firstly, the uni-directional condition $\varepsilon \ll 1$ may be broken when $\mathcal{N}$ becomes unrealistically large, possibly leading to artificial macroscopic backpropagation in direct MB simulations. In the transverse degrees of freedom increasing $\mathcal{N}$ implies decreasing the transverse dimensions by a factor $1/\sqrt{\mathcal{N}}$ if the same diffractive effects are considered. This compensation, in conjuction with a much larger nonlinear polarization, may lead to artificial numerical activation of the divergence term $\nabla(\nabla \cdot \boldsymbol{P})$.

Analysis of conical emission is computationally tractable if one starts out from a propagation equation rather than the full Maxwell equations. In the few-cycle regime, the equations of motion are then the RMB equations, summarized by the first-order propagation equation [Eq. (3.35)] and the von Neumann equation,

$$\partial_z E = \frac{c}{2} \int_{-\infty}^{\tau} \nabla_\perp^2 E \, \mathrm{d}\tau' - \frac{1}{2\epsilon_0 c} \partial_\tau P, \tag{5.4a}$$

$$i\hbar \mathrm{d}_\tau \hat{\rho} = \left[\hat{H}_0 - \hat{\mu} E, \hat{\rho} \right] + i\hbar \hat{R}, \tag{5.4b}$$

where $\hat{\rho}$ is the $N \times N$ dimensional density operator describing the Bloch system. For definiteness, the laser pulse is taken to be linearly polarized in the xy-plane, and propagation axis lies along $+z$. In the following we disregard inhomogeneous broadening, although inhomogeneous damping is straightforwardly incorporated following the procedures summarized in Sec. 3.4.

5.3.1 Numerical solutions to the RMB equations

The RMB equations are favored over the MB equations because they open up the possibility of examining long-distance propagation of laser pulses whose duration may be as short as a single cycle. The extreme bandwidths of single-cycle pulses imply that some of the bandwidth constraints are implicit in the SIT equations are broken, implying that additional energy eigenstates become participants in the laser dynamics. The matrix formalism employed for the optical Bloch equations in Sec. 3.4 is useful for describing such media, and may be immediately coupled to Eq. (5.4a). To evaluate Eq. (5.4), we use the Bloch equation solver summarized in Sec. 3.4, but replace the full Maxwell equations by the first order propagation equation which is solved by a standard differential method.

Scaling and Liouville space

Firstly, Eq. (5.4) is scaled into a dimensionless set of equations where the quantities E and $\hat{\mu}$ are of order unity, and the time and space coordinates are

$$\tau \to \frac{E_c \mu_c}{\hbar} \tau \equiv \frac{\tau}{\tau_c}, \tag{5.5a}$$

$$z \to \frac{\mathcal{N} \mu_c}{2\epsilon_0 c \tau_c E_c}, \tag{5.5b}$$

$$r \to \sqrt{\frac{\mathcal{N} \mu_c}{\epsilon_0 c^2 \tau_c^2 E_c}} r, \tag{5.5c}$$

where μ_c and E_c are characteristic constants. Next, only cylindrically symmetric beams $E(\tau, z, r, \varphi) = E(\tau, z, r)$ are investigated. When the von Neumann equation is moved into Liouville space (recall Sec. 3.4), the dimensionless equations of motion are

$$\partial_z E = \left(\frac{1}{r} \frac{\partial}{\partial r} + \frac{\partial^2}{\partial r^2} \right) \int_{-\infty}^{\tau} E \, \mathrm{d}\tau' - \left\langle\!\left\langle \mu \middle| \check{L}_0 \middle| \rho \right\rangle\!\right\rangle, \tag{5.6a}$$

$$i \, \mathrm{d}_\tau \, |\rho\rangle\!\rangle = \left(\check{L}_0 + E \check{L}_1 \right) |\rho\rangle\!\rangle \, . \tag{5.6b}$$

For completeness, we recall that the free Liouville operator $\check{L}_0$ and the interaction Liouville operator $E\check{L}_1$ are

$$\check{L}_0 = i\,\hat{H}_0^{\mathsf{T}} \oplus \left(-\hat{H}_0\right) + \sum_{k,l}\left[\hat{\gamma}_{kl} \otimes \hat{\gamma}_{kl} - \frac{1}{2}\left(\hat{\gamma}_{kl}^{\mathsf{T}}\hat{\gamma}_{kl}\right) \oplus \left(\hat{\gamma}_{kl}^{\mathsf{T}}\hat{\gamma}_{kl}\right)\right], \tag{5.7a}$$

$$\check{L}_1 = -i\,\hat{\mu}^{\mathsf{T}} \oplus (-\hat{\mu})\,. \tag{5.7b}$$

Discretization

To solve Eq. (5.6) numerically, we apply second order differential Adams-Moulton and Adams-Bashforth linear multistep methods for propagation along $+z$ together with finite differences in the transverse coordinate. The numerical method applied for the integration of the Liouville equation along the temporal coordinate τ is the same as for direct Maxwell-Bloch simulations, with the important exception that staggered temporal grids are no longer used. Discretized variables $E(\tau, z, r) \rightarrow E_{\mathrm{i,j}}^{\mathrm{n}}$ and $|\rho\rangle\!\rangle \rightarrow \left|\rho_{\mathrm{i,j}}^{\mathrm{n}}\right\rangle\!\rangle$ are now stored on the same computational grid

$$z_{\mathrm{i}} = \mathrm{i}\triangle z, \tag{5.8a}$$

$$r_{\mathrm{j}} = \mathrm{j}\triangle r, \tag{5.8b}$$

$$\tau_{\mathrm{n}} = \mathrm{n}\triangle\tau. \tag{5.8c}$$

On a co-located temporal grid Eq. (3.70) does not apply. Instead, the integral is evaluated using linear interpolation between the integration endpoints located at $\tau_{\mathrm{n+1}}$ and τ_{n}. This yields

$$\int_{\tau_{\mathrm{n}}}^{\tau_{\mathrm{n}+1}} \check{L}_I\left(\tau'\right)\mathrm{d}\tau' \approx \frac{E^{\mathrm{n}} + E^{\mathrm{n}+1}}{2}\check{L}_1\triangle\tau \tag{5.9}$$

for Eq. (3.70). Following the subsequent calculations in Sec. 3.4, the numerical update of the density operator is performed according to

$$|\rho^{\mathrm{n}+1}\rangle\!\rangle = \check{U}_0^{1/2}\check{U}_I^{\mathrm{n}+1}\check{U}_0^{1/2}\,|\rho^{\mathrm{n}}\rangle\!\rangle\,, \tag{5.10}$$

where

$$\check{U}_I^{\mathrm{n}+1} = \exp\left(i\,\frac{(E^{\mathrm{n}+1} + E^{\mathrm{n}})\hat{\mu}\triangle t}{2}\right)^{*} \otimes \exp\left(i\,\frac{(E^{\mathrm{n}+1} + E^{\mathrm{n}})\hat{\mu}\triangle t}{2}\right). \tag{5.11}$$

The first-order propagation equation is numerically evaluated by first approximating the integral using Gaussian numerical quadrature,

$$\begin{aligned}\int_{-\infty}^{\tau_{\mathrm{n}+1}} E\mathrm{d}\tau' &\approx \left(\sum_{k=1}^{\mathrm{n}} E_{\mathrm{i,j}}^{k} + \frac{1}{2}E_{\mathrm{i,j}}^{\mathrm{n}+1}\right)\triangle\tau + \mathcal{O}(\triangle\tau^2) \\ &\equiv \left(\Sigma_{\mathrm{i,j}}^{\mathrm{n}} + \frac{1}{2}E_{\mathrm{i,j}}^{\mathrm{n}+1}\right)\triangle\tau + \mathcal{O}(\triangle\tau^2),\end{aligned} \tag{5.12}$$

where $E(\tau \to -\infty) = 0$ for physical pulses.

The radial grid is defined at grid points

$$r_{\mathrm{j}} = \left(\mathrm{j} - \frac{1}{2}\right) \triangle r, \quad \mathrm{j} = 1, 2, \ldots, \tag{5.13}$$

which avoids the singularity at $r = 0$ and the need for pole equations. The radial derivatives are evaluated with 2nd order finite differences

$$\left.\frac{1}{r}\frac{\partial E}{\partial r}\right|_{\mathrm{i,j}}^{\mathrm{n}} \approx \frac{1}{r_j}\frac{E_{\mathrm{i,j+1}}^{\mathrm{n}} - E_{\mathrm{i,j-1}}^{\mathrm{n}}}{2\triangle r} + \mathcal{O}\left(\triangle r^2\right), \tag{5.14a}$$

$$\left.\frac{\partial^2 E}{\partial r^2}\right|_{\mathrm{i,j}}^{\mathrm{n}} \approx \frac{E_{\mathrm{i,j+1}}^{\mathrm{n}} - 2E_{\mathrm{i,j}}^{\mathrm{n}} + E_{\mathrm{i,j-1}}^{\mathrm{n}}}{\triangle r^2} + \mathcal{O}\left(\triangle r^2\right). \tag{5.14b}$$

Evaluation of the radial derivatives on the grid point closest to the origin ($r_1 = \frac{1}{2}\triangle r$) using 2nd order centered finite differences requires knowledge of the field variable in a point directly across the origin. The system is closed by invoking cylindrical symmetry on the centerline and by imposing a perfect electric conductor (PEC) boundary condition [28] on the outer surface. Although the use of a PEC boundary condition result in reflection of outgoing waves, the computational domains used in the simulations below are sufficiently large to prevent waves reaching the outer boundary, and therefore emulate an open medium.

Numerical integration along the propagation coordinate z is performed with a second order Adams-Moulton method (i.e. the implicit trapezoidal method), which together with Eqs. (5.12) and (5.14) gives a rather lengthy expression for Eq. (5.6a):

$$\begin{aligned}
&-\frac{\triangle z\triangle\tau}{4\triangle r^2}\left(1 - \frac{\triangle r}{2r_j}\right)E_{\mathrm{i+1,j-1}}^{\mathrm{n+1}} + \left(1 + \frac{\triangle z\triangle\tau}{2\triangle r^2}\right)E_{\mathrm{i+1,j}}^{\mathrm{n+1}} - \frac{\triangle z\triangle\tau}{4\triangle r^2}\left(1 + \frac{\triangle r}{2r_j}\right)E_{\mathrm{i+1,j+1}}^{\mathrm{n+1}} \\
&= E_{\mathrm{i,j}}^{\mathrm{n+1}} + \frac{\triangle\tau\triangle z}{4r_{\mathrm{j}}\triangle r}\left(\Sigma_{\mathrm{i+1,j+1}}^{\mathrm{n}} + \Sigma_{\mathrm{i,j+1}}^{\mathrm{n}} - \Sigma_{\mathrm{i+1,j-1}}^{\mathrm{n}} - \Sigma_{\mathrm{i,j-1}}^{\mathrm{n}} + \frac{E_{\mathrm{i,j+1}}^{\mathrm{n+1}} - E_{\mathrm{i,j-1}}^{\mathrm{n+1}}}{2}\right) \\
&+ \frac{\triangle\tau\triangle z}{2\triangle r^2}\left(\Sigma_{\mathrm{i+1,j+1}}^{\mathrm{n}} + \Sigma_{\mathrm{i,j+1}}^{\mathrm{n}} - 2(\Sigma_{\mathrm{i+1,j}}^{\mathrm{n}} + \Sigma_{\mathrm{i,j}}^{\mathrm{n}}) + \Sigma_{\mathrm{i+1,j-1}}^{\mathrm{n}} + \Sigma_{\mathrm{i,j-1}}^{\mathrm{n}}\right) \\
&+ \frac{\triangle\tau\triangle z}{4\triangle r^2}\left(E_{\mathrm{i,j+1}}^{\mathrm{n+1}} - 2E_{\mathrm{i,j}}^{\mathrm{n+1}} + E_{\mathrm{i,j-1}}^{\mathrm{n+1}}\right) - \frac{\triangle z}{2}\langle\!\langle \mu \big| \check{L}_0 \big| \rho_{\mathrm{i,j}}^{\mathrm{n+1}} + \rho_{\mathrm{i+1,j}}^{\mathrm{n+1}} \rangle\!\rangle.
\end{aligned} \tag{5.15}$$

Equation (5.15) defines a triangular matrix equation $\mathbb{A}\vec{u} = \vec{b}$ for the column vector $\vec{u} = \left\{E_{\mathrm{i+1,j}}^{\mathrm{n+1}}\right\}$, $\mathrm{j} = 1, 2, \ldots$ and with $\vec{b}$ given by the right-hand side of Eq. (5.15). It is solvable with the Thomas algorithm. Breaking with the quasi-3D model yields extra derivatives in the azimuthal coordinate and will lead to a *block tridiagonal* linear system for the column vector $\vec{u} = \left\{E_{\mathrm{i+1,j,k}}^{\mathrm{n+1}}\right\}$, $\mathrm{j} = 1, 2, \ldots$, $\mathrm{k} = 1, 2, \ldots$ where k is the additional numerical index associated with the azimuthal grid points. This system is solvable by the *block Thomas* algorithm. Thus, for a given time step in Eq. (5.15) we progressively solve for $\vec{u}$

(containing the transverse unknowns) by stepping along the discrete coordinate i. The only complication is that the terms $\langle\!\langle \mu \left| \check{L}_0 \right| \rho^{n+1}_{i+1,j} \rangle\!\rangle$, contained in $\vec{b}$, are not known quantities, calling for an iterative numerical scheme.

Equations (5.15) and 5.10 are coupled through the appearance of $\left|\rho^{n+1}_{i+1,j}\right\rangle\!\rangle$ on the right-hand side of Eq. (5.15) and $E^{n+1}_{i+1,j}$ implicitly via Eq. (5.11). To solve the coupled equation set we impose a predictor-corrector method. This leads to the following procedure:

1. For a given n, i, obtain initial predictions for $\vec{u}$ and $\left|\rho^{n+1}_{i+1,j}\right\rangle\!\rangle$ by an explicit update of Eqs. (5.15) and (5.10). This entails to approximating $\left|\rho^{n+1}_{i+1,j}\right\rangle\!\rangle \approx \left|\rho^{n+1}_{i,j}\right\rangle\!\rangle$ and $E^{n+1}_{i+1,j} \approx E^{n}_{i+1,j}$ in the right-hand sides of Eqs. (5.15) and (5.11), and then inverting the equations.

2. Insert the predicted values into the right-hand sides of the same equations and obtain corrected values for the unknown variables. This process is iterated until a convergence criterion is met.

3. Step along $i \rightarrow i + 1$ until the entire spatial grid is updated, and then take another temporal step $n \rightarrow n + 1$.

5.3.2 Parallelization & Performance

Computer implementations using the formulation detailed above executes rapidly in the plane wave, homogeneously broadened limit. With current computer facilities the execution time is usually on the order of a few seconds for two or three levels. However, numerical parallelization is necessary for propagation in two or three spatial dimensions, particularly when inhomogeneous broadening is incorporated. Efficient computational scaling may be achieved by distributing the Bloch equation calculations over a two-dimensional numerical process grid, where the two dimensions are associated with the inhomogeneous broadening variable and the radial variable, respectively. Each process in this grid is then assigned an equally large chunk of the optical Bloch equations, and all calculations (i.e. the inhomogeneous line average) are first performed locally over each chunk before the simulation data are assembled globally. The datapoints in Fig. 5.3 indicate the wall clock execution time for a two-level RMB simulation on a 200×200 spatial grid. Inhomogeneous broadening is included, and the line is sampled at 256 different values of the inhomogeneous broadening variable. The computer simulation is otherwise propagated for 600 time steps. In this computer implementation, two computing cores are reserved for updating the propagation equation while the remaining cores are allocated to the Bloch equations. Figure 5.3 shows the RMB equations scale very well numerically. One finds, for example, that a 50% reduction in computation time is achieved by increasing the number of processors from 64 to 128.

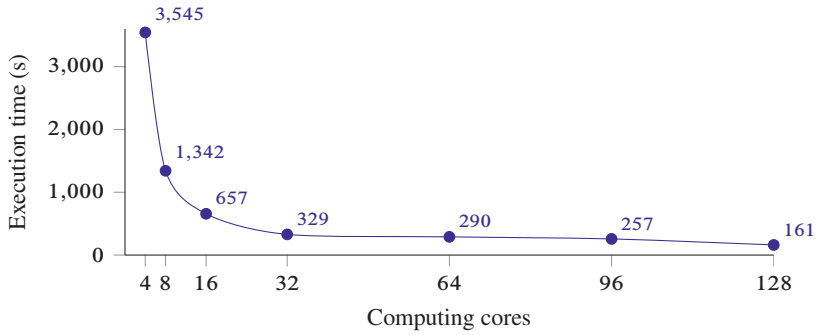

FIG. 5.3: Scalability of the RMB equation solver. The horizontal axis shows the number of computing cores assigned to the simulation, the vertical axis the wall-clock execution time in seconds. The simulations are performed on an SGI Altix ICE X distributed memory cluster with two 8-core Intel Sandy Bridge (2.6 GHz) processors on each node.

5.4 The multi-level RMB sodium model

Having addressed the numerical aspects of the RMB equations we are now in a position to discuss the RMB sodium model in greater detail. One might expect that propagation of ultrashort laser beams tuned further from resonance ($>$ 1 THz) may enhance certain features of CE. Rabi sidebands are then spectrallly placed further from the center frequency of the pump beam, which might lead to clearer distinctions between self-phase modulated spectral broadening and Rabi sideband generation. We will consider, numerically, the propagation of 20 fs pulses detuned $\overline{\Delta}/(2\pi) = 23.5$ THz from the $3s - 3p$ resonance at 589 nm of an atomic sodium vapor. At these conditions the sodium D_1 and D_2 lines are approximately degenerate. Figure 5.4 shows the excitation diagram of the active electron in a sodium atom, and this is the only electron that is assumed to respond to the external laser field. Our sodium Bloch model incorporates the first 5 levels of the s, p, and d orbitals for the active electron. The remaining 10 electrons are assumed to reside in the $1s^2 2s^2 2p^6$ configuration during the entire evolution, based on the presumption that they are tightly bound to the nucleus. These electrons completely fill the inner orbitals and constitute a spherically symmetric wavefunction. Hence, they do not affect the propagation of the external laser field. In addition, fine and hyperfine splittings of the active electron orbitals are disregarded, and the fine structure levels $3^2P_{3/2}$ and $3^2P_{1/2}$ are thus treated as a single $3p$ orbital. We have not tested this approximation explicitly but anticipate that it holds based on the different time scales involved. The fine structure splitting of the $3p$ orbital is around 500 GHz, corresponding to a time constant of 2 ps, while the input pulse is 100 times shorter.

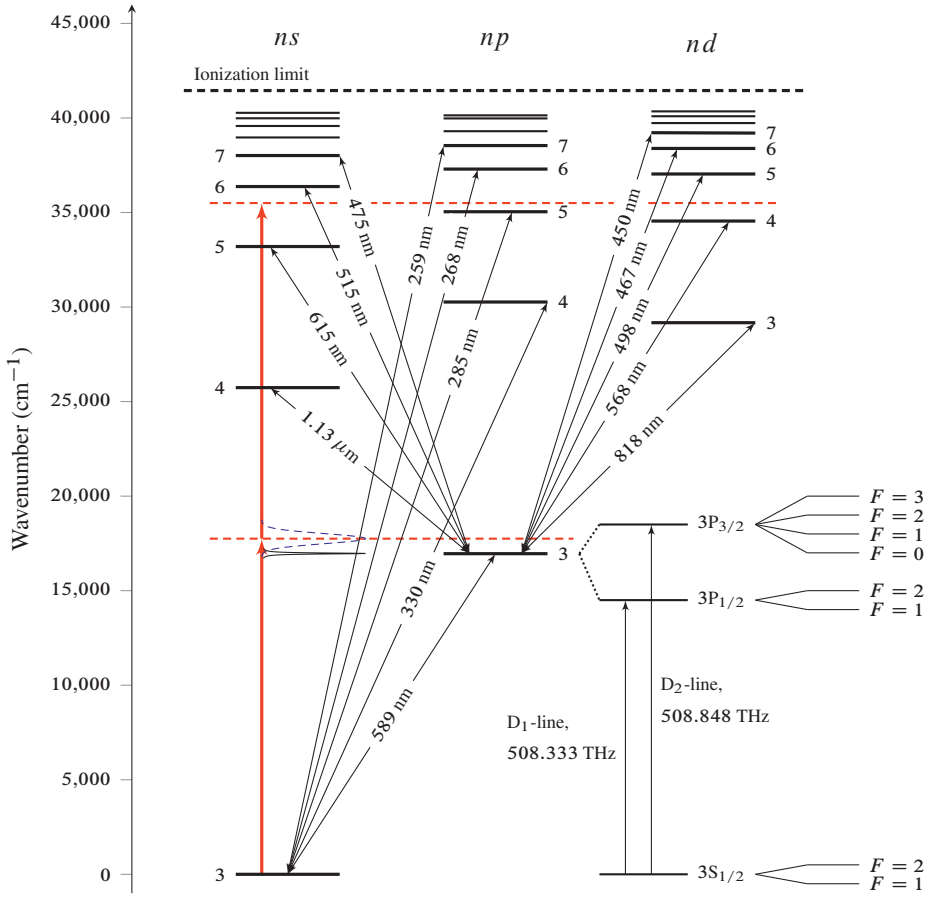

FIG. 5.4: Sodium energy levels for the first five s, p, and d orbitals in the single active electron approximation. The ground state electronic configuration for atomic sodium is $1s^2 2s^2 2p^6 3s\ ^2\mathrm{S}_{1/2}$. A few higher orbitals that are not regarded in our model are shown as unlabeled horizontal lines. Fine and hyperfine levels are ignored. Near-resonant one- and two-photon transitions are indicated with vertical arrows. The two curves shown at the top of the bottom vertical arrow indicate the input pulse spectrum (dashed line) and the $3s - 3p$ absorption line (solid line, assumed to be a Lorentzian with half width $T_2^{-1} = 1$ THz). The detailed D_1 and D_2 lines, shown in the lower right corner, are not plotted to scale. Data are obtained from Sansonetti [136], Kelleher and Podobedova [137], and Steck [138].

In the femtosecond regime Doppler broadening may be disregarded because the pulse duration is orders of magnitude shorter than T_2^*. Spectrally, the pulse bandwidth is on the order of several THz while the Doppler half width is usually on the order of a few GHz. Next, the energy levels are arranged in order of increasing eigenstate energies of the s orbitals first, then for p orbitals, and then finally for the d orbitals. With this ordering

the 15×15 dimensional free Hamiltonian operator and dipole moment operator (projected onto the polarization axis) become

$$\hat{H}_0 = \begin{pmatrix} \hbar\hat{\omega}_s & \hat{0} & \hat{0} \\ \hat{0} & \hbar\hat{\omega}_p & \hat{0} \\ \hat{0} & \hat{0} & \hbar\hat{\omega}_d \end{pmatrix}, \tag{5.16a}$$

$$\hat{\mu} = \begin{pmatrix} \hat{0} & \hat{\mu}_{s\to p} & \hat{0} \\ \hat{\mu}^\dagger_{s\to p} & \hat{0} & \hat{\mu}_{p\to d} \\ \hat{0} & \hat{\mu}^\dagger_{p\to d} & \hat{0} \end{pmatrix}, \tag{5.16b}$$

where $\hat{0}$ is a 5×5 dimensional zero matrix. $\hat{\omega}_s$ is the diagonal matrix

$$\hat{\omega}_s = \mathrm{diag}(\omega_{3s}, \omega_{4s}, \omega_{5s}, \omega_{6s}, \omega_{7s}) \tag{5.17}$$

which contains the eigenstate energies (in units of $\hbar$) of the first five s orbitals. In the same way, $\hat{\omega}_p$ and $\hat{\omega}_d$ contain the eigenstate energies of the p and d orbitals. By convention $\omega_{3s} = 0$ is taken as the reference energy. The partial dipole moment operators $\hat{\mu}_{s\to p}$ and $\hat{\mu}_{p\to d}$ are each in the form

$$\hat{\mu}_{q\to r} = \begin{pmatrix} \mu_{3q,3r} & \mu_{3q,4r} & \mu_{3q,5r} & \mu_{3q,6r} & \mu_{3q,7r} \\ \mu_{4q,3r} & \mu_{4q,4r} & \mu_{4q,5r} & \mu_{4q,6r} & \mu_{4q,7r} \\ \mu_{5q,3r} & \mu_{5q,4r} & \mu_{5q,5r} & \mu_{5q,6r} & \mu_{5q,7r} \\ \mu_{6q,3r} & \mu_{6q,4r} & \mu_{6q,5r} & \mu_{6q,6r} & \mu_{6q,7r} \\ \mu_{7q,3r} & \mu_{7q,4r} & \mu_{7q,5r} & \mu_{7q,6r} & \mu_{7q,7r} \end{pmatrix}, \tag{5.18}$$

where $q = s, r = p$, or $q = p, r = d$. The transition dipole moments μ_i^k are obtained from the oscillator strengths [133]

$$f_{kl} = \frac{2m_\mathrm{e}\omega_{kl}|\mu_{kl}|^2}{3\hbar q_\mathrm{e}^2}, \tag{5.19}$$

where m_e is the electron rest mass, ω_{kl} the transition frequency, and q_e the electron charge. In our level model fine and hyperfine states are grouped into single levels, and an effective dipole moment is obtained for the composite transitions. In this way one avoids dealing with problematically large Bloch dimensions while retaining experimentally observed line intensities. Oscillator strengths and transition frequencies are taken from Sansonetti [136] and Kelleher and Podobedova [137]. For the $3s - 3p$ multiplet the obtained transition dipole moment is $|\mu_{3s,3p}| \approx 3.66 \times 10^{-29}$ Cm.

Incorporation of homogeneous broadening follows Eq. (2.13) where the population relaxation rates γ_{kl} ($k \neq l$) are taken from the Einstein A coefficients [139]

$$A_{kl} = \frac{\omega_{kl}^3 g_k |\mu_{kl}|^2}{3\pi\epsilon_0\hbar c^3 g_l}, \tag{5.20}$$

are obtained from Sansonetti [136] and Kelleher and Podobedova [137]. Here, g_k and g_l are the degeneracies of the respective multiplet levels.

5.5 Computational results of femtosecond CE in atomic sodium

In this subsection we report on computational results where femtosecond conical emission in atomic sodium is observed. We suppose a medium of length $L = 20$ cm and density $\mathcal{N} = 5 \times 10^{21}$ m^{-3}. Under these conditions the forward propagation approximation is valid and is quantitatively justified using typical numbers for sodium: assuming a 2π pulse with a duration of 50 fs propagating resonantly with the $3s - 3p$ transition at the above density yields $E_c \sim 10^8$ V/m and $P_c \sim \mathcal{N}\mu_{3s,3p} \sim 10^{-7}$ Cm^{-2}. This corresponds to $\varepsilon \approx 10^{-4}$ and the one-way approximation is therefore justified. Interaction with a self-induced backward mode can therefore be disregarded. Out of computational necessity we take the decoherence time $T_2 = 1$ ps for each coherence. The equations are numerically integrated for a time $2T_2 = 2$ ps which is sufficiently long for all pulse transients to die out. Disregarding linear absorption and Doppler broadening, the numbers above correspond to a critical power

$$P_{\rm cr} \approx 29 \text{ W}. \tag{5.21}$$

We impose an input pulse with a Gaussian profile in time and space,

$$E(\tau, r) = E_0 \exp\left(-\frac{\tau^2}{2T^2} - \frac{r^2}{2R^2}\right) \sin(\omega_c \tau). \tag{5.22}$$

The pulse duration, waist, and carrier are $T = 20$ fs, $R = 100$ μm, and $\omega_c = 1.065\pi \times 10^{15}$ rad/s $\left(\overline{\lambda} = 563.3 \text{ nm}\right)$. The time-averaged input intensity on the centerline is $I_0 = \epsilon_0 c|E_0|^2/2$, whereas the input peak power is

$$P_0 = \epsilon_0 c \pi R^2 |E_0|^2. \tag{5.23}$$

Equation (5.22) yields a beam divergence angle

$$\begin{aligned} \theta_{\rm d} &= \arctan\left(\frac{R_L(\omega_c)}{L}\right) \\ &\approx 1.47 \text{ mrad}, \end{aligned} \tag{5.24}$$

where

$$R_L(\omega) = R\sqrt{1 + \frac{c^2 L^2}{\omega^2 R^4}} \tag{5.25}$$

is the diffraction-induced beam waist for each frequency component ω in the absence of the material. The associated Rayleigh length is $z_R(\omega) = \omega R^2/c$. These expression are obtained by solving Eq. (5.4) analytically for propagation in vacuum with Eq. (5.22) as

the initial condition [see Eq. (6.3)]. Comparatively small beam waists are used in order to excite only single filaments in the sodium vapor. For comparison, the femtosecond experiments by Vaičaitis and Gaižauskas [109] employed pulse energies of 0.05 mJ, which is almost 100 times larger than what is applied in the computer simulations presented below. Higher input beam waists or energies are not a problem for the RMB equations *per se*, but multiple filaments may form inside the vapor for large input powers. The computational results assume cylindrical symmetry and would not be very meaningful at such conditions.

The parameters above correspond to a spectral pulse bandwidth (FWHM) of 623 cm^{-1} (18.7 THz). The low frequency wing measured at the half width half maximum (HWHM) of the pulse is located at 17129 cm^{-1}. The bandwidth of the $3s-3p$ absorption line is $T_2^{-1}=1$ THz, and the relative detuning between the low frequency wing of the pulse and the high frequency wing of the $3s-3p$ absorption line centered 16967 cm^{-1} is approximately 100 cm^{-1} (3 THz). At this laser detuning linear absorption, and its contribution to the critical power P_{cr}, is non-negligible. The relative detuning between the center frequency of the pulse and the absorption line is 784 cm^{-1} $\left(\overline{\Delta}/(2\pi)\approx 23.5\ \mathrm{THz}\right)$. The spectral placements and bandwidths of the input pulse and the absorption line (assumed to be a Lorentzian) are indicated in Fig. 5.4. At the wavelengths considered the input pulse spectrum also lies close to the resonantly enhanced $3s-6s$ and $3s-4d$ two-photon transitions. The relative two-photon detunings are $-866\mathrm{cm}^{-1}$ (-26 THz) for the $3s-6s$ transition and 957 cm^{-1} (28.7 THz) for the $3s-4d$ transition, respectively. With the exception of changing the input amplitude E_0, these parameters are retained in the computer simulations below.

5.5.1 Linear propagation regime

Figure 5.5 shows the output from a computer solution in the linear propagation regime. The peak amplitude of the input pulse is taken as $E_0=4\times10^4$ V/m, corresponding to a pulse energy of a few femtojoules, an input intensity $I_0=\epsilon_0 c|E_0|^2/2\approx 0.42\ \mathrm{kW/cm}^2$, and an input peak power of $P_0=I_0\pi R^2\approx 66$ mW. The corresponding pulse area on the centerline is $\theta_0\sim10^{-4}$. The solid line in Fig. 5.5(a) shows the input pulse envelope (in units of E_0) on the centerline. The dashed line, plotted against the right vertical axis, shows a corresponding envelope for the output pulse at $z=L$. The normalized pulse envelopes are obtained as the magnitude of the analytic signal,

$$u(\tau,z,r)=\frac{1}{E_0}\left|E(\tau,z,r)+\frac{i}{\pi\tau}\star E(\tau,z,r)\right|, \tag{5.26}$$

where the star symbol ($\star$) denotes a spectral convolution. Corresponding centerline input (solid line) and output (dashed line) pulse spectra are plotted in Fig. 5.5(b) as a function of

wavelength λ. The curves are normalized against the spectral peak magnitude of the input pulse. The input (output) spectrum is plotted against the left (right) vertical axis, and the position of the $3p - 3s$ resonance relative to the pulse spectra is also indicated.

Figure 5.5(c) shows the energy transmission (solid line) through each cross-section z of the material. The dashed line shows the on-axis fluence and is plotted against the right vertical axis. The two curves are individually normalized against the input energy and the input fluence on the centerline. This kind of normalization is used in all plots below (field, spectrum, fluence, energy etc.). The fluence is numerically calculated following Eq. (3.43), which under the simplifying conditions of linear polarization, cylindrical symmetry and comparatively large beam waist becomes

$$F_z(z,r) = \int_{-\infty}^{\infty} \epsilon_0 c \, |E(\omega,z,r)|^2 \, \mathrm{d}\omega \tag{5.27a}$$

$$F_r(z,r) = \int_{-\infty}^{\infty} \frac{i\epsilon_0 c^2}{2\omega} \left(E^*(\omega,z,r) \frac{\partial E(\omega,z,r)}{\partial r} - E(\omega,z,r) \frac{\partial E^*(\omega,z,r)}{\partial r} \right) \mathrm{d}\omega. \tag{5.27b}$$

Moreover, following Eq. (3.40) the components of the "Poynting vector" are given by the integrands in Eq. (5.27).

Standard propagation features are observed in Fig. 5.5. Firstly, the temporal broadening of the on-axis pulse seen in Fig. 5.5(a) is due to strong color dispersion in the neighborhood of the $3s - 3p$ absorption line(s). Secondly, pushing of the pulse spectrum towards blue frequencies is due to the combined effects of spectrally asymmetric linear absorption and diffraction. Frequency components in the red wing have a shorter Rayleigh length [recall Eq. (5.24)] than components in the blue, and are detuned less from resonance. This results in both stronger diffraction and absorption of the red part of the field spectrum. A comparison of the data in Figs. 5.5(a) and (b) shows that the width of the input and output spectra are comparable, but the temporal durations are different. Because the input pulse was transform limited this is equivalent to pulse chirping, which is expected this close to resonance. Thirdly, the decrease in axial fluence is due to the combined effects of absorption and diffraction. For reference, at these parameters the total linear transmission throughout the medium is 47%.

More careful examination of the remaining simulation data for different values of r and z shows that the radial components of the fluence and Poynting vectors are always positive, and the pulse evolution is therefore diffractive for the entire propagation distance. In short, for this simulation we observe a diffractive expansion of the pulse waist during propagation, a frequency chirp, a frequency push to the blue, linear absorption, and decreasing fluence. The maximum population of the $3p$ level is negligible ($< 0.1\%$) and the evolution is therefore linear through the medium.

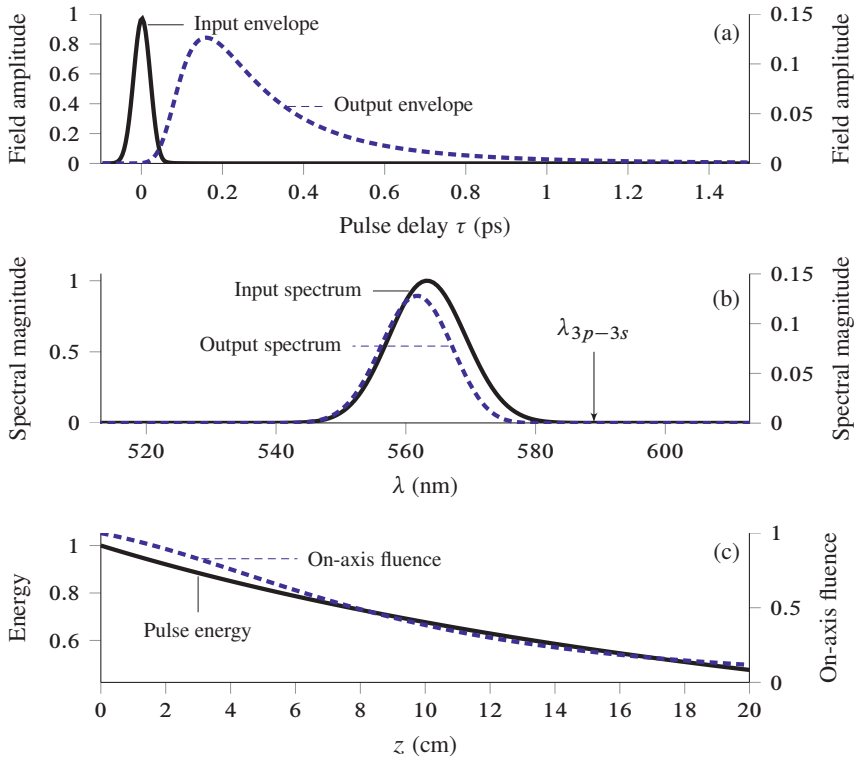

FIG. 5.5: Computer simulation with $\mathcal{N} = 5{\times}10^{15}$ cm^{-3}, $E_0 = 4{\times}10^4$ V/m ($I_0 \approx 0.21$ kW/cm^2), pulse energy of 4.73 femtojoules. (a) On-axis input pulse envelope (solid line), plotted against the left vertical axis. The dashed line shows the on-axis pulse envelope at the output facet and is plotted against the right vertical axis. (b) Normalized input and output pulse spectra on the centerline. The on-axis input spectrum (solid line) is plotted against the left vertical axis, the on-axis output spectrum (dashed line) is plotted against the right vertical axis. (c) The solid line shows the normalized energy transmission through each cross-section z of the vapor and is plotted against the left vertical axis. The dashed line shows the centerline longitudinal fluence $F_z(z, r = 0)$, plotted against the right vertical axis.

5.5.2 Nonlinear propagation regime

With sufficiently high input powers propagation through the vapor results in cone emission. Figures 5.6(A)-(C) show the normalized fluence component $F_z(L, r)$ on a logarithmic color scale at the output facet of the medium for three different input intensities (A) 0.21 kW/cm^2, (B) 21 GW/cm^2, and (C) 42 GW/cm^2. Case (A) refers to the linear propagation regime and is used as a reference for the nonliner cases (B) and (C). Key quantities, such as input power, intensity, and area, are summarized in table 5.1 for the various pulses. The area is defined by the integral of the Gaussian envelope function,

$\theta_0 = \frac{\mu_{3s,3p}E_0}{\hbar}\int_{-\infty}^{\infty} \mathrm{e}^{-\tau^2/(2T^2)}\mathrm{d}\tau.$

TABLE 5.1: Simulation reference data (input).

Simulation	E_0	P_0/P_{cr}	I_0	θ_0/π
(A)	4×10^4 V/m	$\sim 10^{-7}$	0.21 kW/cm^2	$\sim 10^{-4}$
(B)	4×10^8 V/m	≈ 14.1	21 GW/cm^2	2.2
(C)	$4\sqrt{2}\times10^8$ V/m	≈ 28.2	42 GW/cm^2	3.1

The simulation data in Fig. 5.6 are plotted on a logarithmic scale over 4 decades for the various figures, and individual datasets are normalized against the output centerline fluence for the specific simulation. The color range is different for each figure and chosen such that the brightest colors indicate the highest longitudinal fluence F_z on the output facet, and darker colors indicate a lower axial fluence. In each plot black regions indicate regions where F_z is 10^4 times smaller than the maximum output fluence. The input pulse amplitudes and energies used in each simulation are indicated in the caption. The data are plotted as a function of the distance r away from the symmetry axis. Figures 5.6(B) and (C) should be compared to Fig. 5.6(A) which shows the fluence distribution at the output facet in the linear propagation regime. Qualitatively, concentric rings appear around the central beam spot and demonstrates that CE has occured somewhere in the material. Visual examination of the central spot shows that its diameter increases with increased input pulse energy. Strictly speaking, the existence of a diffuse beam spot on the output facet does not rule out CE which is most reasonably described in the far-field in terms of the angular-frequency spectrum. We will address this spectrum later. Note that our computer code does not solve for the azimuthal coordinate and the plots in Fig. 5.6 have been reconstructed by invoking cylindrical symmetry. We observe from the data in Figs. 5.6(B),(C) that the CE ring is located slightly further out in the radial direction for higher pulse energies.

Finer features of the radial profile at the output face of the medium are shown in Fig. 5.7 [the simulation data are otherwise the same as in Fig. 5.6]. The following radial features develop at the exit face of the medium: In the linear propagation regime the radial profile is monotonically decreasing in amplitude as expected. For pulses (B) and (C) (dashed and dotted lines, respectively) bumps and flattenings of the radial profile of the main beam are observed together with CE. The cone emission is observed as a bump in the fluence $F_z(L,r)$ for larger radii, $r \approx 1.4$ mm and $r \approx 1.6$ mm for (B) and (C), respectively. Notably, Fig. 5.7 also shows the apperance of two peaks in the radial profile for pulse (C) at $r = 0$ mm and $r \approx 0.25$ mm. These two bumps demonstrate the appearance of interconnected radial filaments. As we do not solve for the azimuthal coordinate we cannot comment on the stability of these filaments against azimuthal perturbations. The radial spread (FWHM) of the cones, which are observed as two bumps abovebelow

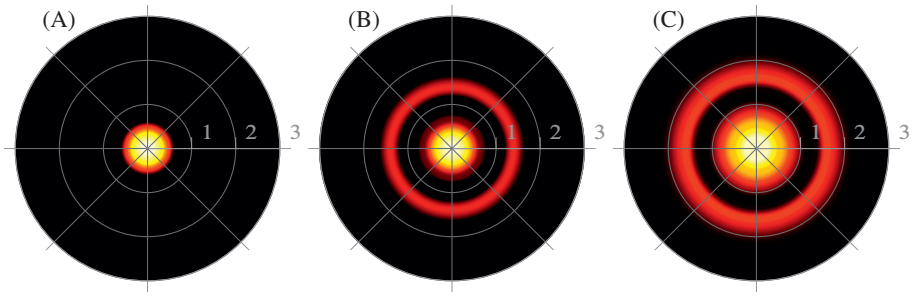

FIG. 5.6: Fluence distribution at the output facet of a sodium vapor with $\mathcal{N} = 5 \times 10^{21}$ m^{-3}. The color-range is 4 decades, darkest colors indicate a fluence less than 10^4 of the peak fluence at the output facet. The labels along the horizontal axes indicate the distance (in mm) from the symmetry line. In each panel the same input pulse is used which is a 20 fs Gaussian centered at 563.3 nm with a 100 μm beam radius. The various input energies used are (A), 4.3 fJ, (B), 472 nJ, (B), 944 nJ. Corresponding peak field amplitudes E_0 and intensities I_0 are (A) $E_0 = 4 \times 10^4$ V/m, $I_0 = 0.21$ kW/cm^2, (B) $E_0 = 4 \times 10^8$ V/m, $I_0 = 21$ GW/cm^2, and (C) $E_0 = 4\sqrt{2} \times 10^8$ V/m, $I_0 = 42$ GW/cm^2.

$r = 1.5$ mm, is approximately 200 μm giving $\Delta r_{\rm CE}/r_{\rm CE} \sim 0.1-0.2$ for the two computer simulations. In addition, where cones are observed the intensity of the CE relative to the input intensity is slightly higher for higher pulse energies. Nonetheless, the CE intensity is comparatively weak since the peak intensity in the cone is 10^{-3} times smaller than the peak intensity of the input pulse. Owing to a large surface area, the energy contained in the cone is nevertheless significant. We define the relative CE energy as

$$\Sigma_{\rm CE} = \frac{\int_{r_{\rm min}}^{r_{\rm max}} F_z(L,r) r \mathrm{d}r}{\int_0^\infty F_z(0,r) r \mathrm{d}r}, \tag{5.28}$$

where $r_{\rm min}$ and $r_{\rm max}$ are chosen so that they contain the entire CE and nothing of the central spot. $\Sigma_{\rm CE}$ describes the ratio between the energy contained in the cone relative to the input energy. Spatial separation between the central spot and the CE is necessary before calculating $\Sigma_{\rm CE}$, and this is clearly the case here. For the above simulations we find $\Sigma_{\rm CE} \approx 1\%$ (A), $\Sigma_{\rm CE} \approx 1.5\%$ (B) for the two cones in Fig. 5.7.

Figure 5.7 may be qualitatively compared with the CE experiments by Paul et al. [32] where particular care was taken to avoid excitation of multiple light filaments. Comparing the dashed line in Fig. 5.7, where only a single filament is excited, with Fig. 9(f) in the paper by Paul et al. [32] demonstrates a favorable qualitative agreement. Strictly speaking, the system examined by Paul et al. [32] is different from the present one, and quantitative comparison is therefore not possible. In addition, we mention that Fig. 5.7 shows the fluence distribution on the output facet rather than the far-field. Some diffractive spreading

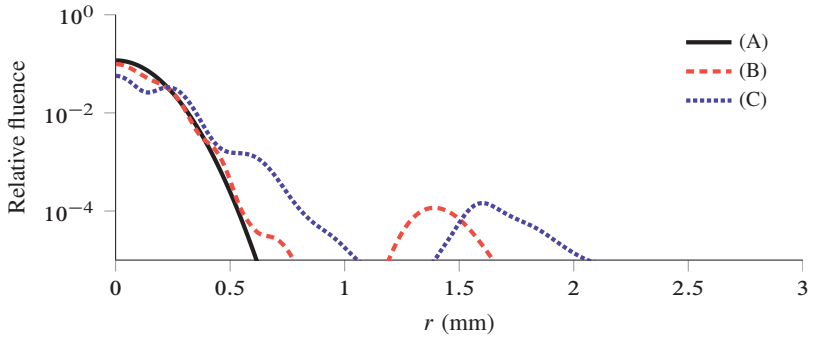

FIG. 5.7: Radial fluence profiles at the output facet of a sodium vapor. The simulation data are the same as in Fig. 5.6.

of the central beam spot must be expected when the central beam spot propagates from the output facet to the detector, which will tend to lower the peak at $r = 0$.

Having observed the formation of ring surrounding the central beam spot we now address the question whether or not this represents conical emission. The color-coded data in Figs. 5.8(A)-(C) show the logarithmic $r - \omega$ spectrum of the various pulses at $z = L$ plotted as a function the relative detuning from the input center frequency ω_c. The vertical coordinate indicates the distance r away from the symmetry axis. Solid lines superimposed on top of each color map show the on-axis output spectral magnitude in each simulation and are plotted against the right vertical axis on a logarithmic scale. All data (color-coded and lines) are normalized against the spectral peak amplitude of the input pulse, and the spectral magnitude at various radial positions may be estimated from the color map included in the various plots. The relative detuning from the resonant $3s - 3p$, $3p - 5s$, $3p - 4d$ one-photon transitions and the resonant $3s - 6s$ two-photon transition are indicated with symbols Δ_i^k. Firstly, a comparison between the spectra in Figs. 5.8(A) and (B) shows that the spectrum of the main beam is pushed primarily to the blue. A spectral hole has developed at 570 nm which is most likely due to one-photon absorption at the $3p - 4d$ transition, indicating that the $3p$ level has been populated somewhere inside the vapor cell. Missing spectral holes at 579 nm and 550 nm which correspond to absorption at the $3s - 4d$ and $3s - 6s$ virtual two-photon transitions show that if the $4d$ and $6s$ levels are populated, then this occurs via one-photon absorption from the $3p$ level and not from virtual transitions directly from the $3s$ level. The pulse in Fig. 5.8(C), which had twice the input energy shows even more spectral holes, with the deepest being at 570 nm. We have not checked the position of each of these holes, but some of these are believed to originate from various Stark-shifted one- and two-photon resonances, while

others are the result of spatiotemporal pulse splitting. In general the $r-\omega$ spectrum has a very complicated structure that cannot be explained by absorption alone, and we examine the allied spatiotemporal $r-\tau$ structure below. CE is readily visible in Fig. 5.8(B) as a continuous streak at $r \sim 1.6$ mm for detunings -35 THz to -75 THz corresponding to the wavelength range 602 nm to 650 nm. For the pulse with twice the energy the CE spectrum extends from approximately 610 nm to 660 nm, and has a particular structure that has been observed in femtosecond CE experiments where the shortest wavelengths of the CE are scattered furthest out into the cone, and longer wavelengths lie further in. In both Fig. 5.8(A) and (B) the spectral peak of the cone appears at frequencies that are complementary to the laser detuning in the sense that the equality $\omega_c - \omega_{3p-3s} \approx \omega_{3p-3s} - \omega_{\mathrm{CE,max}}$ is *weakly* satisfied. For definiteness, $\omega_{\mathrm{CE,max}}$ indicates the position of the spectral peak of the CE. Examination of the $r-\omega$ spectrum for larger detunings (> 50 THz) that are not plotted in Fig. 5.8 shows that this part of the spectrum is negligible.

Figure 5.8 describes the logarithmic $r-\omega$ spectrum at the output facet of the material. We believe that the broadening to the blue side is due to self-phase modulation and we will make our case below. Note that parts of the CE spectrum also coincides with the $3p-5s$ transition. However, we will show below that the cone is a pulse which propagates primarily through regions where the main beam does not, and consequently through regions where the $3p$ level is not populated. Absorption at the 615 nm $3p-5s$ transition is therefore not observed. In summary, one finds the rings shown in Figs. 5.6 consist of red-detuned frequencies in the 600 nm to 650 nm range.

Experimentally, significant transverse reshaping may occur either as a continuous process through the material or even close to $z = L$. The ring-like structure observed in Figs. 5.7 and 5.8 is not necessary for CE, nor is it guaranteed to exist at the exit face of the medium. Experimentally, the spectrum is therefore measured in terms of the angular-frequency $\theta-\omega$ spectrum in the far-field, defined by the double transform

$$E(\omega, z, k_\perp) = \int_0^\infty E(\omega, z, r) J_0(k_\perp r) r \,\mathrm{d}r, \tag{5.29}$$

where J_0 is the 0th order Bessel function of the first kind, $E(\omega, z, r)$ is the $r-\omega$ spectrum (as shown in Fig. 5.8), and θ is related to $k_\perp$ through $\theta \equiv \arctan(ck_\perp/\omega_c) \approx ck_\perp/\omega_c$ in the paraxial approximation. It may be verified from Eq. (3.35) that $|E(\omega, z, k_\perp)|$ is invariant for propagation in free space. The quantity $E(\omega, z, k_\perp)$ describes, in terms of the transverse wavenumber $k_\perp$, the angle each frequency component ω makes with the propagation axis. The transform defined by Eq. (5.29) is the zeroth order Hankel transform, and is equal to the two-dimensional spatial Fourier transform with the understanding that the radial wavenumber is $k_\perp = \sqrt{k_x^2 + k_y^2}$, where k_x and k_y are the transverse wavenumbers in the x- and y-directions, respectively.

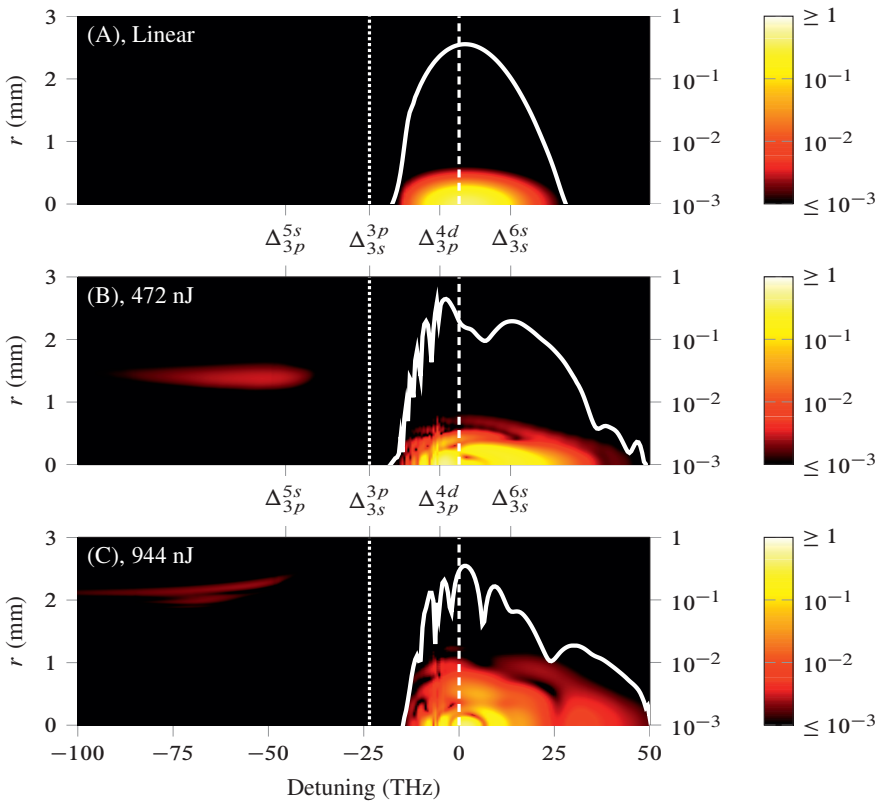

FIG. 5.8: Logarithmic $r-\omega$ spectrum $|E(\omega, L, r)|$ (color-coded) at the output facet. All data are normalized against input peak spectra of the individual simulations. The solid lines shown in each plot indicate the on-axis output spectrum in each simulation. Panels (A)-(C) correspond to simulations (A)-(C) in Fig. 5.6 and all data are plotted relative to the input center frequency. In each figure the dashed vertical line indicates the center frequency of the pulse, the dotted line indicates the position of the $3s-3p$ resonance (at -23.5 THz). Relative detunings where various one- and two-photon transitions become resonant are indicated by symbols Δ_i^k.

Figure 5.9 shows the logarithmic $\theta-\omega$ spectrum corresponding to the $r-\omega$ spectrum shown in Fig. 5.8(B). The data are normalized against the peak magnitude of the input Fourier-Hankel spectrum. We observe an angular structure commonly seen in CE experiments where the spectral peak of the cone is roughly detuned a complimentary amount to the red side of resonance as the pulse is detuned to the blue side. In this case the central peak of the cone is placed at $\lambda \approx 620$ nm which corresponds to a detuning of 25.6 THz from the $3s-3p$ resonance. For completeness, we recall that the input pulse was detuned approximately 23.5 THz from the $3s-3p$ resonance. Figure 5.9 shows that the cone spans

a relatively narrow angular width $\Delta\theta/\theta \sim 0.15$. By following the contour lines of the CE from red to blue we observe that the conically emitted frequency components move upwards in θ as Δ moves closer to Δ_{3s}^{3p}, a feature which has been observed experimentally [32, 110].

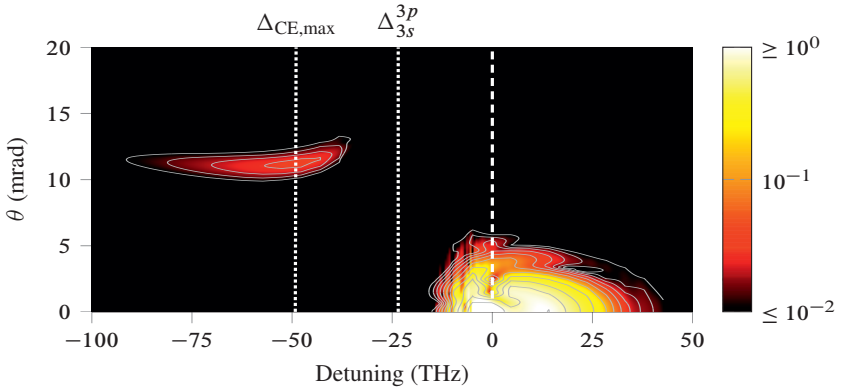

FIG. 5.9: Logarithmic $\theta - \omega$ spectrum $|E(\omega, L, k_\perp)|$ for pulse (B) at the output facet. The horizontal is plotted in terms of the relative detuning $(\omega - \omega_c)/(2\pi)$, the vertical axis in terms of the emission angle $\theta = ck_\perp/\omega_c$. The dotted vertical lines show the locations of the spectral cone peak and the $3s - 3p$ resonance.

Having examined the $r - \omega$ and $\theta - \omega$ spectra at $z = L$ we now locate the geometric origin of the CE inside the vapor cell. The color-coded data in Fig. 5.10(B) show the normalized longitudinal component $F_z(z, r)$ for pulse (B) at all positions (z, r) in the medium and is plotted on a logarithmic scale over 5 decades. The solid line, plotted against the left vertical axis r, indicates the calculated beam waist

$$\overline{R}(z) = \frac{\sqrt{\pi}\int_0^\infty F_z(z,r)r\,\mathrm{d}r}{\int_0^\infty F_z(z,r)\mathrm{d}r}, \tag{5.30}$$

where the $\sqrt{\pi}$ factor is used to normalize such that $\overline{R}(0) = R = 100\ \mu$m. In the same plot, the dotted line indicates the normalized on-axis fluence as a function of position z in the vapor cell, and is plotted against the right vertical axis. The opening angle the dashed line makes with the z-axis indicates the internal CE angle. Figure 5.10(C) shows a corresponding plot for pulse (C). Based on the simulation data we find that the pulses are focused a few centimeters into the vapor cell, evidenced by a decreasing beam waist and an increased fluence. Examination of the $r - \omega$ spectrum during this initial reshaping shows that the pulse spectrum initially broadens symmetrically around its center frequency. The spectrum is pushed to the blue when the pulse amplitude increases further and conical emission occurs. The spectral broadening to the blue observed in Figs. 5.8(B) and (C) is

therefore attributed to self-phase modulation. As expected, pulse (C) which has higher input intensity focuses a shorter distance into the same medium than pulse (B) does. The peak fluence occurs at $z = 6.4$ cm [(B)] and $z = 3.8$ cm [(C)] in the two cases, with amplification factors of 7.1 and 7.7 respectively. The minimum beam waist reached during propagation is approximately 38 μm for both cases, and occurs at z-positions where the axial fluence reaches its maximum. We find that the CE occurs after collapse (i.e. where the centerline fluence has a turning point). By examining the opening angle of the dashed lines shown in Figs. 5.10(B) and (C), the internal angle of CE is found to be $\theta_{\rm i} \approx 10.9$ mrad in both cases. These predictions agree with the calculations based on the $\theta - \omega$ spectrum. Consequently, the CE angle is not strongly dependent on the input pulse amplitude, consistent with experimental observations. The full opening angle of the emitted cone in the far-field would in this case be $\theta_{\rm CE} = 2\theta_{\rm i} \approx 22$ mrad, comparing favorably with femtosecond experiments in sodium at similar densities and detunings [110]. Examination of the CE around the dashed lines shown in Fig. 5.10 shows that the CE energy decreases gradually with further propagation into the medium, a result which is attributed to linear absorption and diffraction.

The appearance of a self-focusing region with a finite longitudinal fluence indicates a saturable nonlinearity through population transfer between the $3s$ and $3p$ orbitals, which is also consistent with an observed spectral hole at the $3p - 4d$ resonance. We now present detailed plots of the spatiotemporal pulse dynamics in the vicinity of the spatial region where the CE occurs for simulation (B). We have observed analogous behaviour for pulse (C) and therefore do not present these simulation data in detail. Figures 5.11-5.13 show the normalized field envelope $u(\tau, z, r)$ at six different z-positions in the material. Figure 5.11(a) shows the pulse envelope in the time-radius plane at the position $z = 5$ cm in the medium, 1.4 mm before collapse occurs (defined by the position z where the fluence is largest). At this propagation depth the pulse is compressed radially while temporal steepening, presumably due to the combined effects of self-focusing and spatiotemporal compression of the SIT type, has caused the peak amplitude to increase by a factor of 3.5. With further propagation the pulse steepens even more and reaches an amplitude of $4.5E_0$ with an even shorter pulse duration after 7 cm, as shown in Fig. 5.11(b). At this propagation depth collapse has initiated and the pulse begins to break up temporally. We remark that the internal oscillations, or "holes", in the pulse spectrum observed at the exit facet [see Fig. 5.8] are, in addition to absorption, spectral signatures of temporal pulse splitting. In fact, for any function $f(\tau) = f_1(\tau - \tau_1) + f_2(\tau - \tau_2)$ where f_1 and f_2 are individual pulses and τ_1 and τ_2 are respective peak pulse delays, the composite power spectrum

$$|f(\omega)|^2 = |f_1(\omega)|^2 + |f_2(\omega)|^2 + 2\,\mathrm{Re}\left[f_1(\omega) f_2^*(\omega) \mathrm{e}^{-i\omega(\tau_2-\tau_1)}\right] \tag{5.31}$$

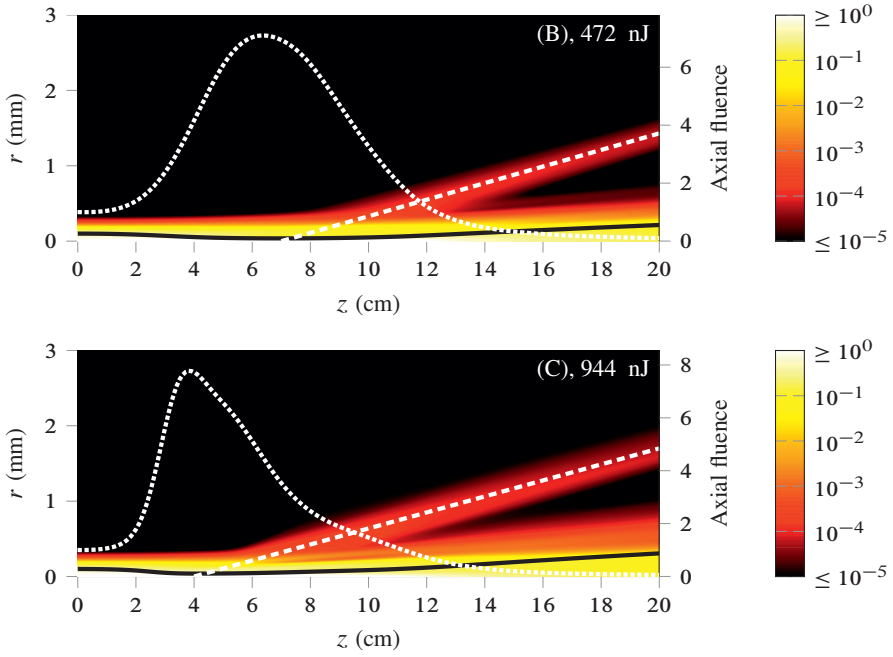

FIG. 5.10: (B) Logarithmic longitudinal normalized fluence F_z (color-coded) for pulse (B). The solid line shows the calculated beam waist $\overline{R}(z)$ and is plotted against the left vertical axis. The dotted line shows the normalized longitudinal fluence F_z on the axis $r = 0$ and is plotted against the right vertical axis. The opening angle of the dashed line indicates the internal CE angle. (C) Same as for (B), but for 944 nJ input pulse energy.

shows that the pulse spectrum contains internal sidelobes depending on the temporal separation $\tau_2 - \tau_1$ between the two pulses. These internal oscillations of the pulse spectrum have physical significance but these features may experimentally average out over many measurements when the timing jitter between the two pulses is severe.

Figures 5.12(a) and (b) show the pulse in the time-radius plane at positions $z = 9$ cm and $z = 11$ cm and depict the temporal dynamics during the initial breakup process (from Fig. 5.10(B) we observe that at this propagation length a conical emission begins to separate from the main beam). Figure 5.12(a) shows that a positive lobe appears behind the main peak. Temporal ripples have developed both on the trailing lobe and in the radial periphery of the main beam. By investigating the $r-\omega$ at this propagation length we have found that the pulse has developed a broadened spectrum together with a red sideband. The axial spectrum is broadened primarily to the blue with a broad spectral "hole" at the driving frequency, which is simply a spectral signature of temporal breakup. In addition, the pulse has developed a hole at 568 nm which indicates aborption at the $3p-4d$ resonant

transition. The temporal ripples are manifestations of coherent temporal beating between the main beam and the generated red sideband, which has not yet escaped from the main pulse. They mark the onset of conical emission. These ripples tend to move outwards in r as the breakup process proceeds; they move away from the main beam with gradually decreasing amplitude. Figure 5.12(b) shows the spatiotemporal dynamics at $z = 11$ cm, slightly further into the material. We find that the pulse amplitude decreases as it elongates temporally and broadens radially. At this stage the absence of temporal modulations (ripples) on the trailing lobe shows that the sideband has completely moved away from the beam axis and into the radial wings of the main pulse.

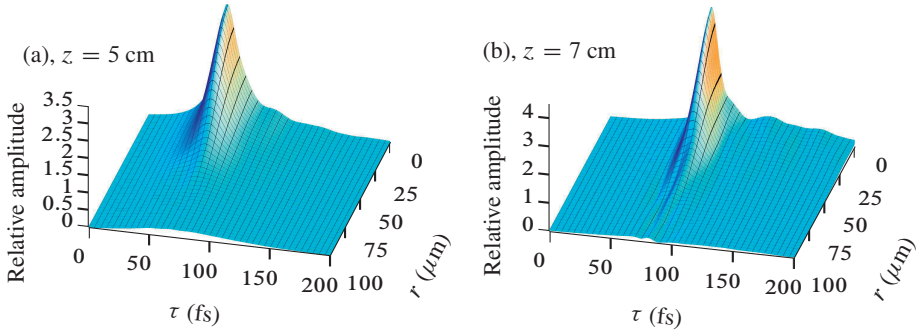

FIG. 5.11: Normalized electric field envelopes $u(\tau, z, r)$ for the time window $\tau \in [0, 200$ fs] and radii $r \in [0, 100\ \mu$m] for different propagation lengths: (a) $z = 5$ cm, (b) $z = 7$ cm.

Figures 5.13(a) and (b) show the spatiotemporal pulse envelope at propagation distances $z = 13$ cm and $z = 15$ cm. We find that the pulse amplitude continues to decrease with further propagation, and this is a general trend until the pulse exits the material at $z = 20$ cm. Note that by following one of the isochronic lines around $\tau \sim 200$ fs in Fig. 5.13(b) we observe that the pulse breakup process occurs primarily close to the centerline which, which has left behind a "bubble-like" pulse shape with a central emptiness on the axis. It is difficult to visually discern the CE pulse in Fig. 5.13 because it moves away from the centerline like a cylindrical wave and correspondingly has a much smaller amplitude than the main beam. Only weak temporal modulations can now be seen in the radial periphery of the main beam. The CE pulse is slightly visible on the isoradial line $r = 1$ mm in Fig. 5.13(b) where it appears as an increase in $u(\tau, r, z)$ close to $\tau = 100$ fs. At this stage the main beam is completely modulated and the conical emission has completely separated from the main beam. That is, the amplitude of the spectral component representing conical emisison is now saturated and does not grow further with propagation distance.

By examining the population disitribution of the $3s$ and $3p$ orbitals we have verified

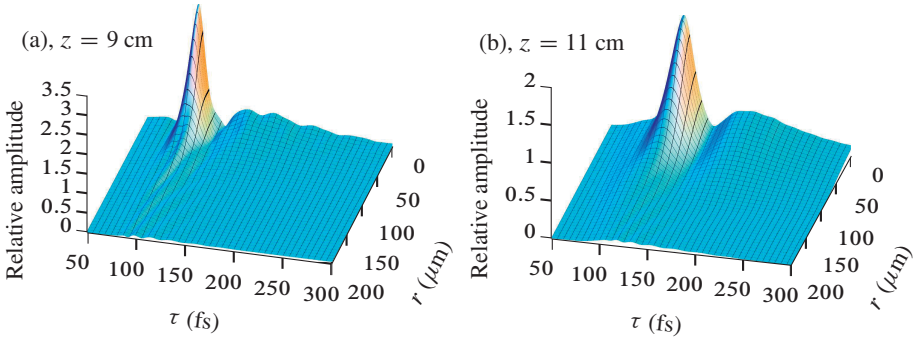

FIG. 5.12: Normalized electric field envelopes $u(\tau, z, r)$ for the time window $\tau \in [50\text{ fs}, 300\text{ fs}]$ and radii $r \in [0, 200\ \mu\text{m}]$ for different propagation lengths: (a) $z = 9$ cm, (b) $z = 11$ cm.

that the pulse splitting mechanism observed is of the SIT type. This splitting, which we will investigate in greater detail in the framework of the paraxial SIT equations in Sec. 5.6, is initiated by a polarization phase dependent absorption; At the leading edge of the pulse in Fig. 5.12(a) the material is coherently excited until the $3s - 3p$ transition is coherently inverted. Under these conditions the relative phase between the polarization and the pulse has switched such that the electric field tends to align the dipoles anti-parallel to the instantenous field direction. The next temporal slice of pulse which enters this spatial region essentially sees an inverted material and becomes amplified as it passes through this region. This effect is cumulative until the active electron is coherently returned back to the $3s$ orbital where E and P again become parallel. For a sufficiently strong pulse this process may repeat itself in such a way that in effect the medium excavates a hole in the middle of the temporal pulse shape, leading to breakup on the centerline, as seen in Figs. 5.12(a) and (b).

It remains now to investigate the conical emission pulse itself. This is done in Fig. 5.14 which shows an inset of Fig. 5.11(f) for the radial range $r = [0.6\text{ mm}, 1.2\text{ mm}]$ and for a time window large enough to contain the entire CE pulse. The color-coding shows the relative amplitude of the field in this spatiotemporal region and can be estimated by the color map included in the figure. To enhance visibility, contour lines whose labels indicate constant contours of $E(\tau, r, z)$ in units of $E_0/1000$ are superimposed on top of the color map. We find that the maximum peak amplitude of the CE pulse, after detaching completely from the main beam, is approximately $8E_0/1000$ and corresponds to an intensity of approximately 1.35 MW/cm^2. The CE is a pulse whose duration defined by its temporal FWHM is estimated as 154 fs from Fig. 5.14. One observes that the rise time of the leading edge of the CE pulse is significantly shorter than the decay time of the tail. In the paraxial approximation the rise time is reasonably measured as the temporal HWHM for

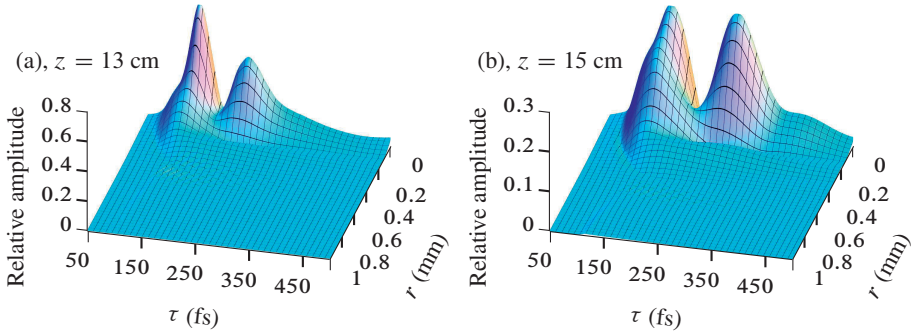

FIG. 5.13: Normalized electric field envelopes $u(\tau, z, r)$ for the time window $\tau \in [50\text{ fs}, 500\text{ fs}]$ and radii $r \in [0, 1\text{ mm}]$ for different propagation lengths: (a) $z = 13$ cm, (b) $z = 15$ cm.

an iso-radial line (i.e. for a constant value of r) that passes through the pulse peak in the time-radius plane for a given z (thus representing a horizontal slice through $r \approx 0.85$ mm in Fig. 5.14). The decay time is estimated in the same way. From Fig. 5.14 we find $\tau_{\text{rise}} = 20$ fs on the front and $\tau_{\text{decay}} = 134$ fs on the tail. In addition, note that the leading edge does not represent an optical shock since $\omega_{\text{CE}}\tau_{\text{r}} \approx 46$. For comparison the rise time of the Gaussian input pulse satisfied $\omega_c T/2 \approx 33$. The reasons for the temporally asymmetric CE pulse remain largely speculative. Since nonlinear interaction of the CE and the material can be disregarded after separation from the main beam, no self-steepening of the CE pulse may take place. We therefore conjecture that the temporal pulse shape is most likely a result of color dispersion arising from the $3s - 3p$ resonance after detachment from the main beam.

5.5.3 The ”missing” sideband

Historically, much of the controversy of CE surrounds the ”missing” blue sideband. This sideband is the main source of the disparity between experimental results and theories based on parametric four wave mixing, which presume that the initial pulse scatters an equal amount of energy into these sidebands, and that these sidebands then propagate with different spatial characteristics. In the steady-state case the generated sidebands are observed symmetrically but propagating at different angles with respect to the optical axis. In fact, for continuous-wave laser operation it can be proven that the emission spectrum of an atom must always be symmetric (with respect to the sidebands) in the Markovian limit under the rotating wave approximation [140]. It is reasonable to suspect that this symmetry is conserved during propagation. For transient excitation, spectral asymmetry of the Rabi sidebands is a natural consequence which is adequately understood from the Rabi

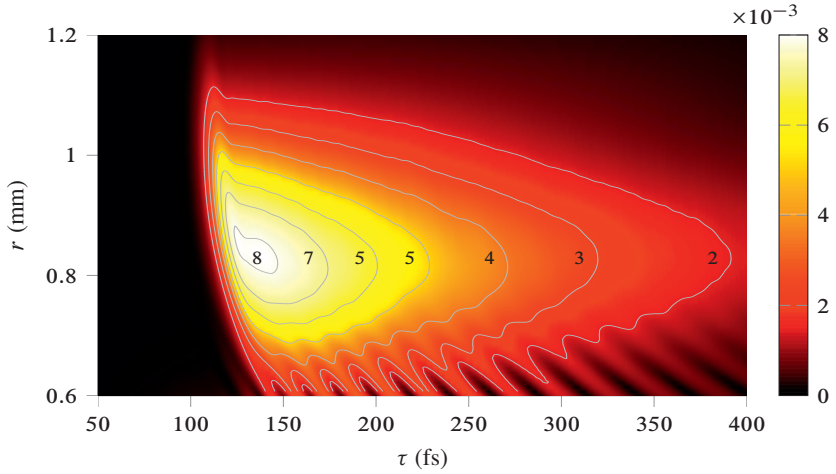

FIG. 5.14: Inset of the spatiotemporal region $r = [0.6\text{ mm}, 1.2\text{ mm}]$ for Fig. 5.11(f). The color coded data shows the conical emission pulse at a propagation distance $z = 15$ cm. Contoured lines labeled $2-8$ indicate the relative amplitude in units of $E_0/1000$.

solution of a two-level atom exposed to a monochromatic electromagnetic field. For pico- and femtosecond excitation one may, as a first approximation, ignore homogeneous relaxations altogether. Moreover, evaluation of laser propagation phenomena is not necessary to obtain a qualitative understanding of the spectral processes involved.

For greatest simplicity we examine a simplified sodium atom where only the two atomic orbitals $|3s\rangle$ and $|3p\rangle$ need to be considered. The atomic wave function is

$$|\Psi\rangle = c_{3s}(t)\mathrm{e}^{-i\omega_{3s}t}\,|3s\rangle + c_{3p}(t)\mathrm{e}^{-i\omega_{3p}t}\,|3p\rangle\,, \tag{5.32}$$

where $|c_{3s}|^2$ and $|c_{3p}|^2$ are the probabilities of observing the electron in the $3s$ and $3p$ states. If a monochromatic field $E = E_0\mathrm{e}^{-i\omega_c t} + \text{c.c.}$ is applied to this atom the Rabi solution for c_{3s} and c_{3p} is [133]

$$c_{3s} = \mathrm{e}^{i\overline{\Delta}t/2}\left[\cos\left(\frac{1}{2}\Lambda t\right) - \frac{i\overline{\Delta}}{\Lambda}\sin\left(\frac{1}{2}\Lambda t\right)\right], \tag{5.33a}$$

$$c_{3p} = i\,\mathrm{e}^{-i\overline{\Delta}t/2}\frac{\Omega}{\Lambda}\sin\left(\frac{1}{2}\Lambda t\right), \tag{5.33b}$$

where $\overline{\Delta} = \omega_c - (\omega_{3p} - \omega_{3s})$, and we have presumed that $c_{3s} = 1$ at $t = 0$. By convention, the Rabi frequency is defined as $\Omega = 2\mu_{3s,3p}E_0/\hbar$ for complex fields. The

complex polarization in units of $\mathcal{N}\mu_{3s,3p}$ is then

$$c_{3s}^{*}c_{3p} = -\frac{\overline{\Delta}\Omega}{2\Lambda^2}\mathrm{e}^{-i\overline{\Delta}t} + \frac{\Omega}{4\Lambda}\left(\frac{\overline{\Delta}}{\Lambda}+1\right)\mathrm{e}^{-i(\overline{\Delta}-\Lambda)t} + \frac{\Omega}{4\Lambda}\left(\frac{\overline{\Delta}}{\Lambda}-1\right)\mathrm{e}^{-i(\overline{\Delta}+\Lambda)t}. \tag{5.34}$$

Equation (5.34) shows that the atom responds at three frequencies ω_c, $\omega_c \pm \Lambda$, corresponding to the driving frequency at ω_c and two Rabi sidebands, symmetrically displaced from the central laser frequency. These three peaks are otherwise known as the Mollow triplet. For resonant excitation $\left(\overline{\Delta}=0\right)$ the Rabi sidebands at $\omega_c \pm \Lambda$ are equally strong, but in the more general case the sideband closest to the line center will always achieve greater gain. We will refer to this sideband as the resonant sideband. Note that Eq. (5.34) only holds for timescales much shorter than the spontaneous emission lifetime. The result is also analogous under substituting $\overline{\Delta} \rightarrow -\overline{\Delta}$. Thus, for a laser tuned to the red side of an optical resonance, the blue sideband is stronger. Note that this asymmetry in the two sidebands is predicted simply due to a non-zero value $\overline{\Delta}/\Lambda$, and does not require evaluation of propagation gain.

Strictly speaking, the expressions above concern only the radiation emitted by the atoms under constant irradiation by a near-resonant laser field. They do not address the radiated spectrum for pulsed excitation, and certainly do not concern the propagated field spectrum. In general, although the generation of new frequencies may be adequately understood from the Rabi solutions, this does not provide a sufficiently detailed explanation of the observed CE spectrum. In particular, it is clear that for sufficiently strong pulses temporal splitting may lead to internal sidelobes in the pulse spectrum, and these are not predicted by Eq. (5.34). However, for pulsed excitation it is reasonable to expect radiated Rabi sidebands whose spectrum lies in the region from $\omega_c \mp \overline{\Delta}$ to $\omega_c \mp \sqrt{\Omega_{\mathrm{max}}^2 + \overline{\Delta}^2}$. When the pulse is tuned to the blue, the resonant Rabi sideband is therefore always placed on the red side of resonance, and vice versa for a laser tuned to the red. If we consider the input pulse (B) with 472 nJ energy and estimate $E_0 \sim 10^9$ V/m (taking into account the effects of self-focusing) we find that $\Lambda \sim 6.4 \times 10^{14}$ rad/s yielding $\overline{\Delta}/\Lambda = 0.2$. The low-frequency wing of the red sideband is then predicted at a detuning of approximately -94 THz from the center frequency, comparing favorably with the simulation data presented in Fig. 5.8(b). In conclusion, the cone emission is therefore believed to be due to the ejection of the resonant Rabi sideband.

5.5.4 Comparison with experiments and other theoretical models

In the preceding sections we analyzed the propagation of 20 fs pulses with nJ pulse energies for a sodium vapor with density $\mathcal{N} = 5 \times 10^{21}$ m^{-3}. It was found that the internal angle of emission for single-filament CE was ~ 11 mrad with CE spectral widths between $50 - 60$ nm depending on the initial pulse energy. Blue-shifted emission complementary to the red-detuned cone was not observed propagating either axially or conically anywhere inside the material. The scattered energy into the cone was on the order of a few percent of the input pulse energy. These results are in agreement with the overall features of CE, and in particular with femtosecond experiments performed in sodium vapors where typical values of the CE angle and spectral widths are reported as $8 - 13$ mrad for 560 nm excitation in a vapor with density 8×10^{21} m^{-3} [110]. Experimentally reported spectral widths of CE are $10-60$ nm for densities in the $4\times10^{21}-2\times10^{22}$ m^{-3} range and similar peak amplitudes ($E_0 \sim 10^8$ V/m). However, the relative spectral placement of the CE observed here lies slightly further to the red than in the experiments reported by Vaičaitis and Paulikas [110]. In their experiments, the broadband CE extended from 600 nm to 640 nm for 120 fs initial pulses with 4 mm input beam waists. We observe CE in the 605 nm to 650 nm range for similar sodium densities but for 6 times shorter pulse durations and 40 times smaller beam waists. For comparison the input intensities used here are higher than experimentally reported values, and this is presumably the reason for the larger CE detuning observed numerically. We use input intensities up to 40 GW/cm^2 while experiments have so far been performed with intensities up to 4 GW/cm^2 [110].

Experimental cross-correlation measurements of the emerging conical light exiting a high-density rubidium vapor cell excited by 100 fs pulses was recently reported by Skenderović et al. [112]. In the series of experiments conducted, the CE light was temporally broadened to several picoseconds and consisted of several subpulses spaced temporally close to each other. The input beam diameter was 2 mm so the findings are not available for quantitative comparison with our numerical calculations. However, the results lend supporting evidence of a pulse splitting picture of CE. Based on a combination of the calculations presented here and the experiment performed by Skenderović et al. [112] we have reason to believe that CE pulses originate together with temporally splitted pulses on the centerline, as two aspects of the same process. Moreover, based on the calculations presented here a carefully designed single-shot experiment should reveal a spatiotemporal structure consisting of a single femtosecond CE pulse coexististing with double axial pulses.

Crenshaw and Cantrell [129] have numerically investigated the propagation of a near resonant (60 GHz detuning) picosecond pulse with an 8π pulse area in a two-level atomic sodium system over comparatively short propagation distances ($\approx$ 7 mm). Although included in their numerical calculations, self-focusing had a negligible influence on prop-

agation. Propagation of their pulse resulted in multiple pulse breakups and somewhat angularly isolated frequency components detuned 30 GHz *above* resonance, which the authors assert is CE. On the whole, the conical emission observed by the authors, both spectral placement and gain, are at odds with experiments. In their language, the isolated Fourier-Hankel component is a result of noncollinear phase matching, arising simply due to temporal breakup with a transverse variation.

Higher conical gain may also occur from spatial beam breakup into multiple filaments through self-focusing of smaller diameter regions of the input beam. Pulse breakup and CE may then occur within each spatial filament, and will presumably lead to higher conical gain. Our numerical integrator invokes symmetry around the centerline and can only describe radial filaments, and therefore breaks down in this regime. The scattered CE energy observed in our numerical simulations, all of which occur from single filaments, are on the order of $1-2\%$ of the transmitted pulse energy and should be observable in atomic sodium. Computational extension to full 3D models for pulse propagation in atomic sodium may be possible, although the Bloch system must most likely be reduced to a smaller dimension through careful consideration of active atomic orbitals.

Incorporation of additional physical effects in our model will most likely lead to qualitatively similar results in the nonlinear regime that we study. There are nevertheless several possible sources of error in our theoretical treatment. On a macroscopic level, the forward propagating approximation is justified, but the possibility of multiple filamentation through symmetry breaking in the azimuthal coordinate is not accounted for. Microscopically, ionization through multi-photon processes may lead to plasma defocusing, which has also been disregarded here on the grounds that the pulse intensities achieved were comparatively small. Neglection of fine-structure splitting can also lead to artificially large dipole moments for composite transitions and the illusion that the entire $3p$ multiplet is activated by the pulse. On the whole, we believe that the largest sources of error are the neglect of ionization and the assumption of cylindrical symmetry.

5.5.5 Comparison with two-level theory

The motivation for using a multi-level model outside the RWA and SVEA was to obtain qualitative and quantitative theoretical predictions for the short pulse excitation regime. The input pulses applied were under the simultaneous presence of one- and two-photon near-resonance conditions. Questions then immediately arise as to which minimum set of parameters can be defined to observe CE, and whether or not the same dynamical picture emerges in a simpler model where additional resonances are neglected. A comparison between the multi-level model and a paraxial two-level model under the RWA and SVEA is therefore warranted in the present context, and we now address this question. Below, we compare one of the computer solutions in Sec. 5.5 with the predictions of a simplified two-

level model. The equations of motion are the paraxial SIT equations, which are discussed in greater detail in Sec. 5.6

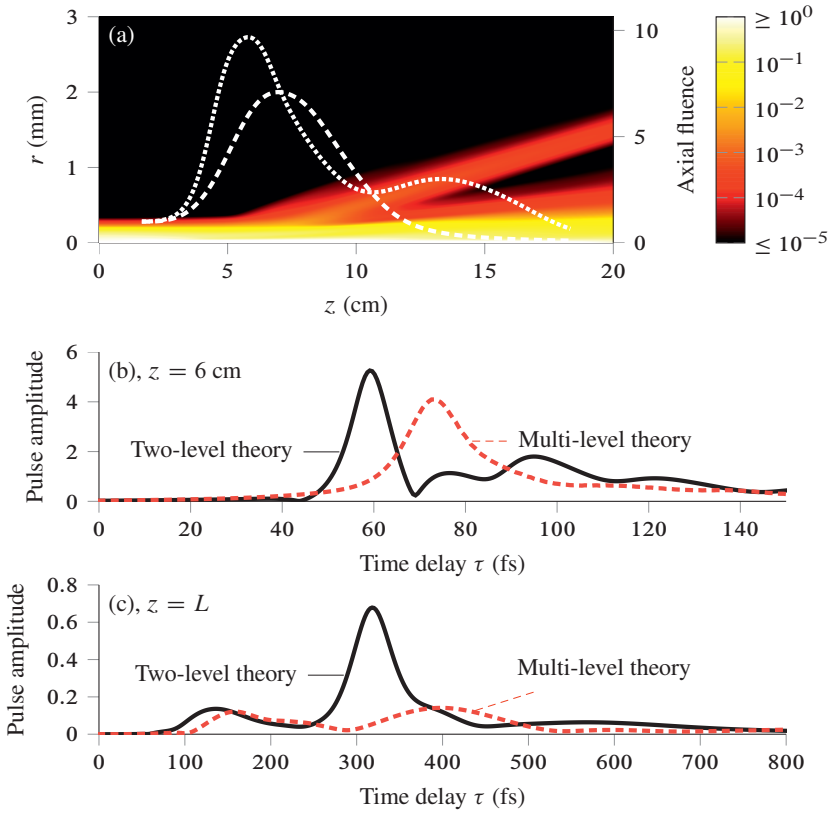

FIG. 5.15: (a) Propagation of a 472 nJ pulse with 20 fs duration in a sodium vapor approximated by two-level theory. The dashed line indicates the on-axis fluence and the dotted line shows the centerline fluence calculated by multi-level theory. (b) Comparison between the centerline pulse temporal shapes for two-level theory (solid line) and multi-level theory (dashed line) at $z = 6$ cm. (c) Same as for (b) but at the output facet $z = L$.

We consider pulse (B) propagating through the two-level vapor characterized by the same material parameters. The color-coded data in Fig. 5.15(a) shows the normalized longitudinal fluence $F_z(z, r)$ at all points z, r in the material together with the centerline fluence (dotted line). This figure should be contrasted with Fig. 5.10(B) which showed analogous computational results for the multi-level RMB sodium model. The dotted line in Fig. 5.15(a), plotted against the right vertical axis, shows the centerline fluence as a function of propagation distance z. For comparison, the dashed line plotted in Fig. 5.15(a)

shows the centerline fluence for the RMB model calculations [see Fig. 5.10(B)]. As expected, we find that CE still occurs. We also find that the maximum axial fluence reached is higher for the two-level model than in the multi-level model, which is most likely due to the neglect of multi-photon processes in the two-level case. In a multi-level model the valence electron is not locked into the $3s$ and $3p$ orbitals and may escape to higher orbitals, which will tend to smooth out self-focusing effects caused by the $3s - 3p$ nonlinearity. In addition, we observe a weak second focusing of the pulses in the two-level model, evidenced by an increasing axial fluence around $z = 13$ cm.

Examination of the spatiotemporal $r - \tau$ data for various positions z in the material (analogous to Fig. 5.11) shows pulse breakup analogous to the predictions of the RMB model. The simulation data are not discussed explicitly because Figs. 5.11, 5.12, and 5.13 are sufficient for understanding the pulse splitting process on a qualitative level. To quantitatively compare the predictions of the paraxial SIT and the RMB equations, Figs. 5.15(b) and (c) show the centerline pulse envelopes at position $z = 6$ cm and $z = L$ for the two models. Overall, quantitative agreement is not found. At $z = 6$ cm a comparison between the two models shows that paraxial SIT theory predicts a higher group velocity than predicted by the RMB theory. This feature can be attributed to the neglect of multi-photon resonances in the two-level case, which will result in stronger self-focusing effects.

At the exit face of the medium [see Fig. 5.15(c)] the two models agree only close to the leading edges of the centerline pulses. Unlike the RMB model the paraxial SIT equations predict a main pulse of relatively large amplitude (up to 60% of the initial amplitude) propagating axially, which is a direct result of refocusing of the main beam after CE. In the multi-level case sufficient energy is lost to higher electronic orbitals to prevent refocusing.

Although CE occurs in both models, and indeed the same break up process is observed, the results change quantitatively and qualitatively. This is not too surprising considering the pulse durations and intensities used. As such, two-level theory is not quantitatively useful for femtosecond excitation.

5.6 Conical emission in the two-level approximation

From the discussions in the previous section it is evident that the two-level approximation did not apply quantitatively to 20 fs pulses, presumably because promotion of the valence electron to the $4d$ state after populating the $3p$ level was neglected in the two-level case. Yet, conical emission has been performed over a wide range of experimentally adjustable parameters, and it is of considerable interest to investigate CE for longer pulses where the two-level restriction is valid. In this case the equations of motion are the paraxial SIT

equations [Eqs. (3.5) and (3.38)],

$$\partial_z \Omega = \frac{i}{2k_c}\nabla_\perp^2 \Omega + i\kappa\langle \varrho_{\Delta,21}\rangle_\Delta, \tag{5.35a}$$

$$i\mathrm{d}_t \hat{\varrho}_\Delta = \left[\widehat{\mathcal{H}}_\Delta, \hat{\varrho}_\Delta\right] + i\hat{\mathcal{R}}_\Delta, \quad \widehat{\mathcal{H}}_\Delta = \begin{pmatrix} 0 & -\frac{1}{2}\Omega^* \\ -\frac{1}{2}\Omega & \Delta - \overline{\Delta} \end{pmatrix}, \tag{5.35b}$$

where we recall $k_c = \omega_c/c$. By convention, the Rabi frequency is defined as $\Omega = 2\mu_{12}\mathcal{E}/\hbar$ where μ_{12} is the transition dipole moment (projected onto the polarization axis) between the two active states.

The numerical method used for obtaining numerical solutions to the paraxial SIT equations is identical to the one considered for the RMB equations with the following exceptions: (i) a complex field envelope is introduced, (ii) Eq. (3.35) is replaced with the paraxial wave equation, and (iii) the multi-level model is replaced by a two-level atom. The inclusion of inhomogeneous broadening implies that the Bloch equations must be solved for a range of atomic detunings Δ. Coupling of the atomic state to the paraxial wave equation occurs through the inhomogeneously averaged polarization $\langle \varrho_{\Delta,21}\rangle$, where, as usual, $g(\Delta)$ is a taken as Gaussian.

Generally speaking, numerical evaluation of Eq. (5.35) in the detuned $\left(\overline{\Delta} \neq 0\right)$, inhomogeneously broadened regime requires a vectorized computer. In our implementation we sample $g(\Delta)$ on a few hundred values of Δ, employ a spatial grid with roughly 500×1500 grid points in the longitudinal and radial coordinates, respectively, and propagate for approximately $10,000$ time steps. The resulting wall clock computation time is around 5 hours on 512 computing cores.

In this section we employ Rubidium as a model medium. The motivation for employing sodium in the previous section was the fine structure splitting of the $3p$ level, which is sufficiently small to treat the $3\mathrm{P}_{1/2}$ and $3\mathrm{P}_{3/2}$ levels degenerately for femtosecond excitation. For picosecond pulses this approximation does hold very well, so we choose ^{87}Rb, which has a fine structure splitting of 7 THz. An alternative medium is ^{133}Cs which has a fine structure splitting of 16 THz, allowing the use of even shorter pulses. We consider the ^{87}Rb D_2 line at ≈ 780 nm, which is characterized by an effective dipole moment [31]

$$|\mu_{12}|^2 = \frac{1}{3}\left|\langle j\,|\hat{\boldsymbol{\mu}}|\,j'\rangle\right|^2 \approx \left|2.07 \times 10^{-29}\ \mathrm{Cm}\right|^2, \tag{5.36}$$

where j and j' are the orbital angular momentum numbers for the ground and excited states. The factor of $1/3$ enters because linearly polarized light interacts with only one component of the dipole operator. We incorporate inhomogeneous broadening, taking $T_2^* = 117$ ps corresponding to an inhomogeneous half width of 10 GHz. The homogeneous lifetimes are taken as $T_1 = 26$ ns and $T_2 = 52$ ns. The numbers are obtained from Steck [31]. Again, we consider cylindrically symmetric beam propagation.

From Eq. (5.35a) the following energy conservation equation in the time domain is found,

$$\nabla \cdot \boldsymbol{J} = i\frac{\omega_c \mathcal{N}|\mu_{12}|}{2\epsilon_0 c}\mathcal{E}^*\langle \varrho_{\Delta,21}\rangle_\Delta + \text{c.c.}, \tag{5.37a}$$

$$J_z = \epsilon_0 c|\mathcal{E}|^2, \quad K_r = \frac{i}{2k_c}\mathcal{E}\partial_r\mathcal{E}^* + \text{c.c.}, \tag{5.37b}$$

where $\boldsymbol{J}$ is an energy current. The fluence is then defined $\boldsymbol{F} = \int_{-\infty}^{\infty}\boldsymbol{J}\mathrm{d}\tau$. Below, we consider Gaussian input pulses,

$$\Omega(\tau, r, 0) = \Omega_0 \exp\left(-\frac{r^2}{2R^2} - \frac{\tau^2}{2T^2}\right). \tag{5.38}$$

5.6.1 Resonant excitation

Before re-addressing propagation on the blue side of resonance, we briefly mention that the existence of transverse effects is not unique to off-resonant propagation. Comparatively strong transverse effects, termed coherent self-focusing, may also occur when a pulse is tuned sufficiently close to an optical resonance. Knowledge of the area theorem in the annular plane wave assumption $\left(\nabla_\perp^2\Omega = 0\right)$ is sufficient for obtaining an adequate understanding of the phenomenon. Let $\Theta(r)$ be the radial profile of the input area on the plane $z = 0$, where the area is largest at $\Theta(r = 0) = \theta_0$. Under the McCall-Hahn conditions, an input beam with a monotonically decreasing radial profile and initial area $\theta_0 < 3\pi$ will reshape into a soliton for distances $r < r_\pi$ from the centerline, where $\Theta(r_\pi) = \pi$. The special shape-kinematic relationship of the hyperbolic secant 2π pulse implies that solitons with higher amplitude propagate faster. In this way the central portion of the beam outruns the radial periphery, and the beam develops a curvature in the time-radius plane. With increasing propagation depth the curvature becomes sufficiently strong to allow diffraction to take over, eventually causing an inwards energy flow towards the centerline. Coherent self-focusing has been investigated both theoretically [141–143] and experimentally [144, 145].

Figure 5.16 shows a computer solution of coherent self-focusing of a beam with initial on-axis area $\theta_0 \approx 2.7\pi$. The data shown in the figure are based on two different computer solutions for Eq. (5.35) with the same initial conditions. The panels in the left column show the spatiotemporal evolution in the annular plane-wave approximation with diffraction artificially switched off. Correspondingly, the panels in the right column shows the evolution when a transverse energy flow is included. Note that we distinguish between transverse reshaping and transverse flow; the former corresponds to a transverse variation depending only on the initial conditions in each uncoupled annular ring of the input pulse; the latter corresponds to a non-zero transverse energy flow. When the Beer's length is

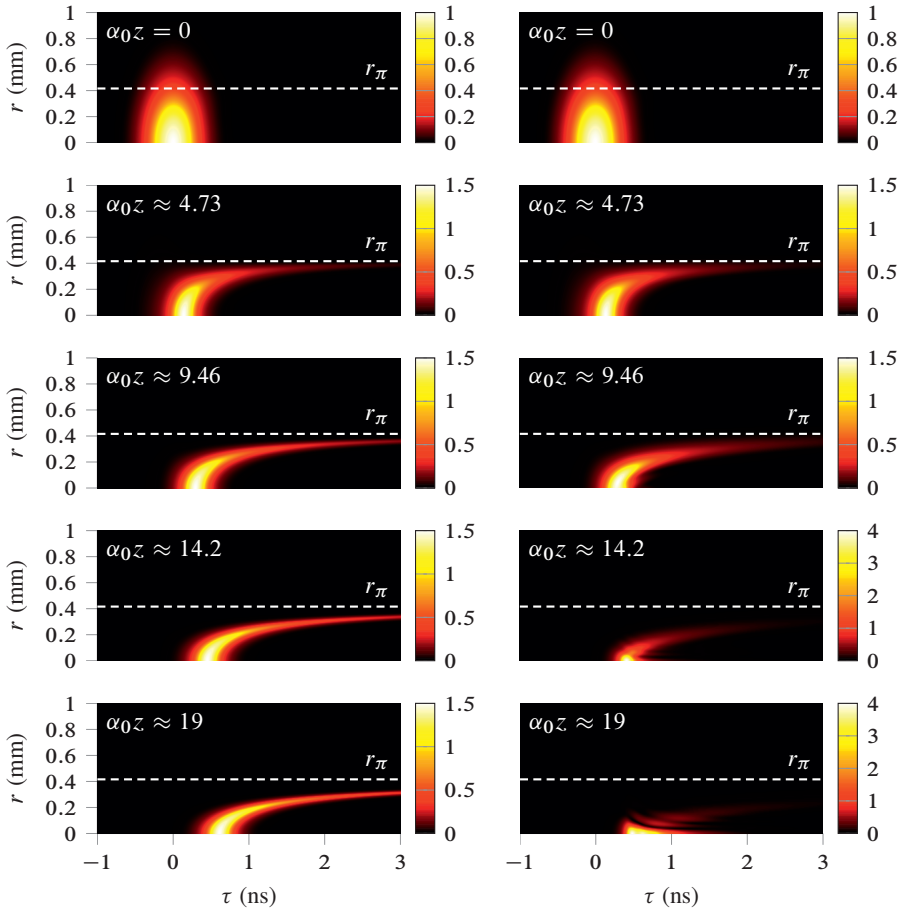

FIG. 5.16: Transverse reshaping of a 250 ps pulse with an initial on-axis area of $\theta_0 \approx 2.7\pi$ propagating in a two-level medium with inhomogeneous dephasing time $T_2^* = 117$ ps. The left column corresponds to spatiotemporal evolution in the annular plane-wave approximation. The data in the column to the right includes transverse coupling. For reference, the input beam waist is 300 μm, the Beer's length is 5.3 mm, and the Rayleigh length is 72 cm. The total length of the propagation region is 10 cm.

shorter than the Rayleigh length the largest contribution to the spatiotemporal reshaping of the pulse is initially due to the nonlinear material response contained $\langle \varrho_{\Delta,21} \rangle_\Delta$, resulting in initial formation of a soliton-like pulse. The contribution from the transverse term $\nabla_\perp^2 \Omega$, which describes diffraction, is initially smaller. In effect, over the first few Beer's length the pulse develops into a hyperbolic secant 2π pulse with a transverse dependence, locked into a "disk" of radius r_π. As the group delay between the centerline pulse and the

radial periphery becomes increasingly larger with further propagation, $\nabla_\perp^2\Omega$ eventually becomes significant and diffraction ultimately leads to self-focusing, as shown in the right hand panels in Fig. 5.16.

5.6.2 Blue detuning

In this subsection we numerically address conical emission of blue-detuned pulses in inhomogeneously broadened media under the two-level restriction. We now consider a ^{87}Rb vapor cell of length $L = 10$ cm and density $\mathcal{N} = 5\times10^{20}$ m^{-3}. The input pulse duration is $T = 20$ ps, the waist is $R = 50\ \mu$m, and the pulse is tuned $\overline{\Delta}/2\pi = 200$ GHz above the D_2 line. Correspondingly, the detuning between the low frequency wing of the pulse and the high-frequency wing of the absorption is roughly

$$\frac{\overline{\Delta}}{2\pi} - \frac{1}{2T_2^*} - \frac{1}{2T} \approx 170\ \text{GHz}, \tag{5.39}$$

and the resonance is therefore well isolated from the initial pulse spectrum (the spectral FWHM of the input pulse is roughly 20 GHz). Following Eq. (5.2) the numbers above yield a critical power of $P_{\rm cr} \approx 109$ W.

Figure 5.17 shows the evolution of the fluence $F_z(z,r)$ and the corresponding beam waist of a Gaussian pulse with input peak power $P_0 \approx 19P_{\rm cr} \approx 2$ kW ($\Omega_0/(2\pi) \approx 160$ GHz). The spatiotemporal evolution of the fluence (color coded data) shows evidence of conical emission, and is generally consistent with the observations made for the RMB equations in the few-cycle pulse regime, with a few important exceptions. Firstly, the cone emission does not have a specific geometric origin in the vapor cell but extends from roughly 4 cm to the entire length of the medium. One may safely characterize the radial expansion of the fluence as cone emission because the opening angle of the "fluence cone" in Fig. 5.17 is roughly 20 mrad, whereas the beam divergence angle of the input pulse was roughly $\theta_{\rm d} \approx 2.5$ mrad. Secondly, after the first self-focus at $z \approx 1.7$ cm the pulse refocuses several times with further propagation, evidenced by a sequence of reappearing peaks in the on-axis energy. Thirdly, the laser beam is trapped during propagation and has clear spatial structure. The calculated beam waist (dashed line) is approximately 47 μm at the exit face of the medium, slightly smaller than the initial beam waist. Moreover, by considering input pulses with the same pulse shape but lower input intensity and power, we find that the cone emission develops further into the material, the beam evolves through fewer self-focusing regions, and the oscillations in the on-axis energy are not as severe, nor as many. Importantly, application of pulses with input peak powers smaller than the critical power $P_{\rm cr}$ did not result in conical emission, indicating that self-focusing may indeed be necessary for the manifestation of CE.

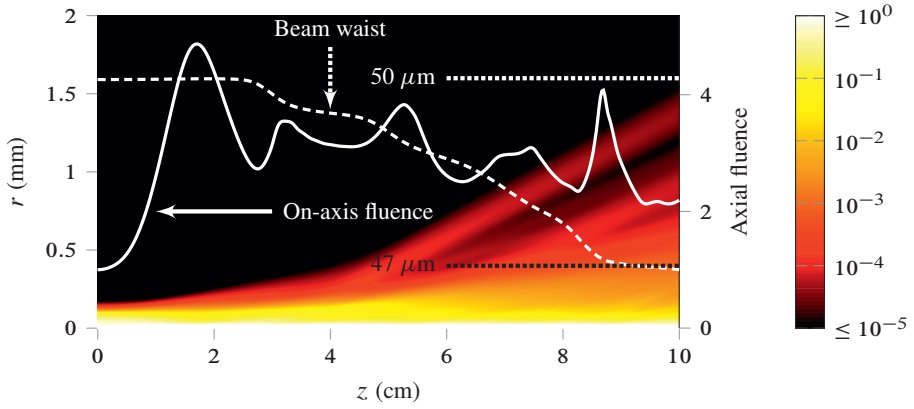

FIG. 5.17: Normalized logarithmic fluence profile $F_z(z,r)$ (color coded) for a 20 ps pulse tuned 200 GHz above an inhomogeneously broadened resonance. The dashed line indicates the calculated beam waist $\overline{R}(z)$ and is plotted versus the two horizontal lines labeled 47 μm and 50 μm, respectively. The solid line indicates the on-axis fluence $F_z(z, r = 0)$ and is plotted against the right vertical axis.

A Fourier-Hankel analysis of the comparatively strong transverse reshaping displayed in Fig. 5.17 exposes numerical evidence of cone emission of a type analogous to the CE observed in experiments. Figure 5.18(a) shows the logarithmic Fourier-Hankel spectrum $|\Omega(\omega, L, k_\perp)|$ at the exit facet of the medium. The data are normalized against the peak of the input Fourier-Hankel spectrum. One finds that the spectrum predicts cone emission with a full opening angle of approximately 40 mrad and that the emitted cone consists of frequencies spanning the detuning range from -300 GHz to -800 GHz. We also observe that the radial compression of the main beam results in an increased beam divergence angle at the exit facet of the medium; The emission angle reaches as high as $\sim$ 10 mrad. In the case of Fig. 5.18(a), the far-field will consist of a large central beam spot surrounded by a diffuse red-detuned ring of light. The CE frequency range compares favorably with the predicted spectral location of the red Rabi sideband. We estimate this by taking into account the effects of self-focusing, which yields an on-axis amplitude of $\sim 3\Omega_0$ [see Fig. 5.18(b)]. The red Rabi sideband is then expected to extend from $-\overline{\Delta}/(2\pi) = -200$ GHz to

$$-\frac{\sqrt{(3\Omega_0)^2 + \overline{\Delta}^2}}{2\pi} \approx -900 \text{ GHz}, \tag{5.40}$$

comparing favorably with actual observed conical emission spectrum. Note that while the main beam pulse spectrum is broadened also to the blue, the red sideband extends to larger detunings, presumably because it receives higher gain than the blue.

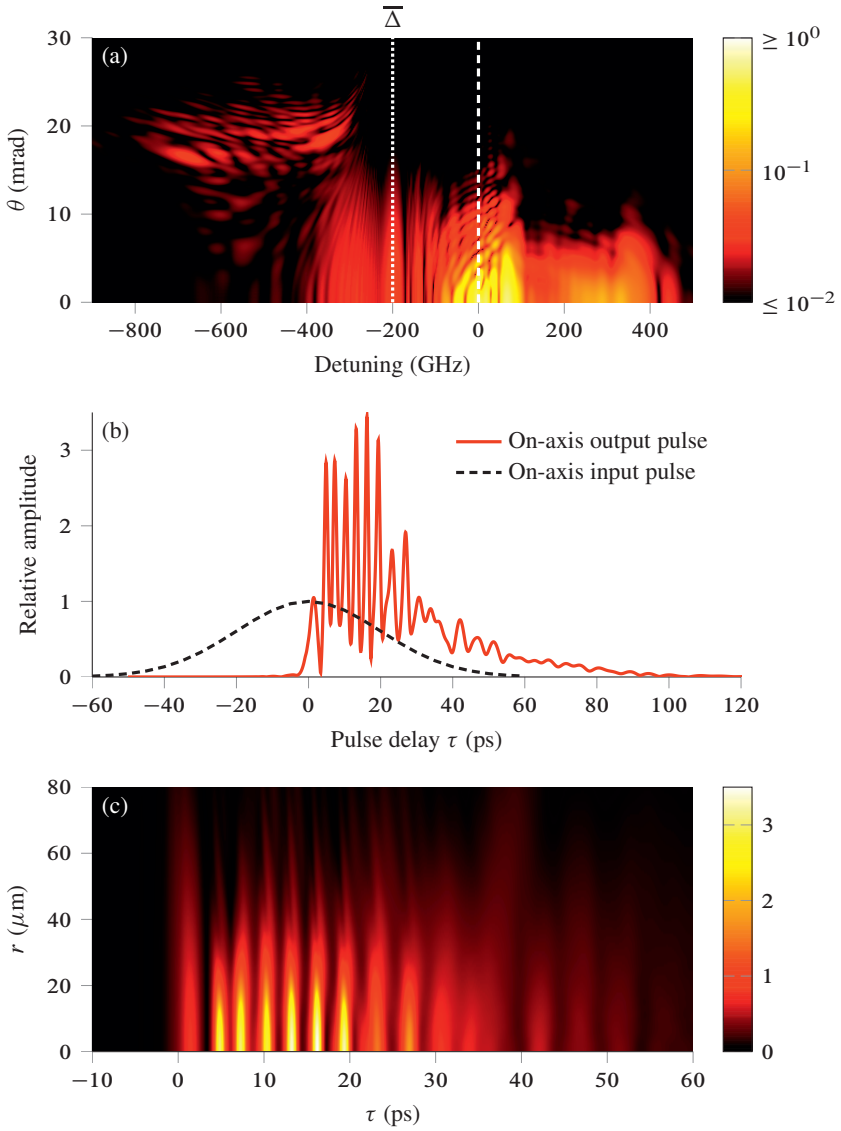

FIG. 5.18: Top panel: Logarithmic Fourier-Hankel spectrum $|\Omega(\omega, z, k_\perp)|$ as a function of the detuning $(\omega_c - \omega)/(2\pi)$ at the exit facet of the medium. Middle panel: On-axis input (dashed line) and output (solid line) temporal pulse shapes. Bottom panel: Spatiotemporal pulse shape $|\Omega(\tau, L, r)|$ at the output facet.

Figure 5.18(b) shows the corresponding on-axis input (dashed line) and output (solid line) temporal pulse shapes. In addition to an overall pulse delay one finds that the on-axis

pulse steepens due to self-focusing and breaks up into several temporal fragments. Examination of the remaining simulation data for different propagation distances shows that the pulse splits into an increasing number of subpulses spaced close to one another. This modulation first appears on the leading edge of the pulse and travels backward towards the tail. The reshaping occurs as a gradual process throughout the medium, with the end result being that the pulse evolves into a envelope-collimated pulse train. The color-coded data in Fig. 5.18(c) show the spatiotemporal structure of the pulse at the output facet of the medium. One finds that the pulse evolves into individual collimated envelope fragments with a transverse structure. Note nevertheless the absence of any step-index form in the radial profile of the beam. In Fig. 5.18 the pulse amplitude decreases gradually with distance into the radial wings.

By applying the Fourier-Hankel transformation to Eq. (5.35a), the paraxial wave equation has a formally exact solution given by

$$\begin{aligned}\Omega(\omega, z, k_\perp) = \Omega(\omega, 0, k_\perp) \exp\left(-i\,\frac{k_\perp^2}{2k_c} z\right) \\ + i\kappa \int_0^z \left\langle \varrho_{\Delta,21}(\omega, z', k_\perp)\right\rangle_\Delta \exp\left[-i\,\frac{k_\perp^2}{2k_c}(z - z')\right] \mathrm{d}z'.\end{aligned} \tag{5.41}$$

An analogous solution to the RMB equations may be obtained by the same procedure. The first term on the right-hand side in Eq. (5.41) corresponds to propagation of the initial pulse in free space whereas the second term describes corrections to this pulse due to reshaping by the material. Equation (5.41) represents a purely formal solution since $\varrho_{\Delta,21}(\tau, z, r)$ generally depends on the entire past history of $\Omega(\tau, z, r)$, ruling out explicit evaluation of the right hand side of the equation in the general case. Nevertheless, letting

$$\langle \varrho_{\Delta,21}(\omega, z, k_\perp)\rangle_\Delta = \left|\langle \varrho_{\Delta,21}(\omega, z, k_\perp)\rangle_\Delta\right| \exp\left[i\,\psi(\omega, z, k_\perp)\right], \tag{5.42}$$

it is immediately apparent that the polarization contribution to the Fourier-Hankel spectrum generally relies not only on the generated amplitude, but also phase-matching of the various frequency components during propagation. We next consider the material quantities in greater detail. Figure 5.19 shows the material inversion $\langle \varrho_{\Delta,22} - \varrho_{\Delta,11}\rangle_\Delta$ in the time-radius plane at various propagation distances. In each panel, the color coding runs from -1 to 1. The solid line, plotted in arbitrary units, indicates the on-axis temporal pulse shape in each case. On the interface $z = 0$ one finds that the maximum inversion reached after interaction with the input beam occurs on the axis and is ≈ -0.5. With increasing propagation distance the axial gain achieved through self-focusing first manifests as appearing undulations on top of the single material inversion curve [see e.g. Fig. 5.19(c)]. These undulations will appear also in the annular plane wave approximation because the input area is $\theta_0 \approx 31\pi$, although to a lesser extent. The radiation reaction of the medium

then tends to temporally modulate the pulse during propagation. The modulation appears as an initial undulation at the leading of the pulse which travels backwards toward the tail with increasing propagation distance. This modulation occurs as a result of multiple inversions and resembles the type of temporal splitting observed in self-induced transparency.

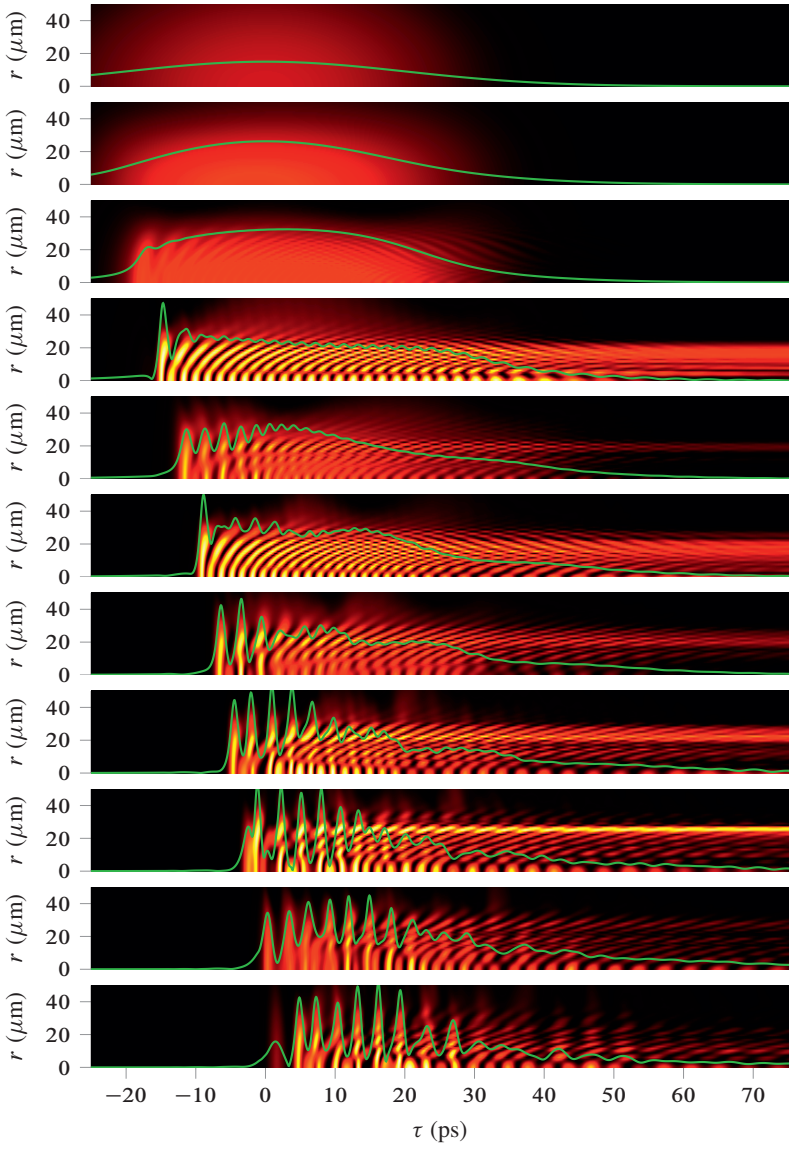

FIG. 5.19: Material inversion at various propagation distance. The color coding runs from -1 to 1 in all plots. The solid line indicates the on-axis temporal pulse amplitude.

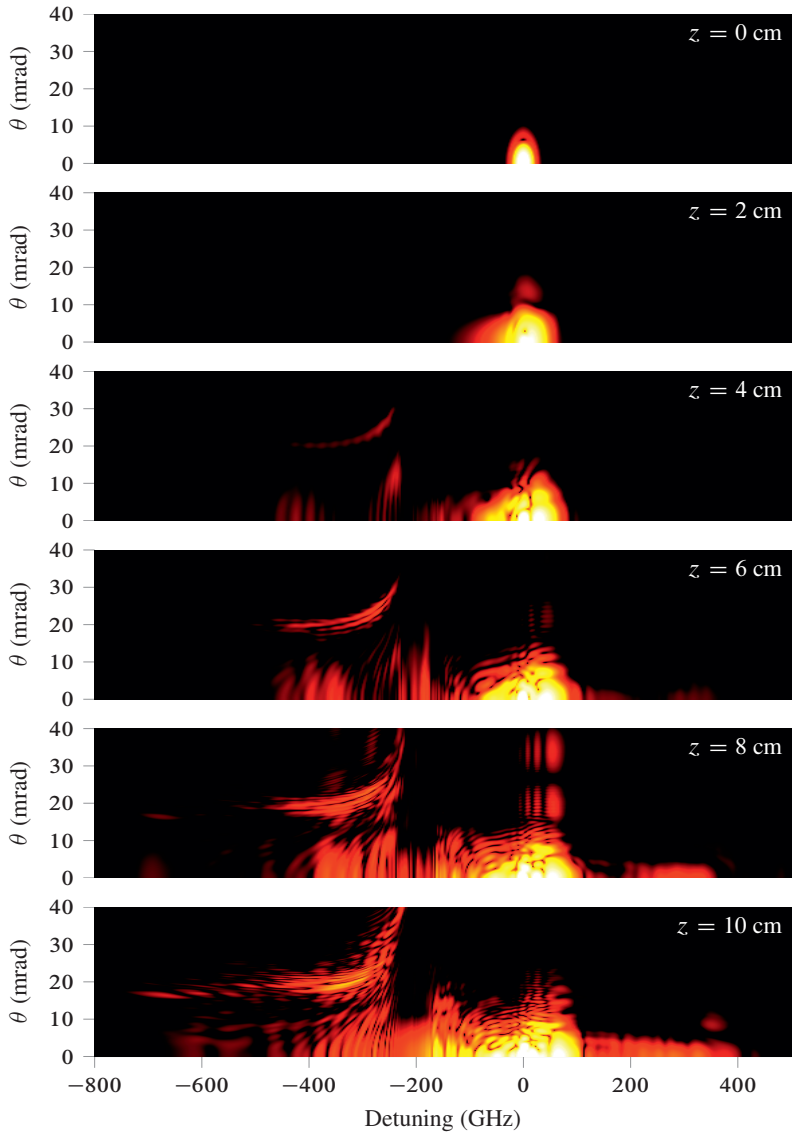

FIG. 5.20: Angular-frequency polarization density $\left|\langle \varrho_{\Delta,21}(\omega, z, k_\perp)\rangle\right|$ at various propagation distance. The data are in arbitrary units but each panel is plotted to the same scale.

Next, Fig. 5.20 depicts the Fourier-Hankel polarization spectrum $|\langle \varrho_{\Delta,21}(\omega, z, k_\perp)\rangle|$ (in arbitrary units) at a few of the same propagation distances considered in Fig. 5.19. We find that as the pulse focuses into the medium somewhat isolated Fourier-Hankel compo-

nents in the polarization density appear after a certain propagation distance. The emission angle $\theta_{\rm CE} \sim 20$ mrad imply that if these components are generated on the centerline, they quickly escape the filament. After being generated, a propagation distance of 2.5 mm is sufficient for complete escape from the main beam (which has a ~ 50 μm waist). Note also a comparatively symmetric spectral broadening of the longitudinal (i.e. $\theta \sim 0$) polarization density. Presently, the most probable explanation for this broadening is due to self-modulation of the driving pulse. In particular, we furthermore note that the total energy contained in the red sideband is generally greater than the energy contained in the blue sideband.

Finally, we briefly mention that we have also reproduced the numerical solutions reported by Crenshaw and Cantrell [128]. While the results reported by Crenshaw and Cantrell [128] did not display evidence of the type of conical emission observed in experiments, an interesting question is whether or not conical emission appears with increasing propagation distance. The answer to this question, taken up by us, remains unresolved because catastrophic self-focusing occured with increasing propagation distance. The hundred-fold increase in the on-axis energy resulted in temporal structures so small that they could not be captured numerically. The problem is rooted in the comparatively large pulse powers implied by Crenshaw and Cantrell's choice of parameters. At the conditions they consider, their parameters yield an initial beam power of 575 W, almost 10^3 times larger than the critical power predicted by Eq. (5.2) as $P_{\rm cr} \approx 0.6$ W. Numerical analysis at these conditions will most likely require a state of the art computational approach which takes into account the possibility of beam filamentation. With the exclusion of inhomogeneous broadening, such calculations are, numerically speaking, certainly realistic and present a natural extension of the work presented above.

5.7 Summary

In this chapter we introduced a quasi three-dimensional multi-level RMB model and a corresponding paraxial SIT model for the propagation of short light pulses in the femtosecond and picosecond pulse regimes. The use of the RMB equations, which are valid even down to single-cycle pulse durations, relaxes some of the strict numerical requirements associated with Maxwell's equations and resulted in a computational formulation applicable to long distance, three-dimensional propagation in multi-level media. Such calculations are not feasible in the MB framework with current computational facilities. Standard differential methods were applied for numerical integration of the RMB equations; finite-differences were used for the propagation equation and an operator splitting method was applied for the optical Bloch equations.

We applied the RMB and paraxial SIT equations in the study of conical emission.

Conical emission is still surrounded by much controversy since no theoretical calculations have, to the best of our knowledge, been able to predict the experimentally observed angular structure. Here, we report on computer solutions that are consistent with observations made in conical emission experiments. In sum, we find that conical emission occurs in the following way:

1. Initial radial compression and symmetric spectral broadening through self-focusing and self-phase modulation.

2. After a sufficient propagation length self-focusing yields sufficient on-axis gain to produce multiple population inversions inside the quasi self trapped light filament. The radiation spectrum from such a driven medium is, broadly speaking, adequately understood from the Rabi solution of a two-level atom. Under the action of the pulse, the driven medium radiates two Rabi sidebands at $\omega_c \pm \Lambda$, where Λ is the generalized Rabi frequency.

3. At the same propagation distance saturation effects on the centerline result in pulse breakup. The radially decreasing intensity profile of the beam in combination with sideband generation leads to a transverse variation in the polarization density which then manifests as cone emission of the red Rabi sideband.

Notably, we find that self-focusing appears to be necessary for the initial replenishment of the centerline intensity which eventually results in cone emission through pulse breakup. The results presented in this chapter resolve some of the underlying questions surrounding conical emission in alkali metal vapors. However, the use of numerical calculations inhibits both quantitative prediction of experimentally predicted universal features and precise isolation of the physical mechanism behind CE. For example, we are unable to quantitatively predict both the emission angle of the red Rabi sideband and the spectral width of the cone, which would depend on the on-axis gain.

Chapter 6

Single-cycle THz propagation in rigid rotor molecular media

6.1 Introduction

When compared to experimental efforts in the microwave, infrared, and optical regions, nonlinear terahertz technology is a research field still in its infancy. The THz spectral region covers, roughly speaking, frequencies between 300 GHz and 3 THz, corresponding to wavelengths shorter than 1 mm but longer than 100 μm, thus occupying the frequency region between microwaves and far-infrared radiation. The three major table-top generation methods for pulsed terahertz are optical rectification (OR), the photoconductive (PC) switch [25], and the air-nitrogen plasma, all of which require pumping by an external femtosecond laser system. In optical rectification, the THz radiation is generated through difference frequency mixing of a femtosecond pulse in a nonlinear crystal. In the case of the PC switch a femtosecond pulse is used to excite carriers in the substrate of an antenna, possibly lithographically made, which then accelerate in the presence of a large DC bias. The resulting current surge in the antenna radiates a THz pulse. In the air-nitrogen plasma it is the fundamental and second harmonic of a femtosecond laser pulse that is responsible for the THz generation. Terahertz pulses may be as short as a single cycle, corresponding to durations of 1 ps or less, depending on the generation mechanism.

Pulsed terahertz (THz) technology [146] is presently emerging as an attractive research field with diverse applications in biomedical imaging [19], spectroscopy [147], and molecular alignment [16, 22, 148–151]. In contrast to material excitations using optical radiation, which predominantly excites valence electrons in the $\sim$ 2 eV range, THz waves excite low-energy modes such as molecular rotations [16, 150–152], lattice vibrations [17], and spin waves [18]. It is, for example, the rotational transitions in light molecules that

make THz a candidate for non-ionizing medical imaging of soft tissue. Several other key applications, such as quantum information [20], chemical selectivity [153], population control [21] etc., rely on an anisotropic molecular angular distribution. Other researchers aim at using angularly localized molecules as an intermediate preparation step for initiating strong field ionization [154], lasing [155], or high harmonic generation (HHG) [23]. Although the field of THz-induced molecular orientation has grown rapidly over the past decade, the first observation of rotationally oriented molecules appears already in the experiments by Harde et al. [156] and Harde and Grischkowsky [157] over 20 years ago. Classically, macroscopic molecular orientations are initiated by the torque a polarized external field exerts through the permanent or induced dipole moment of the molecule. For linearly polarized fields the torsional force is directed in the polar plane and acts to orient the molecules along the instantaneous field direction. After the pulse has passed, the free induction decay (FID) signal of the molecules deteriorates rapidly due to the destructive interference between the continuous, infinite number of classically excited rotational modes, analogous to the free induction decay of an inhomogeneously broadened two-level quantum medium. Quantum mechanically, a resonant pulse coherently excites a finite number of possible angular momentum modes. In the abscence of an external field the interference among the variously excited transitions also lead to initial suppression of the free-induction signal, except for certain rephasing periods when the molecules are orientated and the quantum coherences all radiate in phase at equally spaced time bursts. The space-time behavior of the bursts describe the fidelity of the molecular orientation, and is of practical interest in the linear and nonlinear excitation regimes.

In this chapter we consider the plane wave propagation of single-cycle THz pulses through linear, polar molecules. Linear molecules are molecules with atoms oriented at a 180° degree angle with respect to each other. The most commonly quoted examples of such molecules are carbonyl sulfice (O═C═S) and the hydrogen halides, e.g. cyanide (H—C≡N). There is also a large class of linear non-polar molecules (i.e. molecules without permanent dipole moments) which do not have pure rotational transitions. Most notably are the carbon dioxide molecule (O═C═O) and the nitrogen dimer (N≡N). Rotational motion in such molecules cannot be excited by exerting a field-induced torque through the permanent dipole moment, and is therefore usually initiated by rotational Raman scattering, where the field instead imposes a torque through an induced vibrational dipole moment. Recalling Fig. 2.2 one observes that the application of a non-resonant excitation pulse which interacts via far-detuned vibrational transitions may establish the necessary coherence between the molecules. In the case of the linear molecule shown in Fig. 2.2 it is, for example, Raman scattering through the $|\nu, j = 0\rangle \rightarrow |\nu + 1, j = 1\rangle$ R-branch and $|\nu, j = 2\rangle \rightarrow |\nu + 1, j = 1\rangle$ P-branch chain that establishes a two-photon coherence between the $j = 0$ and $j = 2$ rotational states in the ground vibrational mode.

The excitation of this coherence in a non-polar, linear molecule results in rotational alignment of the molecules, but not orientation, since the molecule has mirror symmetry in the plane parallel to the molecular axis. Two-photon coherence between successive levels j and $j+2$ is analogously established by Raman scattering through higher-lying states. Noting that the rotational lifetimes of linear molecules are comparatively long with respect to THz pulse durations [158], only the coherent regime is investigated in what follows. This chapter is organized as follows. First, we introduce the molecular model in Sec. 6.2 and we analyze the linear propagation regime in Sec. 6.3. A novel computational method which allows evaluating of very large Bloch systems is then presented in Sec. 6.4 and we proceed by presenting fully time-dependent, non-perturbative solutions incorporating over 1000 rotational levels in Sections 6.5, 6.6, and 6.7. Finally, Sec. 6.8 provides a few concluding remarks.

6.2 Physical model

We presume that the THz pulse is polarized along z and propagates along $+x$, and that the propagation occurs without significant transverse coupling in the yz-plane. The propagation of the field follows the first order propagation equation [Eq. (3.35)]

$$\partial_x E = -\frac{1}{2\epsilon_0 c}\partial_\tau P. \tag{6.1}$$

Note that we have chosen a coordinate system where the field propagates along $+x$ rather than $+z$. This choice is invariably unimportant, but allows the use of notational convention in the quantum mechanics literature where angular momentum states are denoted by the quantum numbers representing the total angular momentum and its projection onto the space-fixed z-axis.

The adoption of the plane wave approximation for single-cycle pulses is not necessarily very well justified even for propagation in free space, and before addressing the molecular equations it is reasonable to first discuss the most obvious shortcomings of this model. Note that for propagation in vacuum, an exact solution to Eq. (3.35) exists and may be written down as $E(\omega, x, k_\perp) = E(\omega, 0, k_\perp)\exp\left(-\frac{k_\perp^2}{2k_c}x\right)$. If one supposes, for greatest simplicity, an initial beam with a Gaussian transverse profile,

$$E(\tau, 0, r) = F(\tau)\exp\left(-\frac{r^2}{2R_0^2}\right), \tag{6.2}$$

where $F(\tau)$ is the temporal profile, the exact solution to Eq. (3.35) may be obtained in the frequency domain as

$$E(\omega, x, r) = \frac{R_0}{R(\omega, x)}\exp\left(-\frac{r^2}{2R(\omega, x)}\left(1 + \frac{ix}{x_R(\omega)}\right) + i\psi(\omega, x)\right)F(\omega), \tag{6.3}$$

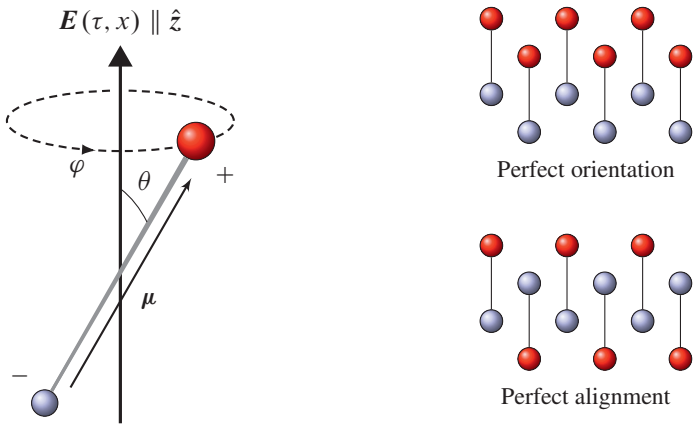

FIG. 6.1: Rigid rotor molecular model. The angles θ and φ are, respectively, the polar and azimuthal angles the molecular axis, defined as the vector from the negative to positive charge, makes with respect to the space-fixed z-axis.

where $R(\omega, x) = R_0\sqrt{1 + x^2/x_R^2(\omega)}$ is the nominal beam waist and $x_R(\omega) = \omega R_0^2/c$ is the Rayleigh length for frequency component ω. The phase $\psi(\omega, x)$ is the Gouy phase shift

$$\psi(\omega, x) = \arctan\left(\frac{x}{x_R(\omega)}\right). \tag{6.4}$$

Equation (6.3) expresses the presence of diffracton-induced transformation of the beam profile and the temporal pulse shape, effects captured only outside the plane wave assumption. Firstly, one notices an overall expansion of the beam waist due to linear diffraction. Notably, the divergence angle of each frequency component ω is generally different; longer wavelengths diffract more strongly than shorter wavelengths. Secondly, the Gouy phase term, which arises from transverse spatial confinement of the beam, indicates a relative change of spectral phase during propagation. Most important is the fact that the Gouy phase change is generally frequency dependent. For broadband signals, and in for particular for single-cycle pulses which have extremely broad spectra, this indicates the possibility of a small amount of free-space chirping accumulated as an effect of propagation. For propagation distances substantially longer every Rayleigh length, $x \gg x_R(\omega)$, the Gouy phase induced chirp dies out since the Gouy phase is $\psi(x \to \infty, \omega) = \pi$. Thus, the neglection of transverse reshaping associated with free space propagation, both waist expansion and phase changes, is then restricted to propagation lenghts $x \ll x_R(\omega)$. For a propagation length of 10 cm and assuming that $x_R(\omega) \sim 1$ m, the initial beam radius of a single-cycle terahertz should be larger than 7 mm, a comparatively large value.

Furthermore, we presume that the material is described by a collection of individual

non-interacting molecules, and that the Born-Oppenheimer approximation is valid for the individual molecules. This decouples the rotational, vibrational and electronic degrees of freedom. In the abscence of interactions that excite molecular vibronic or ro-vibrational motions, the molecule remains in its initial vibrational and electronic state, and only the rotational part of the molecular wave function is affected by the externally applied THz field. We model this part of the molecule as a rigid rotor (see Fig. 6.1). The interaction between the rotor molecules and a classical electromagnetic field $\boldsymbol{E}$ is described by the dipole interaction Hamiltonian

$$\begin{aligned}\widehat{H} &= \frac{\hat{\boldsymbol{J}}^2}{2I} - \boldsymbol{E}\cdot\hat{\boldsymbol{\mu}} \\ &= \sum_{jm}\hbar\omega_{jm}\left|jm\right\rangle\left\langle jm\right| - E\sum_{\substack{jm\\ j'm'}}\mu^{(z)}_{jm,j'm'}\left|jm\right\rangle\left\langle j'm'\right|,\end{aligned} \tag{6.5}$$

where $\hat{\boldsymbol{J}}$ is the angular momentum operator and I is the moment of inertia of the molecule. The first term on the right-hand side of Eq. (6.5) represents free rotational Hamiltonian $\widehat{H}_0$ of the molecule and the second term represents the interaction with the electric field. In the second line of Eq. (6.5), we have expanded the Hamiltonian in the eigenstates $|jm\rangle$ that are simultaneous eigenfunctions of $\hat{\boldsymbol{J}}^2$ and $\hat{J}_z$ with eigenvalues $\hat{\boldsymbol{J}}^2\left|jm\right\rangle = \hbar^2 j(j+1)\left|jm\right\rangle$ and $\hat{J}_z\left|jm\right\rangle = \hbar m\left|jm\right\rangle$, where $\hbar m$ is the projection of the angular momentum of a state $|\psi\rangle = |jm\rangle$ onto the space-fixed z-axis. The dipole moment operator is expanded in the same basis with $\hat{\mu}^{(z)} = \hat{\boldsymbol{\mu}}\cdot\hat{z}$ as the projection of the permanent dipole moment onto the quantization axis. We disregard magnetic field couplings and the eigenstate energies, given by the eigenvalues of $\hat{\boldsymbol{J}}^2$ alone, are therefore independent of the quantum number m. The rotor eigenfrequencies $\omega_{jm} \equiv \omega_j$ are

$$\omega_j = \frac{1}{\hbar}\left\langle jm\left|\frac{\hat{\boldsymbol{J}}^2}{2I}\right|jm\right\rangle \equiv \frac{j(j+1)}{2}\Delta\omega, \tag{6.6}$$

where $\Delta\omega = \hbar/(2I)$ is the fundamental quantum beat frequency of the molecule. In the rigid rotor approximation the energy spacing between adjacent rotational levels is $\hbar(\omega_{j+1}-\omega_j) = (j+1)\hbar\Delta\omega$, and the linear rotational spectrum consists of many equally spaced spectral absorption lines, as shown in Fig. 6.2. As always, the time evolution of the molecules is described by the von Neumann equation

$$i\hbar\mathrm{d}_\tau\hat{\rho} = \left[\frac{\hat{\boldsymbol{J}}^2}{2I},\hat{\rho}\right] - E[\hat{\mu}^{(z)},\hat{\rho}], \tag{6.7}$$

where $\hat{\rho}$ is the rotational part of the density operator of the system.

The solution for $\hat{\rho}(\tau,x)$ completely describes the rotational state of the medium and the solution for $E(\tau,x)$ the propagation of the external field. Apart from the linear interaction

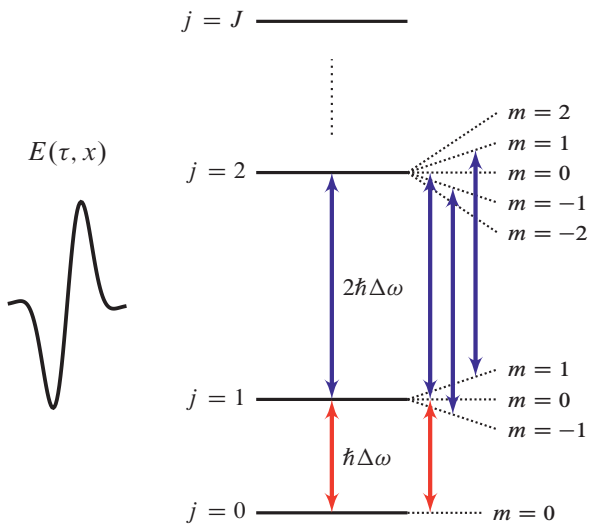

FIG. 6.2: Single cycle pulse interaction with a multi-level system where adjacent energy levels are connected via electric dipole transitions. The pulse spectrum is broad enough to simultaneously excite a large number of molecular eigenstates.

regime, solutions for $\hat{\rho}$ must be obtained numerically. Unlike simple two- or three-level media, $\hat{\rho}$ has a large number of possible non-zero entries and the temporal evolution must be described in terms of the experimental observables defined below.

6.2.1 Polarization

The allowed dipole transitions are found by calculating the entries of $\hat{\mu}^{(z)}$. Using the Wigner 3-j symbols we find that

$$\left\langle jm\left|\hat{\mu}^{(z)}\right|j'm'\right\rangle = \mu_{\mathrm{p}}(-1)^{2j-m}\sqrt{(2j+1)(2j'+1)} \times \begin{pmatrix} j & 1 & j' \\ -m & 0 & m' \end{pmatrix}\begin{pmatrix} j & 1 & j' \\ 0 & 0 & 0 \end{pmatrix}, \tag{6.8}$$

where μ_{p} is the permanent dipole moment of the molecule and we note the optical selection rule for linearly polarized light fields $j' = j \pm 1$, $m' = m$. Evaluating Eq. (6.8) explicitly yields

$$\mu^{(z)}_{jm,j+1\,m} = \mu_{\mathrm{p}}\sqrt{\frac{(1+j)^2 - m^2}{(2j+3)(2j+1)}}. \tag{6.9}$$

The quantum numbers j, m are good quantum numbers since the molecular motion is confined to j-space while no coherence is established between states with different m-numbers. In the suitable coordinate system where $\boldsymbol{E}$ is polarized along z for all times the

interaction potential $\boldsymbol{\mu} \cdot \boldsymbol{E}$ is independent of φ. The force $\boldsymbol{F} = -\nabla\left[\boldsymbol{\mu} \cdot \boldsymbol{E}(\tau)\right]$ exerted by the field on the molecule locks the THz induced rotations in the polar plane,

$$\boldsymbol{F} = -\mu_{\mathrm{p}} E(t) \sin\theta \hat{\boldsymbol{\theta}}. \tag{6.10}$$

System rotations of the molecule around the polarization axis are invariant, leaving the molecules free to rotate in the azimuthal plane. We may show explicitly that the ensemble molecular rotations around the z-axis vanish. This is proven by calculating the temporal evolution of the expectation value of $\hat{J}_z$, which gives

$$\begin{aligned} \mathrm{d}_\tau \langle \hat{J}_z \rangle &= \frac{1}{i\hbar} \mathrm{Tr}\left(\hat{J}_z \left[\frac{\hat{\boldsymbol{J}}^2}{2I} - E\hat{\mu}^{(z)}, \hat{\rho} \right] \right) \\ &= -\frac{E}{i\hbar} \mathrm{Tr}\left(\hat{J}_z \left[\hat{\mu}^{(z)}, \hat{\rho} \right] \right) \end{aligned} \tag{6.11}$$

since

$$\mathrm{Tr}\left(\hat{J}_z \left[\hat{\boldsymbol{J}}^2, \rho \right] \right) = \mathrm{Tr}\left(\left[\hat{J}_z, \hat{\boldsymbol{J}}^2 \right], \hat{\rho} \right) = 0 \tag{6.12}$$

due to the commutivity of $\hat{\boldsymbol{J}}^2$ and $\hat{J}_z$. In the same way we may show that in the abscence of an external field ($\boldsymbol{E} = 0$), the molecules rotate freely since $\left[\hat{J}_x, \hat{\boldsymbol{J}}^2 \right] = \left[\hat{J}_y, \hat{\boldsymbol{J}}^2 \right] = 0$. It remains to show that $\mathrm{Tr}\left(\hat{J}_z \left[\hat{\mu}^{(z)}, \hat{\rho} \right] \right)$ is also zero. Writing out the trace operation explicitly, and expanding $\hat{\rho}$ in the $|jm\rangle$ basis yields

$$\begin{aligned} \mathrm{Tr}\left(\hat{J}_z \left[\hat{\mu}^{(z)}, \hat{\rho} \right] \right) &= \mathrm{Tr}\left(\hat{\mu}^{(z)} \hat{\rho} \hat{J}_z - \hat{J}_z \hat{\rho} \hat{\mu}^{(z)} \right) \\ &= \sum_{\substack{jm \\ j'm' \\ j''m''}} \hbar m \rho_{j'm',j''m''} \left(\delta_{mm''} \delta_{jj''} \mu^{(z)}_{jm,j'm'} - \delta_{mm'} \delta_{jj'} \mu^{(z)}_{j''m'',jm} \right). \end{aligned} \tag{6.13}$$

where we have used $\left\langle jm \middle| \hat{J}_z \middle| j'm' \right\rangle = m\delta_{jj'}\delta_{mm'}$. Here, $\delta_{jj'}$ is the Kronecker delta-function, defined as 1 if $j = j'$ and zero otherwise. Since $\hat{\mu}^{(z)}_{jm,j'm'}$ is non-zero only for $m = m'$ the term inside the paranthesis evaluates to $\left(\delta_{jj''} \mu^{(z)}_{jm,j'm} - \delta_{jj'} \mu^{(z)}_{j''m'',jm} \right) = 0$. The upshot of this result is that linearly polarized lasers do not induce φ-motions; only oscillations in the θ-plane are possible. This result is physically obvious since the torque exerted by $\boldsymbol{E}$ through the permanent dipole moment will cause an alignment of the rotors completely analogous to the alignment a classical dipole experiences in a DC field. This property greatly simplifies the numerical evaluation of Eq. (6.7) and allows computer solutions of single-cycle nonlinear THz propagation in relatively large molecular systems. Note that the rotor molecules are obviously individually rotating in both the φ and θ planes since the initial state of the medium must be taken as a distribution over all the Zeeman

levels. The above result refers only to the macroscopic rotation when an ensemble average is considered; if $\left\langle \hat{J}_z \right\rangle$ is initially zero, it will remain so. Since the initial distribution of the Zeeman levels is isotropic for media in thermal equilibrium, φ-rotations are irrelevant in all that follows below.

It is evident that the molecular polarization will only lie along z when the electric field polarization does. In the following, to condense notation we will omit the superscript (z) and use the notation $\hat{\mu}^{(z)} = \hat{\mu}$. The coupling to Eq. (6.1) occurs via the polarization $P = \mathcal{N}\,\mathrm{Tr}\,(\hat{\mu}\hat{\rho})$ where, by using the selection rules that followed from Eq. (6.8) we find

$$P = \mathcal{N} \sum_{jm=0}^{JM-1} \left(\mu_{jm,j+1\,m} \rho_{j+1\,m,jm} + \mu_{j+1\,m,jm} \rho_{jm,j+1\,m} \right). \tag{6.14}$$

By using $\hat{\mu} = \mu_\mathrm{p} \cos\theta$, we also find that

$$\begin{aligned} P &= \mathcal{N} \langle \hat{\mu} \rangle \\ &= \mathcal{N} \mu_\mathrm{p} \langle \cos\theta \rangle, \end{aligned} \tag{6.15}$$

showing that the orientation $\langle \cos\theta \rangle$ is a direct measure of the polarization.

6.2.2 Energy conservation

During propagation energy is transferred between field and medium. By using $\partial_\tau \mathcal{N} \langle H \rangle = -(\partial_\tau E) P$, Eqs. (6.1) and (6.7) may be combined to a common energy conservation equation

$$\epsilon_0 c \partial_x E^2 + \partial_\tau U = 0, \tag{6.16}$$

where $\epsilon_0 c E^2$ is the instantaneous intensity of the external field and $U = \mathcal{N} \langle H_0 \rangle$ is the internal molecular energy. In the undamped limit considered here optical transparency is mathematically inevitable since excited rotor molecules radiate indefinitely. This manifests itself as an infinitely long coherent transient in pulse and medium, while in reality damping always takes place for sufficiently long time delays and the pulse duration remains finite. In all that follows, our numerical solutions are valid only for time scales considerably shorter than any such relaxation times. The concept of "total energy transmission" is not applicable to our computer simulations because the pulse tail is for computational necessity truncated at a finite numerical integration time. Equation (6.16) may nevertheless be applied unambiguously provided that relaxation times remain comparatively long.

6.2.3 Position space

Although our analytic and computational approach solves for the expansion coefficients of the known wave function basis, it is frequently convenient to represent the molecular

state in coordinate space. The projection of the eigenstates $|jm\rangle$ into position space $\boldsymbol{r}$ is

$$\langle \hat{\boldsymbol{n}}|jm\rangle = Y_j^m(\theta,\varphi), \tag{6.17}$$

where $\hat{\boldsymbol{n}}$ is a unit vector along (θ,φ) and $Y_j^m(\theta,\varphi)$ is the complex spherical harmonic

$$Y_j^m(\theta,\varphi) = (-1)^m \sqrt{\frac{(2j+1)}{4\pi}\frac{(j-m)!}{(j+m)!}} P_j^m(\cos\theta) e^{im\varphi}, \tag{6.18}$$

and $P_j^m(\cos\theta)$ is an associated Legendre polynomial. The probability density σ is defined

$$\begin{aligned} \sigma(\tau,x;\theta,\varphi) &= \langle \hat{\boldsymbol{n}}|\hat{\rho}(\tau,x)|\hat{\boldsymbol{n}}\rangle \\ &= \sum_k p_k \,|\Psi_k(\tau,x;\hat{\boldsymbol{n}})|^2 \end{aligned} \tag{6.19}$$

where the single-molecule wavefunction is given by $\Psi_k(\tau,x;\hat{\boldsymbol{n}}) = \langle \hat{\boldsymbol{n}}|\Psi_k(\tau,x)\rangle$. Expanding Ψ_k into spherical harmonics yields

$$\sigma(\tau,x;\theta,\varphi) = \sum_{\substack{jm \\ j'm'}} \rho_{jm,j'm'} Y_j^m Y_{j'}^{m'^*}. \tag{6.20}$$

The notation $(\tau,x;\theta,\varphi)$ specifies that τ is the delayed time, x is the macroscopic propagation coordinate, and (θ,φ) are internal coordinates for the molecules. Thus $\sigma(\tau,x;\theta,\varphi)$ describes the probability of observing the molecules oriented along (θ,φ) a propagation distance x into the medium at time τ (see Fig. 6.1). Since $\mu^{(z)}_{jm,j'm'} = 0$ for $m \neq m'$ one also has $\rho_{jm,j'm'} = 0$ for $m \neq m'$ when the medium starts out in a completely mixed state. The φ-dependence (but not m-dependence) then falls out of Eq. (6.22) and σ changes to

$$\sigma(\tau,x;\theta) = \sum_{j,j',m} \rho_{jm,j'm} Y_j^m Y_{j'}^{m^*}. \tag{6.21}$$

For numerical convenience, Eq. (6.21) is compactly written

$$\sigma(\tau,x;\theta) = \hat{\rho}(\tau,x) : \widehat{G}(\theta), \tag{6.22}$$

where **:** is the Frobenius product, and $\widehat{G}$ is a matrix operator with entries

$$G_{jm,j'm}(\theta) = Y_j^m(\theta,\varphi) Y_{j'}^{m^*}(\theta,\varphi). \tag{6.23}$$

For density operators, σ is analogous to the probability density $|\Psi(\hat{\boldsymbol{n}})|^2 = |\,\langle \hat{\boldsymbol{n}}|\Psi\rangle\,|^2$ for a pure state $|\Psi\rangle$. Conservation of probability implies that

$$\int_0^\pi \sigma(\tau,x;\theta)\sin\theta d\theta = \frac{1}{2\pi}. \tag{6.24}$$

A realistic theoretical prediction for the molecular shape must incorporate Zeeman levels even when no transitions between the various harmonic ladder systems associated with each quantum number m occur. For example, for media in thermal equilibrium Unsölds theorem shows that $\sigma \to 1/(4\pi)$ only when the Zeeman levels are equally populated for each j. Spherical symmetry of σ indicates that the molecular axes are distributed isotropically over the unit sphere.

6.2.4 Molecular alignment

Transient optical birefringence is measurable [159] and is proportional to the quantity

$$\left\langle \cos^2\theta \right\rangle = \sum_{jm} \rho_{jm,jm} V_{jm,jm} + \rho_{jm,j\pm2\,m} V_{j\pm2\,m,jm}, \tag{6.25}$$

where

$$V_{jm,jm} = \frac{1}{3}\left[1 + 2\frac{j(j+1) - 3m^2}{(2j+3)(2j-1)}\right], \tag{6.26a}$$

$$V_{j-2\,m,jm} = \sqrt{\frac{(j-1)^2 - m^2}{(2j-1)^2}\frac{j^2 - m^2}{(2j-3)(2j+1)}}. \tag{6.26b}$$

The observable $\left\langle \cos^2\theta \right\rangle$ may be further partioned into population and coherences [160, 161],

$$\langle \cos^2\theta \rangle_{\mathrm{p}} = \sum_{jm} \rho_{jm,jm} V_{jm,jm}, \tag{6.27a}$$

$$\langle \cos^2\theta \rangle_{\mathrm{c}} = \sum_{\substack{jm,\\ j'=j\pm2}} \rho_{jm,j'm} V_{j'm,jm}. \tag{6.27b}$$

For a medium with isotropically distributed magnetic sublevels for each j, $\left\langle \cos^2\theta \right\rangle_{\mathrm{p}}$ evaluates to $1/3$.

Equivalently, the orientation and alignment are described in terms of the Legendre moments

$$\begin{aligned} \langle P_\kappa(\cos\theta) \rangle &= \sum_{j,j',m} \rho_{jm,j'm}(\tau, x) \left\langle j'm \middle| P_\kappa(\cos\theta) \middle| jm \right\rangle \\ &\equiv \hat{\rho}(\tau, x) : \hat{L}_\kappa. \end{aligned} \tag{6.28}$$

Using the Wigner $3j$-symbols, the coefficients of the matrices $\hat{L}_\kappa$ are analytically expressable,

$$\begin{aligned} \left\langle jm \middle| \hat{L}_\kappa \middle| j'm \right\rangle &= (-1)^m \sqrt{(2j'+1)(2j+1)} \\ &\quad \times \begin{pmatrix} j' & k & j \\ 0 & 0 & 0 \end{pmatrix} \begin{pmatrix} j' & k & j \\ -m & 0 & m \end{pmatrix}. \end{aligned} \tag{6.29}$$

The odd-even properties of $P_\kappa(\cos\theta)$ imply that odd Legendre moments measure the orientation and even moments measure the alignment. Special values are $\langle P_0(\cos\theta)\rangle = 1$, $\langle P_1(\cos\theta)\rangle = \langle\cos\theta\rangle$, and $\langle P_2(\cos\theta)\rangle = (3\langle\cos^2\theta\rangle - 1)/2$. By the selection rules of the Wigner $3j$-symbols each moment $\langle P_\kappa(\cos\theta)\rangle$ consists of populations and rotational coherences up to order $|j' - j| \leq \kappa$.

6.3 Linearized solution

In the preceding section we introduced the theoretical Maxwell-Bloch model for rigid rotor molecules. It is clear that in the general case exact solutions are unlikely to be obtainable. It is possible, nevertheless, to obtain linearized solutions when the pulse area is small, a result which is interesting in its own right.

6.3.1 Linearization

Firstly, linearization of the model follows from standard time-dependent perturbation expansions of the density operator. We denote the order of the perturbation expansion by incorporating a superscript on $\hat{\rho}$ (e.g. $\hat{\rho}^{[0]}$). The relevant differential equations are the time evolution equations for the population elements $\rho_{jm,jm}$ and the coherence elements $\rho_{j+1\,m,jm}$, which are

$$\mathrm{d}_\tau \rho_{jm,jm} = i\frac{E(\tau)}{\hbar}\left(\mu_{jm,j+1\,m}\rho_{j+1\,m,jm} + \mu_{jm,j-1m}\rho_{j-1m,jm}\right) - \text{c.c.}, \tag{6.30a}$$

$$\begin{aligned}\mathrm{d}_\tau \rho_{j+1\,m,jm} &= -i\left(\omega_{j+1} - \omega_j\right)\rho_{j+1\,m,jm} \\ &\quad + i\frac{\mu_{j+1\,m,jm}\left(\rho_{jm,jm} - \rho_{j+1\,m,j+1\,m}\right)}{\hbar}E(\tau,x) \\ &\quad + i\frac{E}{\hbar}\left(\mu_{j+1\,m,j+2\,m}\rho_{j+2\,m,jm} - \mu_{j-1\,m,jm}\rho_{j+1\,m,jm}\right).\end{aligned} \tag{6.30b}$$

The final terms on the right-hand side of Eq. (6.30b) contain the two-photon coherences $\rho_{j+1\,m,j-1\,m}$, $\rho_{j+2\,m,jm}$ and indicate the presence of a rotational Raman coupling. Assuming that the initial rotational state populations are relatively uninterrupted by the pulse, the first order perturbation solution for the polarization coherence $\rho_{jm,j+1\,m}$ may be written down as

$$\begin{aligned}\rho^{[1]}_{j+1\,m,jm} &= i\frac{\mu_{j+1\,m,jm}\left(\rho^{[0]}_{jm,jm} - \rho^{[0]}_{j+1\,m,j+1\,m}\right)}{\hbar} \\ &\quad \times \int_{-\infty}^{\tau} E(\tau')\mathrm{e}^{i(\omega_{j+1}-\omega_j)(\tau'-\tau)}d\tau',\end{aligned} \tag{6.31}$$

where $\rho^{[0]} = \rho(-\infty, z)$ and $\rho^{[0]}_{jm,j'm'} = 0$ for all $jm \neq j'm'$. That is, the initial state of the medium is assumed to be a completely mixed state. To obtain a measure of how much population is moved away from each state during the action of the pulse, we insert Eq. (6.31) into the right-hand side of Eq. (6.30a) and integrate once with respect to time, which gives the first order solution

$$\begin{aligned}\rho^{[1]}_{jm,jm} - \rho^{[0]}_{jm,jm} = &-\frac{|\mu_{jm,j+1\,m}|^2 \left(\rho^{[0]}_{jm,jm} - \rho^{[0]}_{j+1\,m,j+1\,m}\right)}{\hbar^2} \\ &\times \int_{-\infty}^{\tau} d\tau' \int_{-\infty}^{\tau'} d\tau'' E(\tau')E(\tau'')\mathrm{e}^{i(\omega_{j+1}-\omega_j)(\tau'-\tau'')} \\ &+ \ldots .\end{aligned} \tag{6.32}$$

The dots indicate the presence of additional terms that are of the same order. The largest possible contribution from the integrals is estimated by the triangle inequality

$$\left| \int_{-\infty}^{\tau} E(\tau') \exp[i(\omega_{j+1} - \omega_j)\tau'] d\tau' \right| \leq \int_{-\infty}^{\tau} d\tau' \left| E(\tau') \right| . \tag{6.33}$$

As a rough approximation we may use a boxcar pulse $|E(\tau)| = E_0$ for $0 \leq \tau \leq T$ as a replacement for the magnitude of a single-cycle pulse. When this pulse is replaced into the above integral we obtain

$$\rho^{[1]}_{jm,jm} - \rho^{[0]}_{jm,jm} \leq [\rho^{[0]}_{jm,jm} - \rho^{[0]}_{j+1\,m,j+1\,m}] \frac{|\mu_{jm,j+1\,m}|^2 E_0^2 T^2}{2\hbar^2} + \ldots . \tag{6.34}$$

The linear approximation is essentially a small-area approximation valid if the right-hand side is small compared to $\rho^{[0]}_{jm,jm}$ and in this case Eq. (6.31) may be used to calculate the polarization coherences and the spatiotemporal evolution of the pulse.

To help clarify some of the approximations invoked in deriving analytic solutions, we consider, in the next two subsections only, also the effects of homogeneous damping by introducing phenomenological damping terms $-\gamma\rho_{j+1\,m,jm}$ into the right-hand side of Eq. (6.30b).

6.3.2 Perturbative first-order solution

The linear equations of motion are solved by transforming Eq. (6.1) to the frequency domain,

$$\partial_x E(\omega) = -\frac{i\omega}{2\epsilon_0 c} P(\omega). \tag{6.35}$$

The expressions for the polarization and the coherences $\rho^{[1]}_{j+1\,m,jm}$ in the frequency domain are obtained by taking the Fourier transform of Eq. (6.31). This leads to a standard expression where the polarization coherences are described as quantum-mechanical Lorentz

resonances. Inserting the resulting expressions into Eq. (6.35) yields an evolution equation for E alone in the frequency domain, with exact solution

$$E(\omega, x) = \exp\left(\sum_{j=0}^{J-1} \frac{-\omega\beta_j x}{\omega_{j+1} - \omega_j}\left[A^-(\omega) - A^+(\omega)\right]\right) E(\omega, 0), \tag{6.36}$$

where

$$A^{\pm}(\omega) = \frac{1}{i\omega \pm i(\omega_{j+1} - \omega_j) + \gamma}. \tag{6.37}$$

Equation (6.36) shows that E obeys a frequency domain Beer's law where each frequency component decays exponentially with distance. The coefficients β_j are in the general case given by

$$\beta_j = \frac{\mathcal{N}(\omega_{j+1} - \omega_j)}{2\epsilon_0\hbar c} \sum_{m=-j}^{j} |\mu_{jm,j+1\,m}|^2 \left(\rho^{[0]}_{jm,jm} - \rho^{[0]}_{j+1\,m,j+1\,m}\right). \tag{6.38}$$

When the Zeeman levels are populated isotropically for each j the coefficients become

$$\beta_j = \frac{\mathcal{N}\mu_{\mathrm{p}}^2(j+1)^2\Delta\omega\left(\rho^{[0]}_{j,j} - \rho^{[0]}_{j+1,j+1}\right)}{6\epsilon_0\hbar c}, \tag{6.39}$$

where $\rho^{[0]}_{j,j}$ is the initial population of level j for any m. To revert back to the time domain, the exponential is expanded in its Taylor series and cross-terms are neglected since $A^{\pm}(\omega)$ is sharply peaked around $\mp(\omega_{j+1} - \omega_j)$. In the sharp-line limit $\gamma \ll \omega_{j+1} - \omega_j$,

$$\frac{\omega}{i\omega \pm i(\omega_{j+1} - \omega_j) + \gamma} \approx \frac{\mp(\omega_{j+1} - \omega_j)}{i\omega \pm i(\omega_{j+1} - \omega_j) + \gamma} \tag{6.40}$$

by the same argument. By the convolution theorem $\mathcal{F}^{-1}[A^{\pm}(\omega)E(\omega)] = A(\tau) \star E(\tau)$ the transformation back to the time-domain yields

$$\begin{aligned} E(\tau, x) &= E(\tau, 0) \\ &+ \sum_{j=0}^{J-1} \int_{-\infty}^{\infty} \sum_{n=1}^{\infty} \frac{(-\beta_j x)^n}{n!}\left[A_n^+(\tau') + A_n^-(\tau')\right] E(\tau - \tau', 0)\, d\tau', \end{aligned} \tag{6.41}$$

where $A_n^{\pm}(\omega) = [A^{\pm}(\omega)]^n$ and [162]

$$A_n^{\pm}(\tau) = \frac{\tau^{n-1}}{(n-1)!} \mathrm{e}^{-\gamma\tau \mp i(\omega_{j+1} - \omega_j)\tau} h(\tau), \tag{6.42}$$

where $h(\tau)$ is the unit step function. The convolution integral in Eq. (6.41) represents the reshaping of the pulse due to the molecular response, and $E(\tau, 0)$ represents free transla-

tion in the abscence of a medium. Inserting Eq. (6.42) into Eq. (6.41) yields

$$E(\tau,x) = E(\tau,0) \tag{6.43}$$
$$+\,2\sum_{j=0}^{J-1}\int_0^{\infty}\sum_{n=1}^{\infty}\frac{\left(-\beta_j\tau' x\right)^n}{n!(n-1)!}\frac{1}{\tau'}\mathrm{e}^{-\gamma\tau'}\cos[\left(\omega_{j+1}-\omega_j\right)\tau']E(\tau-\tau',0)d\tau'.$$

The sum over n evaluates to [163]

$$\sum_{n=1}^{\infty}\frac{\left(-\beta_j\tau' x\right)^n}{n!(n-1)!}\frac{1}{\tau'} = -\sqrt{\frac{\beta_j x}{\tau'}}J_1\left(2\sqrt{\beta_j\tau' x}\right), \tag{6.44}$$

where $J_1(x)$ is a Bessel function of the first kind. The final solution for $E(\tau,x)$ in the sharp-line limit is

$$E(\tau,x) = E(\tau,0) \tag{6.45}$$
$$-\,2\sum_{j=0}^{J-1}\int_0^{\infty}\sqrt{\frac{\beta_j x}{\tau'}}J_1\left(2\sqrt{\beta_j\tau' x}\right)\mathrm{e}^{-\gamma\tau'}\cos\left[\left(\omega_{j+1}-\omega_j\right)\tau'\right]E(\tau-\tau',0)d\tau'.$$

To relate the physical significance of Eq. (6.45) to known results, note that if we consider only a single resonant transition, applying Eq. (6.40) in Eq. (6.36) returns an equation describing a linear 0π pulse, first derived by Crisp [30] (Eq. (21) in Crisp's paper). Thus, each j-term in Eq. (6.45) represents a linear 0π-pulse in the undamped limit. This is surprising, considering that the approximations that went into deriving Eq. (6.45) are not the same as those of Crisp [30]. In particular, neither the rotating wave or slowly varying envelope approximations were made. The reason for this agreement, of course, is Eq. (6.40), which presumes that the resonances are narrow, spaced far apart, and respond only at $\omega_{j+1}-\omega_j$. We recall that for quasi-monochromatic pulses propagating in two-level media the pulse area is defined either as the area under the pulse envelope, or equivalently as the Fourier coefficient on the center frequency. As envelopes are not used here we necessarily stick to the latter definition; the 0π-pulse analogy simply enters due to absorption at the various resonance frequencies.

Arlt et al. [164] have derived analogous expressions to Eq. (6.45) under the slowly varying envelope and rotating wave approximations in the context of Rydberg wave packets [165–167]. Equation (6.45) is a generalization of the results derived by Crisp [30] and Arlt et al. [164]; it represents a superposition of various single-cycle 0π pulses.

6.3.3 Impulse solution

Equation (6.45) is a general solution to the linearized sharp-line model. In the special case when $\beta_j = \beta$ the integrand in Eq. (6.45) resonates when $\Delta\omega\tau' = n\pi$, and a pulse

revival might be observed at times $\tau \sim n\pi/\Delta\omega$. When the line strengths of each rotor transition are equal, the time-domain propagation dynamics can be described explictly in terms of pulse revivals without the need of evaluating the complicated integral expression in Eq. (6.45). First, Eq. (6.36) is equivalent to

$$\begin{aligned}\partial_x E = -\sum_{j=0}^{J-1} \beta_j \int_{-\infty}^{\tau} E(\tau', x) \mathrm{e}^{-\gamma(\tau-\tau')} \\ \times \left(\mathrm{e}^{i(\omega_{j+1}-\omega_j)(\tau-\tau')} + \mathrm{e}^{-i(\omega_{j+1}-\omega_j)(\tau-\tau')} \right) d\tau',\end{aligned} \tag{6.46}$$

in the time domain. To proceed further we assume that $\beta_j = \beta =$ constant, but note that this does not hold in general because under more realistic conditions the populations are distributed according to a Maxwell-Boltzmann distribution and the various line intensities are then evidently not the same. The assumption $\beta_j = \beta$ is a crude approximation in the present context valid only closest to the interface $x = 0$ where the Bessel functions in Eq. (6.45) are small and equally phased. However, by invoking this assumption we obtain a compact, analytic solution that is convenient for understanding the linear time-domain molecular response of the system. This solution is included in the present report because Eq. (6.46) is generic for sharp-line, harmonic, multi-level systems for arbitrary pulse durations, and an analysis is relevant also in other physical contexts, most notably in multimode fiber Bragg grating transmission. Under the approximation $\beta_j \sim \beta$ the model has only one length scale, substantially simplifying the analytic description of the spatial evolution. Equation (6.46) is written

$$\partial_x E = -\beta \int_{-\infty}^{\tau} E(\tau', x) \sum_{j=-J}^{J} \mathrm{e}^{(j\Delta\omega-\gamma)(\tau-\tau')} d\tau'. \tag{6.47}$$

The $j = 0$ term contained in Eq. (6.47) does not contribute to the integral unless E has a large DC component. When the spectrum of E lies within the rotational manifold the limit $J \to \infty$ may be taken since the rapidly oscillating exponentials of the added terms average out under the time integration in Eq. (6.47). The sum is evaluated by Poisson resummation

$$\sum_{j=-\infty}^{\infty} \mathrm{e}^{j\Delta\omega(\tau-\tau')} = T_b \sum_{k=-\infty}^{\infty} \delta(\tau - \tau' - kT_b), \tag{6.48}$$

where $T_b = 2\pi/\Delta\omega$ is the quantum beat period of the system. Equation (6.47) evaluates to

$$\partial_x E(\tau, x) = -\alpha \left[\frac{1}{2} E(\tau, x) + \sum_{k=1}^{\infty} \mathrm{e}^{-\gamma k T_b} E(\tau - kT_b, x) \right], \tag{6.49}$$

where $\alpha = \beta T_b$ is the reciprocal characteristic length scale. Equation (6.49) is solved exactly with the Ansatz

$$E(\tau, x) = \sum_{k=0}^{\infty} g_k(x) \mathrm{e}^{-\alpha x/2 - \gamma k T_b} E(\tau - k T_b, 0), \tag{6.50}$$

where $E(\tau - kT_b, 0)$ is the input pulse shifted an amount kT_b in time. Replacing Eq. (6.50) into Eq. (6.49) yields a recursive equation for the unknown algebraic factors $g_k(x)$:

$$\partial_x g_k(x) = -\alpha \sum_{l=0}^{k-1} g_l(x). \tag{6.51}$$

The boundary condition on $x = 0$ gives $g_0 = 1$ and all other terms are solved for by recursive integration. The first few terms are summarized in Table 6.1.

TABLE 6.1: The x-dependence of the driving pulse g_0 and the first four impulses

$g_0(x)$	1
$g_1(x)$	$-(\alpha x)$
$g_2(x)$	$-(\alpha x) + \frac{1}{2}(\alpha x)^2$
$g_3(x)$	$-(\alpha x) + (\alpha x)^2 - \frac{1}{6}(\alpha x)^3$
$g_4(x)$	$-(\alpha x) + \frac{3}{2}(\alpha x)^2 - \frac{1}{2}(\alpha x)^3 + \frac{1}{24}(\alpha x)^4$
$g_5(x)$	$-(\alpha x) + 2(\alpha x)^2 - (\alpha x)^3 + \frac{1}{6}(\alpha x)^4 - \frac{1}{120}(\alpha x)^5$

Equation (6.50) shows that the pulse evolves into a series of impulses following the driving pulse $k = 0$ which decays exponentially with propagation distance, an expected result interpreted as follows: As the pulse enters into the material it excites a coherent superposition of molecular eigenstates in the material (i.e. a rotational wave-packet) which oscillates freely in the abscence of the pulse. Due to the harmonic spacing of the energy levels and equal line intensities, the rotational wave packet rephases at times $\tau = kT_b$ and emit radiation. Under idealized conditions linear dispersive broadening cancels and the emitted radiation is a temporal copy of the input pulse, homogeneously damped by a factor $\mathrm{e}^{-\gamma k T_b}$. The inequality $\gamma T_b \ll 1$ is satisfied for a wide class of media (e.g. the hydrogen halides) and the pulse train described by Eq. (6.50) may be very long. According to Eq. (6.36), the pulse spectrum looks like an inverse frequency comb. In optically thin materials $\alpha x \ll 1$ these impulses have the same amplitude and are π radians out of phase with the driving field, and have been termed commensurate THz echoes [156, 157] in the context of terahertz excitation.

6.4 Numerical procedure

We showed in Sec. 6.2 that the total number of levels of rigid rotor molecules are $(J+1)^2$. For $J = 31$, 1024 levels need to be incorporated into the equation for the propagating field, corresponding to $(J+1)^4 = 1,048,576$ entries in the density operator. This can be further reduced by the hermiticity and trace requirements to $524,799$ unique coefficients. The composite system represented by the hundreds of thousands of coupled, nonlinear partial differential equations is considered to be of substantial complexity in a pulse propagation context. Presently, computer solutions of coherent single-cycle pulse propagation have only been presented for a handful of levels [53, 168, 169]. Nonetheless, we will show that large systems are computationally tractable by using a clever arrangement of the Zeeman levels.

6.4.1 Subspace formulation

Recalling that for linearly polarized THz pulses the transition dipole moment $\hat{\mu}$ is non-zero only for transitions $j \rightarrow j \pm 1$, $m \rightarrow m$ it is immediately realized that $\hat{\rho}$ is very sparse. Arranging the (finite-dimensional) state vector $|\psi\rangle$ in order of largest negative m to largest positive m, and within each block from smallest j to largest j, the dipole moment operator may be written as the diagonal sum

$$\begin{aligned}\hat{\mu} &= \begin{pmatrix} \overbrace{\begin{pmatrix} 0 \end{pmatrix}}^{m=-J} & & & \\ & \overbrace{\begin{pmatrix} 0 & \mu_{J-1\,m,\,Jm} \\ \mu_{Jm,J-1\,m} & 0 \end{pmatrix}}^{m=-J+1} & & \\ & & \ddots & \\ & & & \overbrace{\begin{pmatrix} 0 \end{pmatrix}}^{m=J} \end{pmatrix} \\ &= \bigoplus_{m=-J}^{m=J} \hat{\mu}^{(m)},\end{aligned} \tag{6.52}$$

where $\hat{\mu}^{(m)}$ is a $(J-|m|+1)\times(J-|m|+1)$ dimensional Hermitian matrix. The empty entries in Eq. (6.52) are filled with zeros. $\bigoplus$ is the direct matrix sum, and Eq. (6.52) defines a block diagonal matrix with entries $\hat{\mu}^{(m)}$. Note that the direct sum $\bigoplus$ should not be confused with the Kronecker sum $\oplus$ which was used in Chapter 5, Sec. 3.4 for the numerical calculation of the interaction propagator. We may also decompose the density operator and the free Hamiltonian as block diagonal matrices, leading to corresponding

expressions

$$\widehat{H}_0 = \bigoplus_{m=-J}^{m=J} \widehat{H}_0^{(m)}, \tag{6.53a}$$

$$\hat{\rho} = \bigoplus_{m=-J}^{m=J} \hat{\rho}^{(m)}. \tag{6.53b}$$

We are allowed to do this because, by virtue of the fact that the entries of $\hat{\mu}$ and $\widehat{H}_0$ are non-zero only for $m = m'$, so are the entries of $\hat{\rho}$ (provided that the medium starts out in a completely mixed state). Multiplying a block diagonal matrix by another matrix of the same block-diagonal form will return the same matrix shape. That is,

$$\left(\bigoplus_m \widehat{\mathcal{O}}_1^{(m)}\right)\left(\bigoplus_m \widehat{\mathcal{O}}_2^{(m)}\right) = \bigoplus_m \widehat{\mathcal{O}}_1^{(m)}\widehat{\mathcal{O}}_2^{(m)} \tag{6.54}$$

where $\widehat{\mathcal{O}}_1^{(m)}\widehat{\mathcal{O}}_2^{(m)}$ is a normal matrix product. This allows the von Neumann equation to be written

$$i\hbar \mathrm{d}_\tau \bigoplus_{m=-J}^{m=J} \hat{\rho}^{(m)} = \bigoplus_{m=-J}^{m=J} \left[\widehat{H}_0^{(m)} - E\hat{\mu}^{(m)}, \hat{\rho}^{(m)}\right], \tag{6.55}$$

which of course allows solutions in terms of each block m

$$i\hbar \mathrm{d}_\tau \hat{\rho}^{(m)} = \left[\widehat{H}_0^{(m)} - E\hat{\mu}^{(m)}, \hat{\rho}^{(m)}\right]. \tag{6.56}$$

Equation (6.56) is an exact decomposition of Eq. (6.7) for linearly polarized fields. The interpretation of the decomposition is straightforward. Since the molecules are initially distributed over all azimuthal rotation modes (m-modes) but no coherence can be established between the various modes, we may decompose the density operator into each subspace m and solve only for the θ-motion of each mode, leaving φ-rotations as frozen variables incorporated into the initial conditions of $\hat{\rho}$. This process reduces the $(J+1)^2 \times (J+1)^2$ dimensional density operator into $2J+1$ partial density operators $\hat{\rho}^{(m)}$ with different dimensions, each of which describe the θ-motion of the molecule for a given φ-mode. The partial density operator with the largest dimension is obviously $\hat{\rho}^{(m=0)}$ which has dimension $(J+1) \times (J+1)$. The initial population in the $m = \pm J$ is not coupled to the external field, and $\rho^{(-J)}$ and $\rho^{(J)}$ are therefore of dimension 1×1.

The number of non-zero entries in the decomposed density operator is substantially reduced compared to the full case but nonetheless remains comparatively large. For $J = 31$, the total number of non-zero elements in the reduced density operator is 21,856, and 700 GB of hard drive space is needed to store these elements on a 1000×4000 spatiotemporal grid when single-precision complex arithmetic is used. Evidently, storage of

the density operator is both time consuming and resource exhaustive, necessitating calculation of observables during run-time. These may be calculated on each subspace m,

$$\begin{aligned} \mathrm{Tr}\left(\hat{\mathcal{O}}_1\hat{\mathcal{O}}_2\right) &= \mathrm{Tr}\left(\bigoplus_{m=-J}^{m=J}\hat{\mathcal{O}}_1^{(m)}\hat{\mathcal{O}}_2^{(m)}\right) \\ &= \sum_{m=-J}^{m=J}\mathrm{Tr}\left(\hat{\mathcal{O}}_1^{(m)}\hat{\mathcal{O}}_2^{(m)}\right). \end{aligned} \tag{6.57}$$

Equation (6.57) allows calculations in terms of partial operators instead of full ones, avoiding the need for large matrix multiplications. In the same way, Eq. (6.22) becomes

$$\sigma(\tau, x; \theta) = \sum_{m=-J}^{J}\hat{\rho}^{(m)}(\tau, x) : \hat{G}^{(m)}(\theta), \tag{6.58}$$

where $\hat{G}^{(m)}(\theta)$ is a $(J - |m| + 1) \times (J - |m| + 1)$ dimensional matrix with entries

$$G_{k,k'}^{(m)}(\theta) = Y_{|m|+k-1}^{m}(\theta, \varphi)Y_{|m|+k'-1}^{m^*}(\theta, \varphi), \tag{6.59}$$

where $k, k' \in [1, J - |m| + 1]$. An analogous expression is found for $\hat{L}_\kappa^{(m)}$ describing the Legendre moments. Evaluation of $\hat{G}^{(m)}(\theta)$ and $\hat{L}^{(m)}$ require run-time numerical evaluation. Here, the spherical harmonics are calculated by using the freely available software library `SHTOOLS` [170], and the Wigner $3j$ coefficients were calculated using a Root Rational Fraction program [171] by Stone and Wood [172].

6.4.2 Discretization

The discretization of Eqs. (6.1) and (6.56) follows the results of Chapter 5, Sec. 5.4, with the exception that the diffraction term $\nabla_\perp^2$ is discarded. The propagation equation is then solved with an implicit trapezoidal method and the Bloch equations using the operator splitting method in the interaction picture. This set of equations is coupled in the same way as the full three-dimensional model, and we have used a predictor-corrector method to iterate the solutions to convergence. Furthermore, note that we do not, for greatest simplicity, incorporate relaxations here, so the transformation to Liouville space is unnecessary.

Computer implementations of Eq. (6.1) and (6.56) require parallelization when J becomes large. Our code is based on the Message Passing Interface, where one computing core is used for updating the propagation equation, and $2J + 1$ cores are used for updating the density operator, allocating one core to each partial density matrix. The typical execution time of parallelized computer codes based on the above decomposition is determined by the serial execution time of the largest partial density matrix. Using $J = 31$ (1024 total levels) on a 500×1000 spatiotemporal grid, our code executes in about 10 minutes.

We have also developed computer codes based on the full Eq. (6.7) and parallelized the Bloch equation solver using distributed matrix calculations. These codes did not scale very well unless the system became very large. At $J = 31$, codes based on distributed matrix routines execute orders of magnitude slower than subspace methods. However, since the code solves for the full density operator the approach might hold merit for elliptically polarized light fields for which the subspace decomposition above is not valid.

6.4.3 Comparison with analytic solutions

To verify the reliability of our analytic results and our numerical method we present the results of various computer simulations below. We take the density $\mathcal{N} = 10^{18}$ cm^{-3}, corresponding to a vapor pressure of 31 torr. The permanent dipole moment is taken as $\mu_{\rm p} = 5 \times 10^{-29}$ Cm, the quantum beat period as $T_b = 5$ ps. We consider $J = 31$ which gives 1024 states in total. The propagation length is $L = 10$ cm. Our choice of parameters does not represent a particular medium.

TABLE 6.2: Parameters used for computer simulations.

Variable	*Symbol*	*Value*
Density	$\mathcal{N}$	10^{18} cm^{-3}
Quantum beat period	T_b	5 ps
Dipole moment	$\mu_{\rm p}$	5×10^{-29} Cm
Rotational levels	$J+1$	32
Number of levels	$(J+1)^2$	1024
Propagation length	L	10 cm

Choice of input pulse

Since the DC component radiated by a finite-size source propagates evanescently, a basic propagation requirement prior to reaching the medium is that the DC Fourier coefficient of the input pulse is zero [173]. For this reason we reject the use of Gaussian pulses where the DC level depends strongly on the carrier-envelope phase in the single-cycle regime [33]. Instead, we apply a Poisson input pulse [174],

$$E(\tau,0) = \frac{1}{2} E_0 \mathrm{e}^{i\phi} \left(1 - \frac{i\omega_c \tau}{s}\right)^{-(s+1)} + \text{c.c.} \tag{6.60}$$

The parameters s, ω_c, and ϕ describe the duration, location of the spectral peak, and the spectral phase. The pulse described by Eq. (6.60) has a zero DC coefficient and is anti-symmetric with respect to τ for $\phi = 0$ and symmetric for $\phi = \pi/2$. For s close to unity Eq. (6.60) describes a single-cycle pulse, and for large s the limiting form of

Eq. (6.60) is a Gaussian pulse with carrier frequency ω_c, carrier-envelope phase ϕ, and duration $T = \sqrt{2s}/\omega_c$. Pulse chirping is taken into account by treating ω_c as a complex parameter [174]. In this subsection, we take $E_0 = 5 \times 10^6$ V/m, $\phi = \pi/2$, $s = 3$, and $\omega_c = 3\pi \times 10^{12}$ rad/s. This choice of parameters represents an asymmetric single-cycle pulse consisting of two main "carrier lobes" where the first lobe is positive $E > 0$ and the second negative $E < 0$. The input pulse we use is shown as solid line in Fig. 6.3(b). Taking the Fourier transform of Eq. (6.60) gives

$$\widetilde{E}(\omega, 0) = 2\pi E_0 \mathrm{e}^{i\phi} \left(\frac{s}{\omega_c}\right)^{s+1} \frac{\omega^s \mathrm{e}^{-s\omega/\omega_c}}{\Gamma(s+1)} h(\omega), \tag{6.61}$$

where Γ is the Gamma factorial function and $h(\omega)$ the unit step function in the frequency domain. With the parameters above, Eq. (6.60) describes a spectrum which peaks at 1.5 THz and extends up to approximately 5 THz. The input pulse spectrum is plotted in the top panel in Fig. 6.4.

The backpropagation and linear approximations are well satisfied for our chosen parameters: We find for example $P/(\epsilon_0 E_0) \sim 10^{-2}$ [see Fig. 6.3(b)], and this is the case for all of our computer simulations. The "infinite-ladder" approximation used in Eq. (6.48) is satisfied since the highest-lying molecular transition lies outside the pulse spectrum.

Impulse solution

First, we consider linear evolution under the condition of equal line strengths. This assumption gives an optical thickness $\alpha L \approx 22.5$. Figure 6.3 shows the propagation of the Poisson pulse over the first 16 absorption lengths. According to Eq. (6.50), the driving pulse is followed by a sequence of impulses propagating at the vacuum light velocity and which are spaced exactly one quantum beat period apart. These features are captured in our computer simulation. The color coding in Fig. 6.3(a) shows the magnitude of the electric field in units of E_0 and the recurring impulses are readily observed at times that are integer multiples of T_b. Figure 6.3(b) shows the near single-cycle pulse close to the interface at $x \approx 0$ (solid line, plotted against the left vertical axis). Plotted against the right vertical axis in the same plot is the molecular orientation $\langle \cos\theta \rangle$ at $x \approx 0$. Rotational wave packet revivals are readily observed as recurring orientations at every $\tau = kT_b$. It is obvious that orientation is achieved in the linear interaction regime since the polarization is directly proportional to $\langle \cos\theta \rangle$. The angular distribution is, however, perturbed very little from the isotropic distribution as $\langle \cos\theta \rangle$ is small. We find $\langle \cos\theta \rangle_{\max} < 0.015$, indicating very weak molecular orientation.

To expose the pulse evolution in greater detail, we compare in Fig. 6.4 the computer solution with the analytic solution in Eq. (6.50) after the pulse has propagated an optical distance $\alpha x = 3$. The solid line in Fig. 6.4(a) shows the computer solution for the electric

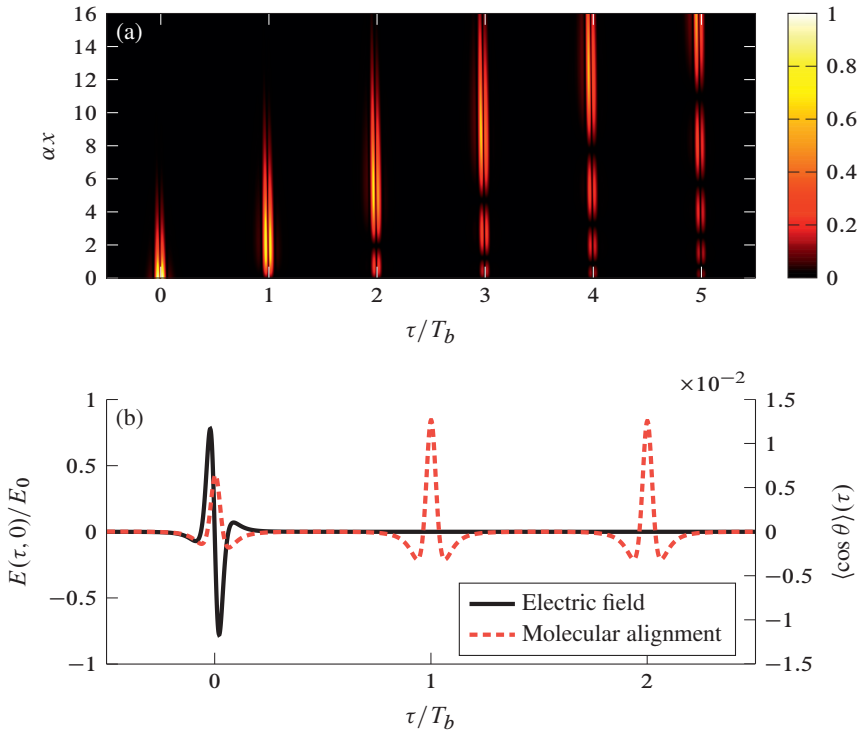

FIG. 6.3: (a) Propagation of the Poisson test pulse in Eq. (6.60) for the first 4 quantum beat periods and for $x \in [0, 16\alpha^{-1}]$. The horizontal axis is the time τ in units of T_b, the vertical axis is the penetration depth x in units of α^{-1}, and the color coding shows the magnitude of the electric field in units of $E_0 = 5 \times 10^6$ V/m. (b) Temporal evolution of the pulse (solid) in units of E_0 and molecular orientation $\langle\cos\theta\rangle(\tau)$ (dashed line, plotted against the second vertical axis) close to the interface $x = 0$ for the first two quantum beat periods.

field, and revivals occur at each rephasing period $\tau = kT_b$. The amplitudes of the impulses in the computer solution are in excellent agreement with the predictions of the analytic impulse solution (Fig. 6.4(a), dashed line) and leaves no doubt about the reliability of our computer simulations. Correspondingly, Fig. 6.4(b) shows the temporal evolution of the orientation $\langle\cos\theta\rangle$ for the computer solution. We find that the orientation is one order of magnitude smaller than at the entrance facet [recall Fig. 6.3(b)], which is understandably due to strong spectral absorption at the various resonance frequencies close to the interface. An important propagation-induced phase reversal of the orientation is also observed. The phase difference between the first orientation revival at $\alpha x = 0$ and $\alpha x = 3$ is precisely π.

In the coherent regime the polarization and the electric field are, at times, antiparal-

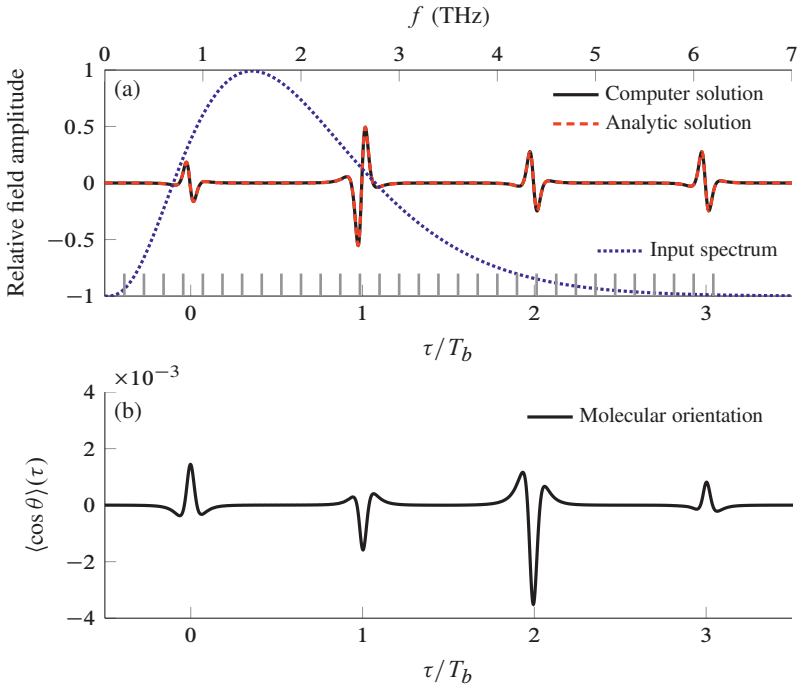

FIG. 6.4: (a) Comparison between the analytic solution in Eq. (6.50) (dotted line) and a computer solution (solid line) using the Poisson input pulse with peak amplitude $E_0 = 5 \times 10^6$ V/m. The data are taken a propagating distance $\alpha x = 3$ into the medium. The pulse spectrum (dotted line) is plotted in arbitrary units against the top horizontal axis. The vertical bars near the baseline indicate the spectral location of the various resonance lines. (b) The temporal evolution of the orientation $\langle \cos\theta \rangle(\tau)$ at $\alpha x = 3$.

lel. Careful examination of Fig. 6.3(b) shows that at the trailing edge of the input pulse $\langle \cos\theta \rangle < 0$ and $E > 0$. To emphasize this point, consider the polarization P after the resummation:

$$\partial_\tau P(\tau, x) = \alpha \epsilon_0 c \left[E(\tau, x) + 2 \sum_{k=1}^{\infty} E(\tau - k T_b, x) \right], \tag{6.62}$$

which shows that the polarization does not in general follow the instantaneous electric field. Close to the interface $x = 0$ and for times $\tau < T_b/2$ the polarization is excited quasi-statically by the pulse,

$$P(\tau, 0) \approx \alpha \epsilon_0 c \int_{-\infty}^{\tau} E(\tau', 0) d\tau'. \tag{6.63}$$

Close to the leading edge of the driving pulse in Fig. 6.3(b) where the field is negative, $\langle\cos\theta\rangle$ is negative and the molecules are parallel with the electric field. The rotors remain parallel until the electric field switches direction and the molecules become oriented opposite to the external field. In comparison to molecular alignment using static electric fields, this result is counterintuitive and warrants an explanation. It suffices to consider a classical dielectric response $P(\omega) = \chi(\omega)E(\omega)$ where $\chi(\omega) = \chi^*(-\omega)$. For an isolated quantum Lorentz resonance

$$\chi(\omega) = \chi_0 \left(\frac{1}{\omega_0 - \omega} + \frac{1}{\omega_0 + \omega} \right), \tag{6.64}$$

$P(\tau)$ evaluates to $P(\tau) = \chi_0 \int_{-\infty}^{\tau} \sin[\omega_0(\tau-\tau')]E(\tau')d\tau'$ and the medium responds only at the resonance frequency ω_0. When $E(\omega)$ overlaps with ω_0 and has a spectral bandwidth exceeding the absorption linewidth by orders of magnitude the pulse may reverse polarity faster than the medium can follow. This manifests as anti-parallel electric and polarization field vectors, opening up the possibility of a radiation reaction that transfer energy back to the pulse. The effect has been known for a long time, and is the primary mechanism for the optical transparency of the linear 0π pulse in the zero damping limit, first predicted by Crisp [30] and later observed by Varoquaux [175] and Rothenberg [103]. In essence, Eq. (6.50) is the multi-level superposition of linear 0π pulses when the absorption coefficients associated with each rotor transition are equal. The quantum beats at time delays that are multiple integers of T_b are manifestations of coherent beating between these pulses.

The two panels in Fig. 6.5 show the probability density for the linear simulation close to the interface at $x \approx 0$. The color-coding in the top panel shows $\sigma(\tau, x \approx 0; \theta)$ for times $\tau \in [-T_b/2, 4.5T_b]$, and reading the plot from left to right, the probability distribution of the molecular axes over the polar angle θ may be read at each time τ by following the color-coding vertically along the θ-axis. At the isochronic line $\tau = -T_b/2$ the probability density is constant $= 1/(4\pi)$ over θ, and the molecular axis of the rotor molecules are distributed isotropically over the unit sphere. Moving horizontally towards $\tau \sim 0$ the probability density on the northern hemisphere is slightly higher than at the southern, indicating that the rotor molecules are lining up with the first carrier lobe of the external THz field. Note that the molecules do not favor up/down; the accumulation of molecules oriented along $+z$ is due to the quasi-static orientation the leading pulse edge $E > 0$ imparts on the molecules [recall Eq. (6.63)]. Moving from $\tau \sim 0$ and towards longer times, the molecules dephase in the absence of the external field and, the alignment diminishes and $\sigma(\tau, x \approx 0; \theta)$ moves towards its isotropic value of $1/(4\pi)$ at $\tau = T_b/2$. When $\tau \rightarrow T_b$ the first wave-packet revival is observed as an increased probability density at $\theta = 0$ and a decreased density at $\theta = \pi$. This process repeats itself for longer times resulting in the re-emergence of an oriented ensemble at times that are integer multiples of T_b. Note

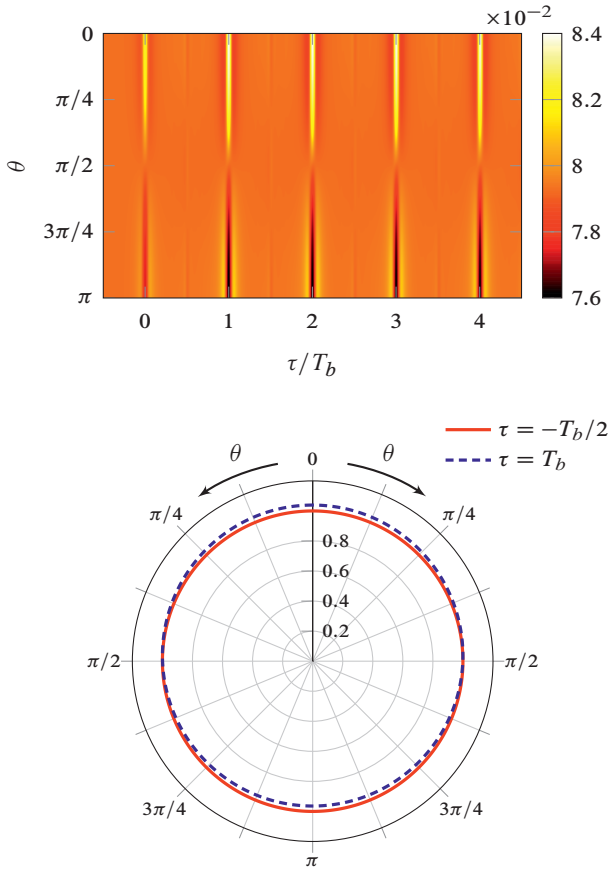

FIG. 6.5: Computer solution showing molecular probability density at $x = 0$ in the linear propagation regime. Top panel: The color-coded data indicate the value of $\sigma(\tau, x = 0; \theta)$ at various times and polar angles. The time τ reads from left to right along the horizontal axis, and the polar angle θ from top (north pole) to bottom (south pole) along the vertical axis. Bottom panel: Cross-section of the probability density through the polar plane for two different times $\tau = -T_b/2$ (solid line) and $\tau = T_b$ (dashed line). The distance from the origin indicates the value of σ in each case (the labels on the vertical axis indicate the distance from the origin in units of 4π).

that at half integer revival times $\tau = (k + 1/2)T_b$ then $\langle \cos\theta \rangle = 0$ but $\langle \cos^2\theta \rangle_c \neq 0$. For the above simulation data, we have $\langle \cos^2\theta \rangle \approx 1/3$ and $\langle \cos^2\theta \rangle_c \sim 10^{-4}$ such that the molecules are weakly aligned, but not oriented, at half quantum beat periods.

Although the molecules re-orient at each integer quantum beat period the probability density of the rotor molecules is only slightly perturbed. The bottom panel in Fig. 6.5 shows a cross-section of $\sigma(\tau, x \approx 0; \theta, \varphi)$ through the molecular polar plane for two different times $\tau = -T_b/2$ (solid line) and $\tau = T_b$ (dashed line). The lines are plotted

for the entire polar cross-section, with the understanding that $\sigma(\tau, 0; \theta)$ is symmetric with respect to the transformation $\theta \to 2\pi - \theta$. The radial distance from the origin of the plot out to the two curves indicate the value of σ in each case. We have verified that probability is conserved in our simulations to a precision better than 10^{-5}. For $\tau = -T_b/2$ the initial condition for ρ show that molecular axes are distributed evenly over the unit sphere. At the first revival $\tau = T_b$, we find that the distribution is only slightly pushed into the northern hemisphere, demonstrating that the molecular orientation is not particularly strong.

The case of thermal equilibrium

For a medium in thermal equilibrium the initial state of the medium prior to the action of the pulse is

$$\rho(\tau \to -\infty, x) = \frac{1}{Z} \exp\left(-\frac{\hat{H}_0}{k_B T}\right), \tag{6.65}$$

where $Z = \mathrm{Tr}\left(\exp\left[-\hat{H}_0/(k_B T)\right]\right)$ is the partition function. The line intensities associated with each $j \to j+1$ transition are evidently different in the thermal and idealized cases. We now consider linear propagation of the input pulse discussed above, but this time through a thermal medium at $T_a = 300$ K. Analogous to Fig. 6.3(a), Fig. 6.6 shows the spatiotemporal evolution of $|E(\tau, x)|$ over the first 4 quantum beat periods for the entire propagation length. We find that close to the entrance interface $x = 0$, wave packet revivals are observed at each time $\tau = kT_b$. As the driving pulse and impulses propagate further into the material the roles of the Bessel factors in Eq. (6.45) become noticeable and the pulse revivals disperse. Evidently, close to the interface the Bessel functions in Eq. (6.45) may be expanded in a power series and the integrand resonates at $\tau' = 2\pi/(\Delta\omega)$ since all $\beta_j x$ are comparatively small with respect to the first abscissa of the Bessel function such that $J_1\left(2\sqrt{\beta_j \tau' x}\right) > 0$. Following Eq. (6.41), dispersion is negligible for $\beta_j x \ll 1$. After a sufficient propagation length the Bessel factors with the largest β_j change from positive to negative and phases of the polarization components associated with the strongest absorption lines are reversed relative to the weakest lines. Thus, when the driving pulse has penetrated a sufficient distance into the material the various rigid rotor transitions are, due to different level degeneracies and populations, excited with different amplitudes and phases. As the first impulse is emitted close to the interface it effectively enters into a medium predominantly prepared by excitation of the strongest resonance lines. This impulse, which is approximately a copy of the initial pulse, reinforces this response for the later impulses, leading to additional dephasing among the various polarization components. In the spectral domain, an equivalent description is that spectral holes are only found at the strongest absorption lines during propagation, and the pulse develops a more complicated temporal structure. Note that molecular dephasing of

rotational wave packets due to centrifugal distortion of the molecule for higher rotational modes has been discussed by Harde et al. [156]. Here, we show that for an extended medium dephasing also occurs as a result of propagation.

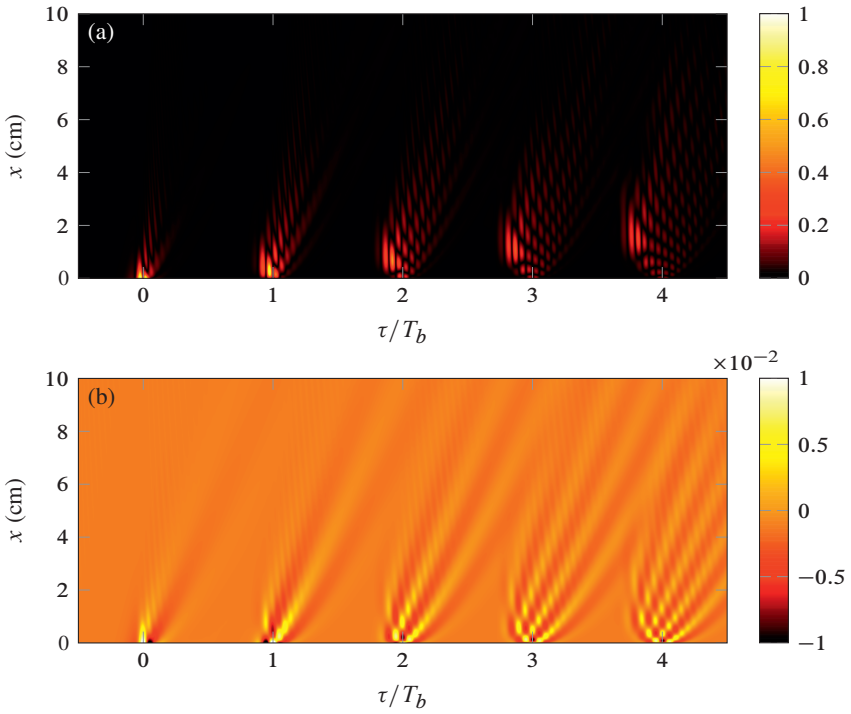

FIG. 6.6: Computer solution for linear single-cycle THz excitation of a molecular ensemble initially in thermal equilibrium. The color coding in the top and bottom panels show the field magnitude $|E(\tau, x)|$ and the molecular orientation $\langle \cos\theta \rangle(\tau, x)$, respectively.

The color-coding in bottom panel of Fig. 6.6 shows the value of $\langle \cos\theta \rangle(\tau, x)$ for the entire simulation region and demonstrates the dispersion of the induced molecular orientation. Like the pulse, recurring periods of orientation are found at times $\tau = kT_b$ close to the interface $x \approx 0$. With increasing x, propagation-induced dispersion of the rotational wavepacket becomes noticeable and is observed as temporal broadening of the orientational revivals in Fig. 6.6(b).

6.5 Nonlinear propagation

Having reviewed the single-cycle linear pulse propagation regime we now turn our attention to nonlinear propagation. Below, we consider three cases (I) $E_0 = 10^8$ V/m, (II)

$E_0 = 10^9$ V/m, and (III) $E_0 = 5 \times 10^9$ V/m. In each case, the medium is initially prepared as a thermal ensemble following Eq. (6.65) with $T_a = 300$ K. Practical limitations prevent us from propagating pulses with even higher amplitudes since the time scale $\tau_c \sim 1$ fs implies a very fine temporal resolution. Propagation over the first few quantum beat periods then require hundreds of thousands of temporal grid points, and we have been unwilling to spend much computation time on such scenarios.

6.5.1 Weakly nonlinear regime (I)

First, we investigate the propagation of a pulse with amplitude $E_0 = 10^8$ V/m and intensity $I_0 = \epsilon_0 c|E_0|^2/2 = 1.32$ GW/cm^2, which places the interaction of this pulse with the material in the nonlinear regime. Figure 6.7 shows the rotational population distribution

$$w_j(\tau, x) = \sum_m \rho_{jm,jm}(\tau, x) \tag{6.66}$$

close to the interface $x \approx 0$ for $\tau \in [-T_b/5, T_b/5]$. The time window is sufficiently large to contain the entire input pulse. On the $(\tau = -T_b/5, w_j)$-plane the height of the bars show the initial Maxwell-Boltzmann distribution prior to the pulse interaction. Initially, the rotational level with the highest population is $j = 5$. We find that as the pulse enters into the medium a significant amount of population is moved to higher rotational states, evidenced by a shift in the peak of w_j from $j = 5$ at $\tau = -T_b/5$ to $j = 10$ at $\tau = T_b/5$ in Fig. 6.7.

To expose the molecular state in more detail during and after the pulse interaction close to the interface at $x \approx 0$, the panels in Fig. 6.8 show the probability density for various times $\tau/T_b \in [-0.10, 1.05]$. For comparison, the dashed line in the panel with $\tau/T_b = -0.05$ shows the uniform probability density of $1/(4\pi)$. The panel with $\tau = T_b$ in Fig. 6.8 may be contrasted with Fig. 6.5(b) which showed a corresponding plot for linear interaction. Like in Fig. 6.5, the angle θ runs from the top of each panel and clockwise and counter-clockwise around the panel [the simulation data is symmetrized such that $\sigma(\tau, x; \theta) = \sigma(\tau, x; 2\pi - \theta)$]. The temporal evolution of σ is observed by reading the panels from left to right, top to bottom. We find from the panel with $\tau/T_b = -0.05$ that as the pulse first enters into the material the leading edge of the pulse pushes σ slightly down into the southern hemisphere, which is shown by a small shift in the center of mass of σ towards the south pole. The panel immediately to the right shows the probability density at $\tau = 0$ and demonstrates that the rotor molecules are oriented primarily along $+z$ ($\theta < \pi/2$). The reason for the sudden change in orientation, from slightly towards $-z$ to sharply along $+z$, is due to the double leading lobe structure on the input pulse seen in Fig. 6.3(b). While the first, small negative carrier lobe will tend to orient the molecules along $\theta = \pi$, the first main carrier lobe, which is much stronger, acts

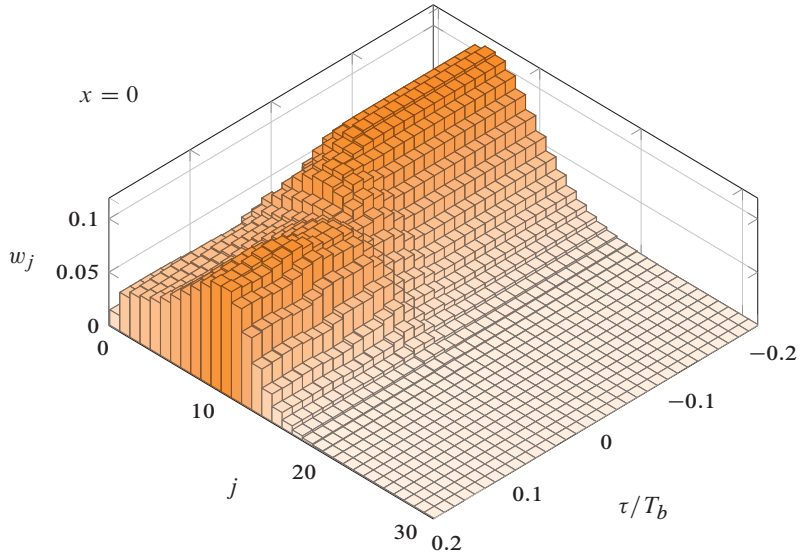

FIG. 6.7: (I) Rotational state population distribution $w_j = \sum_{m=-j}^{j} \rho_{jm,jm}$ close to the interface $x = 0$. The time window, measured in units of T_b, is sufficiently large to contain the entire driving pulse.

to orient the rotor molecules along $\theta = 0$. When the field phase reverses at $\tau = 0$ and the subsequent large negative carrier lobe also enters into the medium, the orientation is reversed and at time $\tau/T_b = 0.05T_b$ the molecules are found in the southern hemisphere. The subsequent panels show the near field-free dephasing and rephasing of the molecules. From $\tau/T_b = 0.05$ to $\tau/T_b = 0.5$ the rotor molecules gradually move away from an oriented ensemble to an aligned one. At the quarter revival period $\tau/T_b = 0.25$ both the orientation $\langle\cos\theta\rangle$ and the alignment $\langle\cos^2\theta\rangle_c$ are approximately zero. At $\tau/T_b = 0.5$, $\langle\cos\theta\rangle \approx 0$ but $\langle\cos^2\theta\rangle \sim 0.1$ (see Fig. 6.9), showing that at half-integer quantum revival periods the molecules are aligned, but not oriented. The up/down symmetry of the medium at the entrance interface is preserved at half-revival times, but not at integer revivals times. Moving on from $\tau/T_b = 0.50$ and towards $\tau/T_b = 1$ the molecules gradually re-orient. We observe this for $\tau/T_b = 0.95$ where $\rho(\tau, x \approx 0; \theta)$ peaks at $\theta = \pi$, indicating that the bulk of the rotor molecules are oriented along $-z$. A short time later, at $\tau/T_b = 1$, the ensemble is oriented along $+z$. Note that the orientation at $\tau/T_b = -0.05$ is weak compared to the orientation at $\tau/T_b = 0.95$, while the orientation at $\tau/T_b = 0$ and $\tau/T_b = 1$ are quantitatively comparable. The reason is that the evolution up to $\tau/T_b = -0.05$ occurs in the linear regime while the large degree of orientation along $-z$ at $\tau/T_b = 0.95$ is due to nonlinear interaction with the entire pulse.

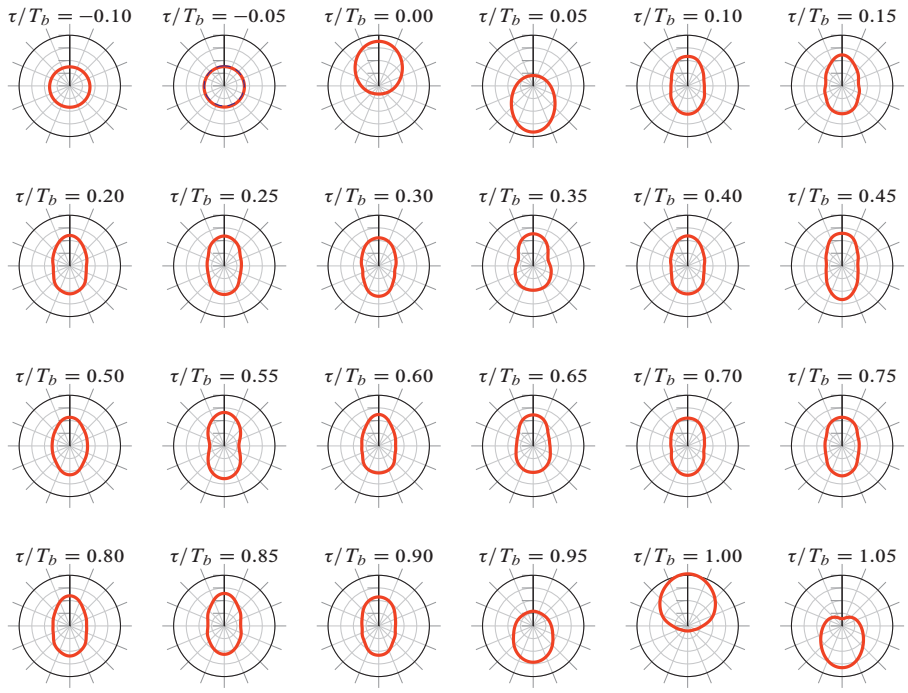

FIG. 6.8: (I) Rigid rotor molecular probability density. Each panel shows the probability density at $x = 0$ for various times τ under nonlinear interaction with a single-cycle THz pulse ($I_0 \approx 1.3$ GW/cm^2). The time between each panel is $0.05T_b$.

The distorted probability densities shown in Fig. 6.9 quantitatively show the angular distribution of the molecules. To examine this data in greater detail and estimate the order of the wavepacket, Fig. 6.10(a) shows the corresponding evolution of the first few Legendre moments $\langle P_\kappa(\cos\theta)\rangle$ over the same time period. Note that $\langle P_\kappa(\cos\theta)\rangle$ are experimental observables, measurable by photoelectron imaging [176] or nonlinear optical spectroscopy. The maximum value of the first two moments $\langle P_1(\cos\theta)\rangle$ and $\langle P_2(\cos\theta)$ as a function of time in Fig. 6.9 is 0.4 and 0.15 respectively, showing that the molecules are both oriented and aligned. For the higher moments $\langle P_3(\cos\theta)\rangle$ and $\langle P_4(\cos\theta)\rangle$ the peak values are more modest and equal to 0.05 and 0.025 in the two cases. Moments of higher order are smaller, with $\langle P_5(\cos\theta)\rangle_{\max} \sim 0.01$ and $\langle P_6(\cos\theta)\rangle_{\max} \sim 0.006$. Recalling that coherences up to order $|j' - j| \leq \kappa$ are present in the expression for the Legendre moments of order κ, we find that the excitation of the interface occurs as a multi-photon process up to approximately fourth order.

The propagation of the THz field, the orientation $\langle\cos\theta\rangle$ and the alignment $\langle\cos^2\theta\rangle$

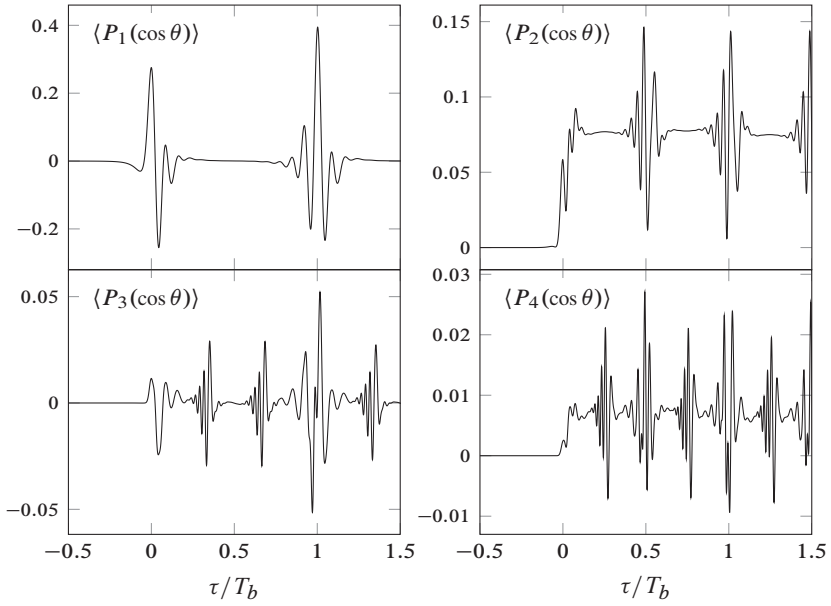

FIG. 6.9: (I) First few Legendre moments $\langle P_\kappa(\cos\theta)\rangle$ close to the interface $x \approx 0$.

(measured as $\langle P_2 \cos\theta\rangle$) are shown in panels (b) and (c) in Fig. 6.10. Overall, we find that the pulse propagates nonlinearly only over the first few millimeters in the sample and then falls back into the linear propagation regime. Figure 6.10 shows that strong molecular orientations are achieved in this spatial region of the material. We find that $\langle\cos\theta\rangle_{\max} \approx 0.4$ whereas $\langle\cos\theta\rangle_{\max} \sim 10^{-2}$ was found in the linear regime. Figure 6.10(c) shows the corresponding evolution for the alignment. We recall that $\langle P_2(\cos\theta)\rangle = 0$ for thermal molecules with isotropically distributed Zeeman levels and that $\langle P_2(\cos\theta)\rangle$ contains the Raman coherences $\rho_{jm,j\pm2m}$ and population terms. Close to the baseline in Fig. 6.10(c) the slow increase in $\langle P_2(\cos\theta)\rangle$ is due to population transfer to higher angular momentum orbitals. The population distribution is asymmetric in the Zeeman levels since $\langle\cos^2\theta\rangle_{\mathrm{p,max}} \sim 0.38$ whereas a value of $1/3$ is obtained for an isotropic population distribution. The rapid oscillations seen at half and integer revival times are due to the excitation of rotational Raman coherences, indicating the presence of two-photon resonant transitions of the type $j \to j+1 \to j+2$. From the color-coding in Fig. 6.10(c) we note, importantly, that $\langle P_2(\cos\theta)\rangle \sim 0$ for $x > 1$ cm, showing that the pulse falls back into the linear interaction regime after only a short propagation distance.

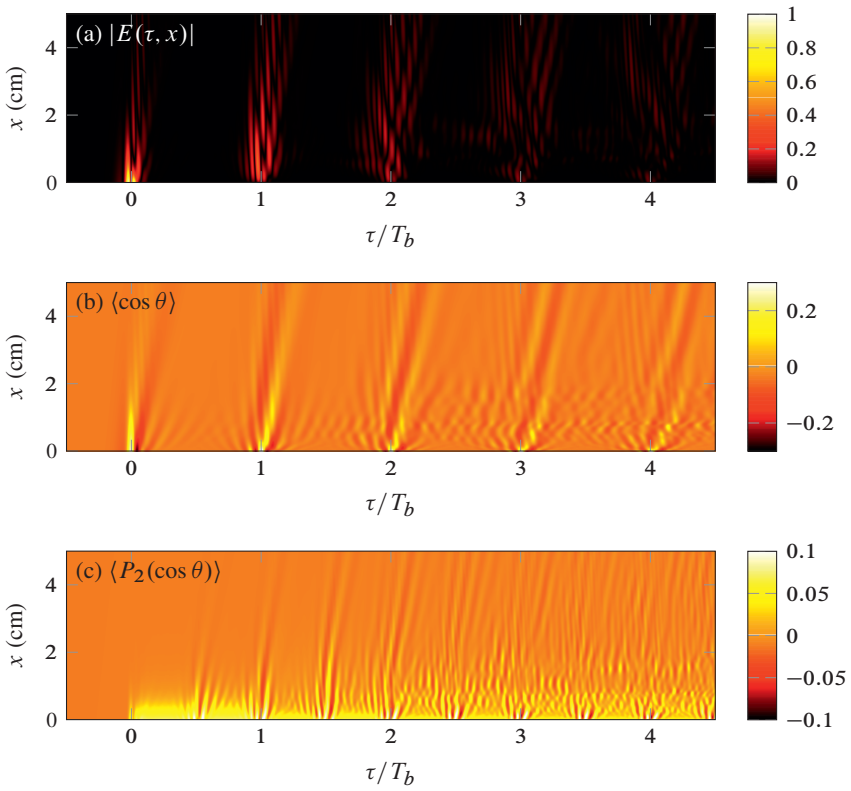

FIG. 6.10: (I) Top panel: Spatiotemporal evolution of the electric field $|E(\tau, x)|$ in units of E_0. Middle panel: The molecular alignment $\langle \cos\theta \rangle$. Bottom panel: The second order Legendre moment $\langle P_2(\cos\theta)$.

6.5.2 Intermediate nonlinear regime (II)

Below, we consider the propagation of a pulse with amplitude $E_0 = 10^9$ V/m. The temporal resolution for this simulation is $\triangle\tau \approx 1.25$ fs, about 4 times higher than the critical sampling period $\triangle\tau_{\text{crit}} = \pi/\omega_J \approx 5$ fs required by the Nyquist-Shannon sampling theorem. Relative to the input pulse then $\triangle\tau f_{\max} = 6.25 \times 10^{-3}$ where $f_{\max} = 5$ GHz is the upper cut-off frequency [see Fig. 6.4].

The excitation of the interface with this pulse results in a complex excitation of the medium. The color-coding in the various panels in Fig. 6.11 show the probability density close to $x \approx 0$ for two chosen time windows, one large enough to contain the first few quantum beat periods and one showing the temporal evolution around the first revival in greater detail. The solid line running horizontally across each panel indicates the value of $\langle \cos\theta \rangle$, and is plotted in arbitrary units against the baseline $\theta = \pi/2$. In the top panel

the maximum probability density near the leading edge of the input pulse at $\tau \lesssim 0$ is as high as 0.9 indicating that the molecules are strongly oriented along $+z$ by the leading positive lobe of the input pulse. At the same isochronic line σ is approximately zero for $\theta \geq \pi/2$ and all the molecules are therefore found in the northern hemisphere. Note that the polarization is close to saturation since $\langle \cos\theta \rangle \leq 1$. A short time later $\tau \gtrsim 0$ when the negative carrier lobe penetrates into the material, the orientation of the molecules is reverted so that they are pointing along $\theta = \pi$ with approximately 0 observation probability along $\theta = 0$. The subsequent dephasing of the rotor molecules shows that the probability density is higher at the poles $\theta = 0$ and $\theta = \pi$ than at the equator $\theta = \pi/2$. In the almost field-free dephasing of the material we therefore find that the molecules are aligned, but not oriented. Recalling that the expression for σ contains all coherences $\rho_{jm,j'm}$, the rapid temporal oscillations and the accumulation of probability on the poles for $\tau \gtrsim 0$ shows that the molecules are excited into a coherent superposition of higher-order angular momentum states. The higher order coherences oscillate rapidly in the abscence of an external field and they are responsible for the complicated temporal structure of σ seen in Fig. 6.11(a). The most likely explanation for the weak oscillations of the orientation $\langle \cos\theta \rangle$ observed in Fig. 6.11(a) at periods between the pulse revivals is that the molecules are excited into a wave-packet consisting of fewer jm-modes where complete destructive interference of the macroscopic polarization does not occur.

The color-coding in the bottom panel in Fig. 6.11 shows the probability density in greater detail during the first pulse revival around $\tau/T_b = 1$ close to $x \approx 0$. During the evolution up to the first recurrence the wave packet oscillates rapidly like an aligned ensemble where accumulation of probability is observed at the poles $\theta = 0$ and $\theta = \pi$. Revival is first observed as a peak in σ at $\tau \gtrsim T_b$ at $\theta = 0$ in Fig. 6.11(b) and occurs slightly after $\tau = T_b$. The revival process occurs in multiple stages where the probability density oscillates between the north and south poles, indicating a rapidly changing polarization spanning several cycles.

The panels in Fig. 6.12 show the propagation of the field $E(\tau, z)$ and the orientation $\langle \cos\theta \rangle$ for this pulse. Compared with linear propagation [see Fig. 6.6(a)], we find that the driving pulse propagates a substantially longer distance into the medium than in both the linear and weakly nonlinear (I) regimes. During this propagation the driving pulse is continuously reshaped by the medium and travels with a slightly reduced group velocity. Comparing Fig. 6.12(b) with Fig. 6.10(b) we find that the orientation $\langle \cos\theta \rangle$ is maintained to a considerable during the propagation of the driving pulse and orientations as high as 0.9 are observed. The later impulses for both medium and field are somewhat blurred and have no clear spatiotemporal structure.

To expose the reshaping of the pulse in even greater detail, the panels in Fig. 6.13 shows the electric field (solid line) for various propagation lengths and for a time window

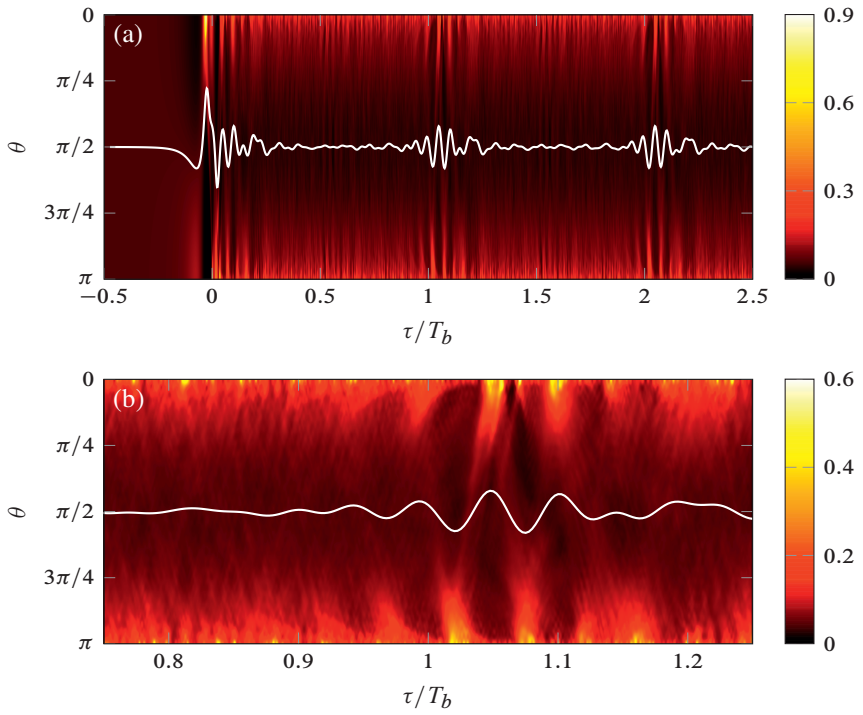

FIG. 6.11: (II) Top panel: Probability density σ as a function of time τ and polar angle θ at the first spatial grid point $x \approx 0$. Bottom panel: Inset of (a) for $\tau \in [0.75T_b, 1.25T_b]$.

large enough to contain the driving field and the first revival pulse. For comparison, the dashed line in each panel shows the propagation of the same pulse in the linear regime. Reading the panels in Fig. 6.12 left to right, top to bottom, only the leading carrier lobe of the driving pulse is seen to be significantly affected over the first few centimeters of propagation. A pulse revival appears at $\tau \approx T_b$ after a few millimeters of propagation, but that the relative amplitude of this impulse is small compared to the predictions of linear theory. Comparing the panels $z \approx 0$ and $z = 6$ mm shows that the while the leading carrier lobe is attenuated, the trailing lobe is slightly amplified during propagation. At $z \approx 0$ and $z = 6$ mm the maximum amplitudes of the trailing carrier lobe are $|E(\tau, x \approx 0)| \approx 0.78$ and $|E(\tau, x = 6\,\text{mm})| \approx 0.85$ respectively. Further propagation shows that as the leading lobe is continuously attenuated the trailing lobe remains relatively constant and a secondary positive field region appears on the driving pulse tail. Correspondingly, the pulse becomes increasingly temporally symmetric during propagation (see Fig. 6.13 for $z = 6$ mm). This type of reshaping occurs over the first few centimeters of the medium before the pulse falls back into the linear propagation regime for $x \gtrsim 5$ cm. The bottom

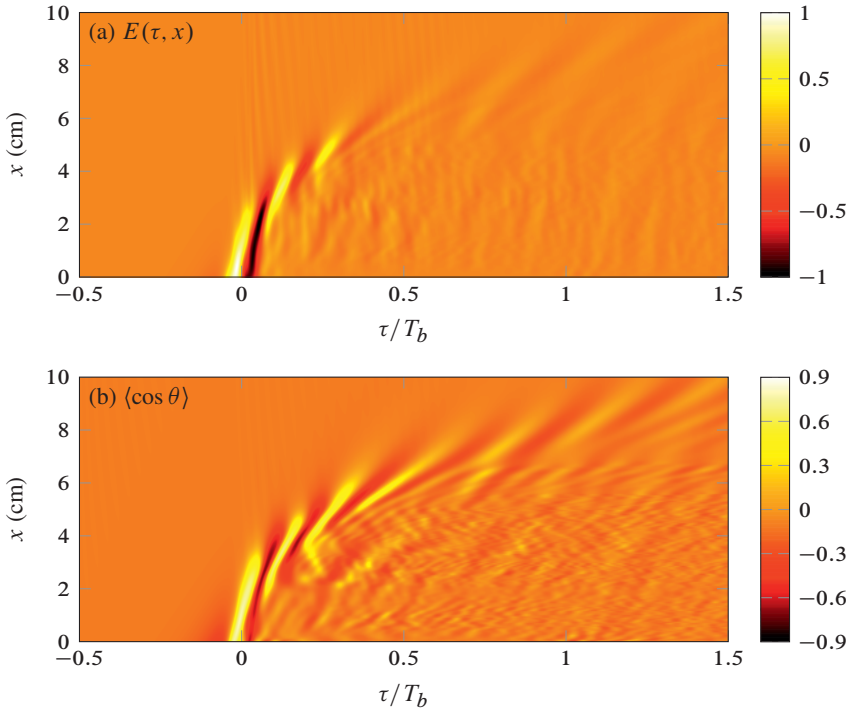

FIG. 6.12: (II) Propagation of a single-cycle THz pulse with amplitude $E_0 = 5 \times 10^8$ V/m. Top panel: The instantaneous electric field value $E(\tau, x)$ (in units of E_0). Dark and bright areas show regions with $E(\tau, x) < 0$ and $E(\tau, x) > 0$ respectively. Bottom panel: Same as (a), but for $\langle\cos\theta\rangle$.

row in Fig. 6.13 shows the electric field profile at the far end of the medium. At $x = 9$ cm only a high-frequency weak-amplitude precursor field remains for both the driving pulse and the revivals in both the linear and nonlinear propagation regimes. Except for an overall dispersive group delay, these fields, which are most likely the high-frequency content of the input pulse, change very little with propagation distance.

6.5.3 Strongly nonlinear regime (III)

Finally, we consider the propagation of a pulse with amplitude $E_0 = 5 \times 10^9$ V/m. Such pulses are presently available from linear accelerators where field amplitudes as high as 4.4 GV/m have been reported recently [177, 178]. The various panels in Fig. 6.14 show the full field $E(\tau, x)$ (dashed lines) and the internal energy $\langle\hat{H}_0\rangle$ (solid lines, in units of $\hbar\omega_J$) for various propagation lengths. We recall that when $\frac{\partial}{\partial\tau}\langle\hat{H}_0\rangle > 0$ energy is transferred from the field to the medium and vice versa if $\frac{\partial}{\partial\tau}\langle\hat{H}_0\rangle < 0$. We find that

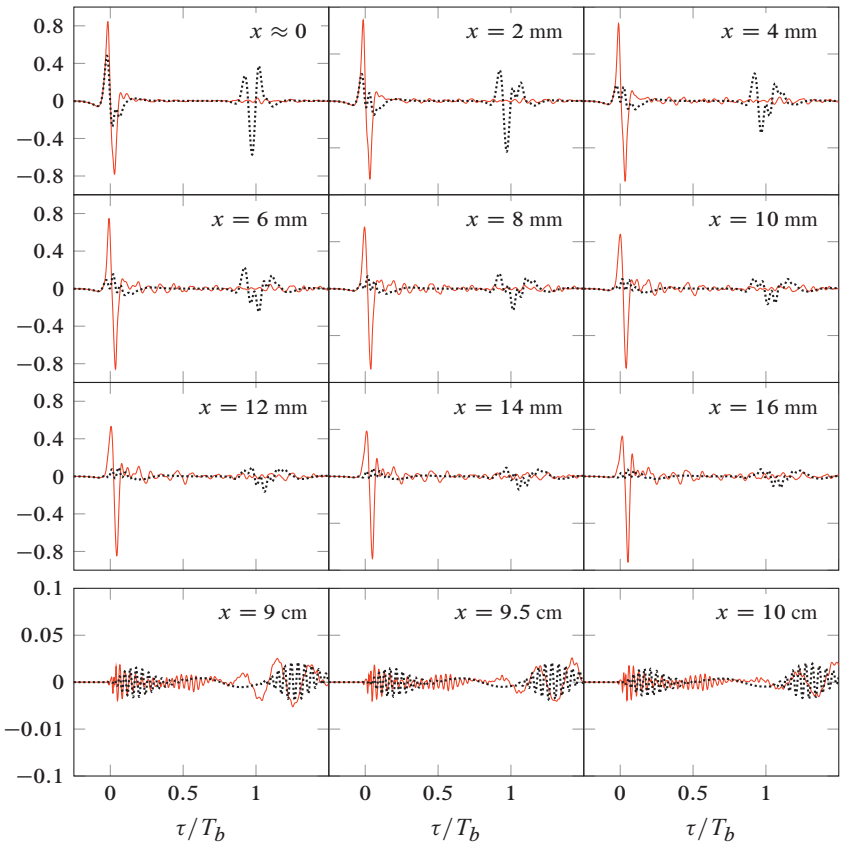

FIG. 6.13: (II) Temporal electric field profiles at various propagation lengths z (indicated in each panel). Solid and dashed lines show input pulses with amplitudes $E_0 = 10^9$ V/m (solid) and $E_0 = 5 \times 10^6$ V/m (dashed).

as the pulse enters into the medium the internal energy $\langle \hat{H}_0 \rangle$ of the medium is saturated, evidenced by the appearance of several temporal peaks in $\langle \hat{H}_0 \rangle$. The leading bump in $\langle \hat{H}_0 \rangle$ observed in Figs. 6.14(a) and (b) are almost certainly due to coherent return occuring when $\frac{\partial}{\partial \tau} E$ switches from negative to positive on the small, negative, leading edge (i.e. the part before the first carrier lobe). The larger, more rapid, oscillations occur for the medium as a whole, and are analogous to the Rabi oscillations [179] that take place when a longer pulse coherently saturates a single atomic line transition. We term these oscillations as collective Rabi oscillations because they relate to the inversion of the medium as a whole rather than to a single transition. As the pulse propagates deeper into the material the leading edge of the field is absorbed by the material. When the next slice of pulse enters

into the medium, which is fully saturated, some of the energy lost by the leading edge is returned to the pulse. This process then repeats itself several times under each carrier cycle and the pulse develops self-oscillations superimposed on top of the two carrier lobes, as seen in Fig. 6.14(b). Further propagation reinforces this behaviour; the leading edge of the pulse is absorbed and parts of the first main carrier lobe are enhanced, leading to temporal steepening of the leading pulse edge, as seen in panels (b)-(d) in Fig. 6.14.

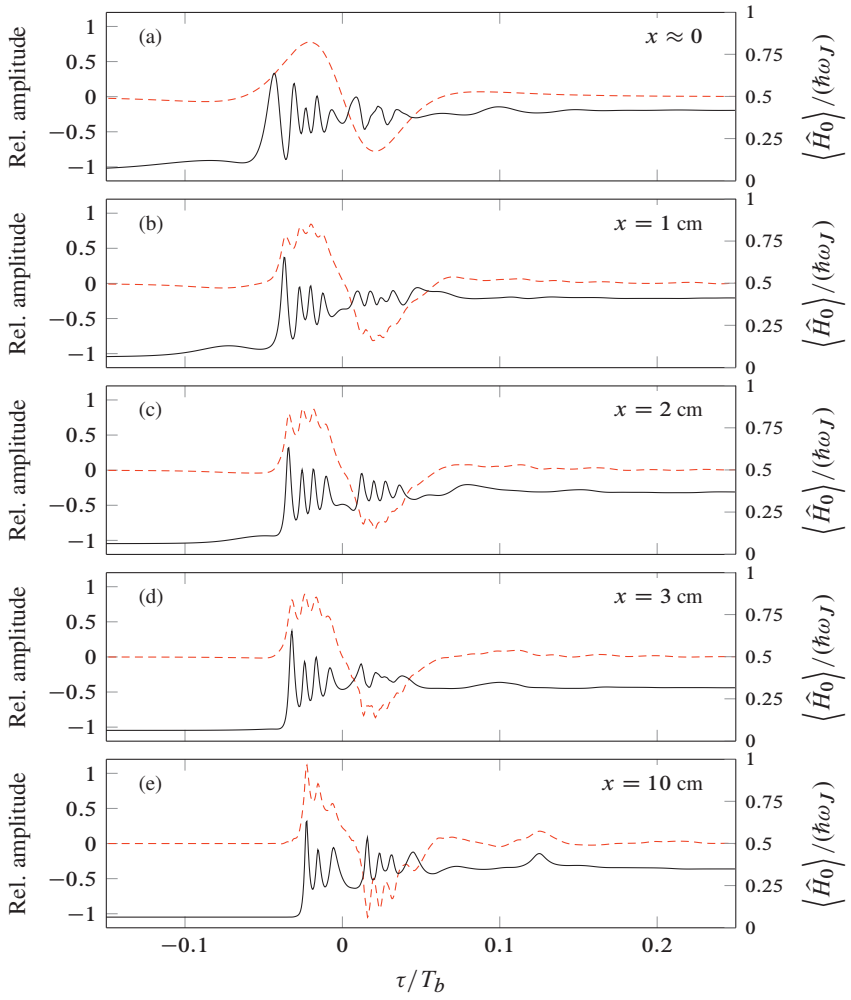

FIG. 6.14: (III) Electric field profiles (dashed line, plotted against the left vertical axis) and internal molecular energy $\langle H_0 \rangle$ (solid line, plotted against the right vertical axis) in units of $\hbar\omega_J$ for various propagation lengths x (indicated in each panel).

Note that coherent energy return was observed also in the linear regime, then due to a rapid phase reversal of the electric field. Here, the process is distinctly different as energy is returned under each carrier lobe without reversing the sign of E. From Eq. (6.16) it is verified that

$$\frac{\partial U}{\partial \tau} = E \frac{\partial P}{\partial \tau}, \tag{6.67}$$

so that when $\frac{\partial U}{\partial \tau}$ goes from positive to negative under a single carrier lobe then the polarization driving term goes from absorbing to amplifying. This mechanism is reminiscent of self-induced transparency (SIT), which is a process where the leading edge of a sufficiently strong pulse is absorbed as it drives an atomic line transition to inversion, resulting in a polarization "flip" (i.e. phase reversal) that allows the trailing edge to coherently regain the energy lost by the front. Transparency of the driving pulse is not observed here since the final energy state is $\langle \hat{H}_0 \rangle(\tau) > \langle \hat{H}_0 \rangle(\tau \to -\infty)$. However, the driving pulse energy is conserved to a considerable extent when compared to the linear regime. The energy of the field shown in the bottom panel in Fig. 6.14 is approximately 80% of the input pulse energy, whereas in the linear regime less than 2% of the energy of the driving pulse (defined as the fluence delivered in time $T_b/2$) was preserved after exiting the medium. The preservation of the fluence is due to saturation effects. Scaling Eq. (6.16) by E_0^2 leads to

$$\frac{\partial}{\partial x}\mathcal{E}^2(\tau, x) = -\frac{1}{\epsilon_0 c E_0^2}\frac{\partial U}{\partial \tau}, \tag{6.68}$$

where $\mathcal{E} = E/E_0$ is a quantity of order unity. In the linear regime $U \propto E_0^2$ [see Eq. (6.34)] and the effective absorption length scale is constant in the linear regime. When U is saturated further increases in E_0 will result in coherent energy return rather than increased absorption. The pulse behavior in Fig. 6.14 is therefore understood to be the results of *coherent bleaching* of the medium.

To further investigate the behavior of the medium under this pulse excitation, Fig. 6.15 shows the orientation $\langle \cos\theta \rangle$ as a function of time for the same propagation lengths. In Fig. 6.15(a) we find that when the pulse enters into the material the small leading edge of the pulse acts to orient the molecules into the southern hemisphere before the first main carrier lobe enters. When this part of the pulse enters into the medium the molecules become oriented along the field direction into the northern hemisphere. Coherent saturation under this part of the pulse leads to an oscillatory motion of the rotor molecules around $\langle \cos\theta \rangle \sim 0.25$, and the wiggling motion continues until the secondary carrier lobe brings the molecules back to the equator. Further propagation into the material shows that leading molecular alignment is diminished as the leading part of the pulse is absorbed. A particularly striking feature - entirely quantum in nature - is observed in Fig. 6.15(c). Here, one observes that the molecules that are initially oriented along $-z$ by the leading pulse edge are not brought up into the nortern hemisphere as the main carrier lobe - now

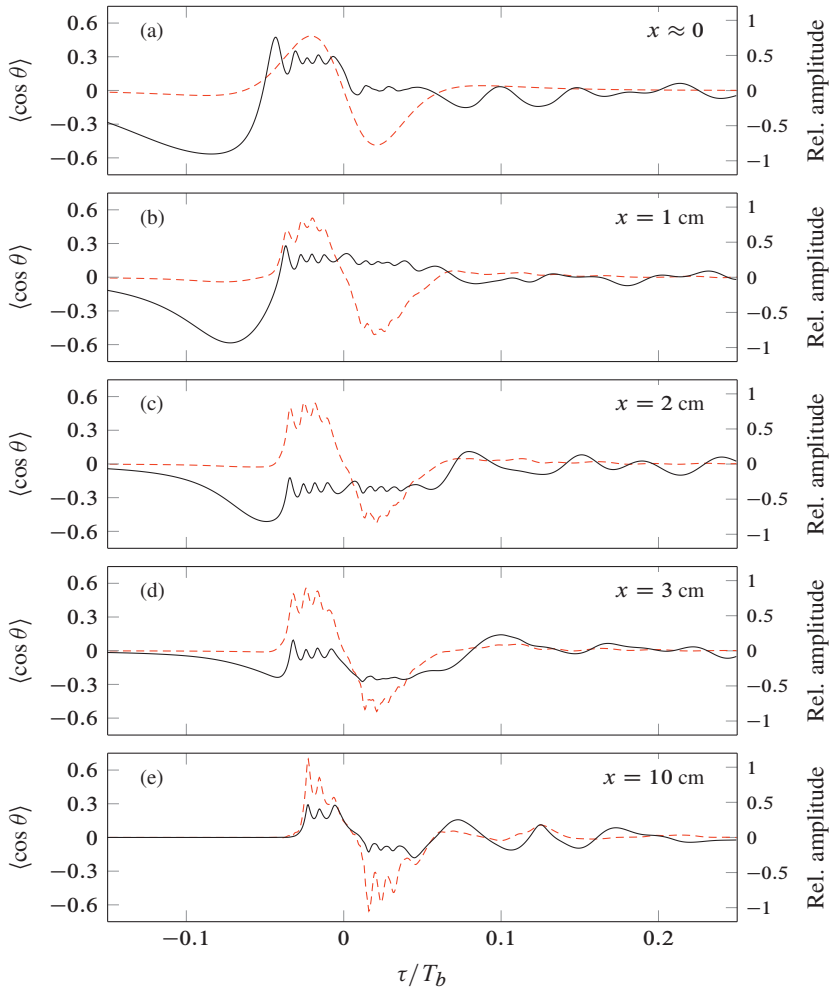

FIG. 6.15: (III) Molecular orientation $\langle \cos\theta \rangle$ (solid line, plotted against the left vertical axis) at various propagation lengths x. Plotted against the right vertical axis are the electric field curves from Fig. 6.14.

encoded by self-oscillations - enters into the medium. This behavior is not expected in a classical model. Loosely speaking, the process occurs due to rapid coherent saturation of the medium close to the pulse edge. By the time the rotor molecules have ramped up enough inertia to orient themselves along $+z$, an inversion of the various level populations has occured which essentially switches the sign of the polarization driving terms, causing the dipoles to wiggle in the southern hemisphere - antiparallel to the electric field direction. Note that this feature is not linked to the pulse shape itself, but to the inver-

sion that the pulse drives. For example, if one considers the pulse shape in Fig. 6.15(c), but with weaker amplitude such that Rabi flopping does not occur, the polarization and electric field become parallel under the first main lobe. With increasing propagation the antiparallel orientations are deteriorating - which is understandably due to absorption of the leading pulse edge that initially caused orientation in the southern hemisphere prior to the arrival of the main carrier lobes.

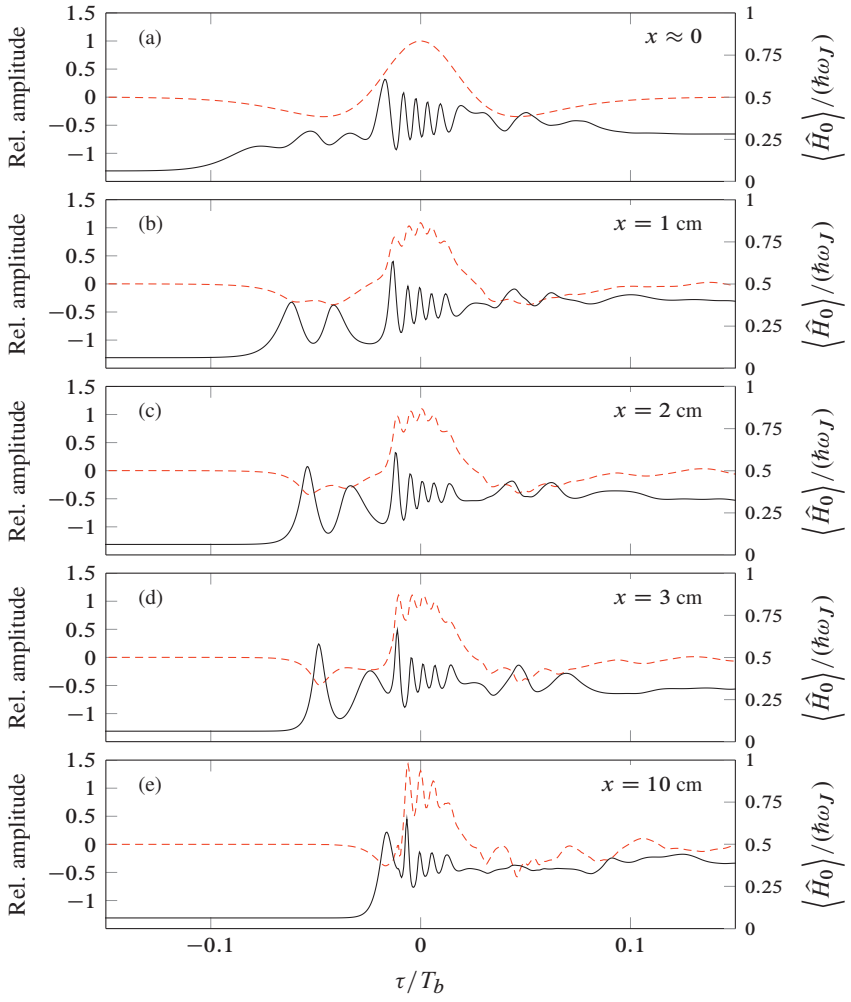

FIG. 6.16: Molecular aligment and electric field reshaping of an initially symmetric THz pulse. The input field amplitude is $E_0 = 5 \times 10^9$ V/m.

6.6 The symmetric single-cycle pulse

The excitation of the medium generally depends on the full electric field rather than the envelope profile. Finally, we investigate propagation of the symmetric single-cycle Poisson pulse defined by $\varphi = 0$, but consider otherwise the same parameters as in subsection 6.5.3. The symmetric Poisson pulse has a temporal structure consisting of a small negative carrier lobe followed by a stronger positive carrier lobe which is trailed by another negative carrier lobe. Recalling Eq. (6.61), the energies of the symmetric and anti-symmetric Poisson pulses are equal. Analogous to Figs. 6.14 and 6.15, Fig. 6.16 shows the reshaping of the symmetric single-cycle pulse. On a qualitative level, the same propagation characteristics appear. That is, as the pulse enters into the material it drives a sequence of collective Rabi flops under the main carrier lobe. Under each flop, energy is coherently returned to the pulse, which develops self-oscillations with increasing penetration depth. However, detailed examination of the simulation data exposes a few key differences between the anti-symmetric and symmetric pulses. Notably, the absence of a secondary carrier lobe for the symmetric pulse results in a pulse which resembles a single self-steepened main carrier lobe encoded by self-oscillations. Importantly, examination of the pulse spectrum shows that the DC Fourier coefficient remains small during propagation.

Notably, one might speculate if the self-oscillations eventually lead to pulse splitting analogous to the SIT type. The results of this conjecture are negative, as further propagation of the pulses shown in Figs. 6.14 and 6.16 gradually results in deterioration of the driving pulse.

6.7 Verification of Bloch model

To verify that our Bloch model is physically realistic at the parameters presently studied we investigate the propagated spectrum. Figure 6.17 depicts the logarithmic power spectrum $|E(\omega, z)|^2$ for the same propagation lengths shown in Fig. 6.14. The spectra are calculated from data obtain on the interval $[-T_b/2, 1.5T_b]$ tapered by a Blackman-Harris window. We find that as the pulse steepens several sidelobes appear on the high-frequency side of its spectrum, which is understandably due to the self-oscillations encoded onto the carrier lobes. Importantly, the spectral sidelobes appear up to ~ 40 THz, which is not high enough to overlap resonantly with the fundamental vibrational transition which occurs for frequencies $f_{\text{vibr}} > f_J - f_0 \approx 100$ THz. In short, the self-steepening process is therefore predicted to occur without smoothing effects from the fundamental vibrational transition.

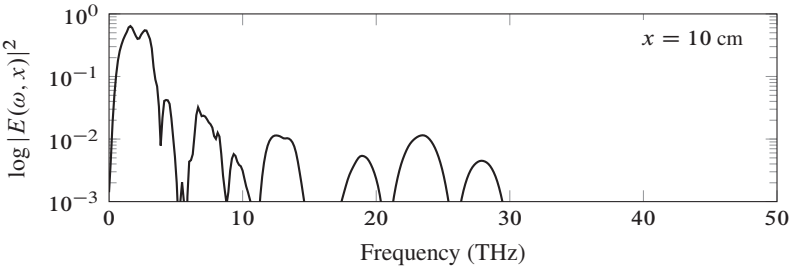

FIG. 6.17: (III) Logarithmic spectral energy density at the output facet $x = 10$ cm. The initial field strength is $E_0 = 5 \times 10^9$ V/m and the data are normalized against the spectral peak of the input pulse.

6.8 Chapter summary

We have introduced a multi-level RMB model for the propagation of single-cycle THz pulses in rigid-rotor molecular media. In the linear propagation regime the equations of motion are solved analytically and the solutions are then analogous to the linear 0π-pulse, generalized to the single-cycle multi-level regime. In the time-domain, this solution appears as dispersive temporal beats at each integer quantum beat period. In the idealized case where the line strengths of each transition are equal, propagation induced color dispersion cancels and the pulse revivals are then temporal copies of the input pulse, with a possible phase of π. Formal decomposition of the density operator into azimuthal rotation modes led to a mathematical formulation where only the polar part of the molecular rotation is solved for, leaving the azimuthal rotations as frozen variables incorporated into the initial conditions. The formulation led to very efficient numerical evaluation of the governing equations, allowing investigation of complicated Bloch systems. Numerical investigations of symmetric and asymmetric single-cycle pulse propagation in the nonlinear regime showed that coherent bleaching effects lead to increased transmission of the driving pulse. Induced collective Rabi oscillations resulted in coherent energy return to the pulse, which manifests as self-steepening and self-oscillations in the time domain.

Chapter 7

Conclusions

In this thesis we have explored various theoretical semi-classical models for coherent propagation of multi-, few-, and single-cycle pulses through atomic and molecular media. The purpose of this work was to detail numerical methods applicable to these regimes. Our central findings, summarized below, pertain to the development of such algorithms and their applications to certain nonlinear wave propagation problems.

We investigate the possibility of exciting linear and nonlinear optical precursors in the nano- and pico-second pulse regimes. Numerical calculations of pulses tuned to an alkali metal D-line show that such precursors may originate in room temperature or hot alkali metal vapors by application of pulses with initial pulse areas larger than π, and durations comparable to the inhomogeneous lifetime. Comparatively large temporal separation (up to tens of nanoseconds) between the main pulse, which is a 2π hyperbolic secant soliton, and the precursor is achieved when the input area is close to π. These results offer a comparatively straightforward way of measuring optical precursors. Injection of pulses with durations significantly longer than the inhomogeneous lifetime does not result in an optical precursor because the atoms then rapidly absorb the precursor-part of the spectrum before temporal separation between the two pulses occurs. In physical terms the formation of the precursor is due to the onset of an optical soliton; the low group velocity offered by low-energy self-induced transparency pulses is then responsible for temporal separation. The precursor, which is essentially a 0π pulse spectrally located around the absorption wings of the transition line, may individually interact linearly or nonlinearly with the material by exciting the Doppler detuned atoms.

A general-purpose numerical method for the inhomogeneously broadened, multi-level Maxwell-Bloch equations was presented. The composite method used an operator splitting method for the optical Bloch equations and a pseudospectral method for Maxwell's equations. Overall, the method is applicable to bi-directional propagation of pulses of

arbitrary duration, polarization, and amplitude along all three spatial coordinates, but is in practice limited to comparatively short propagation lengths due to numerical requirements on the spatial resolution. We applied this method to nonlinear pulse propagation in dense, inhomogeneously broadened two-level media under the plane wave assumption. It is shown that when the forward wave approximation of Maxwell's equations is not valid, self-induced transparency solitons lose energy with increasing propagation distance due to co-excitation of a backward mode, even when the injected pulse duration fits in safely between the two transverse lifetimes. The presence of the backward mode interferes with the main pulse's ability to coherently return the medium back to the ground state and leads to temporal elongation of the forward pulse. Ultimately, the pulse will temporally broaden to timescales comparable to the decoherence time of the medium and is then rapidly absorbed. An important practical question, not resolved in this thesis, concerns the experimental differentiation of backscattering effects and decoherence. Investigation of energy transmission alone is shown to be insufficient in isolating backpropagation as a singular loss mechanism; decoherence essentially leads to the same energy-distance decay curve. A possible experimental signature of the onset of backpropagation may nonetheless lie in the reflected signal as the combination of reflection and coherent saturation of the interface may lead to a significant Doppler shift of the reflected laser pulse. Isolation of backpropagation as a singular loss mechanism will most likely be an experimental hurdle; it is implied that the input pulse duration must be considerably shorter than the homogeneous lifetime of the medium. The most promising candidates for observing backpropagation are inhomogeneously broadened high-pressure alkali metal vapors, or condensed phase media with comparatively large transition dipole moments and short Beer lengths, such as liquid dyes or doped semiconductors.

Drawing on a generalized paraxial wave equation derived by disregarding the possibility of backward wave propagation we report on a computational method for long distance propagation of pulses of arbitrary duration through atomic or molecular media. The method mitigates the shortcomings of direct Maxwell methods and is based on an operator splitting method for the optical Bloch equations and standard differential methods for the propagation equation. Furthermore, circumvention of the rotating wave approximation allows application of off-resonant pulses. We apply this method to the propagation of 20 fs pulses tuned 23.5 THz above the D-lines in an atomic sodium vapor. The computational results show that conical emission, a phenomenon historically surrounded by much controversy, occurs after sufficient on-axis gain through self-focusing. The gain leads to spatiotemporal pulse breakup of a type reminiscent of the temporal splitting of self-induced transparency pulses. Our computational results are supported by additional numerical calculations of the inhomogeneously broadened paraxial SIT equations for ^{87}Rb. The computational results agree with the overall experimental features of conical emission

and resolve some of the underlying questions surrounding the phenomenon. On the other hand, the use of numerical calculations inhibit quantitative prediction of some of the experimentally observed universal features of cone emission, and future analytical analysis is definitely called for. The exception is the conical emisson angle versus density dependence $\theta_{\mathrm{CE}} \propto \sqrt{\mathcal{N}}$, which follows from scaling of the equations of motion. We suggest that conical emission occurs as a result of asymmetric Rabi sideband generation inside a quasi self-trapped light filament; the emission of the red sideband occurs as a result of a transverse dependence of spatiotemporal pulse breakup. Experimentally, measurements of the on-axis and conical temporal pulse profiles, either through the use of streak camera or single-shot frequency resolved optical grating (FROG) techniques, are likely to return a definite answer to our numerical predictions. Another possible theoretical and experimental complication, not investigated here, is fragmentation of the initial laser beam into individual filaments by self-focusing of smaller diameter regions. A numerical analysis of such scenarios is nevertheless feasible with current computational facilities and represents a natural extension of the work presented in this thesis. Since the numerical solution is expected to vary rapidly in the region surrounding the initial beam profile, a viable numerical approach would be to employ a Cartesian grid with numerical clustering in this region. With exclusion of inhomogeneous broadening, such numerical calculations are slightly more expensive than those presented in this thesis.

Finally, we considered the plane wave, nonlinear propagation of linearly polarized single-cycle terahertz pulses through linear, polar molecules. While previous analytical and computational results account only for a handful of possible energy eigenstates, we demonstrate that the use of a generalized propagation equation in conjunction with a reduction of the Bloch system through decomposition into various Zeeman levels offer a strong computational advantage. The decomposition isolates the rotational motion to the polar plane, leaving azimuthal rotations as frozen variables incorporated into the initial conditions, leading to a dramatic reduction in the underlying complexity of the nonlinear equations of motion. At the parameters we consider the Bloch system is reduced from over 10^6 to roughly $25,000$ unknown entries in the density operator. The evolution equations are solved analytically in the linear propagation regime. The results show that the initial pulse, which has an octave-spanning spectral width, excites a broad molecular rotational wave packet with a definite revival time. At each rotational wave packet revival the medium emits some of the radiation that was initially locked into the molecules by the driving pulse. In an idealized case where intensity of the various rotational lines are equal, we show that temporal dispersion of the emitted impulses cancels such that the rotational wave packet emits a temporal copy of the driving pulse. For media initially in thermal equilibrium propagation-induced dispersion of each impulse leads to temporal broadening and mixing of the various wave packet emissions. In both the idealized and thermal cases

the solutions bear a close resemblance to the linear 0π pulse. Furthermore, we supplement these analytical calculations by computer solutions in the nonlinear propagation regime. It is shown that as the input intensity increases the rotational wave packet revivals are suppressed to a considerably degree. Coherent bleaching effects initiated by collective Rabi flopping furthermore lead to self-steepening and self-modulation of the single-cycle input pulse. Compared to the linear propagation regime, one finds that the fidelity of the pulse is preserved to a considerable extent during propagation. For sufficiently strong pulses coherent bleaching effects lead to increased transmission of the driving pulse.

Bibliography

[1] D. Grischkowsky, "Self-focusing of light by potassium vapor," Phys. Rev. Lett. **24**, 866 (1970), URL http://link.aps.org/doi/10.1103/PhysRevLett.24.866.

[2] D. Grischkowsky and J. A. Armstrong, "Self-defocusing of light by adiabatic following in rubidium vapor," Phys. Rev. A **6**, 1566 (1972), URL http://link.aps.org/doi/10.1103/PhysRevA.6.1566.

[3] S. E. Harris, "Electromagnetically induced transparency," Physics Today **50**, 36 (1997), URL http://link.aip.org/link/?PTO/50/36/1.

[4] M. Fleischhauer and M. D. Lukin, "Dark-state polaritons in electromagnetically induced transparency," Phys. Rev. Lett. **84**, 5094 (2000), URL http://link.aps.org/doi/10.1103/PhysRevLett.84.5094.

[5] L. V. Hau, S. E. Harris, Z. Dutton, and C. H. Behroozi, "Light speed reduction to 17 metres per second in an ultracold atomic," Nature **397**, 594 (1999), ISSN 0028-0836, URL http://dx.doi.org/10.1038/17561.

[6] S. Chu and S. Wong, "Linear pulse propagation in an absorbing medium," Phys. Rev. Lett. **48**, 738 (1982), URL http://link.aps.org/doi/10.1103/PhysRevLett.48.738.

[7] L. J. Wang, A. Kuzmich, and A. Dogariu, "Gain-assisted superluminal light propagation," Nature **406**, 277 (2000), ISSN 0028-0836, URL http://dx.doi.org/10.1038/35018520.

[8] S. L. McCall and E. L. Hahn, "Self-induced transparency by pulsed coherent light," Phys. Rev. Lett. **18**, 908 (1967), URL http://link.aps.org/doi/10.1103/PhysRevLett.18.908.

[9] S. L. McCall and E. L. Hahn, "Self-induced transparency," Phys. Rev. **183**, 457 (1969), URL http://link.aps.org/doi/10.1103/PhysRev.183.457.

[10] C. K. N. Patel and R. E. Slusher, "Self-induced transparency in gases," Phys. Rev. Lett. **19**, 1019 (1967), URL http://link.aps.org/doi/10.1103/PhysRevLett.19.1019.

[11] H. M. Gibbs and R. E. Slusher, "Peak amplification and breakup of a coherent optical pulse in a simple atomic absorber," Phys. Rev. Lett. **24**, 638 (1970), URL http://link.aps.org/doi/10.1103/PhysRevLett.24.638.

[12] R. E. Slusher and H. M. Gibbs, "Self-induced transparency in atomic rubidium," Phys. Rev. A **5**, 1634 (1972), URL http://link.aps.org/doi/10.1103/PhysRevA.5.1634.

[13] H. M. Gibbs and R. E. Slusher, "Sharp-line self-induced transparency," Phys. Rev. A **6**, 2326 (1972), URL http://link.aps.org/doi/10.1103/PhysRevA.6.2326.

[14] J. J. Bannister, H. J. Baker, T. A. King, and W. G. McNaught, "Self-induced transparency and resonant self-focusing in atomic iodine vapor," Phys. Rev. Lett. **44**, 1062 (1980), URL http://link.aps.org/doi/10.1103/PhysRevLett.44.1062.

[15] M. C. Hoffmann and J. A. Fülöp, "Intense ultrashort terahertz pulses: generation and applications," Journal of Physics D: Applied Physics **44**, 083001 (2011), URL http://stacks.iop.org/0022-3727/44/i=8/a=083001.

[16] S. Fleischer, Y. Zhou, R. W. Field, and K. A. Nelson, "Molecular orientation and alignment by intense single-cycle thz pulses," Phys. Rev. Lett. **107**, 163603 (2011), URL http://link.aps.org/doi/10.1103/PhysRevLett.107.163603.

[17] T. K. Cheng, L. H. Acioli, J. Vidal, H. J. Zeiger, G. Dresselhaus, M. S. Dresselhaus, and E. P. Ippen, "Modulation of a semicondutor to semimetal transition at 7 thz via coherent lattice vibrations," Applied Physics Letters **62**, 1901 (1993), URL http://scitation.aip.org/content/aip/journal/apl/62/16/10.1063/1.109537.

[18] T. Kampfrath, A. Sell, G. Klatt, A. Pashkin, S. Mahrlein, T. Dekorsy, M. Wolf, M. Fiebig, A. Leitenstorfer, and R. Huber, "Coherent terahertz control of antiferromagnetic spin waves," Nat Photon **5**, 31 (2011), ISSN 1749-4885, URL http://dx.doi.org/10.1038/nphoton.2010.259.

[19] X. Yin, B. Ng, and D. Abbott, *Terahertz Imaging for Biomedical Applications: Pattern Recognition and Tomographic Reconstruction* (Springer, 2012), ISBN 9781461418207, URL http://books.google.no/books?id=rl6-zhzybxQC.

[20] K. F. Lee, D. M. Villeneuve, P. B. Corkum, and E. A. Shapiro, "Phase control of rotational wave packets and quantum information," Phys. Rev. Lett. **93**, 233601 (2004), URL http://link.aps.org/doi/10.1103/PhysRevLett.93.233601.

[21] C. Wu, G. Zeng, Y. Gao, N. Xu, L.-Y. Peng, H. Jiang, and Q. Gong, "Controlling molecular rotational population by wave-packet interference," The Journal of Chemical Physics **130**, 231102 (2009), URL http://scitation.aip.org/content/aip/journal/jcp/130/23/10.1063/1.3155063.

[22] H. Stapelfeldt and T. Seideman, "*Colloquium* : Aligning molecules with strong laser pulses," Rev. Mod. Phys. **75**, 543 (2003), URL http://link.aps.org/doi/10.1103/RevModPhys.75.543.

[23] R. Velotta, N. Hay, M. B. Mason, M. Castillejo, and J. P. Marangos, "High-order harmonic generation in aligned molecules," Phys. Rev. Lett. **87**, 183901 (2001), URL http://link.aps.org/doi/10.1103/PhysRevLett.87.183901.

[24] T. Brabec and F. Krausz, "Intense few-cycle laser fields: Frontiers of nonlinear optics," Rev. Mod. Phys. **72**, 545 (2000), URL http://link.aps.org/doi/10.1103/RevModPhys.72.545.

[25] D. H. Auston, K. P. Cheung, and P. R. Smith, "Picosecond photoconducting hertzian dipoles," Applied Physics Letters **45**, 284 (1984), URL http://link.aip.org/link/?APL/45/284/1.

[26] G. Krauss, S. Lohss, T. Hanke, A. Sell, S. Eggert, R. Huber, and A. Leitenstorfer, "Synthesis of a single cycle of light with compact erbium-doped fibre technology," Nat Photon **4**, 33 (2010), URL http://dx.doi.org/10.1038/nphoton.2009.258.

[27] M. Y. Shverdin, D. R. Walker, D. D. Yavuz, G. Y. Yin, and S. E. Harris, "Generation of a single-cycle optical pulse," Phys. Rev. Lett. **94**, 033904 (2005), URL http://link.aps.org/doi/10.1103/PhysRevLett.94.033904.

[28] A. Taflove and S. C. Hagness, *Computational electrodynamics: The finite difference time-domain method* (Artech House, Inc., 2005), 3rd ed.

[29] R. W. Ziolkowski, J. M. Arnold, and D. M. Gogny, "Ultrafast pulse interactions with two-level atoms," Phys. Rev. A **52**, 3082 (1995), URL http://link.aps.org/doi/10.1103/PhysRevA.52.3082.

[30] M. D. Crisp, "Propagation of small-area pulses of coherent light through a resonant medium," Phys. Rev. A **1**, 1604 (1970), URL http://link.aps.org/doi/10.1103/PhysRevA.1.1604.

[31] D. A. Steck, Tech. Rep., Oregon Center for Optics and Department of Physics, University of Oregon (2010), URL http://steck.us/alkalidata/rubidium87numbers.pdf.

[32] B. D. Paul, M. L. Dowell, A. Gallagher, and J. Cooper, "Observation of conical emission from a single self-trapped beam," Phys. Rev. A **59**, 4784 (1999), URL http://link.aps.org/doi/10.1103/PhysRevA.59.4784.

[33] T. Brabec and F. Krausz, "Nonlinear optical pulse propagation in the single-cycle regime," Phys. Rev. Lett. **78**, 3282 (1997), URL http://link.aps.org/doi/10.1103/PhysRevLett.78.3282.

[34] F. Bloch and A. Siegert, "Magnetic resonance for nonrotating fields," Phys. Rev. **57**, 522 (1940), URL http://link.aps.org/doi/10.1103/PhysRev.57.522.

[35] C. S. Chang and P. Stehle, "Quantum-electrodynamical theory of atoms interacting with high-intensity radiation fields," Phys. Rev. A **4**, 641 (1971), URL http://link.aps.org/doi/10.1103/PhysRevA.4.641.

[36] J. J. Maki, M. S. Malcuit, J. E. Sipe, and R. W. Boyd, "Linear and nonlinear optical measurements of the lorentz local field," Phys. Rev. Lett. **67**, 972 (1991), URL http://link.aps.org/doi/10.1103/PhysRevLett.67.972.

[37] M. J. Ablowitz, D. J. Kaup, A. C. Newell, and H. Segur, "Method for solving the sine-gordon equation," Phys. Rev. Lett. **30**, 1262 (1973), URL http://link.aps.org/doi/10.1103/PhysRevLett.30.1262.

[38] M. J. Ablowitz, D. J. Kaup, A. C. Newell, and H. Segur, "Nonlinear-evolution equations of physical significance," Phys. Rev. Lett. **31**, 125 (1973), URL http://link.aps.org/doi/10.1103/PhysRevLett.31.125.

[39] M. J. Ablowitz, D. J. Kaup, and A. C. Newell, "Coherent pulse propagation, a dispersive, irreversible phenomenon," Journal of Mathematical Physics **15**, 1852 (1974), URL http://link.aip.org/link/?JMP/15/1852/1.

[40] G. L. Lamb, "Coherent-optical-pulse propagation as an inverse problem," Phys. Rev. A **9**, 422 (1974), URL http://link.aps.org/doi/10.1103/PhysRevA.9.422.

[41] G. L. Lamb, "Analytical descriptions of ultrashort optical pulse propagation in a resonant medium," Rev. Mod. Phys. **43**, 99 (1971), URL http://link.aps.org/doi/10.1103/RevModPhys.43.99.

[42] L. Allen and J. H. Eberly, *Optical Resonance and Two-Level Atoms* (Dover, New York, 1987), 2nd ed.

[43] D. J. Kaup, "Coherent pulse propagation: A comparison of the complete solution with the mccall-hahn theory and others," Phys. Rev. A **16**, 704 (1977), URL http://link.aps.org/doi/10.1103/PhysRevA.16.704.

[44] J. C. Diels and E. L. Hahn, "Phase-modulation propagation effects in ruby," Phys. Rev. A **10**, 2501 (1974), URL http://link.aps.org/doi/10.1103/PhysRevA.10.2501.

[45] J. C. Diels and E. L. Hahn, "Carrier-frequency distance dependence of a pulse propagating in a two-level system," Phys. Rev. A **8**, 1084 (1973), URL http://link.aps.org/doi/10.1103/PhysRevA.8.1084.

[46] G. L. Lamb, "Phase variation in coherent-optical-pulse propagation," Phys. Rev. Lett. **31**, 196 (1973), URL http://link.aps.org/doi/10.1103/PhysRevLett.31.196.

[47] P. J. Caudrey, J. D. Gibbon, J. C. Eilbeck, and R. K. Bullough, "Exact multisoliton solutions of the self-induced transparency and sine-gordon equations," Phys. Rev. Lett. **30**, 237 (1973), URL http://link.aps.org/doi/10.1103/PhysRevLett.30.237.

[48] M. D. Crisp, "Distortionless propagation of light through an optical medium," Phys. Rev. Lett. **22**, 820 (1969), URL http://link.aps.org/doi/10.1103/PhysRevLett.22.820.

[49] J. H. Eberly, "Optical pulse and pulse-train propagation in a resonant medium," Phys. Rev. Lett. **22**, 760 (1969), URL http://link.aps.org/doi/10.1103/PhysRevLett.22.760.

[50] J. L. Shultz and G. J. Salamo, "Experimental observation of the continuous pulse-train soliton solution to the maxwell-bloch equations," Phys. Rev. Lett. **78**, 855 (1997), URL http://link.aps.org/doi/10.1103/PhysRevLett.78.855.

[51] J. C. Eilbeck, J. D. Gibbon, P. J. Caudrey, and R. K. Bullough, "Solitons in nonlinear optics. i. a more accurate description of the 2 pi pulse in self-induced

transparency," Journal of Physics A: Mathematical, Nuclear and General **6**, 1337 (1973), URL http://stacks.iop.org/0301-0015/6/i=9/a=009.

[52] R. K. Bullough, P. J. Caudrey, J. C. Eilbeck, and J. D. Gibbon, "A general theory of self-induced transparency," Optical and Quantum Electronics **6**, 121 (1974), ISSN 0306-8919, 10.1007/BF01421994, URL http://dx.doi.org/10.1007/BF01421994.

[53] R. K. Bullough, P. M. Jack, P. W. Kitchenside, and R. Saunders, "Solitons in laser physics," Physica Scripta **20**, 364 (1979), URL http://iopscience.iop.org/1402-4896/20/3-4/011.

[54] A. I. Maimistov, A. M. Basharov, S. O. Elyutin, and Y. M. Sklyarov, "Present state of self-induced transparency theory," Phys. Rep. **191**, 1 (1990), ISSN 0370-1573.

[55] R. K. Bullough and F. Ahmad, "Exact solutions of the self-induced transparency equations," Phys. Rev. Lett. **27**, 330 (1971), URL http://link.aps.org/doi/10.1103/PhysRevLett.27.330.

[56] M. Lax, W. H. Louisell, and W. B. McKnight, "From maxwell to paraxial wave optics," Phys. Rev. A **11**, 1365 (1975), URL http://link.aps.org/doi/10.1103/PhysRevA.11.1365.

[57] H. Leblond, H. Triki, and D. Mihalache, "Derivation of a generalized double-sine-gordon equation describing ultrashort-soliton propagation in optical media composed of multilevel atoms," Phys. Rev. A **86**, 063825 (2012), URL http://link.aps.org/doi/10.1103/PhysRevA.86.063825.

[58] M. Geissler, G. Tempea, A. Scrinzi, M. Schnürer, F. Krausz, and T. Brabec, "Light propagation in field-ionizing media: Extreme nonlinear optics," Phys. Rev. Lett. **83**, 2930 (1999), URL http://link.aps.org/doi/10.1103/PhysRevLett.83.2930.

[59] M. Kolesik and J. V. Moloney, "Nonlinear optical pulse propagation simulation: From maxwell's to unidirectional equations," Phys. Rev. E **70**, 036604 (2004), URL http://link.aps.org/doi/10.1103/PhysRevE.70.036604.

[60] A. V. Husakou and J. Herrmann, "Supercontinuum generation of higher-order solitons by fission in photonic crystal fibers," Phys. Rev. Lett. **87**, 203901 (2001), URL http://link.aps.org/doi/10.1103/PhysRevLett.87.203901.

[61] M. Kolesik, J. V. Moloney, and M. Mlejnek, "Unidirectional optical pulse propagation equation," Phys. Rev. Lett. **89**, 283902 (2002), URL http://link.aps.org/doi/10.1103/PhysRevLett.89.283902.

[62] P. Kinsler, "Optical pulse propagation with minimal approximations," Phys. Rev. A **81**, 013819 (2010), URL http://link.aps.org/doi/10.1103/PhysRevA.81.013819.

[63] P. L. Kelley, "Self-focusing of optical beams," Phys. Rev. Lett. **15**, 1005 (1965), URL http://link.aps.org/doi/10.1103/PhysRevLett.15.1005.

[64] M. Wu, S. Chen, K. J. Schafer, and M. B. Gaarde, "Ultrafast time-dependent absorption in a macroscopic three-level helium gas," Phys. Rev. A **87**, 013828 (2013), URL http://link.aps.org/doi/10.1103/PhysRevA.87.013828.

[65] J. R. Freeman, J. Maysonnave, S. Khanna, E. H. Linfield, A. G. Davies, S. S. Dhillon, and J. Tignon, "Laser-seeding dynamics with few-cycle pulses: Maxwell-bloch finite-difference time-domain simulations of terahertz quantum cascade lasers," Phys. Rev. A **87**, 063817 (2013), URL http://link.aps.org/doi/10.1103/PhysRevA.87.063817.

[66] P. Kumar and A. K. Sarma, "Gaussian and sinc-shaped few-cycle-pulse-driven ultrafast coherent population transfer in <math><mi>ÎŻ</mi></math>-like atomic systems," Phys. Rev. A **85**, 043417 (2012), URL http://link.aps.org/doi/10.1103/PhysRevA.85.043417.

[67] F. Schlottau, M. Piket-May, and K. Wagner, "Modeling of femtosecond pulse interaction with inhomogeneously broadened media using an iterative predictor corrector fdtd method," Opt. Express **13**, 182 (2005), URL http://www.opticsexpress.org/abstract.cfm?URI=oe-13-1-182.

[68] B. Bidégaray, A. Bourgeade, and D. Reignier, "Introducing physical relaxation terms in bloch equations," Journal of Computational Physics **170**, 603 (2001), ISSN 0021-9991, URL http://www.sciencedirect.com/science/article/pii/S002199910196752X.

[69] C. Besse, B. BidÃľgaray-Fesquet, A. Bourgeade, P. Degond, and O. Saut, "A maxwell-bloch model with discrete symmetries for wave propagation in nonlinear crystals: an application to kdp," ESAIM: Mathematical Modelling and Numerical Analysis **38**, 321 (2004), ISSN 1290-3841, URL http://www.esaim-m2an.org/action/article_S0764583X04000159.

[70] A. Bourgeade and O. Saut, "Numerical methods for the bidimensional maxwellâĂŞbloch equations in nonlinear crystals," Journal of Computational Physics **213**, 823 (2006), ISSN 0021-9991, URL http://www.sciencedirect.com/science/article/pii/S0021999105004183.

[71] Q.-H. Liu, in *Antennas and Propagation Society International Symposium, 1997. IEEE., 1997 Digest* (1997), vol. 1, pp. 122–125 vol.1.

[72] B. Fornberg, *A practical guide to pseudospectral methods*, Cambridge monographs on applied and computational mathematics (Cambridge University Press, Cambridge, 1996), ISBN 0-521-49582-2, URL http://opac.inria.fr/record=b1098317.

[73] M. Frigo and S. G. Johnson, "The design and implementation of FFTW3," Proceedings of the IEEE **93**, 216 (2005), special issue on "Program Generation, Optimization, and Platform Adaptation".

[74] T.-W. Lee and S. C. Hagness, "Pseudospectral time-domain methods for modeling optical wave propagation in second-order nonlinear materials," J. Opt. Soc. Am. B **21**, 330 (2004), URL http://josab.osa.org/abstract.cfm?URI=josab-21-2-330.

[75] J.-P. Berenger, "A perfectly matched layer for the absorption of electromagnetic waves," Journal of Computational Physics **114**, 185 (1994), ISSN 0021-9991, URL http://www.sciencedirect.com/science/article/pii/S0021999184711594.

[76] S. Blanes, F. Casas, J. A. Oteo, and J. Ros, "A pedagogical approach to the magnus expansion," European Journal of Physics **31**, 907 (2010), URL http://stacks.iop.org/0143-0807/31/i=4/a=020.

[77] R. B. Sidje, "Expokit: a software package for computing matrix exponentials," ACM Trans. Math. Softw. **24**, 130 (1998), ISSN 0098-3500, URL http://doi.acm.org/10.1145/285861.285868.

[78] R. Marskar and U. Österberg, "Multilevel maxwell-bloch simulations in inhomogeneously broadened media," Opt. Express **19**, 16784 (2011), URL http://www.opticsexpress.org/abstract.cfm?URI=oe-19-18-16784.

[79] R. Marskar and U. L. Österberg, "Backpropagation and decay of self-induced-transparency pulses," Phys. Rev. A **89**, 023828 (2014), URL http://link.aps.org/doi/10.1103/PhysRevA.89.023828.

[80] W. Forysiak, R. G. Flesch, J. V. Moloney, and E. M. Wright, "Doppler shift of self-reflected optical pulses at an interface: Dynamic nonlinear optical skin effect," Phys. Rev. Lett. **76**, 3695 (1996), URL http://link.aps.org/doi/10.1103/PhysRevLett.76.3695.

[81] A. M. Alhasan, J. Fiutak, and W. Miklaszewski, "The influence of the atomic relaxation on the resonant propagation of short light pulses," Zeitschrift für Physik B Condensed Matter **88**, 349 (1992), ISSN 0722-3277, 10.1007/BF01470924, URL http://dx.doi.org/10.1007/BF01470924.

[82] V. P. Kalosha and J. Herrmann, "Formation of optical subcycle pulses and full maxwell-bloch solitary waves by coherent propagation effects," Phys. Rev. Lett. **83**, 544 (1999), URL http://link.aps.org/doi/10.1103/PhysRevLett.83.544.

[83] S. Hughes, "Breakdown of the area theorem: Carrier-wave rabi flopping of femtosecond optical pulses," Phys. Rev. Lett. **81**, 3363 (1998), URL http://link.aps.org/doi/10.1103/PhysRevLett.81.3363.

[84] J. Xiao, Z. Wang, and Z. Xu, "Area evolution of a few-cycle pulse laser in a two-level-atom medium," Phys. Rev. A **65**, 031402 (2002), URL http://link.aps.org/doi/10.1103/PhysRevA.65.031402.

[85] D. V. Novitsky, "Propagation of subcycle pulses in a two-level medium: Area-theorem breakdown and pulse shape," Phys. Rev. A **86**, 063835 (2012), URL http://link.aps.org/doi/10.1103/PhysRevA.86.063835.

[86] L. Brillouin, *Wave Propagation and Group Velocity* (Academic Press, New York, 1960).

[87] A. Sommerfeld, *Lectures on Theoretical Physics* (Academic Press, New York, 1950).

[88] K. E. Oughstun and G. C. Sherman, *Electromagnetic Pulse Propagation in Causal Dielectrics* (Springer-Verlag, Berlin, 1994).

[89] P. Pleshko and I. Palócz, "Experimental observation of sommerfeld and brillouin precursors in the microwave domain," Phys. Rev. Lett. **22**, 1201 (1969), URL http://link.aps.org/doi/10.1103/PhysRevLett.22.1201.

[90] J. Aaviksoo, J. Lippmaa, and J. Kuhl, "Observability of optical precursors," J. Opt. Soc. Am. B **5**, 1631 (1988), URL http://josab.osa.org/abstract.cfm?URI=josab-5-8-1631.

[91] H. Jeong, A. M. C. Dawes, and D. J. Gauthier, "Direct observation of optical precursors in a region of anomalous dispersion," Phys. Rev. Lett. **96**, 143901 (2006), URL http://link.aps.org/doi/10.1103/PhysRevLett.96.143901.

[92] S. Du, C. Belthangady, P. Kolchin, G. Y. Yin, and S. E. Harris, "Observation of optical precursors at the biphoton level," Opt. Lett. **33**, 2149 (2008), URL http://ol.osa.org/abstract.cfm?URI=ol-33-18-2149.

[93] D. Wei, J. F. Chen, M. M. T. Loy, G. K. L. Wong, and S. Du, "Optical precursors with electromagnetically induced transparency in cold atoms," Phys. Rev. Lett. **103**, 093602 (2009), URL http://link.aps.org/doi/10.1103/PhysRevLett.103.093602.

[94] S.-H. Choi and U. Österberg, "Observation of optical precursors in water," Phys. Rev. Lett. **92**, 193903 (2004), URL http://link.aps.org/doi/10.1103/PhysRevLett.92.193903.

[95] R. R. Alfano, J. L. Birman, X. Ni, M. Alrubaiee, and B. B. Das, "Comment on "observation of optical precursors in water"," Phys. Rev. Lett. **94**, 239401 (2005), URL http://link.aps.org/doi/10.1103/PhysRevLett.94.239401.

[96] U. Österberg, D. Andersson, and M. Lisak, "On precursor propagation in linear dielectrics," Optics Communications **277**, 5 (2007), ISSN 0030-4018, URL http://www.sciencedirect.com/science/article/pii/S0030401807004221.

[97] C. L. Palombini and K. E. Oughstun, "Optical precursor fields in nonlinear pulse dynamics," Opt. Express **18**, 23104 (2010), URL http://www.opticsexpress.org/abstract.cfm?URI=oe-18-22-23104.

[98] B. Macke and B. Ségard, "Optical precursors with self-induced transparency," Phys. Rev. A **81**, 015803 (2010), URL http://link.aps.org/doi/10.1103/PhysRevA.81.015803.

[99] M. D. Crisp, "Propagation of step-function light pulses in a resonant medium," Phys. Rev. A **5**, 1365 (1972), URL http://link.aps.org/doi/10.1103/PhysRevA.5.1365.

[100] R. Marskar and U. L. Österberg, "Linear and nonlinear optical precursors in inhomogeneously broadened two-level media," Phys. Rev. A **86**, 063826 (2012), URL http://link.aps.org/doi/10.1103/PhysRevA.86.063826.

[101] F. A. Hopf and M. O. Scully, "Theory of an inhomogeneously broadened laser amplifier," Phys. Rev. **179**, 399 (1969), URL http://link.aps.org/doi/10.1103/PhysRev.179.399.

[102] J. Eberly, "Area theorem rederived," Opt. Express **2**, 173 (1998), URL http://www.opticsexpress.org/abstract.cfm?URI=oe-2-5-173.

[103] J. E. Rothenberg, D. Grischkowsky, and A. C. Balant, "Observation of the formation of the 0π pulse," Phys. Rev. Lett. **53**, 552 (1984), URL http://link.aps.org/doi/10.1103/PhysRevLett.53.552.

[104] H. Jeong and U. Österberg, "Coherent transients: optical precursors and 0π pulses," J. Opt. Soc. Am. B **25**, B1 (2008), URL http://josab.osa.org/abstract.cfm?URI=josab-25-7-B1.

[105] D. Sarkisyan, B. D. Paul, S. T. Cundiff, E. A. Gibson, and A. Gallagher, "Conical emission by 2-ps excitation of potassium vapor," J. Opt. Soc. Am. B **18**, 218 (2001), URL http://josab.osa.org/abstract.cfm?URI=josab-18-2-218.

[106] D. Pentaris, T. Efthimiopoulos, N. Merlemis, and V. Vaicaitis, "Axial and conical parametric emissions from potassium atoms under two-photon fs excitation," Applied Physics B **98**, 383 (2010), ISSN 0946-2171, URL http://dx.doi.org/10.1007/s00340-009-3801-8.

[107] J. Krasinski, D. J. Gauthier, M. S. Malcuit, and R. W. Boyd, "Two-photon conical emission," Optics Communications **54**, 241 (1985), ISSN 0030-4018, URL http://www.sciencedirect.com/science/article/pii/0030401885903001.

[108] M. Kauranen, J. J. Maki, A. L. Gaeta, and R. W. Boyd, "Two-beam-excited conical emission," Opt. Lett. **16**, 943 (1991), URL http://ol.osa.org/abstract.cfm?URI=ol-16-12-943.

[109] V. Vaičaitis and E. Gaižauskas, "Conical fluorescence emission from sodium vapor excited with tunable femtosecond light pulses," Phys. Rev. A **75**, 033808 (2007), URL http://link.aps.org/doi/10.1103/PhysRevA.75.033808.

[110] V. Vaičaitis and S. Paulikas, "Conical four-wave mixing in sodium vapour excited by femtosecond laser pulses," Applied Physics B **89**, 267 (2007), ISSN 0946-2171, URL http://dx.doi.org/10.1007/s00340-007-2795-3.

[111] V. Vaicaitis, in *Conference on Lasers and Electro-Optics/Quantum Electronics and Laser Science and Photonic Applications Systems Technologies* (Optical Society of America, 2005), p. JWB83, URL http://www.opticsinfobase.org/abstract.cfm?URI=CLEO-2005-JWB83.

[112] H. Skenderović, T. Ban, N. Vujičić, D. Aumiler, S. Vdović, and G. Pichler, "Cone emission induced by femtosecond excitation in rubidium vapor," Phys. Rev. A **77**, 063816 (2008), URL http://link.aps.org/doi/10.1103/PhysRevA.77.063816.

[113] D. Aumiler, T. Ban, and G. Pichler, "Femtosecond laser-induced cone emission in dense cesium vapor," Phys. Rev. A **71**, 063803 (2005), URL http://link.aps.org/doi/10.1103/PhysRevA.71.063803.

[114] W. Chalupczak, W. Gawlik, and J. Zachorowski, "Conical emission in barium vapour," Optics Communications **99**, 49 (1993), ISSN 0030-4018, URL http://www.sciencedirect.com/science/article/pii/0030401893907038.

[115] A. Couairon, E. Gaižauskas, D. Faccio, A. Dubietis, and P. Di Trapani, "Nonlinear x-wave formation by femtosecond filamentation in kerr media," Phys. Rev. E **73**, 016608 (2006), URL http://link.aps.org/doi/10.1103/PhysRevE.73.016608.

[116] D. Faccio, M. A. Porras, A. Dubietis, F. Bragheri, A. Couairon, and P. Di Trapani, "Conical emission, pulse splitting, and x-wave parametric amplification in nonlinear dynamics of ultrashort light pulses," Phys. Rev. Lett. **96**, 193901 (2006), URL http://link.aps.org/doi/10.1103/PhysRevLett.96.193901.

[117] F. Bragheri, D. Faccio, A. Couairon, A. Matijosius, G. Tamošauskas, A. Varanavičius, V. Degiorgio, A. Piskarskas, and P. Di Trapani, "Conical-emission and shock-front dynamics in femtosecond laser-pulse filamentation," Phys. Rev. A **76**, 025801 (2007), URL http://link.aps.org/doi/10.1103/PhysRevA.76.025801.

[118] C. Conti, S. Trillo, P. Di Trapani, G. Valiulis, A. Piskarskas, O. Jedrkiewicz, and J. Trull, "Nonlinear electromagnetic x waves," Phys. Rev. Lett. **90**, 170406 (2003), URL http://link.aps.org/doi/10.1103/PhysRevLett.90.170406.

[119] C. Conti, "X-wave-mediated instability of plane waves in kerr media," Phys. Rev. E **68**, 016606 (2003), URL http://link.aps.org/doi/10.1103/PhysRevE.68.016606.

[120] M. Kolesik, E. M. Wright, and J. V. Moloney, "Dynamic nonlinear x waves for femtosecond pulse propagation in water," Phys. Rev. Lett. **92**, 253901 (2004), URL http://link.aps.org/doi/10.1103/PhysRevLett.92.253901.

[121] Y. Meyer, "Multiple conical emission from near resonant laser propagation in dense sodium vapor," Optics Communications **34**, 439 (1980), ISSN 0030-4018,

URL http://www.sciencedirect.com/science/article/pii/0030401880904125.

[122] J. F. Valley, G. Khitrova, H. M. Gibbs, J. W. Grantham, and X. Jiajin, "cw conical emission: First comparison and agreement between theory and experiment," Phys. Rev. Lett. **64**, 2362 (1990), URL http://link.aps.org/doi/10.1103/PhysRevLett.64.2362.

[123] D. J. Harter and R. W. Boyd, "Conical emission due to four-wave mixing enhanced by the ac stark effect in self-trapped filaments of light," Opt. Lett. **7**, 491 (1982), URL http://ol.osa.org/abstract.cfm?URI=ol-7-10-491.

[124] B. D. Paul, J. Cooper, A. Gallagher, and M. G. Raymer, "Theory of optical near-resonant cone emission in atomic vapor," Phys. Rev. A **66**, 063816 (2002), URL http://link.aps.org/doi/10.1103/PhysRevA.66.063816.

[125] D. J. Harter and R. W. Boyd, "Four-wave mixing resonantly enhanced by ac-stark-split levels in self-trapped filaments of light," Phys. Rev. A **29**, 739 (1984), URL http://link.aps.org/doi/10.1103/PhysRevA.29.739.

[126] R. W. Boyd, M. G. Raymer, P. Narum, and D. J. Harter, "Four-wave parametric interactions in a strongly driven two-level system," Phys. Rev. A **24**, 411 (1981), URL http://link.aps.org/doi/10.1103/PhysRevA.24.411.

[127] R. C. Hart, L. You, A. Gallagher, and J. Cooper, "Failures of the four-wave mixing model for cone emission," Optics Communications **111**, 331 (1994), ISSN 0030-4018, URL http://www.sciencedirect.com/science/article/pii/003040189490474X.

[128] M. E. Crenshaw and C. D. Cantrell, "Temporal and spatial modulation in laser-pulse propagation," Opt. Lett. **13**, 386 (1988), URL http://ol.osa.org/abstract.cfm?URI=ol-13-5-386.

[129] M. E. Crenshaw and C. D. Cantrell, "Conical emission as a result of pulse breakup into solitary waves," Phys. Rev. A **39**, 126 (1989), URL http://link.aps.org/doi/10.1103/PhysRevA.39.126.

[130] I. Golub, G. Erez, and R. Shuker, "Cherenkov emission due to laser-induced moving polarisation in sodium," Journal of Physics B: Atomic and Molecular Physics **19**, L115 (1986), URL http://stacks.iop.org/0022-3700/19/i=4/a=004.

[131] Y. Ben-Aryeh, "Cooperative effects in cone emission from laser-pumped two-level atoms," Phys. Rev. A **56**, 854 (1997), URL http://link.aps.org/doi/10.1103/PhysRevA.56.854.

[132] L. You, J. Mostowski, J. Cooper, and R. Shuker, "Cone emission from laser-pumped two-level atoms," Phys. Rev. A **44**, R6998 (1991), URL http://link.aps.org/doi/10.1103/PhysRevA.44.R6998.

[133] R. W. Boyd, *Nonlinear Optics* (Academic Press, Inc., 1992).

[134] C. F. McCormick, D. R. Solli, R. Y. Chiao, and J. M. Hickmann, "Saturable nonlinear refraction in hot atomic vapor," Phys. Rev. A **69**, 023804 (2004), URL http://link.aps.org/doi/10.1103/PhysRevA.69.023804.

[135] M. Mohebi, M. J. Soileau, and E. W. V. Stryland, "Effect of linear absorption on self-focusing," Opt. Lett. **13**, 758 (1988), URL http://ol.osa.org/abstract.cfm?URI=ol-13-9-758.

[136] J. E. Sansonetti, "Wavelengths, transition probabilities, and energy levels for the spectra of sodium," Journal of Physical and Chemical Reference Data **37**, 1659 (2008), URL http://scitation.aip.org/content/aip/journal/jpcrd/37/4/10.1063/1.2943652.

[137] D. E. Kelleher and L. I. Podobedova, "Atomic transition probabilities of sodium and magnesium. a critical compilation," Journal of Physical and Chemical Reference Data **37**, 267 (2008), URL http://scitation.aip.org/content/aip/journal/jpcrd/37/1/10.1063/1.2735328.

[138] D. A. Steck, Tech. Rep., Oregon Center for Optics and Department of Physics, University of Oregon (2010), URL http://steck.us/alkalidata/sodiumnumbers.pdf.

[139] R. Loudon, *The Quantum Theory of Light (Oxford Science Publications)* (Oxford University Press, USA, 2000), 3rd ed., ISBN 0198501765.

[140] C. Cohen-Tannoudji and S. Reynaud, "Dressed-atom description of resonance fluorescence and absorption spectra of a multi-level atom in an intense laser beam," Journal of Physics B: Atomic and Molecular Physics **10**, 345 (1977), URL http://stacks.iop.org/0022-3700/10/i=3/a=005.

[141] N. Wright and M. C. Newstein, "Self-focusing of coherent pulses," Optics Communications **9**, 8 (1973), ISSN 0030-4018, URL http://www.sciencedirect.com/science/article/pii/0030401873903234.

[142] J. de Lamare, M. Comte, and P. Kupecek, "Spatial distortions of laser pulses in coherent on-resonance propagation: Large-scale self-focusing," Phys. Rev. A **50**, 3366 (1994), URL http://link.aps.org/doi/10.1103/PhysRevA.50.3366.

[143] J. de Lamare, P. Kupecek, and M. Comte, "Spatial distortions of laser pulses in coherent on-resonance propagation: Small-scale self-focusing," Phys. Rev. A **51**, 4289 (1995), URL http://link.aps.org/doi/10.1103/PhysRevA.51.4289.

[144] H. M. Gibbs, B. Bölger, F. P. Mattar, M. C. Newstein, G. Forster, and P. E. Toschek, "Coherent on-resonance self-focusing of optical pulses in absorbers," Phys. Rev. Lett. **37**, 1743 (1976), URL http://link.aps.org/doi/10.1103/PhysRevLett.37.1743.

[145] H. Gibbs, B. Bölger, and L. Baede, "On-resonance self-focusing of optical pulses propagating coherently in sodium," Optics Communications **18**, 199 (1976), ISSN 0030-4018, URL http://www.sciencedirect.com/science/article/pii/0030401876904193.

[146] T. Kampfrath, K. Tanaka, and K. A. Nelson, "Resonant and nonresonant control over matter and light by intense terahertz transients," Nat Photon **7**, 680 (2013), ISSN 1749-4885, URL http://dx.doi.org/10.1038/nphoton.2013.184.

[147] M. C. Beard, G. M. Turner, and C. A. Schmuttenmaer, "Terahertz spectroscopy," The Journal of Physical Chemistry B **106**, 7146 (2002), http://pubs.acs.org/doi/pdf/10.1021/jp020579i, URL http://pubs.acs.org/doi/abs/10.1021/jp020579i.

[148] S. Fleischer, R. W. Field, and K. A. Nelson, "Commensurate two-quantum coherences induced by time-delayed thz fields," Phys. Rev. Lett. **109**, 123603 (2012), URL http://link.aps.org/doi/10.1103/PhysRevLett.109.123603.

[149] T. Seideman, "Rotational excitation and molecular alignment in intense laser fields," The Journal of Chemical Physics **103**, 7887 (1995), URL http://link.aip.org/link/?JCP/103/7887/1.

[150] T. Seideman, "Revival structure of aligned rotational wave packets," Phys. Rev. Lett. **83**, 4971 (1999), URL http://link.aps.org/doi/10.1103/PhysRevLett.83.4971.

[151] T. Seideman, "On the dynamics of rotationally broad, spatially aligned wave packets," The Journal of Chemical Physics **115**, 5965 (2001), URL http://link.aip.org/link/?JCP/115/5965/1.

[152] C.-C. Shu and N. E. Henriksen, "Field-free molecular orientation induced by single-cycle thz pulses: The role of resonance and quantum interference," Phys. Rev. A **87**, 013408 (2013), URL http://link.aps.org/doi/10.1103/PhysRevA.87.013408.

[153] S. Fleischer, I. S. Averbukh, and Y. Prior, "Selective control of molecular rotation," Journal of Physics B: Atomic, Molecular and Optical Physics **41**, 074018 (2008), URL http://stacks.iop.org/0953-4075/41/i=7/a=074018.

[154] I. V. Litvinyuk, K. F. Lee, P. W. Dooley, D. M. Rayner, D. M. Villeneuve, and P. B. Corkum, "Alignment-dependent strong field ionization of molecules," Phys. Rev. Lett. **90**, 233003 (2003), URL http://link.aps.org/doi/10.1103/PhysRevLett.90.233003.

[155] A. G. York and H. M. Milchberg, "Broadband terahertz lasing in aligned molecules," Opt. Express **16**, 10557 (2008), URL http://www.opticsexpress.org/abstract.cfm?URI=oe-16-14-10557.

[156] H. Harde, S. Keiding, and D. Grischkowsky, "Thz commensurate echoes: Periodic rephasing of molecular transitions in free-induction decay," Phys. Rev. Lett. **66**, 1834 (1991), URL http://link.aps.org/doi/10.1103/PhysRevLett.66.1834.

[157] H. Harde and D. Grischkowsky, "Coherent transients excited by subpicosecond pulses of terahertz radiation," J. Opt. Soc. Am. B **8**, 1642 (1991), URL http://josab.osa.org/abstract.cfm?URI=josab-8-8-1642.

[158] D. Weber and S. S. Penner, "Rotational line width measurements on no, hcl, and hbr," The Journal of Chemical Physics **21**, 1503 (1953), URL http://scitation.aip.org/content/aip/journal/jcp/21/9/10.1063/1.1699288.

[159] M. Cho, M. Du, N. F. Scherer, G. R. Fleming, and S. Mukamel, "Off-resonant transient birefringence in liquids," The Journal of Chemical Physics **99**, 2410 (1993), URL http://scitation.aip.org/content/aip/journal/jcp/99/4/10.1063/1.465256.

[160] S. Ramakrishna and T. Seideman, "Intense laser alignment in dissipative media as a route to solvent dynamics," Phys. Rev. Lett. **95**, 113001 (2005), URL http://link.aps.org/doi/10.1103/PhysRevLett.95.113001.

[161] S. Ramakrishna and T. Seideman, "Dissipative dynamics of laser induced nonadiabatic molecular alignment," The Journal of Chemical Physics **124**, 034101 (pages 11) (2006), URL http://link.aip.org/link/?JCP/124/034101/1.

[162] A. D. Poularikas, *Transforms and Applications Handbook; 3rd ed.*, Electrical Engineering Handbook (CRC Press, Hoboken, 2010).

[163] M. Abramowitz and I. Stegun, *Handbook of Mathematical Functions* (Dover Pub., 1965).

[164] J. Arlt, C. Weiss, G. Torosyan, and R. Beigang, "Coherent pulse propagation and the dynamics of rydberg wave packets," Phys. Rev. Lett. **79**, 4774 (1997), URL http://link.aps.org/doi/10.1103/PhysRevLett.79.4774.

[165] P. Goy, J. M. Raimond, M. Gross, and S. Haroche, "Observation of cavity-enhanced single-atom spontaneous emission," Phys. Rev. Lett. **50**, 1903 (1983), URL http://link.aps.org/doi/10.1103/PhysRevLett.50.1903.

[166] G. Alber, H. Ritsch, and P. Zoller, "Generation and detection of rydberg wave packets by short laser pulses," Phys. Rev. A **34**, 1058 (1986), URL http://link.aps.org/doi/10.1103/PhysRevA.34.1058.

[167] J. Parker and C. R. Stroud, "Coherence and decay of rydberg wave packets," Phys. Rev. Lett. **56**, 716 (1986), URL http://link.aps.org/doi/10.1103/PhysRevLett.56.716.

[168] A. Tarasishin, S. Magnitskii, V. Shuvaev, and A. Zheltikov, "Evolution of ultrashort light pulses in a two-level medium visualized with the finite-difference time domain technique," Opt. Express **8**, 452 (2001), URL http://www.opticsexpress.org/abstract.cfm?URI=oe-8-7-452.

[169] H. Leblond and D. Mihalache, "Models of few optical cycle solitons beyond the slowly varying envelope approximation," Physics Reports **523**, 61 (2013), ISSN 0370-1573, URL http://www.sciencedirect.com/science/article/pii/S0370157312003511.

[170] M. Wieczorek, "Shtools, a tool for working with spherical harmonics,", URL http://shtools.ipgp.fr/.

[171] A. Stone and C. P. Wood, "Root rational fraction program for calculating wigner 3j symbols,", URL http://www-stone.ch.cam.ac.uk/documentation/rrf/index.html.

[172] A. Stone and C. Wood, "Root-rational-fraction package for exact calculation of vector-coupling coefficients," Computer Physics Communications **21**, 195 (1980), ISSN 0010-4655, URL http://www.sciencedirect.com/science/article/pii/0010465580900405.

[173] A. E. Kaplan, "Diffraction-induced transformation of near-cycle and subcycle pulses," J. Opt. Soc. Am. B **15**, 951 (1998), URL http://josab.osa.org/abstract.cfm?URI=josab-15-3-951.

[174] A. April, *Ultrashort, Strongly Focused Laser Pulses in Free Space* (InTech, 2010), chap. 16, pp. 356–382.

[175] E. Varoquaux, G. A. Williams, and O. Avenel, "Pulse propagation in a resonant medium: Application to sound waves in superfluid ^3B," Phys. Rev. B **34**, 7617 (1986), URL http://link.aps.org/doi/10.1103/PhysRevB.34.7617.

[176] Y.-i. Suzuki and T. Seideman, "Mapping rotational coherences onto time-resolved photoelectron imaging observables," The Journal of Chemical Physics **122**, 234302 (2005), URL http://scitation.aip.org/content/aip/journal/jcp/122/23/10.1063/1.1926282.

[177] D. Daranciang, J. Goodfellow, M. Fuchs, H. Wen, S. Ghimire, D. A. Reis, H. Loos, A. S. Fisher, and A. M. Lindenberg, "Single-cycle terahertz pulses with > 0.2 v/[a-ring] field amplitudes via coherent transition radiation," Applied Physics Letters **99**, 141117 (pages 3) (2011), URL http://link.aip.org/link/?APL/99/141117/1.

[178] Z. Wu, A. S. Fisher, J. Goodfellow, M. Fuchs, D. Daranciang, M. Hogan, H. Loos, and A. Lindenberg, "Intense terahertz pulses from slac electron beams using coherent transition radiation," Review of Scientific Instruments **84**, 022701 (pages 10) (2013), URL http://link.aip.org/link/?RSI/84/022701/1.

[179] I. I. Rabi, "Space quantization in a gyrating magnetic field," Phys. Rev. **51**, 652 (1937), URL http://link.aps.org/doi/10.1103/PhysRev.51.652.